



ČESKÉ VYSOKÉ UČENÍ TECHNICKÉ V PRAZE

Fakulta stavební

Doktorský studijní program: **STAVEBNÍ INŽENÝRSTVÍ**

Studijní obor: **Fyzikální a materiálové inženýrství**

Mgr. Denis Davydov

**VISCO-ELASTO-PLASTICKÉ VLASTNOSTI CEMENTOVÉ
PASTY**

VISCO-ELASTO-PLASTIC PROPERTIES OF CEMENT PASTE

DISERTAČNÍ PRÁCE K ZÍSKÁNÍ AKADEMICKÉHO TITULU Ph.D.

Školitel: **Prof. Ing. Milan Jirásek, DrSc.**

Praha, leden 2010

Contents

1	General Introduction	18
1.1	Introduction	19
1.1.1	Research Motivation	19
1.1.2	Research Objectives	19
1.2	Cement Paste System	21
1.2.1	Chemistry, Morphology, Hydration Kinetic	21
1.2.2	Creep and Shrinkage Mechanisms in Cement Paste	36
1.3	Basic Creep Modeling	48
1.3.1	Compliance and Relaxation Functions	48
1.3.2	Several Other Approaches for Creep Modeling	54
1.4	Modelling of Microstructure of Cement	59
1.5	State of the Art: Models of the C-S-H Structure and Creep Theories	61
1.5.1	C-S-H Microstructure	61
1.5.2	Microstructural Creep Theories	66
1.6	Conclusions	78
2	Homogenization Techniques	80
2.1	Mean Field Elastic Homogenization	81
2.2	Mean Field Strength Homogenization	86
2.2.1	Introduction	86
2.2.2	Effective Strain Rate Approach	87
2.2.3	LCC Homogenization Method	90
2.3	Fast Fourier Transform Homogenization Method	98
2.3.1	Formulation	98
2.3.2	Algorithm	100
3	Nanoindentation	102
3.1	Analytical Solutions for Indentation Problem	103
3.1.1	Elastic Material	103
3.1.2	Viscoelastic Material	104

3.2	Matrix-inclusion Heterogeneity	108
3.3	Conclusions	110
4	Finite Element Method	111
4.1	Mathematical Formulation of Plastic Model	112
4.1.1	Return Mapping Algorithm	112
4.1.2	Algorithmic Tangent Stiffness Matrix	114
4.2	Large-strain Formulation	119
4.2.1	Multiplicative Decomposition	119
4.2.2	Numerical Implementation Details in FEM Software Adina	121
4.3	Dimensionless Form of Constitutive Equations	123
4.4	Numerical Aspects of the Considered System of Nonlinear Equations	125
4.4.1	Elliptic Case	125
4.4.2	Hyperbolic Case	127
4.4.3	Consistent Tangent Matrix	128
4.5	Check of the Implementation of Elliptic Yield Criteria	130
4.6	Analysis of NI with Matrix-pore Model	133
4.7	Multicycle Loading and Norton Visco-plastic Model	135
4.8	Conclusions	138
5	Analysis of Nanoindentation Results	139
5.1	Introduction	140
5.2	Materials and Preparation	142
5.3	Methods	144
5.4	Results and Discussion	147
5.4.1	Repeatability of SNI and Packing-Density Fit	147
5.4.2	Comparison of SNI Volume Fractions with Data from BSE and XRD	148
5.4.3	Choice of Penetration Depth	150
5.4.4	“Manual” and “Grid” Indentation Methods	153
5.4.5	Comparison of the Results Between Prague and Vienna NI Groups	156
5.5	Conclusion	156
6	Homogenization of Cement Paste Properties	160
6.1	Introduction	161
6.2	Investigated Materials and Microstructures	163
6.2.1	Material Properties of Cement Phases	163
6.3	Utilized Methods	165
6.3.1	Finite Elements Method	166

6.3.2	Particle Model for Cement Paste	167
6.4	Results and Discussion	175
6.4.1	Real Microstructure	175
6.4.2	Modeled Microstructure	176
6.5	Conclusions	178
7	Conclusions	180
7.1	Conclusions	181
7.1.1	Experiments	181
7.1.2	Homogenization	182
7.1.3	FE Analysis of NI Experiment	182

List of Tables

1.2.1 Classification of pores	34
1.5.1 Summary of the nano-models of the C-S-H (after [51]).	61
1.5.2 Indentation modulus, M , and volume fraction, f , for the C-S-H _{LD} and C-S-H _{HD} phases as determined from indentation measurements of white Portland cement paste specimens mixed at a water/cement ratio of 0.5 and given the curing time and temperature indicated (after [53])	64
1.5.3 Theoretical relationship between relative humidity and pore size. Larger pores will empty (dry) and smaller pores will remain saturated (after [54])	66
5.4.1 Results of SNI analysis of 20×20 indents at $20 \mu\text{m}$ spacing under 2-30-2-2 mN loading performed on white cement at age 28 days.	147
5.4.2 Volume fraction of phases determined by SNI, BSE and XRD on white cement at age 28 days.	149
5.4.3 Application of scaling relationships to results of SNI on white cement at age 28 days with different loading programs. $R^2 (M)$ and $R^2 (H)$ are R-squared correlation for indentation moduli and hardness respectively. . .	150
5.4.4 Self-consistent homogenization of cement paste elastic properties based on XRD volume fractions compared with results from NI at the level of cement paste.	153
6.2.1 Chemical composition of the investigated cements measured by Rietveld analysis.	164
6.2.2 Assumed material properties of the cement paste phases.	164
6.4.1 Comparison of elastic and inelastic properties of the RVE predicted by the investigated methods.	175

List of Figures

1.2.1	Different scales of the concrete micro structure	22
1.2.2	Formation of separated hydration shells over the time according to the grain size. The middle column shows the situation after about one day, all grains are surrounded by a thin shell of C-S-H separated by around $1\ \mu m$ from the underlying grain. The column on the right shows the situation in the mature paste. Small grains (top) hydrate completely in the first stage and remain as hollow shells of hydration product. Medium size grains (middle) for a thicker rim of C-S-H as the grain continues to hydrate, perhaps with a small hole at the center. Grains larger than about $15\ \mu m$ hydrate to fill in the gap between shell and grain. (after [93])	24
1.2.3	Frequency plot (left) and spatial distribution(right) of indentation modules based on the 10×10 grid of nanoindentation measurements. Results are for a Portland cement paste mixed at the w/c ratio 0.5 and cured for 28 days at 20 C (after [53] and [54])	25
1.2.4	Effect of water/cement ratio on the structure of hardened cement paste (after [108])	26
1.2.5	Summary of the microstructural development of a grain of cement. (a) Unhydrated section of polymineral grain (b) -10min. Some C_3A reacts with calcium sulfate in solution. Amorphous, aluminate-rich gel forms on the surface and short AFt $C_6\bar{A}\bar{S}_3H_{32}$ rods nucleate at edge of gel and in solution. (c) -10h. Reaction of C_3S to produce “outer” product C-S-H on AFt rod network leaving $1\mu m$ between grain surface and hydrated shell. (d) – 18h. Secondary hydration of C_3A reacts with any AFt $C_6\bar{A}\bar{S}_3H_{32}$ inside shell forming hexagonal plates of AFm. Continuing formation of “inner” product reduces separation of anhydrous grain and hydrated shell. (f) – 14 days. Sufficient “inner” C-S-H has formed to fill in the space between grain and shell. The “outer” C-S-H has become more fibrous. (g) – years. The remaining anhydrous material reacts to form additional “inner” product C-S-H. The ferrite phase appears to remain unreacted. (after [89])	27

1.2.6	Particle distribution of silica fume and its affect on the packing (after [108])	28
1.2.7	Heat evolution during the hydration of C_3S and C_3A (after [108])	28
1.2.8	Microstructure of a commercial clinker (BSE image). Light-gray crystals of allite and darker round crystals of belite can be seen in a matrix of the interstitial phases-ferrite (light) and aluminate (darker). Porosity (black) can also be seen (after [89])	29
1.2.9	Scanning electron micrograph of anhydrous cement grains showing the wide range of particle sizes. Small crystals of calcium sulfate can be seen on the surfaces of the larger grains (after [89])	29
1.2.10	Illustration of the “wall” effect (after [92])	30
1.2.11	Structure of the interfacial transition zone between rounded, dense, natural aggregate and Portland cement matrix (after [108])	31
1.2.12	Comparative stress-strain curves for aggregate, paste and concrete, the quasi-brittle behavior of concrete illustrates the importance of the ITZ for the macroscopic properties of concrete (after [92])	31
1.2.13	Average porosity in ITZ at various ages (after [92])	32
1.2.14	Distribution of porosity in the ITZ of concretes with and without silica fume (after [92])	32
1.2.15	BSE image of concrete, exposed for 10 years in a wet cold climate (after [93])	33
1.2.16	Scale of the pore-size distribution and their relationship with the w/c ratio (after [108])	34
1.2.17	Degree of hydration measured by XRD/Rietveld and BSE/IA (after [91])	35
1.2.18	Amount of unreacted cement measured by XRD/Rietveld and BSE/IA (after [91])	35
1.2.19	Shrinkage strain of the concrete sample for one cycle of drying and wetting (after [73])	36
1.2.20	(a) The loss of water at room temperature from a Portland cement mortar sample is shown as a function of relative humidity; (b) The corresponding shrinkage is shown as a function of water loss. Note the points A, B, and C identify the same points in both figures (after [73])	37
1.2.21	Time-dependent strain in concrete subjected at age 28 days to the sustained load for 90 days and then 30 days without the load (after [73]) . .	43
1.2.22	Influence of relative humidity on (a) drying shrinkage and (b) creep of concrete (after [73])	45
1.2.23	Pickett’s effect	47

1.3.1	Compliance function shown by unit creep curves for different ages at loading (after [57])	49
1.3.2	Relaxation function of concrete (after [57])	50
1.3.3	Creep isochrones at high stress (after [57])	50
1.3.4	a) Non-aging Kelvin chain, b) aging Kelvin chain, c) Maxwell chain (after [57])	53
1.3.5	Deviatoric reversible and irreversible mechanism for basic creep used by Benboudjema (after [14])	55
1.3.6	Volumetric reversible and irreversible mechanism for basic creep used by Benboudjema (after [14])	55
1.4.1	Microstructure 50x50x50 μm , $w/c = 0.24$, initial (left) and at the degree of hydration of 0.63 (right). Red = C_3S , cyan = C_2S , green = $CCCA$, yellow = $CCCCAF$, black = porosity, violet = C-S-H, blue = CH(after [111])	60
1.5.1	2-D scheme of C-S- H_{HD} (left) and C-S- H_{LD} (right) at water/cement ratio = 0.4 (after [51])	62
1.5.2	Micromechanical prediction (solid line) of the indentation modulus of an aggregation of spherical particles (with $m_s=65$ GPa) versus the packing density (1-porosity). The experimental modulus values of C-S- H_{LD} and C-S- H_{HD} are also plotted, using the packing densities of C-S-H globules specified by the colloid model (after [53])	63
1.5.3	Distribution of the creep parameters A and $1/B$ determined from multiple indents across a grid on each paste. Assignment of the peaks to C-S- H_{LD} and C-S- H_{HD} at left for parameter A is based on the indentation module (after [53])	64
1.5.4	The intermediate C-S- H_{LD} structure, consisting of a relatively loose packing of 5 nm globules. Shown is a 2D slice from a 3D nanostructure generated by a computer simulation based on autocatalytic growth of spheres. The smaller squares are spheres (globules) lying just above or below the plane. The overall packing density is 52% and each globule on average contacts 6.3 nearest neighbors (after [53])	66
1.5.5	Sliding between C-S-H sheets resulting in breaking and reconstitution of hydrogen bonds	68
1.5.6	Compliance of hydrated cement paste ($w/c = 0.5$) after re-saturation from different drying pre-treatments (after [101])	69
1.5.7	Structural model in solidification theory (after [9])	70

1.5.8	(a) Idealized microstructure of hardened cement paste; (b) micropore in the cement gel, disjoining pressure P_d and microprestress S ; (c) Kelvin chain structural model with flow element and microprestress relaxation mechanism; (d) dependence of flow viscosity on microprestress (after [12])	72
2.1.1	Eshelby's problem: single inclusion in an infinite matrix subjected to remote uniform strains	82
3.1.1	a) Illustration of the load-penetration P-h curve; b) Trapezoidal loading program used in a nanoindentation experiment; c) Indentation of material by a rigid axisymmetric indenter	103
3.1.2	a) Experimental $F(t)$ curve and its fit in dimensionless form; b) Experimental penetration depth $h(t)$ and the corresponding fit by a porous logarithmic creep model	107
3.2.1	Axially symmetric FE model for the study of the effect of inhomogeneity on Oliver-Pharr procedure	108
3.2.2	Normalized difference between the elastic modulus evaluated by Oliver-Pharr procedure (E_{op}) and the actual modulus of inclusion (E_0) for different normalized indentation depths (h/R) and different ratios between matrix and inclusion moduli $(E_1 - E_0)/E_0$	109
4.4.1	Isolines of yield equation (4.1.14) (a) and flow equation (4.1.12) (b) with trial and final stress states. Unmarked grid corresponds to zero.	126
4.4.2	Isolines of yield equation (4.1.14) (a) and flow equation (4.1.12) (b) with relatively big trial and final stress states. Unmarked grid corresponds to zero.	127
4.4.3	Case $A > 0$. Left: yield surface $f(p, q)$, parametric line $(p(\lambda), q(\lambda))$, yield surface $f(\lambda)$ and its derivative $df/d\lambda$; Right: Dependence of final stress p, q on λ . Solution corresponds to $\lambda \approx 100$	128
4.4.4	Case $p^T < -B/2A$. Left: yield surface $f(p, q)$, parametric line $(p(\lambda), q(\lambda))$, yield surface $f(\lambda)$ and its derivative $df/d\lambda$; Right: Dependence of final stress p, q on λ	129
4.4.5	Case $p^T > -B/2A$. Left: yield surface $f(p, q)$, parametric line $(p(\lambda), q(\lambda))$, yield surface $f(\lambda)$ and its derivation $df/d\lambda$; Right: Dependence of final stress p, q on λ	129
4.5.1	Plane-strain formulation of one-element shear in Adina	130
4.5.2	Comparison of the results in the case of the perfect shear	130
4.5.3	Plane-strain formulation of the volumetric load in Adina	131

4.5.4	Comparison of the results in the case of the volumetric load	131
4.5.5	Plane-strain formulation of the uniaxial load in Adina	132
4.5.6	Comparison of the results in the case of the uniaxial load	132
4.6.1	Part of the mesh, used in FEM study of NI experiment	133
4.6.2	Maximum principal plastic strain	133
4.6.3	Mesh after indentation about 50 nm for von Mises model with (b) and without (a) hardening.	134
4.7.1	Nanoindentation loading program	135
4.7.2	Axially symmetric FE model of nanoindentation experiment	136
4.7.3	Response calculated with Norton's viscoplastic model.	137
5.1.1	a) Illustration of the load-penetration curve; b) trapezoidal loading pro- gram used in a NI experiment; c) indentation of a substrate by a rigid axisymmetric indenter.	140
5.1.2	(a) A transmission electron microscope (TEM) micrograph showing outer C-S-H and inner C-S-H present in a hardened C_3S paste with $w/c =$ 0.4 hydrated at 20°C for 8 years. White arrows indicate the boundary between inner C-S-H and outer C-S-H; the inner C-S-H is in the upper left part of the micrograph. (b) An enlargement of a region of inner C-S-H. (c) An enlargement of a fibril of outer C-S-H. (Reprinted with permission from [85]).	143
5.3.1	Example of Gaussian mixture deconvolution of NI data with clustering: a) plane of parameters M and H , b) plane of parameters H and C	146
5.4.1	Porosity obtained from scaling relationship fit for C-S- H_{HD} and C-S- H_{LD} from 400 indents with 2-30-2-2 mN loading.	148
5.4.2	BSE image analysis: a) $200 \times 200 \mu m^2$ ($144 \times 144 px$) crop of the 1250×850 μm^2 image; b) image histogram.	149
5.4.3	Porosity of C-S- H_{HD} and C-S- H_{LD} , obtained with scaling relationships applied to 4 grids, each with 100 indents, at different loading levels: a) 1-30-1-1 mN, b) 2-30-2-2 mN, c) 4-30-4-4 mN, d) 5-30-5-5 mN.	151
5.4.4	Results of SNI with four phases depending on maximum load: a) Inden- tation modulus, b) hardness, c) creep parameter, d) weights in Gaussian mixture model, e) maximum penetration depth.	152
5.4.5	BSE (bottom) and AFM (top; after indentation; average plane is sub- tracted) images illustrating the proposed "manual" indentation technique and the choice of NI points for white AALBORG cement paste with $w/c = 0.4$	154

5.4.6	AFM image with prescribed points for NI in Hysitron software. The scan size is 34 nm.	155
5.4.7	Comparison of the “grid” (g , 600 random indents) and “manual” (m , 21 indents into C-S- H_{HD}) indentation techniques on a white cement paste sample $w/c = 0.4$, hydrated for 18 months in saturated conditions; the time of exposure to room conditions is around 14 days.	156
5.4.8	BSE (bottom) and AFM (top; after indentation; average plane subtracted) images showing the regions selected for C-S- H_{HD} indentation of alite paste.	157
5.4.9	Indentation moduli histogram for alite sample with $w/c = 0.4$, $h_{max} = 230 \pm 49$ nm (72 indents).	158
5.4.10	Comparison of NI results obtained from 400 indents using the “grid” indentation done by the Prague (P) and Vienna (V) groups on the same white cement paste sample, $w/c = 0.4$, age = 2 months.	158
6.2.1	Particle size distribution curves, a), and cumulative particle size distribution curves, b), for Cem A and Cem C.	165
6.2.2	Calorimetric record of heat of hydration of Cem A and Cem C cement pastes.	166
6.3.1	Comparison of the considered yield surfaces for C-S-H.	166
6.3.2	Comparison of Young’s moduli of the struts predicted by the FFT and FEM , respectively, for Cem A after 1, 7 and 28 days of hydration, respectively.	168
6.3.3	Comparison of the tensile strengths of the struts predicted by the FFT and FEM , respectively, for Cem A after 1, 7 and 28 days of hydration, respectively.	169
6.3.4	Comparison of Young’s moduli of the struts predicted by the FFT and FEM , respectively, for Cem C after 1, 7 and 28 days of hydration, respectively.	169
6.3.5	Comparison of the tensile strengths of the struts predicted by the FFT and FEM , respectively, for Cem C after 1, 7 and 28 days of hydration, respectively.	170
6.3.6	Comparison of tensile and compressive strengths of the struts for Cem A, a), and Cem C, b), considering the (2.2.63) yield criterion. $f_t = f_c$ for the $J2$ plasticity yield criterion.	170

6.3.7	Comparison of Young's modulus, a), tensile strengths, b), of the struts predicted by the <i>FFT</i> and <i>FEM</i> , respectively, and comparison of tensile and compressive strengths, c), on microstructures of NIST Cem with edges of $60\ \mu\text{m}$ (red dots) and $150\ \mu\text{m}$ (black dots).	171
6.3.8	Material models of the struts: elastic domain. Brittle cracking occur when the domain is reached for $\omega > \omega_0$ and plastic yielding for $\omega < \omega_0$. .	171
6.3.9	Microstructure of $60 \times 60 \times 60\ \mu\text{m}$ used for initial comparison of the methods - three mutually orthogonal cut planes going through the center of the microstructure.	172
6.3.10	Elastic stain in all phases, a), and plastic strain in C-S-H after the last step of the full non-linear <i>FEM</i> analysis in Abaqus for RVE ₆₀ . The microstructure was loaded in direction 1.	172
6.3.11	Comparison of stress-strain curves predicted by the particle model with and without cracking and the stress-strain curve from the full nonlinear <i>FEM</i> analysis in Abaqus.	173
6.3.12	Simulations of the uniaxial tensile test, a), and the uniaxial compressive test, b), on the NIST cement microstructure of 60 and $150\ \mu\text{m}$ assuming <i>J2</i> and (2.2.63) yield condition, respectively.	174
6.4.1	Simulations of the uniaxial tensile test, a), and the uniaxial compressive test, b), on Cem A microstructures.	176
6.4.2	Simulations of the uniaxial tensile test, a), and the uniaxial compressive test, b), on Cem C microstructures.	177
6.4.3	Compressive and tensile strength, modeled with particle model and elastic limit approximation via <i>FFT</i> for CemA and CemC $150\ \mu\text{m}$ RVE microstructures at different age.	177
6.4.4	Elastic moduli calculated with <i>FFT</i> and <i>PM</i> for CemA and CemC microstructures at different age.	178

ACKNOWLEDGMENTS

Before all other acknowledgments, I would like to express my gratitude to my thesis advisor, Prof. Ing. Milan Jirásek, DrSc., who was always ready to help me with an advise or answer my questions regarding the mathematical background of certain topics.

Several other personalities from the university were involved in this thesis. Special thanks belong to Prof. Ing. Petr Kabele, Ph.D., for his help in early stages of this project, in particular with modeling of nanoindentation in Adina, RNDr. Lubomír Kopecký for his help and will to study my samples in BSE microscope, Doc. Ing. Bořek Patzák, Ph.D., for his advice and help with OOFEM software and implementation of contact conditions and material models, Doc. Ing. Vít Šmilauer Ph.D., for many suggestions dealing with homogenization and help in debugging the implementation of FFT algorithm, Ing. Jan Skoček for his will to cooperate in studying elasto-plastic homogenization, which resulted in a join publication, Prof. Ing. Henrik Stang, Ph.D., and Ing. Bruno Capra, Ph.D., who organized my secondment periods and welcomed me in Oxand, Fontainebleau, France and DTU, Lyngby, Denmark respectively, Prof. Dipl.Ing. Roman Lackner, Ph.D., and his student Dipl.Ing. Christian Pichler, Ph.D., for fruitfull discussions on scaling relationships as well as for the help in nanoindentation sample preparation and testing, Doc. Ing. Jiří Němeček, Ph.D., and Ing. K. Forstová, Ph.D., for introduction to CSM and Hysitron nanoindentation machines, among others.

I would also like to thank all members of MC-RTN and Nanocem consortium for fruitful discussions during meetings, workshops and conferences. And especially Prof. Karen Scrivener, the main organizer of MC-RTN I did my study in, and Marie-Alix Dalang-Secréta for her great help in the administrative part of the project.

I gratefully acknowledge the European Community for the full support under the Marie Curie Research Training Network MRTN-CT-2005-019283 “Fundamental understanding of cementitious materials for improved chemical, physical and aesthetic performance”. At last, I would like to thank all MC-RTN students for great moments shared together during all courses in different parts of Europe. And of course I appreciate the encouragement and patience of my relatives, particularly my parents and my wife Natalya.

Czech Technical University in Prague
Faculty of Civil Engineering

Abstract

Visco-elasto-plastic properties of cement paste

by Denis Davydov

In this PhD thesis, several open questions related to the experimental protocol and processing of data acquired by the nano-indentation (NI) technique are investigated. The volume fractions of mechanically different phases obtained from statistical NI (SNI) analysis are shown to be different from those obtained by back-scattered electron (BSE) image analysis and X-ray diffraction (XRD) method on the same paste. Judging from transmission electron microscope (TEM) images, the representative volume element of low-density calcium-silicate hydrates (C-S-H) can be considered to be around 500 nm, whereas for high-density C-S-H (C-S-H_{HD}) it is about 100 nm. This poses a question of choosing the right penetration depth for NI experiment. Changing the maximum load from 1 mN to 5 mN, the effect of penetration depth on the experimental results is studied. As an alternative to the SNI method, a “manual” indentation method is proposed, which combines information from BSE and atomic-force microscopy (AFM), coupled to the NI machine. The AFM allows to precisely indent a high-density C-S-H rim around unhydrated clinkers in cement paste. Yet the results from that technique still show a big scatter.

In the case of the ordinary Portland cement paste, a simple relationship linking the strength of the cement paste with its porosity was proposed and widely used for a long time. However, in today’s blended cements, systems with higher porosity and higher strength at the same time are often found. Thus, the arrangement of the phases in the RVE plays an important role and the simple relationship cannot be used anymore. It is well understood that the modeling of microstructures of such systems and models linking microstructures with mechanical properties are necessary for the strength prediction. In the present thesis, the mean-field strength homogenization approach, approaches based on numerical solutions of linear-elastic problems and a modified particle model for concrete are utilized to predict the tensile and compressive strength of measured and modeled microstructures. Critical aspects of each method are identified, discussed and compared with other methods. It is verified that analytical methods based on the second-order stress estimates do not reflect the actual microstructure and significantly overestimate strengths compared to results obtained by numerical methods. Further, it is verified and quantified that the perfectly brittle strength estimate differs significantly from the strengths obtained

from particle model for cement microstructures and thus only nonlinear material models and nonlinear simulations can provide satisfactory results. The modified particle model provides a robust modeling tool with results matching favorable results of a full nonlinear finite element analysis with significantly reduced computational costs. Further, the effect of cracking of the C-S-H is investigated using the particle model. These results have been obtained in collaboration with Jan Skoček, PhD student at the Danish Technical University, who has been developing particle modeling for cement paste [96].

Based on the self-consistent homogenization scheme and Laplace-Carson transform, a semi-analytical procedure for solution of indentation of matrix-pore visco-elastic composite is proposed. Its applicability is demonstrated on a test example. The tip shape can be arbitrary, as long as it is described by constants $C_0 - C_8$. In order to add plastic behavior, elasto-plastic matrix-pore Drucker-Prager model is implemented in two Finite Element (FE) programs: Adina (in Fortran) and OOFEM (in C++). The study of an elliptic-hyperbolic perfectly plastic constitutive equation reveals certain numerical problems while solving the resulting system of nonlinear equations. These problems lead to false and physically meaningless solutions or low accuracy of the solution. Detailed numerical procedure formulated in 1D is proposed for both elliptic and hyperbolic cases, which allows to overcome the problems mentioned above. FE study of nanoindentation experiment using proposed [110] matrix-pore elasto-plastic constitutive equations clearly reveals the following effect. During the first few iterations, the elements that are in contact with the tip become perfectly plastic, the zone with which the tip is in contact allows any (infinite) displacements without transfer of forces to adjacent elements. As a result, it leads to absolute compaction of these elements and negative volume. A similar effect is demonstrated for von Mises elasto-plastic model. Isotropic hardening is shown to help to overcome this issue. Therefore, it seems that scaling relationships for NI experiments for any model should be obtained using FEM with appropriate loading range, which would correspond to experimentally observed penetration depths.

LIST OF SYMBOLS AND ABBREVIATIONS

- \mathbf{x} - position vector in R^3
 \mathbf{E} - macroscopic strain
 $\mathbf{u}(\mathbf{x})$ - displacements
 f_r - volume fraction of phase r in RVE
 $\boldsymbol{\varepsilon}(\mathbf{x})$ - microscopic strain
 $\boldsymbol{\Sigma}$ - macroscopic stress
 $\boldsymbol{\sigma}$ - microscopic stress
 \mathbb{A}_r - localization tensor
 \mathbb{I} - fourth order unit tensor
 \mathbb{C} - elastic stiffness tensor
 $\langle \rangle_V$ - averaging over the volume
 \mathbb{C}_{hom} - homogenized stiffness tensor
 \mathbb{P}_r^m is the fourth-order Hill tensor in Eshelby problem
 \mathbb{S}_r^m - is the Eshelby tensor of phase r
 K - macroscopic bulk modulus
 G - macroscopic shear modulus
 \mathbf{d} - microscopic strain rate
 π_i - maximum dissipation capacity (support function)
 G_r - strength domain
 \mathbf{v} - displacement speed
 \mathbf{D} - macroscopic strain rate
 Π^{hom} - maximum dissipation capacity of homogenized media
 $K(\mathbf{D})$ - set of kinematically admissible strain rates
 I'_1 - first invariant of strain rate \mathbf{d}
 J'_2 - second invariant of strain rate \mathbf{d}
 $\boldsymbol{\delta}$ - deviator part of strain rate \mathbf{d}
 k^r - microscopic bulk moduli
 μ^r - microscopic shear moduli
 \mathbf{d}^r - strain rate measure in Effective Strain Rate approach
 $f_v = \text{tr}(\mathbf{f})$ - volumetric constant for any \mathbf{f}
 $f_d = \text{sqrts} : \mathbf{s}$ - deviatoric constant for any tensor \mathbf{f} , with $\mathbf{s} = \mathbf{f} - \frac{1}{3}f_v\mathbf{I}$ - its deviatoric part
 $\boldsymbol{\Delta}$ - deviatoric part of macroscopic strain rate \mathbf{D}
 W - macroscopic strain rate energy
 w - microscopic strain rate energy
 A_c - crosssection of indenter's tip
 h - penetration depth in NI

P - load force in NI

$M = \frac{E}{1-\nu}$ - indentation moduli

$\hat{\bullet}(s)$ is a Laplace-Carson transform of $\bullet(t)$

ϵ^{pl} - total plastic strain

\mathbb{C}^{el} - elastic constitutive tensor

ϵ - total strain

σ^T - trial stress

$\Delta\epsilon$ - strain increment

$p = -\frac{1}{3} \sigma : \mathbf{I}$

$q = \sqrt{\frac{3}{2} \mathbf{S} : \mathbf{S}}$ - deviator part of stress

q^T - q , corresponding to trial stress

\mathbf{S}^T - deviatoric trial stress

ϵ_d^{el} - deviatoric part of elastic strains

ϵ_d^T - deviatoric part of trial strains

f - yield function

\mathbb{C}^{alg} - algorithmic tangent stiffness

\mathbf{n} - direction of deviatoric stress

${}^t_0\mathbf{F}$ - deformation gradient from initial configuration to current at time t

${}^t_\tau\mathbf{F}^{ve}$ elastic deformation gradient from relaxed configuration τ to current t

${}^\tau_0\mathbf{F}^p$ plastic deformation gradient from initial configuration to elastically relaxed τ

J^{ve} - visco-elastic jacobian

J^p - plastic jacobian

\mathbf{R}, \mathbf{U} - elements of polar decomposition

\mathbf{H} - right logarithmic Hencky measure

σ - Cauchy stress

$\bar{\sigma} = (R^{ve})^T \cdot \sigma \cdot R^{ve}$ - rotated Cauchy stress

$\tau = J \sigma$ - Kirchoff stress

$\bar{\tau} = J (R^{ve})^T \cdot \sigma \cdot R^{ve}$ - rotated Kirchoff stress

1 General Introduction

1.1 Introduction

1.1.1 Research Motivation

Concrete is one of the most widely used materials in the world. It has several advantages such as low market price, wide availability of raw materials and sufficient mechanical performance for its application. Currently, there is no other material which can completely substitute concrete in the construction industry.

Yet, the physics and chemistry of concrete are very complex. The material can be considered at least on four scales: concrete, mortar, cement paste, individual hydration products.

Engineering approaches still consider simplified codes for design of structures. These codes are fitted against a large experimental database, which is different for different codes. Therefore different results are produced by different codes for the same problem. The same situation appears in the industry where trial-and-error method is mostly used in development of new mixtures. This is very costly and can be potentially replaced by virtual (numerical) experiments.

In order to progress in design of new concrete, multi-disciplinary (chemistry, physics and atomistic modeling, mechanics) studies have to be done.

The current project represents a part of such studies done within the Marie Curie Research Training Network (*MC – RTN*) devoted to cementitious materials. The project deals with the visco-elasto-plastic properties of cement paste and its phases, measured by the nanoindentation technique.

1.1.2 Research Objectives

From the mechanical point of view, one has to deal with homogenization techniques for elastic, viscous or plastic properties of Representative Volume Elements (RVE) of cement paste, which can be obtained from different hydration models. Mortar and concrete levels can be considered in a similar but more simplified fashion since there is no need for complex microstructure models, RVE can be generated numerically based on particle size distribution of sand particles (in the case of mortar) or gravel and rock (in the case of concrete).

Since measurements of mechanical properties of bulk phases present in cement paste are still out of reach, nanoindentation technique is the only possible solution to that problem. Yet, an analytical solution of the contact problem can be obtained only for a homogeneous medium, but it is still commonly applied to cement paste, which is heterogeneous.

Therefore, the objectives of the current study are to improve understanding of C-S-H

mechanical properties and procedures of their identification using nanoindentation experiment, as well as application and study of different elasto-plastic homogenization techniques at the level of cement paste.

1.2 Cement Paste System

1.2.1 Chemistry, Morphology, Hydration Kinetic

Cement paste and concrete itself are very complex heterogeneous materials, with different structure at different RVE ranging from nanometer scale to macroscopic decimeter scale. It consists of amorphous and crystalline phases plus pores. Kinetics of processes during hydration impacts the phase distribution and hence microstructure. The temperature is not concerned explicitly.

Let us consider the microstructure at four different scales:

1. $10^{-9} - 10^{-6}$ m - C-S-H, polymineral grains content:
 - a) Polymineral grains of of several main minerals:
 - C_3S - alite, Tricalcium Silicate, ≈ 60 ;
 - C_2S - belite, Dicalcium Silicate, ≈ 15 ;
 - C_4AF - ferrite, Tetracalcium aluminoferrite, ≈ 4
 - C_3A - aluminate, Tricalcium aluminate, ≈ 4
 - b) Admixtures:
 - Silica fume ($<0.1 \mu m$), is used to densify the packing;
 - c) C-S-H - Calcium-Silica-Hydrate:
 - $C-S-H_{HD}$ has a short-range order, nano porous
 - $C-S-H_{LD}$ amorphous, intermixed with capillary pores[90]
2. $10^{-6} - 10^{-4}$ m - cement paste
 - a) Polymineral grains
 - b) Porous C-S-H
 - c) Portlandite CH, pure hexagon crystals
 - d) Big air voids (pores) due to mixing
 - e) Gypsum $C\bar{S}H_2$, spread over the grain surface, 2% (in unhydrous grain)
 - f) Monosulfate $C_4A\bar{S}H_{12}$ - AFm
 - g) Ettringite $C_6A\bar{S}_3H_{32}$ - ettringite (Calcium alumina trisulfat) - AFt, hexagonal crystals, rods/needles less than a μm across
 - h) Calcium aluminate hydrate C_4AH_{13}
 - i) Hydrogarnet $C_3(A, F)H_6$

3. $10^{-4} - 10^{-3}m$ - mortar

- a) Cement paste
- b) Sand particles

4. $10^{-3} - 10^{-2}m$ - concrete

- a) Aggregate particle: gravel, rock, etc
 - porosity of aggregates induce diffusive flow of water, so w/c ratio should be increased
 - water adsorption to the surface play important role for ITZ
- b) Mortar

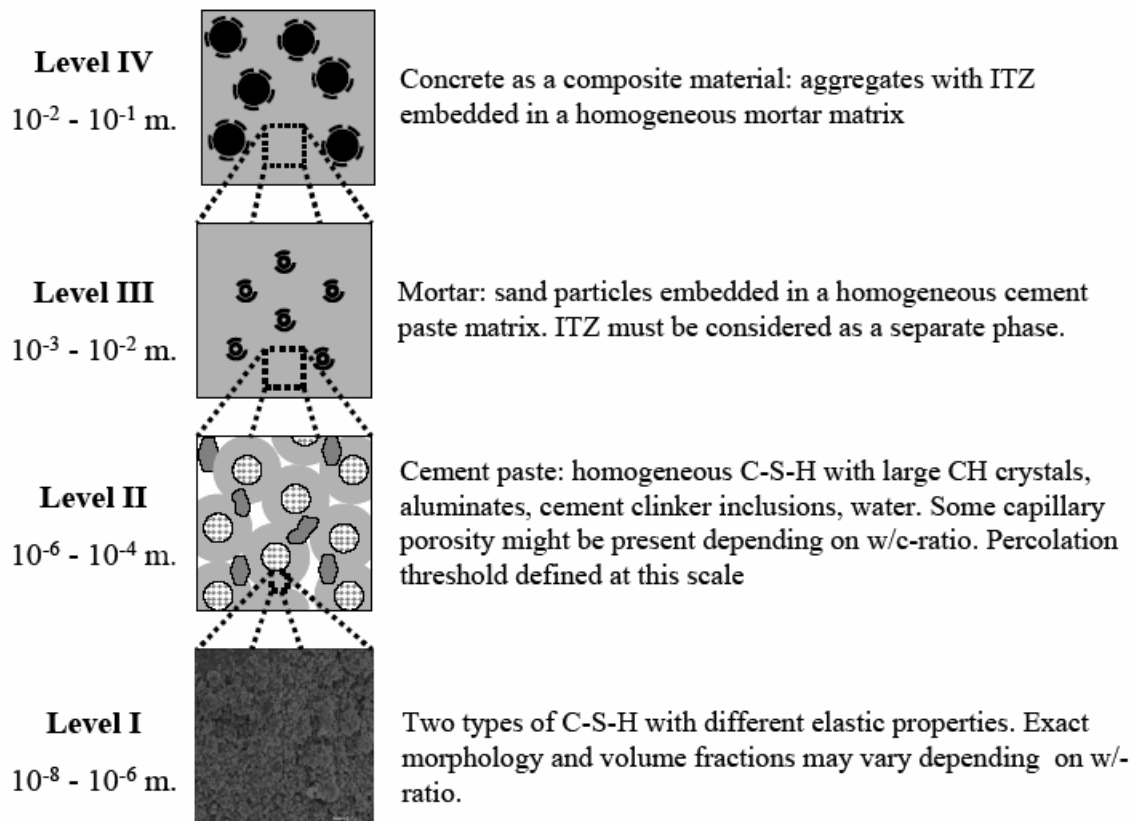


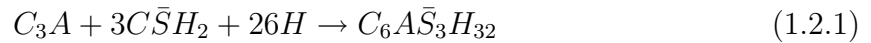
Figure 1.2.1: Different scales of the concrete micro structure

Cement chemistry notation is used throughout; C = CaO; S = SiO_2 ; A = Al_2O_3 ; F = Fe_2O_3 ; \bar{S} = SO_3 ; H = H_2O ;

Level I

At the lower scale there are fine products of hydration, mainly C-S-H gel, which is formed in the hydration of the C_3S and C_2S .

Before discussing the structure of C-S-H let us mention the first reaction to arise (within the first 10 minutes) if the gypsum is added, even if it seems not to have strong affect on microstructure from mechanical point of view. When the cement grains come in contact with water the hydration is limited to the outer surface of the grain. Gypsum plays a prominent role in this. The first reaction to arise is between water, C_3A and gypsum $C\bar{S}H_2$.



It forms the relatively hard shell of ettringite crystals (AFt $C_6A\bar{S}_3H_{32}$) at the surface of the cement grains. The ions forming ettringite are highly mobile in cement pastes, as witnessed by the recrystallisation of ettringite into pores and voids in mature concretes [92]. This layer is more or less impermeable to water so the hydration slows down. After a few hours this shell is broken due to chemical reactions in the shell and due to pressure building up in the cement grains. If no gypsum was added to the cement, the initial hard ettringite shell would not develop. Instead, very rapidly tetra calcium aluminate hydrates (C_4AH_{13}) would form, which are not stable and which disintegrate after some time. The process hydration now can proceed.

In the moist state (1-3h) C-S-H has an exfoliated filmy, foil-like ($0.5\mu m$) morphology. It is well known that there are at least two types of “dried” C-S-H, correlated to the two different types of hydration of clinker compounds:

1) C-S-H_{LD} - low density, outer C-S-H. During early stage of hydration, nucleation and growth of C-S-H site at the border of the initial grain and grow outside of it. C-S-H forms in the open capillary pore system during the rapid early hydration period.

The corresponding chemical reaction dominates hydration:



2) C-S-H_{HD} - high density, inner C-S-H. Later produced due through-solution mechanism (12-18h) of reaction - migration of ions inside the shell of outer C-S-H. It forms more slowly in more constricted areas of the microstructure. The chemical reaction is



It is primarily formed in a space confined by the existing C-S-H layer. Both these reactions produce calcium hydroxide (CH) hexagon crystals which precipitate in the water filled pores and have a very high mobility. Furthermore, it has been suggested [92] that silica

inhibits the nucleation of calcium hydroxide, which favors the precipitation as far from the cement grains as possible. Their size varies from fine crystals 10^{-8}m to large crystals 10^{-6}m . We will consider later case primarily. So-called “Hadley grains” (hollow shells) can appear during hydration (Fig. 1.2.2).

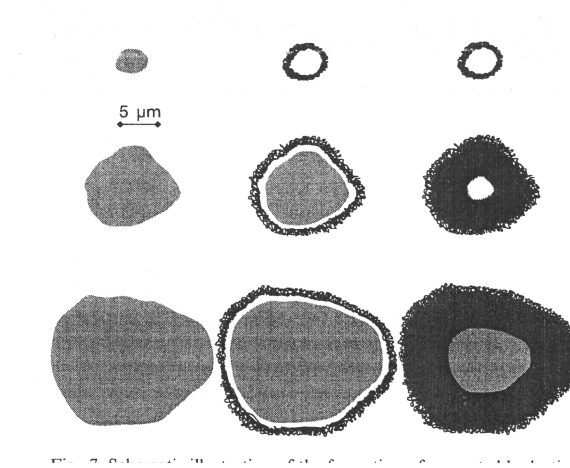


Figure 1.2.2: Formation of separated hydration shells over the time according to the grain size. The middle column shows the situation after about one day, all grains are surrounded by a thin shell of C-S-H separated by around $1\text{ }\mu\text{m}$ from the underlying grain. The column on the right shows the situation in the mature paste. Small grains (top) hydrate completely in the first stage and remain as hollow shells of hydration product. Medium size grains (middle) for a thicker rim of C-S-H as the grain continues to hydrate, perhaps with a small hole at the center. Grains larger than about $15\text{ }\mu\text{m}$ hydrate to fill in the gap between shell and grain. (after [93])

C-S-H_{LD} has a fibrillar morphology, where are plenty of space. By contrast, C-S-H_{HD} has a more dense morphology of honeycomb. The initial amount of w/c ratio influences the ratio of C-S-H_{LD} to C-S-H_{HD} types.

It is known from the experiments and from the chemical-physical models that the volume fraction at $w/c = 0.5$ for C-S-H_{LD} and C-S-H_{HD} is about $0.3/0.7$ [53].

Based on nanoindentation tests on nondegraded and calcium leached cement paste, the paper [28] also confirms the existence of two types of C-S-H (Fig. 1.2.3). The authors found that the frequency distribution of the elastic modulus of the C-S-H matrix shows a clear bimodal structure, particularly in the degraded state. Moreover, they propose a two-step homogenization model, which predicts the macroscopic elastic properties of cement pastes.

It should be noted that what is measured by the indentation technique is the homogenized properties of the two types of C-S-H at the length scale of at least tens of nanometers, whereas it is well established that C-S-H has porosity at length scales down to about 1

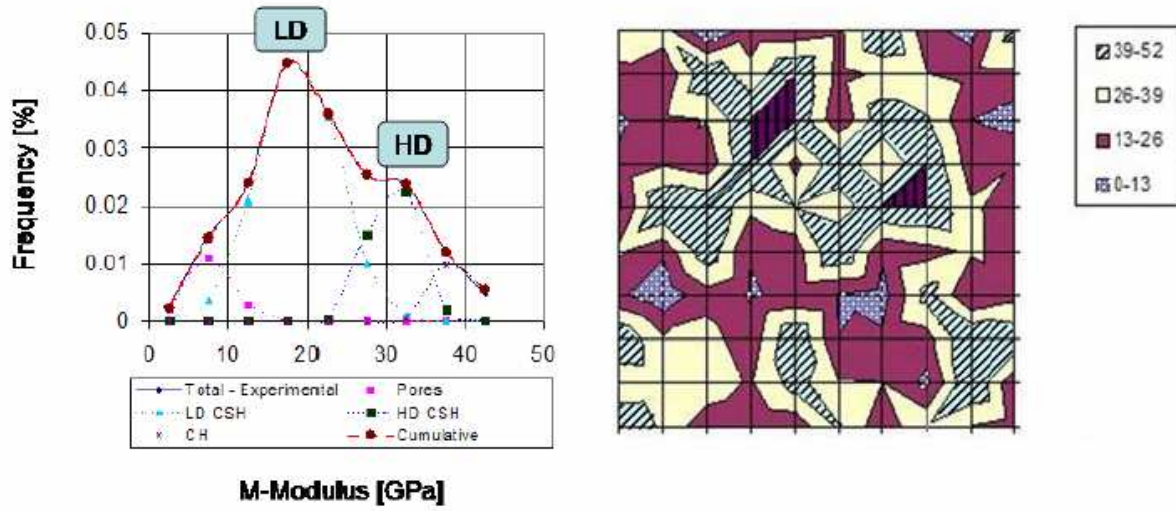


Figure 1.2.3: Frequency plot (left) and spatial distribution(right) of indentation modules based on the 10x10 grid of nanoindentation measurements. Results are for a Portland cement paste mixed at the w/c ratio 0.5 and cured for 28 days at 20 C (after [53] and [54])

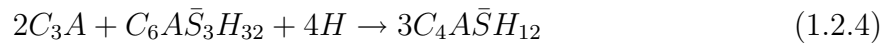
nm.

There is no unified opinion regarding the morphology. Van Mier [108] considers both $C-S-H_{LD}$ and $C-S-H_{HD}$ as needle-like, fibrous structures, the outer needles are longer (less dense) and the inner are shorter.

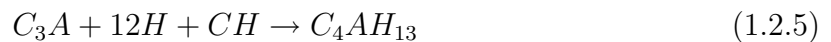
There are other models of microstructure and growth of C-S-H in the literature, for example a ribbon-like structure of $C-S-H_{LD}$ and its kinetics [44]. A major complication is caused by the fact that the microstructure of cement paste continues to change even as it undergoes loading and/or drying.

Water is the important part of the microstructure since its removal from the smallest pores during drying causes shrinkage and its presence in the smallest pores is necessary for creep under the load [51].

In the microstructure there are also other products of hydration. After the initial supply of sulfate (gypsum) is depleted, additional hydration of C_3A with fine ettringite crystals forms hexagonal plates of monosulfoaluminates (AFm):



If one assumes that all ettringite is consumed in the previous reaction, C_3A starts to hydrate with CH to produce calcium aluminate hydrate:



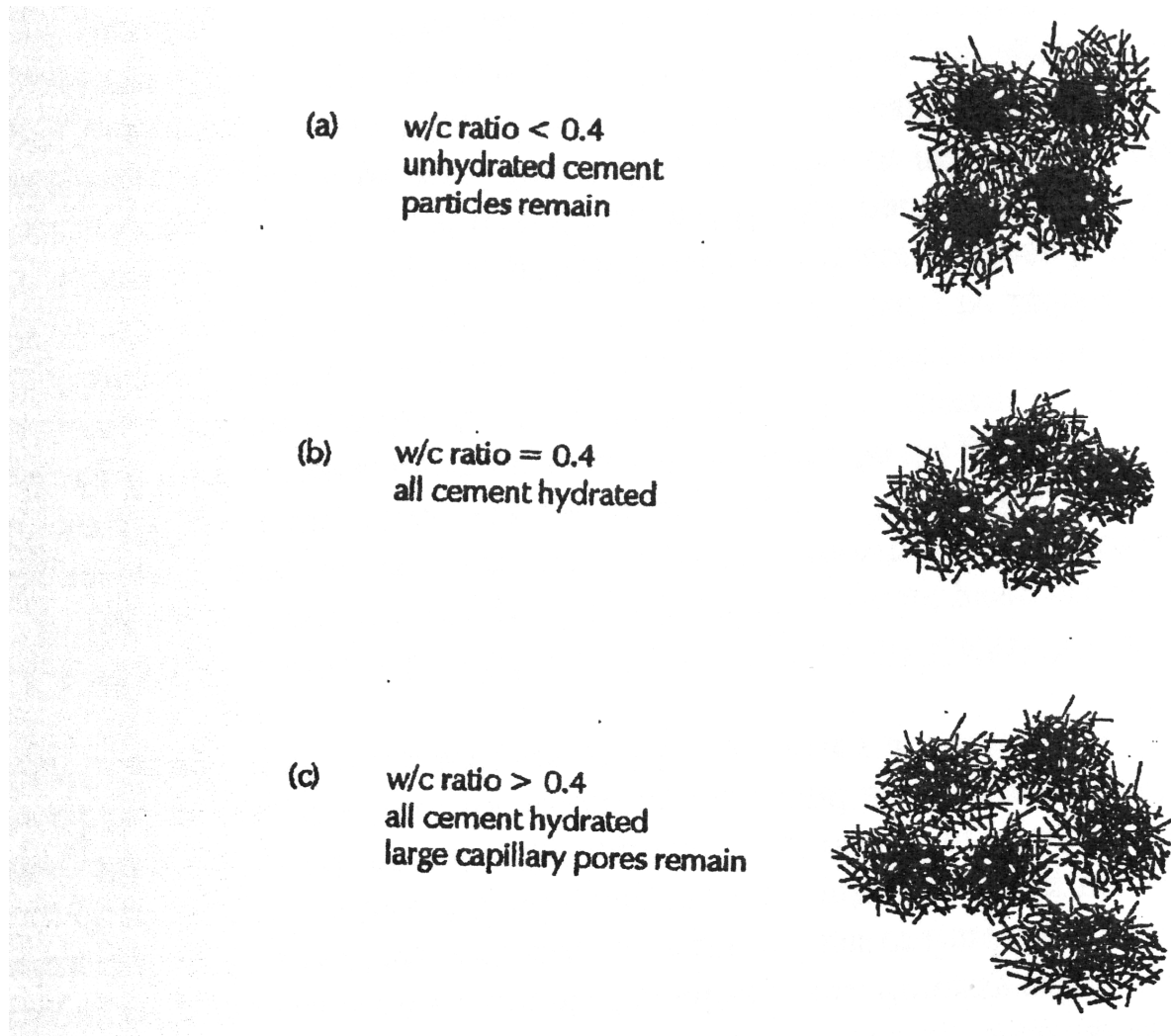


Figure 1.2.4: Effect of water/cement ratio on the structure of hardened cement paste (after [108])

The product of the ferrite reaction is hydrogarnet:



Several other aluminum-bearing compounds are known to form under various conditions.

Summary of microstructural development can be seen from Fig. 1.2.5. It should be mentioned that C-S-H itself has a nanoporosity (C-S-H gel porosity). There can also be some micro air voids. Sometimes additional phases are added, for example silica fume, which is formed by particles $< 0.1 \mu\text{m}$. It helps to increase the packing density of the grains in the ITZ near aggregate.

At the scale of C-S-H, independently of the morphology model of the C-S-H, there are two bonds: primary – rest-valences of molecules at the C-S-H surface (direct chemical

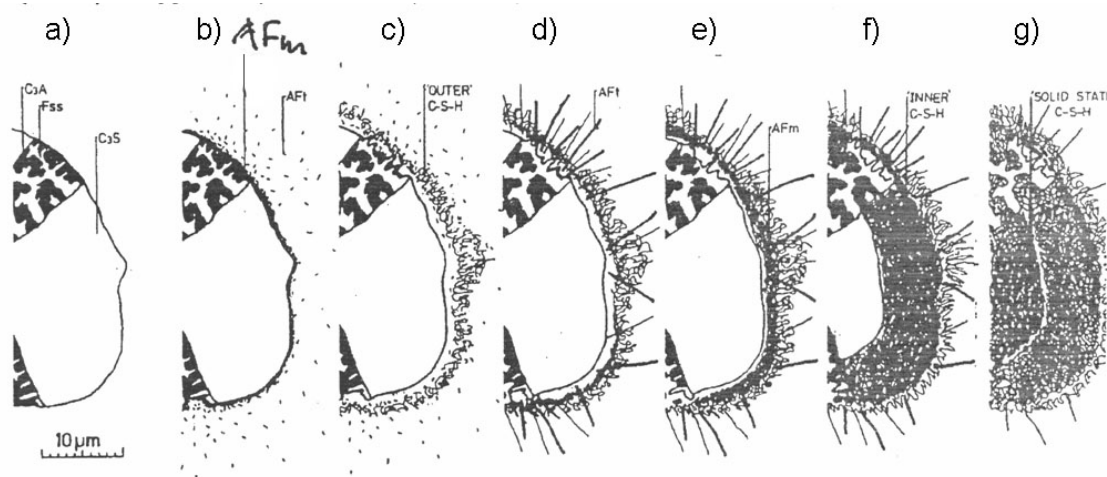


Figure 1.2.5: Summary of the microstructural development of a grain of cement. (a) Unhydrated section of polymineral grain (b) -10min. Some C_3A reacts with calcium sulfate in solution. Amorphous, aluminate-rich gel forms on the surface and short AFt $C_6A\bar{S}_3H_{32}$ rods nucleate at edge of gel and in solution. (c) -10h. Reaction of C_3S to produce “outer” product C-S-H on AFt rod network leaving $1\mu m$ between grain surface and hydrated shell. (d) -18h. Secondary hydration of C_3A reacts with any AFt $C_6A\bar{S}_3H_{32}$ inside shell forming hexagonal plates of AFm. Continuing formation of “inner” product reduces separation of anhydrous grain and hydrated shell. (f) -14 days. Sufficient “inner” C-S-H has formed to fill in the space between grain and shell. The “outer” C-S-H has become more fibrous. (g) - years. The remaining anhydrous material reacts to form additional “inner” product C-S-H. The ferrite phase appears to remain unreacted. (after [89])

bonds) and secondary – Van-der-Walls forces (physical attraction between the surfaces). Mechanical interlock is also possible.

Another point of interest is the heat of hydration. All of the aforementioned reactions are exothermic, which means that heat is released during the reactions (the amount depends on the original compound of the composition). Due to the localization and short time span, thermal gradients can lead to initial tensile stresses, which can cause thermal cracking. There exists commercial cement which tries to minimize heating.

Drying can also lead to the cracks through shrinkage and appearing eigenstresses (non-elastic stresses).

The rate of heat evolution during hydration can be seen from Fig. 1.2.7.

All aforementioned reactions are balanced assuming all of the hydration products are saturated. Consideration of the dried samples demands re-balancing of equations. (AFt: $C_6A\bar{S}_3H_{32}$, $C_6A\bar{S}_3H_7$; AFm: $C_4A\bar{S}H_{12}$, $C_4A\bar{S}H_8$)

Another group of phases at this scale are clinkers. Cement grains almost always contain

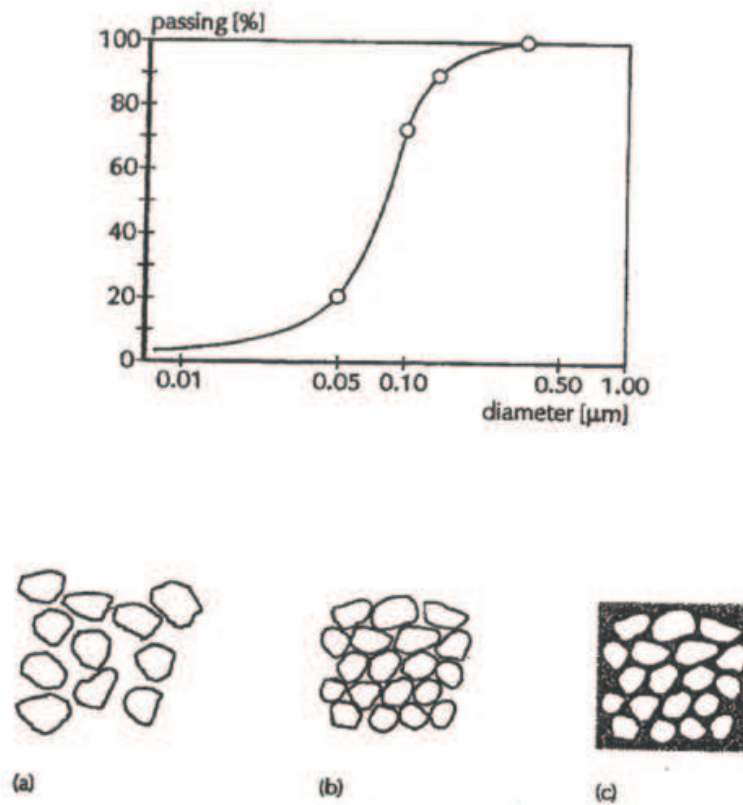


Figure 1.2.6: Particle distribution of silica fume and its affect on the packing (after [108])

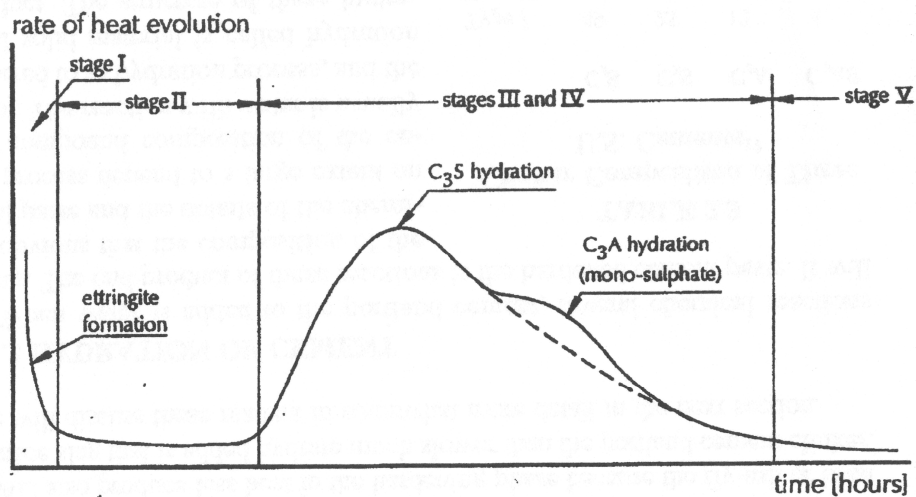


Figure 1.2.7: Heat evolution during the hydration of C_3S and C_3A (after [108])

more than one phase. Alite crystals have a hexagonal morphology and they are dominant (approx. 60% of initial unhydrated grain). Bellite has a more rounded shape. In the ideal case they will look like:

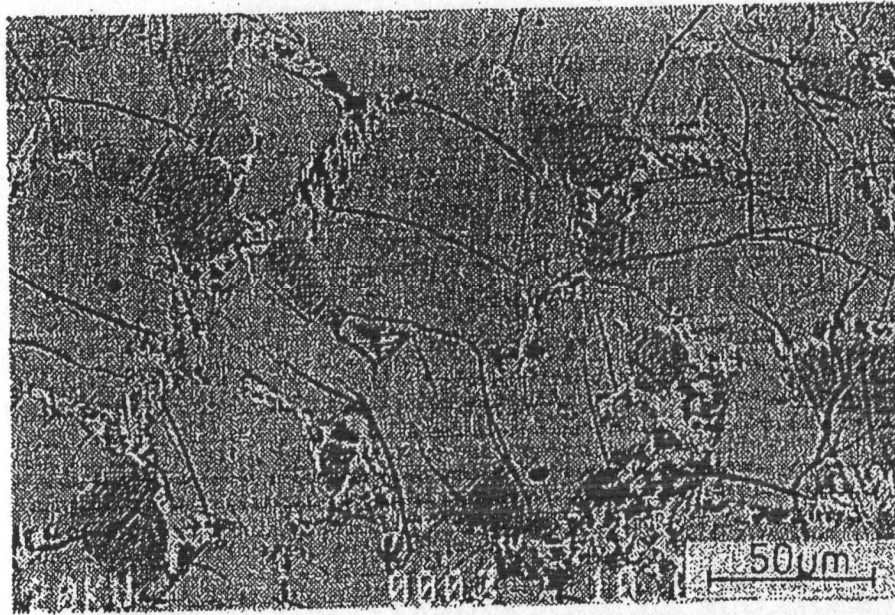


Figure 1.2.8: Microstructure of a commercial clinker (BSE image). Light-gray crystals of allite and darker round crystals of belite can be seen in a matrix of the interstitial phases-ferrite (light) and aluminates (darker). Porosity (black) can also be seen (after [89])

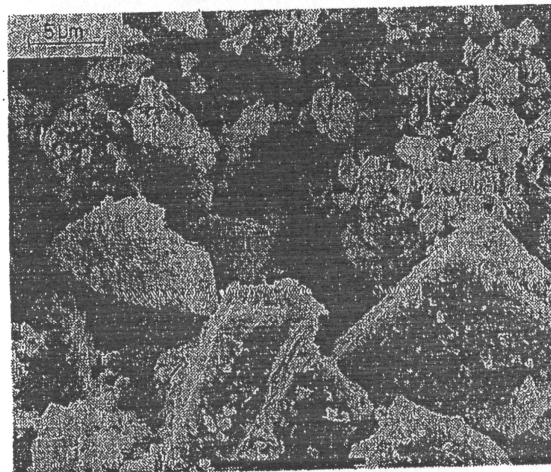


Figure 1.2.9: Scanning electron micrograph of anhydrous cement grains showing the wide range of particle sizes. Small crystals of calcium sulfate can be seen on the surfaces of the larger grains (after [89])

Level II

The C-S-H gel together with the unhydrated grains, large CH crystals, air-voids (macro-

porosity due to mixing and/or high w/c ratio) and other products of hydrations (mono-sulfates and ettringite) form the second level of concrete microstructure at the scale $10^{-6} - 10^{-4}\text{m}$. Freshly matured material (early stage) can be considered as a pure viscous liquids with zero shear modulus. Cement grains are disconnected. Solid phase is build up due to growth of hydration products, mainly C-S-H, after 3-4 hours. The set point at which solid phases become connected is generally referred to as the solid percolation threshold. This is affected by the w/c ratio.

Level III

The third scale corresponds to the mortar and consists of a cement paste, sand inclusions and the Interfacial Transition Zone (ITZ). The ITZ has its own morphology which differs from the so-called “bulk” cement paste. So-called “wall-effect” of packing appears (Fig. 1.2.10), which results in a denser packing of the small grains near the aggregate particle.

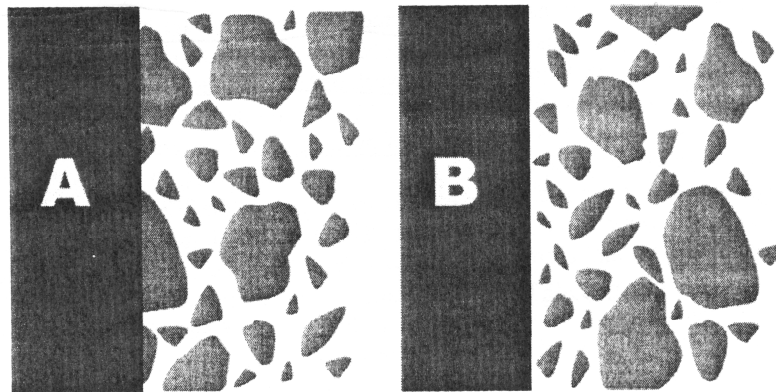


Figure 1.2.10: Illustration of the “wall” effect (after [92])

Due to very high mobility of the CH crystals over the C-S-H, they also appear in this zone filling the pores during the hydration. CH itself is a very weak particle which leads to the weakness of the ITZ. It is known there is a preferential orientation of CH crystals with the c -axis parallel to the aggregate surface [92].

ITZ also depends on the aggregate particle surface (sawn, polished, broken). For example for the porous aggregate the “boundary” between aggregate and ITZ is diffuse, so we can not actually define the sharp boundary in that case. The size of ITZ is comparable with the size of grains.

The wall effect plays a big role in the mechanical properties of concrete. This can be seen from the simple comparison of the stress-strain curves Fig. 1.2.12. ITZ also affect the disposition of pores Fig. 1.2.13. As it was said the presence of silica fume can increase the density of packing and so decrease volume fraction of pores Fig. 1.2.14.

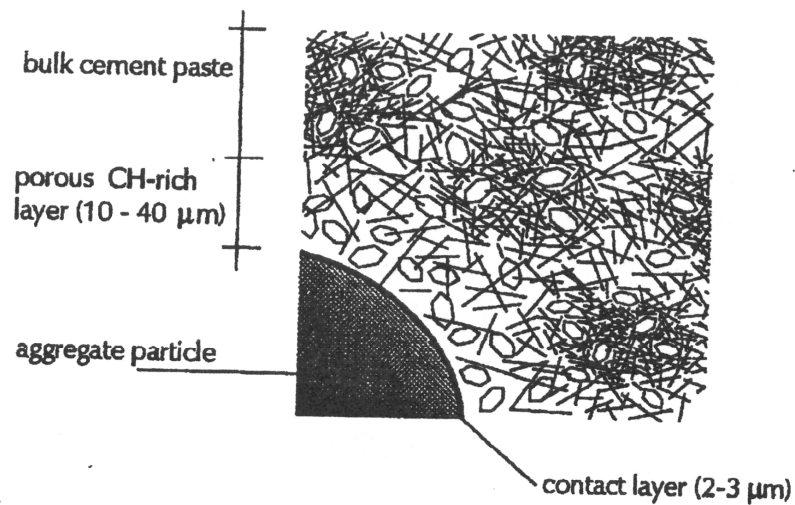


Figure 1.2.11: Structure of the interfacial transition zone between rounded, dense, natural aggregate and Portland cement matrix (after [108])

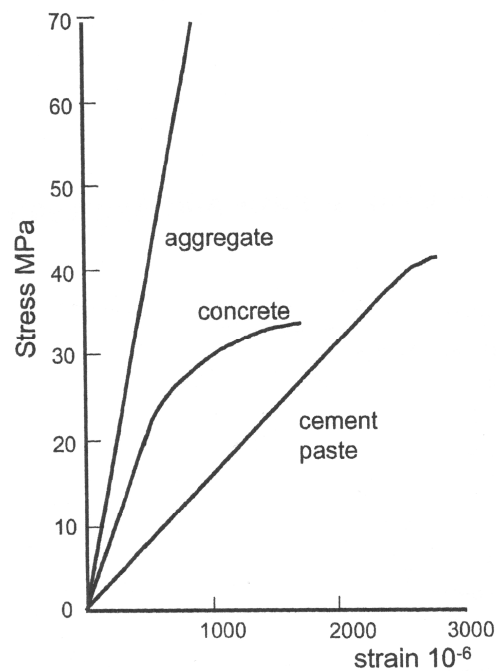


Figure 1.2.12: Comparative stress-strain curves for aggregate, paste and concrete, the quasi-brittle behavior of concrete illustrates the importance of the ITZ for the macroscopic properties of concrete (after [92])

Moreover, the presence of ITZ debates the term “bulk” for the paste [92]: “from the surface area of the aggregate and the volume of paste it can be calculated that the average thickness of paste around aggregate particles is only of the order of 50 μm and the typical

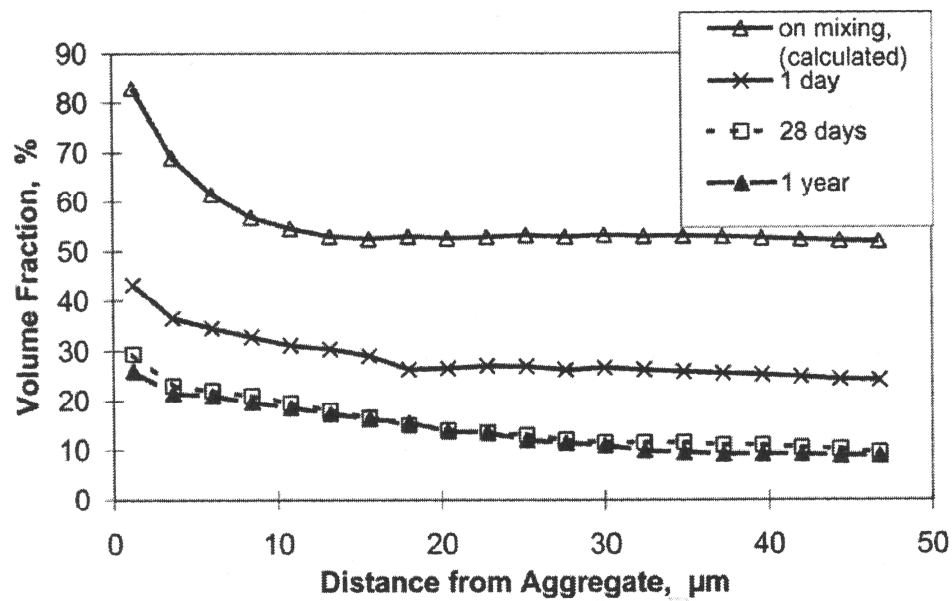


Figure 1.2.13: Average porosity in ITZ at various ages (after [92])

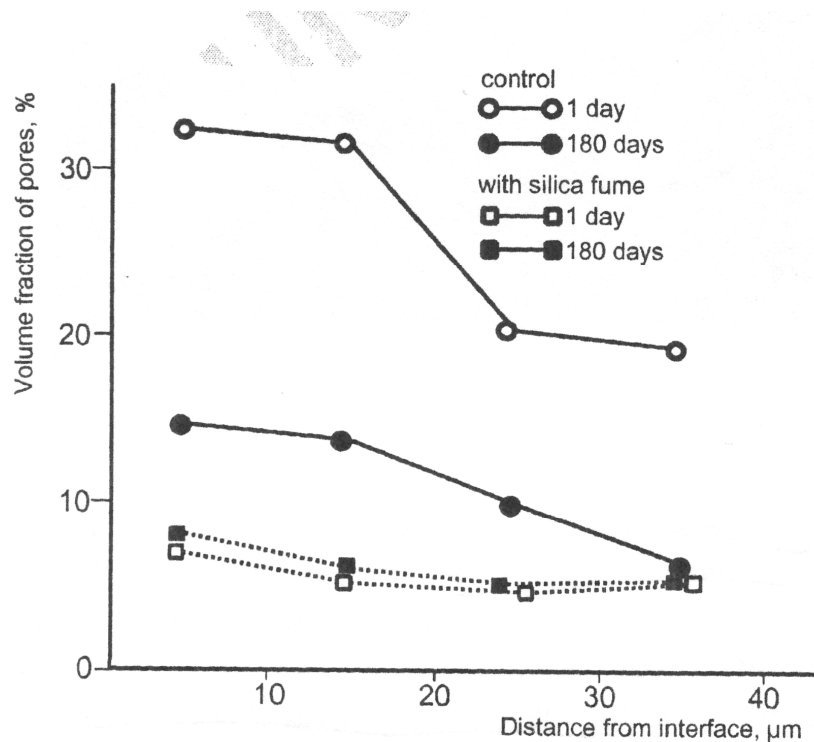


Figure 1.2.14: Distribution of porosity in the ITZ of concretes with and without silica fume (after [92])

maximum distance between aggregates seen in sections of concrete is only a few hundreds microns (with the “lengthening factor” 1.2 due to difference between 2D and 3D), and

the thickness of “wall effect” is around $15\text{ }\mu\text{m}$ ”.

Example of the microstructure with the sand can be seen in Fig. 1.2.15.

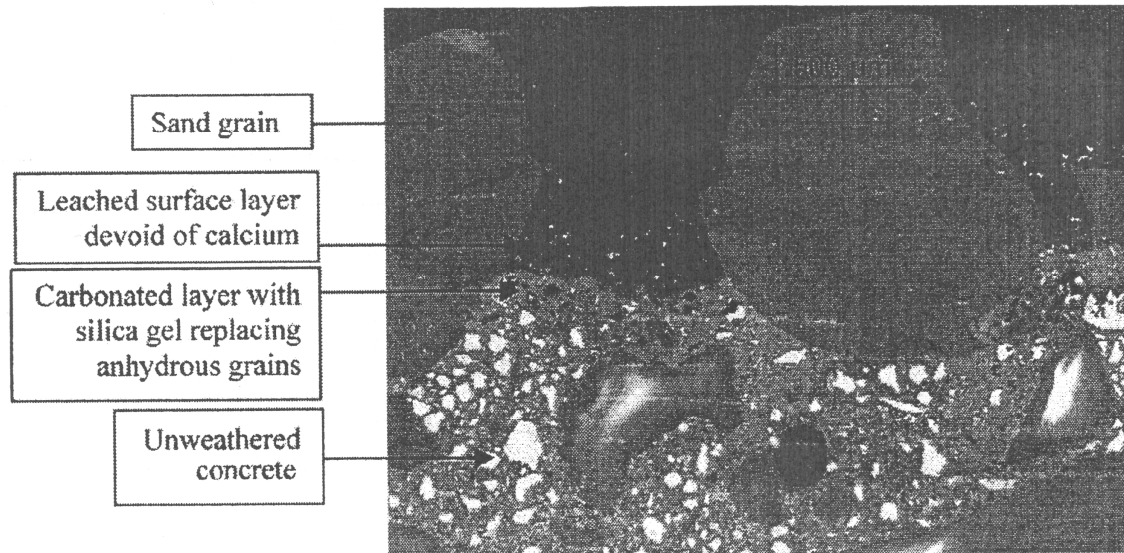


Figure 1.2.15: BSE image of concrete, exposed for 10 years in a wet cold climate (after [93])

Level IV

Concrete is considered at this level. It consists of the aggregate particles (such as gravel, rock, etc) and the mortar. The porosity of the particle and water adsorption ability at the surface can affect the flow of water and increase the effective w/c ratio of the mixture. This scale is similar to the scale of mortar. The difference is that aggregate particles have a wider scale of sizes. This helps to optimize packing.

It should be noted that pores appear at all levels of the structure. From nano pores in cement gel, micro capillary pores between the C-S-H and macro (\sim millimeter) pores due to mixing (air voids). Several techniques exist to decrease latter effect. For example, MDF cement is produced with optimal squeezing and vibration to minimize macro air-voids.

Mindess and Young proposed classification of pores, depicted on Tab. 1.2.1.

It should be emphasized that there is a considerable overlap in both the size range and the different pore types.

Another factor affecting porosity is a chemical shrinkage. It is caused by the fact that the volume of hydration products is less than the initial volume of water plus cement grain.

Let us say few words about one of the main components – water. Usually water is classified into: physical adsorbed water (about 15% of cement weights), chemically adsorbed water (about 25%) and capillary water (free water in capillary pores). These quantities

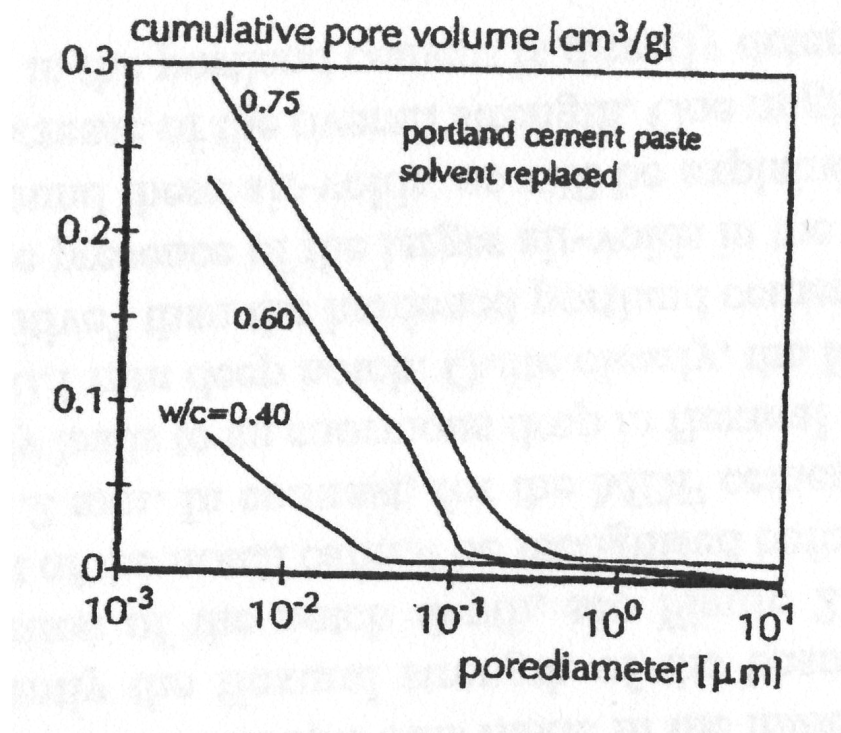


Figure 1.2.16: Scale of the pore-size distribution and their relationship with the w/c ratio (after [108])

Classification of the pores in cement according to size, after Mindess and Young			
Designation	Diameter	Description	Properties affected
Capillary Pores	> 50 nm	Large capillaries	Strength, permeability
	10 - 50 nm	Medium capillaries	Strength, permeability, shrinkage (high RH)
Gel Pores	2.5 - 10 nm	Small (gel) capillaries	Shrinkage (to 50% RH)
	0.5 - 2.5 nm	Micropores	Shrinkage, creep
	< 0.5 nm	Interlayers	Shrinkage, creep

Table 1.2.1: Classification of pores

are approximate and can be less due to usage of, for example, superplasticizers.

w/c ratio seems to be a main implicit characteristic affecting such macro-mechanically observable effects as creep, shrinkage, elasticity. Of course it affects porosity.

It is obvious that during hydration the amount of unreacted cement decreases. But for the mechanical properties it is interesting to know the rates of hydration even if the hydration continues for decades. Fig. 1.2.17 and Fig. 1.2.18 show the evolution of these characteristics.

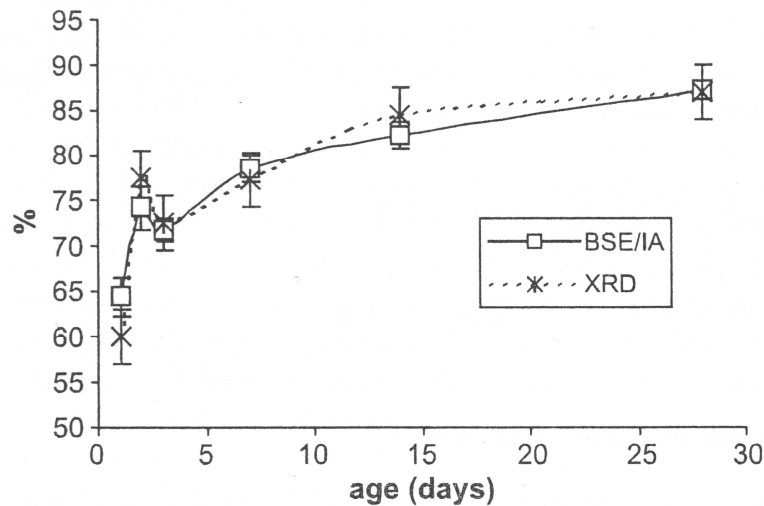


Figure 1.2.17: Degree of hydration measured by XRD/Rietveld and BSE/IA (after [91])

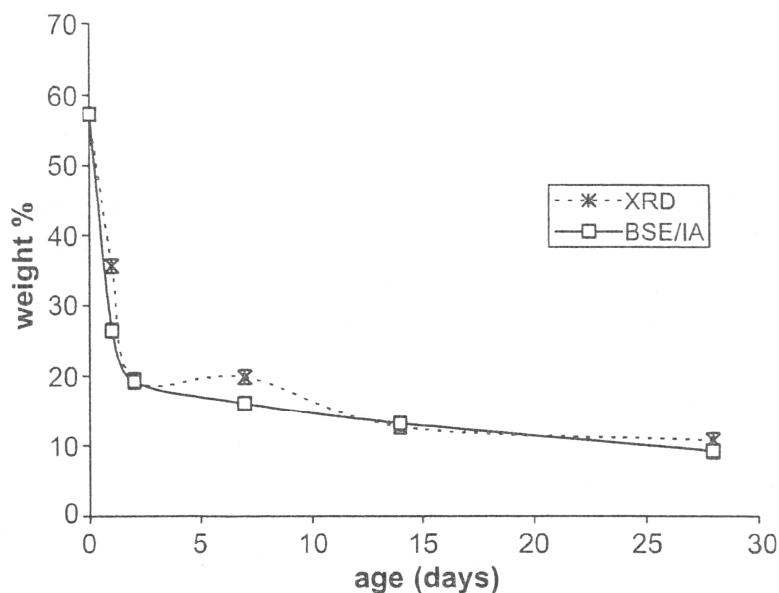


Figure 1.2.18: Amount of unreacted cement measured by XRD/Rietveld and BSE/IA (after [91])

From these figures it can be seen that after approx. 5 days the kinetics slows down and, probably, the microstructure stabilizes.

1.2.2 Creep and Shrinkage Mechanisms in Cement Paste

In concrete structures one should consider the changes of volume and length which occur during the hydration and in service.

Withdrawal of water from concrete stored in unsaturated air causes **drying shrinkage**. It is caused mainly by the increase of capillary tension of pore water and solid surface tension of pore walls, engendered by diffusion of pore water out of the specimen. A part of this movement is **irreversible** and should be distinguished from the **reversible** moisture movement caused by alternating storage under wet and dry conditions. The change in the volume of drying concrete is not equal to the volume of water removed. The loss of free water from capillary pores, which takes place first, causes little or no shrinkage. But it should be noted, however, that if the hydration is not complete, the removal of free water will severely restrict the further hydration of the paste.

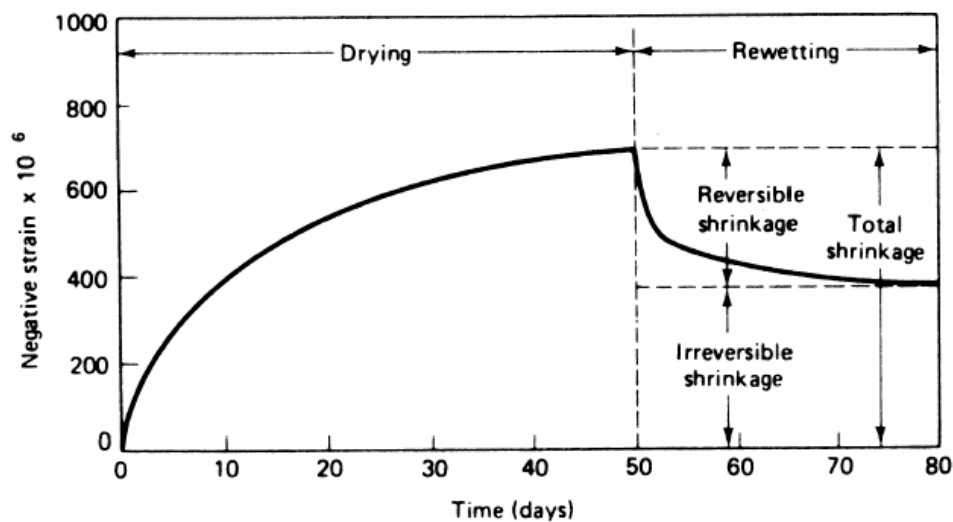


Figure 1.2.19: Shrinkage strain of the concrete sample for one cycle of drying and wetting (after [73])

As drying continues, the adsorbed water is removed and the change in the volume of unrestrained cement paste at that stage is approximately equal to the loss of a water layer one molecule thick from the surface of all the hydration products.

Different stages of water loss are presented in Fig. 1.2.20:

The interlayer water is called the "combined water" in Fig. 1.2.20 and it is also known as the "water of hydration" which is chemically combined in the C-S-H structure. At high temperatures (over 180°C) this water can be driven out of the structure, but it is not removed by any mechanism at room temperature. There is also a similarity between the shrinkage of Portland cement products and wood.

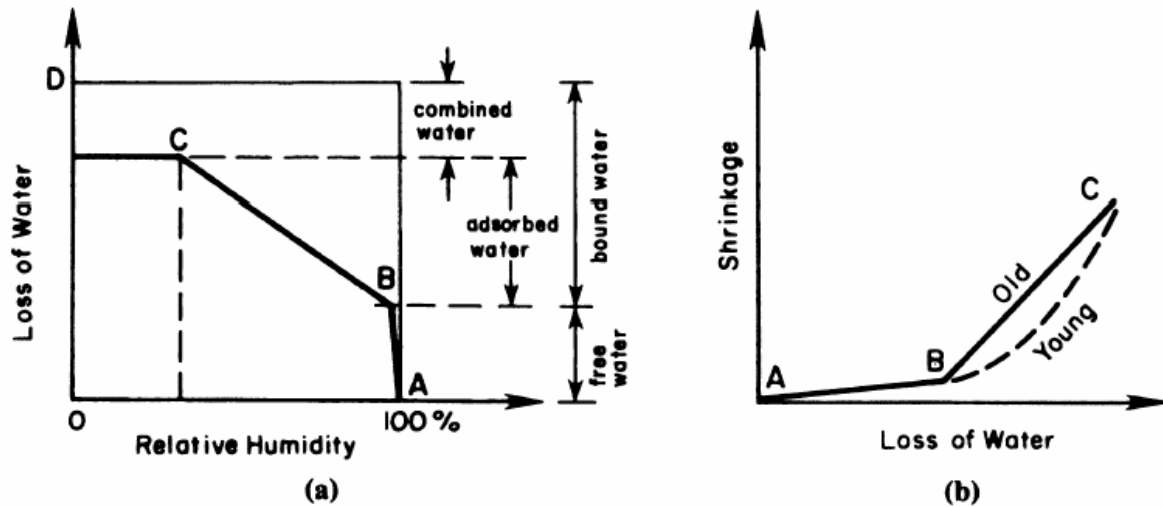


Figure 1.2.20: (a) The loss of water at room temperature from a Portland cement mortar sample is shown as a function of relative humidity; (b) The corresponding shrinkage is shown as a function of water loss. Note the points A, B, and C identify the same points in both figures (after [73])

Shrinkage is volumetric and does not produce shear strains. The drying shrinkage is finite because the loss of water is finite.

Two cracking modes can occur. In very first hour the first mode corresponds to the domain of water contents for which the liquid phase is still contiguous, and is reflected by cracks that are rather shallow and irregular, limited to the upper surface of the concrete. The second mode is long-term, very slow drying. Cracks are more straight and are oriented by the geometry of the structure (the boundary conditions), and their opening evolves very slowly.

In contrast to chemical shrinkage (will be mentioned later), the kinetics of drying shrinkage does not reflect that of the micro-mechanism that causes it within the material (water-vapor phase change with capillary tension), but reflects the spread within the structure of the phenomenon that engenders it: the degree of drying varies across the thickness of the part (this applies during most of the transient phase) between its maximum value (at the surface) and its minimum value (at the core). The apparent shrinkage is therefore related to the mean value of this degree in the volume.

The slowness of the process also indicates the importance of the gradients that develop in the first phase of the process, which produce eigenstresses known to lead to shallow cracking of the structures.

There is also the **chemical shrinkage** due to the difference between the volume of input and output products of reaction. The volumetric balance shows a deficit of the order of 10% of the volume of hydrates formed. This reduction of the relative volume

occupied by the liquid phase in the pore space therefore leads, like drying, to a strain of the mineral matrix. Noting that pressurizing a fluid that filled the pores would cause an apparent swelling, it can be seen that, conversely, the tensions in the liquid phase (which follow, precisely, the laws of surface tension, up to pore sizes of a few nanometers) cause a contraction of the matrix, called shrinkage. So the capillary tension is the origin. This shrinkage is also finite due to the fact that reactions stop after one year of hydration approximately. So the shrinkage of cement paste and concrete is bounded.

Sealed sample is said to undergo **autogenous** shrinkage. Sealed conditions exclude any drying. The deformation is induced by chemical shrinkage, capillary effects and restrained by deformation of the paste skeleton. That is why autogenous shrinkage is less than chemical shrinkage.

Autogenous shrinkage remains less than 10^{-4} in concretes with the w/c ratio greater than 0.45, but it increases quickly when this ratio falls below 0.40, and can reach $3 \cdot 10^{-4}$. This is simply an effect of pore size: the tensions in the liquid phase (which engender a compression of the mineral matrix) vary inversely with the pore size at the interface with the gaseous phase. Autogenous shrinkage is basically an intrinsic phenomenon, which can nearly always be regarded as uniform in the volume of a structural element.

Hydration products of Portland cement form a complex gel. This colloidal and micro-porous system has a huge internal surface and therefore interacts strongly with water. The water layers close to the surface of gel particles are structured and if the moisture content is high enough (equilibrium moisture content at $RH > 50\%$) an electric double layer is formed. The distance between two opposing surfaces of gel particles is given by the balance of different attractive and repulsive forces. Most important for the attractive component are Van-der Waals attractive forces and capillary pressure. These attractive forces are balanced by the disjoining pressure which is mainly originated by an overlap of the electric double layer and at close distances by a change of chemical potential of the structured adsorbed water layers. If the moisture content in the micro-pores is changed either by drying (exogenous, diffusion mechanism) or by progressive hydration (endogenous or also called autogenous, chemical mechanism) a new equilibrium distance between the surfaces of gel particles is established. A moisture change results in a volume change which is at the origin of shrinkage and in case of rehumidification of swelling. Autogenous shrinkage is an overall effect in the cement paste and is much smaller than the chemical shrinkage due to restriction of the skeleton.

Real mechanisms can be formulated only on the basis of an inverse analysis of the observed deformation of a drying specimen taking creep and crack formation into consideration. As this complex procedure has hardly been carried out so far most shrinkage models remain purely speculative or they can be considered as a first approximation in

the best case. The presence of the micro-cracks is experimentally observable by, for example, fluorescence light microscope[49] (moisture profiles were recorded by NMR). When the tensile stresses near the drying surface exceed the tensile strength of the materials, a system of parallel cracks with an orientation perpendicular to the drying surface develops (in case of self-restraining of the material; no aggregate effect). Typical width of cracks is less than 50 μm , and therefore they are called microcracks. What kind of restrain - self restrained or aggregate restraint - is more important depends on the material.

The formation of microcracks reduces "ideal" drying shrinkage (elastic case). Application of compression stress can reduce the crack formation and so increase the shrinkage. Shrinkage should not be considered without acting stresses taking into account. This applied compressive load favors formation of microcracks running parallel to the direction of the load and induces anisotropy.

The influence of the shrinkage and microcracking on the concrete is modeled in [86]. Sadouki consider the concrete as a two phase material consisting of aggregates embedded in a cement-based matrix by means of "Numerical Concrete" model. Moisture distribution and creep of the matrix have been considered. Heat flow, moisture transfer and deformation and crack formation under load are modeled at the level of concrete by FE software DIANA.

Phenomenologically shrinkage can be subdivided according to the driving forces into a series of different processes:

- capillary shrinkage
- dissolution shrinkage
- thermal shrinkage
- drying shrinkage
- chemical shrinkage (induced by hydration)

Some of these processes follow one another as concrete ages and others take place simultaneously.

Non-linear diffusion process of drying can be simulated numerically. Change in relative humidity induce local (in material point) shrinkage deformation

$$\varepsilon = \alpha_h \Delta h \quad (1.2.7)$$

where α_h is linear hygral deformation.

This deformation in continuous material is restrained so it induces stress. Stress-free shrinkage is considerably higher. High tensile stress is built up in the dry outer zones.

A rigorous analysis shows that under usual climatic conditions tensile strength of the material is quickly reached. Then softening in the highly stressed zones begins and finally real cracks are being formed. Shrinkage strain increases quickly as soon as drying begins. But softening within the dry outer zones prevents a further increase of tensile stress and as a consequence shrinkage evolution slows down. At the moment when real cracks are formed shrinkage is further slowed down. Shrinkage evolution in general depends on non-linear diffusion process of moisture in concrete, damage (tensile strength and strain softening) and crack formation. So difference in hygral gradients for different strength concrete should not be attributed to specific mechanism but rather coupling with damage and cracking. It is very important to distinguish between apparent mechanism (e.g. dependence of shrinkage on damage) and real physical mechanisms (e.g. capillary forces). Under certain applied load to the RVE the damage due to shrinkage induce anisotropy to the material behavior. With the application of a compressive load shrinkage in the direction of the applied load increases as crack formation normal to the direction of the applied load is gradually becoming less probable. But this couplings is not enough to explain the Picketts effect - difference between total deformation of a loaded drying specimen and sum of creep of a sealed but loaded specimen and shrinkage of a drying but unloaded specimen (Fig. 1.2.23). Hence there must be another phenomenon which is neglected.

It is well known that the main creep phase is C-S-H. When hydration rate becomes negligible (typically after a few weeks), the main part of shrinkage is nothing but the viscoplastic response of C-S-H to the internal stress which is applied by the liquid phase on the pore surface. The evolution of the porosity, free water amount and capillary pressure is of grate importance in that case. Presence of the capillary pores and their effect on viscous deformation of CSH can explain the fact that the kinetics of shrinkage is not proportional to the kinetics of hydration and decelerates less rapidly (in a pure elastic behavior, shrinkage will be proportional to the capillary pressure, thus will stop with them; at the opposite, a pure viscous behavior will produce a constant flow).

Decreasing of the shrinkage rate with constant capillary can be explained by:

- relaxation of the stresses (stress redistribution) by viscous C-S-H (decreasing of the probability of breaking and slipping within C-S-H)
- diminution of the distance between elastic inclusions so decreasing of the stress concentrators number and transfer of the stresses to the aggregates and all elastic particles.

The relationship between the humidity and the radius of the largest saturated pores is given by Kelvin's equation. For relative humidities below 90% his radius is in the range of nanometers, where attractive and repulsive surface forces become dominant.

Three mechanisms have been identified in order to explain drying shrinkage[13]:

- variation in surface energy
- variation in disjoining pressure
- variation in capillary underpressure

Shrinkage due to variation in surface energy

When a dry gel particle takes up water by adsorption the surface energy is diminished and the particle expands. This phenomenon is expressed by the Bingham equation:

$$\Delta l/l_0 = k (\gamma_0 - \gamma) \quad (1.2.8)$$

where Δl is the length change, l_0 the length of a dry specimen, k a constant, γ_0 and γ are the surfaced energies of dry and wet particles respectively. The thickness of the adsorbed water film can be related to the vapor pressure p by means of Gibbs's adsorption equation:

$$\Delta G = -R T \int n \, d(\ln p) \quad (1.2.9)$$

where ΔG is the change in free energy that can also be expressed as the change in surface energy $\Delta\gamma$ for a given surface area A ,

$$\Delta G = A \, \Delta\gamma \quad (1.2.10)$$

and thus, combining (1.2.8), (1.2.9), (1.2.10) give a relationship between length change due to the variation in surface energy as a function of relative humidity p/p_0

$$\Delta l/l_0 \approx \int n \, d(\ln p) \quad (1.2.11)$$

It has been experimentally shown that this relationship describes shrinkage of microporous materials such as hardened cement paste and concrete for relative humidities smaller than 40%.

Shrinkage due to variation in disjoining pressure

Beyond 40% R.H. the change in humidity does not modify the surface energy significantly. Therefore the nevertheless observed length change can no longer be explained by the relationship (1.2.11) and a further mechanism referred to as disjoining pressure becomes dominant. In 1974 Derjaguin defines the disjoining pressure as a superposition of three forces, which are simultaneously acting on surfaces separated by a thin water film. These forces are of Van-der Waals type (attractive), electrostatic and steric (repulsive). The latter, described by the DLVO theory of colloids, depend on both surface charge and

ionic strength of solution. Disjoining pressure depends on the structure, general properties of the intervening liquid layer and temperature. It usually has several maximum at certain temperatures. Viscosity of the liquid near the interfaces is not constant also [112].

Disjoining pressure of water takes place between two silica surfaces with a distance from 300\AA to 1000\AA . This distance just takes place in the pore size range between meso gel pores and micro capillaries of cement paste. The behavior of pore water in this pore size range is influenced not only by adsorbed water layers but also by condensed water of capillaries.

Shrinkage from variation in capillary underpressure

The capillary porous system of hardened cement paste is a reminiscence of the initial water filled interstitial volume between unhydrated cement particles. The mean radius within this system is in the range of 10 to 20 nm.

After the start of drying, most of the water loss is from these capillaries. The corresponding shrinkage mechanisms is described by the following Laplace equation:

$$\Delta p = p_g - p_l = 2 \sigma_{1/g} 1/r \quad (1.2.12)$$

where p_g and p_l are the pressure of the gaseous and liquid phases respectively, $\sigma_{1/g}$ the liquid/gas interface tension and r the radius of the meniscus which appears as soon as drying starts. (1.2.12) shows that the progressive diminution of r (drying) causes an elevation of the pressure difference, which results in a volume contraction.

The reason why gel surfaces, which should attract because of the capillary effect, do not coalesce is that these particles are surrounded by electric charges and by structured water molecules, which repel. Therefore, in the range of 50-100% R.H. the attractive capillary effect and the repulsive disjoining pressure coexist. At very low distance attractive forces are both capillary and Van-der Waals type. Capillary forces are approximately independent of relative humidity RH whereas disjoining forces are lowered due to drying. It is assumed that capillary forces are almost independent of relative humidity due to the balancing effect between variation of underpressure and variation of surface. On the other hand, if for a given pore solution the disjoining pressure is considered to be constant (which should be the case in a saturated solution), the disjoining force is varying with surface and thereafter with relative humidity. Thus, in the case of a drying process the surfaces are coming closer as disjoining force and equilibrium distance are lowered. This volume increase can be measured as shrinkage.

If the pore solution was not saturated drying would increase its ionic strength which in turn could lead to a change of disjoining pressure.

In [20] Brooks also stated the explanation of Picketts effect in capillary pores pressure

and their effect on creep - enlargement of the local stress due to not saturated pores. The stress acting on the solid phase due to the presence of the pores in cement paste is assumed to be similar to the stress concentration effect of holes in metals subjected to external loading. It is postulated that drying creep is the result of an increase in stress acting on the solid gel when water is first removed from the gel pores at the same time as the external load is applied.

Variation of capillary pressure can also be caused by loading state. One consider single pore in infinite body loaded uniaxially. Poisson coefficient of concrete is less than 0.5. Consequently, the curvature radius of menisci in the capillarie increases under tension and decreases under compression, that weakens capillary stress under tension and enhances it under compression.

If we now assume a load is applied to the concrete, we find that it has an effect on the long-time dimensions of the concrete sample. **Creep** can be defined as the increase in strain under a sustained stress; and since this increase can be several times larger than the strain immediately after loading, creep is of considerable importance in structural mechanics.

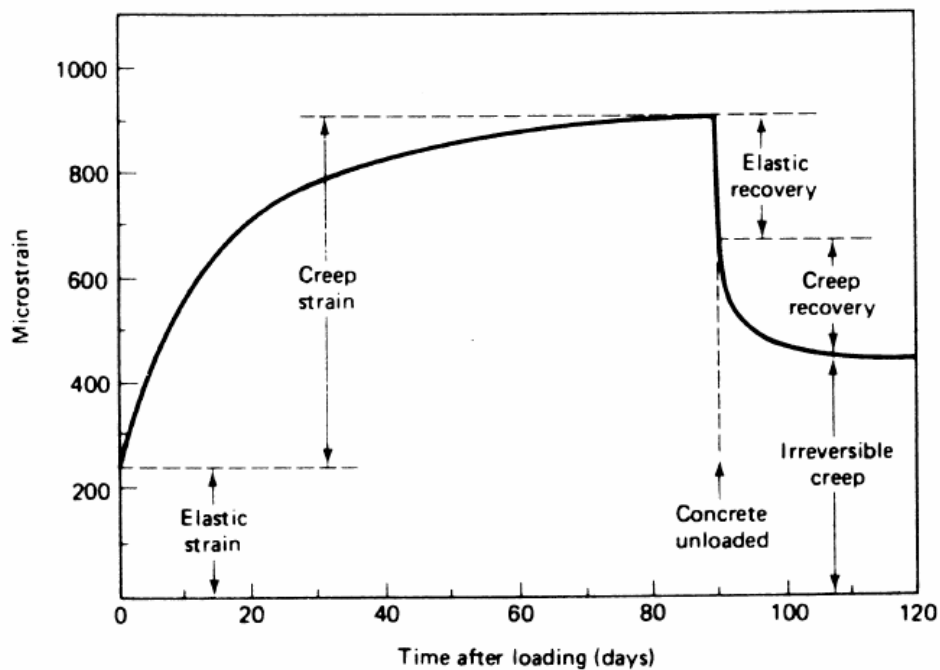


Figure 1.2.21: Time-dependent strain in concrete subjected at age 28 days to the sustained load for 90 days and then 30 days without the load (after [73])

The effects of creep is in addition to the shrinkage. The evolution of the deformation of concrete in time is schematically shown in Fig. 1.2.21. Under normal conditions of loading, the instantaneous strain recorded depends on the rate of application of the load and thus

includes not only the elastic strain but also some creep. It is difficult to differentiate accurately between the immediate elastic strain and early creep, but this is not of practical importance as it is the total strain induced by the application of load that matters. If the stress is removed after some period of time, there is an instantaneous recovery of the elastic strain and then slower recovery of some of the creep, but not all. If the concrete is reloaded at some later date, instantaneous and creep deformations develop again, as shown.

Creep in concrete is a post-elastic phenomenon. In practice, drying shrinkage and viscoelastic behavior such as creep usually take place simultaneously. Considering the various combinations of loading, restraining, and humidity conditions, the following terms are defined:

True or Basic Creep: is defined as the creep that occurs under conditions that there is no drying shrinkage or moisture movement between concrete and ambient environment.

Drying Creep: is the additional creep that occurs when the specimen under load is also drying.

Time-dependent shear strains are associated with creep.

Factors influencing shrinkage and creep:

1. Relative Humidity in cement: One of the most important factors for both shrinkage and creep is the relative humidity of the medium surrounding the concrete. There is a striking similarity between the drying creep and the shrinkage as shown in Fig. 1.2.22. Concrete which exhibits high shrinkage also generally shows high creep. This does not mean that the two phenomena are due to the same cause, but they may both be linked to the same aspect of structure of hydrated cement paste. It should not be forgotten that concrete cured and loaded at a 100% relative humidity (sealed conditions) exhibits creep and that creep produces no loss of water from the concrete to the surrounding medium, nor is there any gain in weight during creep recovery.
2. Aggregate:
 - a) Modulus of elasticity
 - b) Aggregate contentAny increment of these two factors reduce the drying shrinkage and creep
3. Cement:
 - a) w/c ratio: For a constant cement content an incremental increase in w/c ratio increases both drying shrinkage and creep

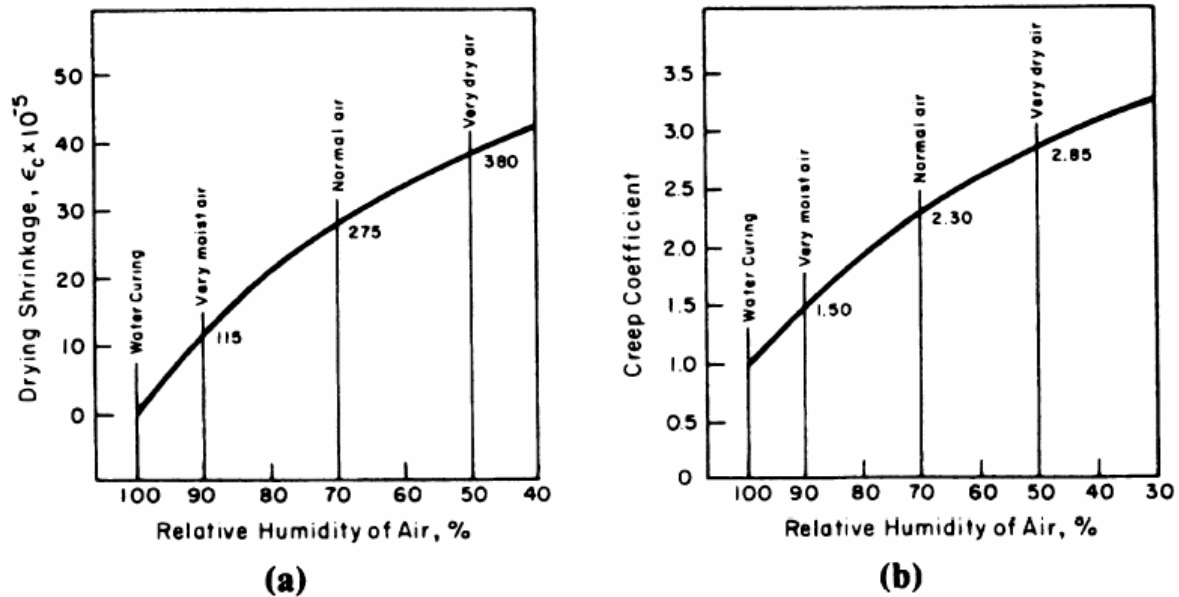


Figure 1.2.22: Influence of relative humidity on (a) drying shrinkage and (b) creep of concrete (after [73])

- b) cement content: For a constant w/c ratio an incremental increase in cement content reduces the creep but increases the drying shrinkage. This is the only case in which an opposite effect exists
4. Relative Humidity in environment An incremental increase in relative humidity of air intensifies both the drying shrinkage and creep. Relative humidity represents the boundary condition for the diffusion equation, the influence of relative humidity should come as the multiplying factor to the shrinkage curve.
 5. Geometry of the concrete element: Theoretical thickness $h = 2A/P$, A - section area, P - perimeter. An incremental increase in the theoretical thickness h reduces the drying shrinkage and creep.
 6. Temperature: Given the same curing history for two specimens, the one that is kept at a higher temperature will have more creep and drying shrinkage than the other one.
 7. Age of loading: There is a direct proportionality between the magnitude of sustained stress and the creep of concrete. Because of the effect of aging on creep, at a given stress level, lower creep values were obtained for the longer period of curing before the application of the load. Shrinkage (is not affected by this factor) can be reduced by aging before drying to increase the rigidity of the network.

Since it is capillary forces which are responsible for drying shrinkage, it can be reduced also by changing surface tension of the liquid (by solvent exchange or increase of the temperature). Also pore size decreases during the shrinkage.

The tendency of a body (solid network) to warp or crack during drying does not depend on the capillary pressure; damage results only from a gradient in the pressure that causes differential shrinkage. The magnitude of the gradient depends on the permeability, modulus, and size of the material, and on the rate of evaporation. Experimental approaches to measure permeability within the framework of Biot's theory are presented in [46].

Although the nature of creep is still uncertain, its partly reversible character suggests that the deformation may consist of a partly reversible visco-elastic movement (consisting of a purely viscous phase and a purely elastic phase) and possibly also a non-reversible plastic deformation.

For stresses not exceeding about one-half of the cylinder strength, creep strains are directly proportional to stress. Creep also depends on the average ambient relative humidity, being about twice larger for 50% than for 100% humidity. This is so because part of the reduction in volume under sustained load is caused by an outward migration of free pore water which evaporates into the surrounding atmosphere. Other things being equal, creep is larger for low-strength than for high-strength concretes. Also the extent of drying before application of load influences the magnitude of creep. As mentioned in [101], Hannant found that further creep and swelling are not significant when dried specimens are re-saturated with organic fluids.

In [1] authors consider two apparent mechanisms of creep:

"The short characteristic time of the first mechanism on the order of 10 days. It suggests a stress-induced water movement towards the largest diameter pores (characteristic distance of the order of 0.1–1 mm). This short-term creep mechanism was first suggested by Ruetz (1966), and pursued by Wittmann (1982); it may be attributed to a change of the hygral equilibrium in the gas filled space which generates strain and stresses (and eventually microcracking), which results in the short-term component of creep. The activation energy of this first mechanism could be that of permeation in the saturated capillary pores (which could explain why basic creep of predried concrete samples fades out). Recent experimental results show evidence that this short-term creep under uniaxial compression occurs under increasing volume.

The second mechanism corresponds to an irreversible viscous behavior, and seems to be more related to viscous flow in the hydrates (slippage between layers which is increasingly inhibited over time, particularly if the hydrates start to lose water). This long-term creep occurs under almost constant volume, which is consistent with a viscous slippage mechanism. A dislocation-type mechanism within the C-S-H sheets of hydrated cement

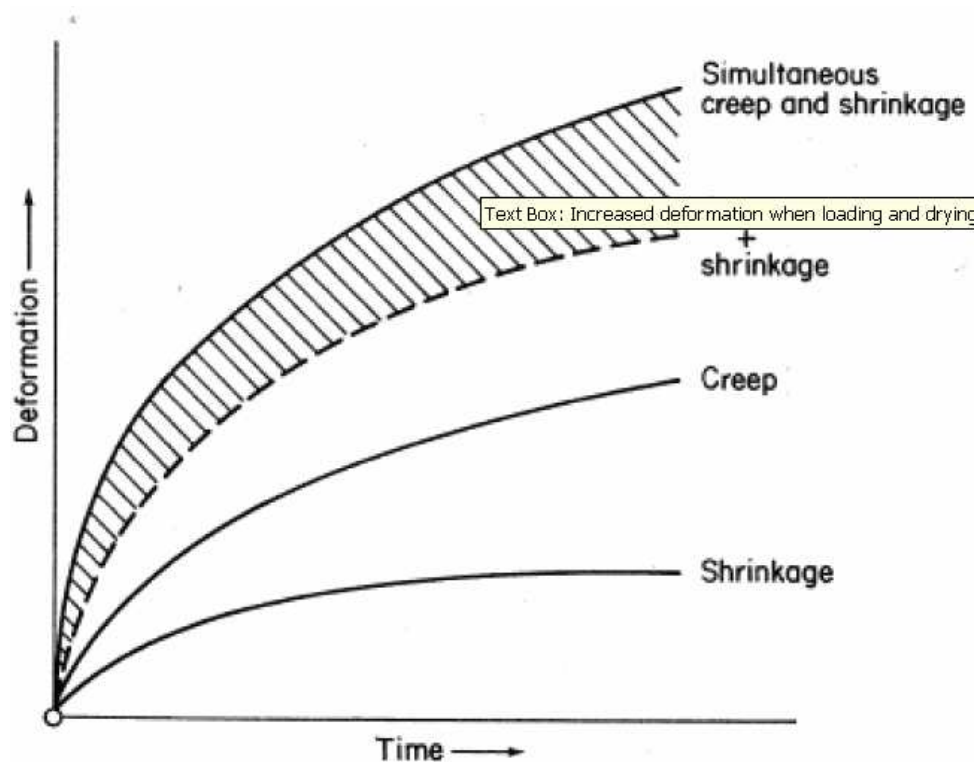


Figure 1.2.23: Pickett's effect

paste has been recently suggested for this long-term creep (Bazant et al., 1997) “

Bazant [5] considers the following main physical mechanisms that allow making inferences for the proper mathematical form of the creep and shrinkage prediction model:

1. Solidification as a mechanism of aging, particularly at early times.
2. Microprestress relaxation as a mechanism of long-time aging [12, 11].
3. Bond ruptures caused by stress-influenced thermal excitations controlled by activation energy (Wittmann).
4. Diffusion of pore water.
5. Surface tension, capillarity, free and hindered adsorption, and disjoining pressure.
6. Cracking caused by self-equilibrated stresses and applied load.
7. Chemical processes causing autogenous volume change and microprestress.

A draft to creep test recommendation RILEM was presented in [1].

1.3 Basic Creep Modeling

1.3.1 Compliance and Relaxation Functions

For the prediction of the risk of cracking in young concrete reliable materials models are needed for the creep and relaxation of hardening concrete. To describe the creep effect (viscous behavior) in cement and/or concrete one of the common approach is to use the compliance function. There are several models based on this approach [101, 78, 12, 11] which propose different functions. It is also very important to distinguish between **creep models for early-ages** (such as microprestress-solidification theory and B3 model) and basic creep models for **hydrated concrete**. Creep models for early-ages should consider hydration process either explicitly (homogenization approaches) or implicitly in the model parameters (compliance, load-bearing Bazant's concept, model codes). But from the mathematical point of view all of them are usually based on the same formulation. One more general consideration is that creep in tension and compression is usually not distinguished, however experimentally early-aged concrete is shown to have different creep properties in compression and tension [56, 3] (tensile creep is higher).

First, let us review some basic aspects of mathematical formulation and then consider different models for early-aged and hydrated concrete.

The main ideas to model basic creep are the following. If the stresses less than about 50% of the strength limit are considered, the creep law is generally assumed to be linear with respect to the stress history $\sigma(t)$ [27]. For uniaxial constant stress σ applied at concrete age t' the corresponding strain $\varepsilon(t)$ will be

$$\varepsilon(t) = \sigma J(t, t') \quad (1.3.1)$$

where $J(t, t')$ is the uniaxial compliance function, a material property characterizing creep.

The linearity of equation (1.3.1) represents the principle of superposition (in time). Decomposing every stress history into infinitesimal steps $d\sigma(t')$ one can write

$$\varepsilon(t) = \int_0^t J(t, t') d\sigma(t') + \varepsilon_0(t) \quad (1.3.2)$$

$\varepsilon_0(t)$ - initial strain; in general it includes shrinkage ε_{sh} , thermal strain and cracking strain.

The integral in (1.3.2) is the Stieltjes integral, in which piece-wise continuous histories $\sigma(t)$ (with jumps) are admitted. If there is a jump from σ^- to σ^+ at time t_j then the contribution to the integral from the jump is $(\sigma^+ - \sigma^-)J(t, t_j)$. For the case of sudden application of the initial stress σ_1 which will vary afterwards continuously as $\sigma(t)$, (1.3.2)

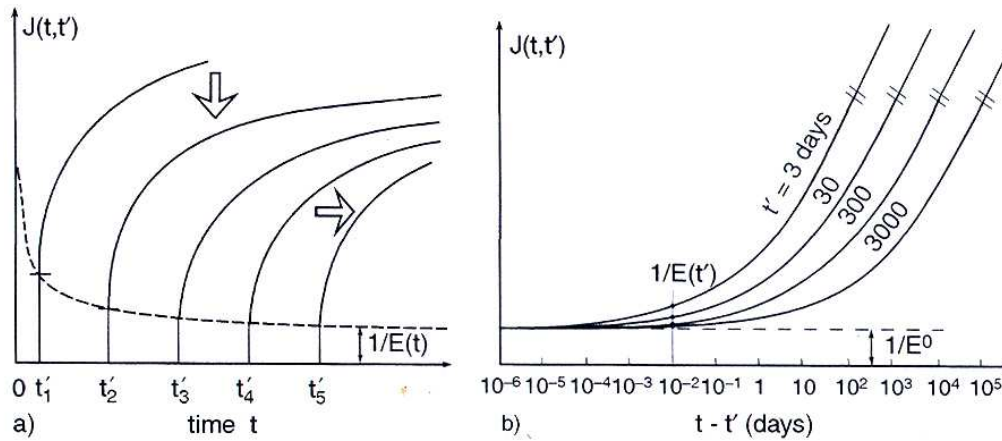


Figure 1.3.1: Compliance function shown by unit creep curves for different ages at loading (after [57])

may be written in terms of the Riemann integral:

$$\varepsilon(t) = \sigma_1 J(t, t_1) + \int_{t_1}^t J(t, t') \frac{d\sigma(t')}{dt'} dt' + \varepsilon_0(t) \quad (1.3.3)$$

If the strain history is prescribed, (1.3.3) represents a Volterra integral equation with the kernel $J(t, t')$. One can solve the relaxation function $R(t, t')$ (Fig. 1.3.2), which represents the uniaxial stress history $\sigma(t)$ caused by a constant strain $\varepsilon = 1$ enforced at any age t' ($t' \leq t$), and write the superposition principle in its inverse form:

$$\sigma(t) = \int_0^t R(t, t') d[\varepsilon(t') - \varepsilon_0(t')] \quad (1.3.4)$$

If neither $\sigma(t)$ nor $\varepsilon(t)$ is prescribed, (1.3.3) and (1.3.4) represent a uniaxial stress-strain relation of creep. If the compliance function depends only on the time lag, $J(t, t') \equiv J_0(t - t')$, one has the general stress-strain relation of classical linear viscoelasticity of polymers which exhibit no aging. In latter case one can apply Laplace transform methods, which can not be applied for aging linear viscoelasticity.

It is very important to know that the creep and compliance function are not independent. Definition of only one function is required. Their dependence in general case can be described by (1.3.5).

$$1 = R(t', t') J(t, t') + \int_{t'}^t J(t, \tau) dR(\tau, t') \quad (1.3.5)$$

If the compliance function depends only on time lag $t - t'$ the relationship between

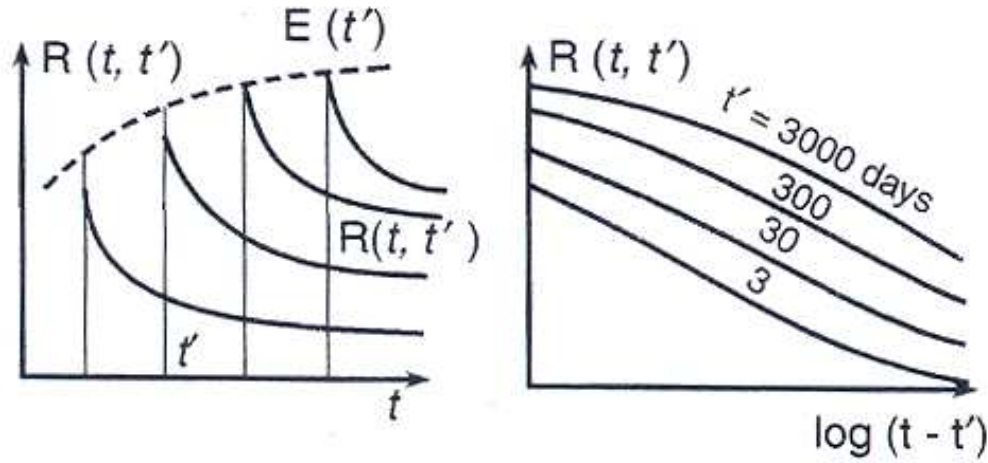


Figure 1.3.2: Relaxation function of concrete (after [57])

compliance and relaxation could also be expressed in the Laplace domain as

$$(s J(s))^{-1} = s R(s) \quad (1.3.6)$$

If the stress exceeds about one half of the strength limit, creep becomes nonlinear, which is due to time-dependent growth of microcracks. The nonlinear creep behavior is best shown by plotting the so-called stress-strain isochrones, obtained by conducting constant load creep tests at different stress levels.

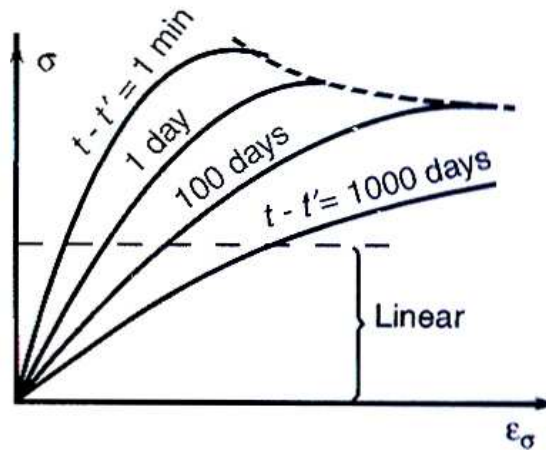


Figure 1.3.3: Creep isochrones at high stress (after [57])

To generalize the uniaxial constitutive equation one can write:

$$\epsilon(t) = \mathbb{C}_v : \int_0^t J(t, t') d\sigma(t') + \epsilon_0(t) \quad (1.3.7)$$

$$\boldsymbol{\sigma}(t) = \mathbb{D}_v : \int_0^t R(t, t') d[\boldsymbol{\varepsilon}(t') - \boldsymbol{\varepsilon}_0(t')] \quad (1.3.8)$$

\mathbb{C}_v - unit elastic compliance tensor, corresponding to Young's modulus $E=1$. \mathbb{D}_v - unit elastic stiffness tensor; $\mathbb{D}_v \equiv \mathbb{C}_v^{-1}$. In the engineering notation for isotropic material \mathbb{C}_v has the form:

$$C_v = \begin{bmatrix} 1 & -v & -v & 0 & 0 & 0 \\ & 1 & -v & 0 & 0 & 0 \\ & & 1 & 0 & 0 & 0 \\ & & & 2(1+v) & 0 & 0 \\ sym. & & & & 2(1+v) & 0 \\ & & & & & 2(1+v) \end{bmatrix} \quad (1.3.9)$$

The aforementioned equations consider isotropy of concrete and Poisson's ratio for creep of concrete to be time-independent and about the same as the elastic Poisson's ratio, both being about 0.18.

From the computational point of view, the history integral (1.3.7) can be approximated by a sum according to the trapezoidal rule or the midpoint rule. But in large structural systems the storage of the entire stress history at each integration point of each finite element and the evaluation of history integrals in such way can be computationally expensive.

The computation can be made much more efficient by approximating the integral-type stress-strain relations (1.3.7) (1.3.8) with rate-type stress-strain relations based on Kelvin chain or Maxwell chain spring-dash pot model of aging viscoelasticity, previous history is reflected by the current values of several internal variables.

The compliance function is approximated by the Dirichlet series:

$$J(t, t') \approx \frac{1}{E_0} + \sum_{i=1}^M \frac{1}{D_i(t')} [1 - \exp(-\frac{t-t'}{\tau_i})] \quad (1.3.10)$$

where τ_i - are fixed parameters called the retardation times, E_0 is the asymptotic modulus, and $D_i(t')$ are age-dependent modulus which can be determined, for example, by least-square fitting of the 'exact' compliance function or from the so-called continuous retardation spectrum. Retardation times should cover the entire time range of interest and must be not too far apart in logarithmic time scale. It is recommended to distribute the retardation times in a geometric progression with quotient 10, taking $\tau_1 \leq 0.3\tau_{\min}$ and $\tau_M \geq 0.5\tau_{\max}$ where τ_{\min}, τ_{\max} - the shortest and longest time delay after an instantaneous load application for which the response should be accurately reproduced.

If we now substitute (1.3.10) into (1.3.7), we obtain:

$$\boldsymbol{\varepsilon}(t) = \sum_{i=0}^M \boldsymbol{\varepsilon}_i(t) \quad (1.3.11)$$

where

$$\boldsymbol{\varepsilon}_0 = \mathbb{C}_v : \int_0^t \frac{1}{E_0} d\boldsymbol{\sigma}(t') = \mathbb{C}_v : \frac{\boldsymbol{\sigma}(t)}{E_0} \quad (1.3.12)$$

$$\boldsymbol{\varepsilon}_i = \mathbb{C}_v : \int_0^t \frac{1}{D_i(t')} [1 - \exp(-\frac{t-t'}{\tau_i})] d\boldsymbol{\sigma}(t') \quad i = 1, 2, \dots, M \quad (1.3.13)$$

It is obvious that unit number 0 is an elastic spring of stiffness E_0 . To find the rheological model of other units one can differentiate (1.3.13):

$$\dot{\boldsymbol{\varepsilon}}_i = C_v : \int_0^t \frac{1}{\tau_i D_i(t')} \exp(-\frac{t-t'}{\tau_i}) d\boldsymbol{\sigma}(t') \quad (1.3.14)$$

Combining (1.3.13) and (1.3.14) one can write:

$$\boldsymbol{\varepsilon}_i(t) + \tau_i \dot{\boldsymbol{\varepsilon}}_i(t) = \mathbb{C}_v : \int_0^t \frac{d\boldsymbol{\sigma}(t')}{D_i(t')} \quad (1.3.15)$$

In the non-aging case $D_i(t) = D_i = \text{const}$:

$$D_i \boldsymbol{\varepsilon}_i + \tau_i D_i \dot{\boldsymbol{\varepsilon}}_i = \mathbb{C}_v : \boldsymbol{\sigma}(t) \quad (1.3.16)$$

which corresponds to the parallel coupling of the elastic spring of stiffness D_i and the damper of viscosity $\eta_i = \tau_i D_i$. So in the non-aging case the approximation of the compliance function by the Dirichlet series (1.3.10) corresponds to the Kelvin chain with constant properties.

In the case of an aging material, differentiating (1.3.15) one can obtain:

$$\dot{\boldsymbol{\varepsilon}}_i(t) + \tau_i \ddot{\boldsymbol{\varepsilon}}_i(t) = \mathbb{C}_v : \frac{\dot{\boldsymbol{\sigma}}(t)}{D_i(t)} \quad (1.3.17)$$

If we consider Kelvin unit with variable parameters, the corresponding differential equation is:

$$E_i(t) \dot{\boldsymbol{\varepsilon}}_i + \frac{d}{dt} [\eta_i(t) \boldsymbol{\varepsilon}_i] = \mathbb{C}_v : \dot{\boldsymbol{\sigma}}(t) \quad (1.3.18)$$

Comparing (1.3.18) with (1.3.17) one can conclude that in this case:

$$\begin{aligned} \eta_i(t) &= \tau_i D_i(t) \\ E_i(t) &= D_i(t) - \dot{\eta}_i(t) = D_i(t) - \tau_i \dot{D}_i(t) \end{aligned} \quad (1.3.19)$$

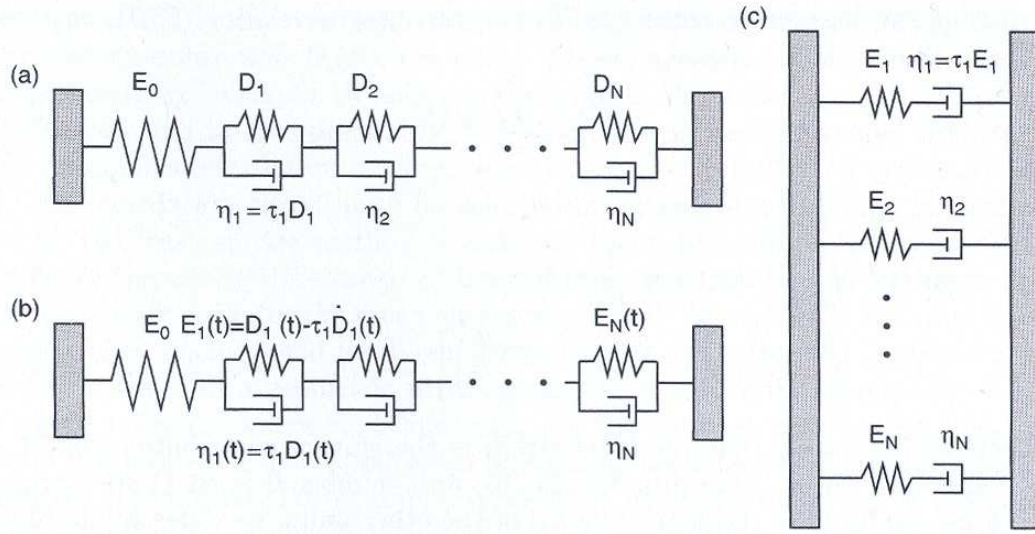


Figure 1.3.4: a) Non-aging Kelvin chain, b) aging Kelvin chain, c) Maxwell chain (after [57])

History is “held” in the finite number of internal variables that characterize individual units of the corresponding rheological chain.

From the computational point of view it is better to introduce “internal” variables $\gamma_i(t)$ and to rewrite the second-order differential equation (1.3.17) as two first-order differential equations

$$\begin{aligned}\gamma_i(t) &= \tau_i \dot{\epsilon}_i(t) \\ \dot{\gamma}_i(t) + \frac{1}{\tau_i} \gamma_i(t) &= \mathbb{C}_v : \frac{\dot{\sigma}(t)}{D_i(t)}\end{aligned}\tag{1.3.20}$$

which can be integrated numerically.

In the solidification theory for concrete creep, which will be described later, the compliance function is expressed as:

$$J(t, t') = \int_{t'}^t \frac{1}{v(\theta)} \dot{\Phi}(\theta - t') d\theta\tag{1.3.21}$$

where Φ is the compliance function of the non-aging constituent, $v(\theta)$ -relative volume of the solidified material.

Approximating $\Phi(t)$ by Dirichlet series

$$\Phi(t) = \sum_{i=1}^M \frac{1}{D_i} \left[1 - \exp\left(-\frac{t}{\tau_i}\right) \right]\tag{1.3.22}$$

one can obtain a system of equations similar to (1.3.20):

$$\begin{aligned}\gamma_i(t) &= \tau_i v(t) \dot{\epsilon}_i(t) \\ \dot{\gamma}_i(t) + \frac{1}{\tau_i} \gamma_i(t) &= \mathbb{C}_v : \frac{\dot{\sigma}(t)}{D_i(t)}\end{aligned}\tag{1.3.23}$$

Dependence on the maturity of the material is in the definition of $\gamma_i(t)$.

No characteristic time at which the creep evolution would qualitatively change is seen in experiments, and so the creep rate should follow a power law. This is the only law, which exhibits $f(t1)/f(t2) = f(t1/t2)$ for any $t1$ and $t2$. It comes from the following consideration: If physical process $f(t)$ involves no characteristic time, it must be self-similar for short and long time. By a similar argument, if a structure possesses no characteristic dimension, then the structural response must again scale as a power function of size. For $\theta \ll t$ there can be no appreciable aging during creep, so $\dot{J} \propto \theta^{n-1}$. As for the opposite asymptotic behavior $\theta \gg t'$, creep and aging act together, so $\dot{J} \propto t^{-1}$.

The most famous function for compliance are the **Double Power Law**, **Triple Power Law** and **Log Double Power Law**.

1.3.2 Several Other Approaches for Creep Modeling

To this moment \mathbb{C}_v was considered as a constant. But there are models [14] which use a time-dependent Poisson ratio, latter allows to describe the long-term creep of concrete in more appropriate way and to have a better agreement with the experiments. In [14] Benboudjema et al. propose a basic creep model under multiaxial compressive stresses. They consider creep Poisson ratio not to be constant with time. Latter depends upon the multiaxial character of the stress state and thus is non-isotropic. Using splitting of the creep strain process to a spherical part and a deviatoric part they consider two different mechanisms of creep.

The spherical creep mechanism concerns water movements in both capillarity space (reversible) and intrinsic porosity (irreversible), driven by hydrostatic component of the stress tensor (Fig. 1.3.5). The macroscopic spherical loading is firstly transmitted to the water absorbed between the hydrated products, in the form of a pressure. The water involved will therefore migrate reversibly to the non-saturated capillary space, without any increase of the capillary pore pressure. When the skeleton is progressively loaded, the macroscopic spherical loading is then retransmitted to the water absorbed in the intrinsic porosity of the hydrates, which will migrate to the capillary pore too, but this movement is now irreversible due to the capillary tension. Several tests confirmed the partially reversible character of the spherical creep strain. The first mechanism has been related to the short-term creep. As for the second mechanism, the water migration is

much slower due to the high complexity of the microstructure of the hydrated products, and is therefore related to the long-term creep ((1.3.27)).

The macroscopic deviatoric loading is transmitted at the microporosity scale, which will drive the sliding of the C-S-H sheet. Deviatoric creep strain also has a reversible and an irreversible component. The water absorbed near the C-S-H gel wall (with a great absorption energy) is responsible for the reversible aspect of the deviatoric creep ; after unloading, it will drive back the C-S-H sheet sliding, due to its load-bearing character. After some water layers, the absorption energy is much lower, therefore the movement of this water is not reversible (Fig. 1.3.5, (1.3.30)). Water migration in both nano and micro-porosities is modeled by the Poiseuille equation by assuming cylindrical connected porosity. The behavior of the hydrated and the unhydrated cement particles is assumed to be elastic.

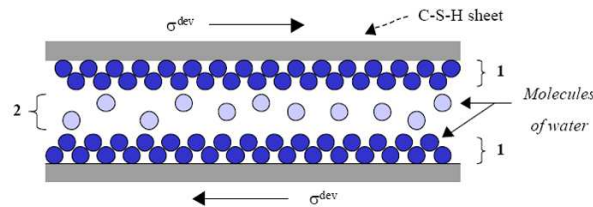


Figure 1.3.5: Deviatoric reversible and irreversible mechanism for basic creep used by Benboudjema (after [14])

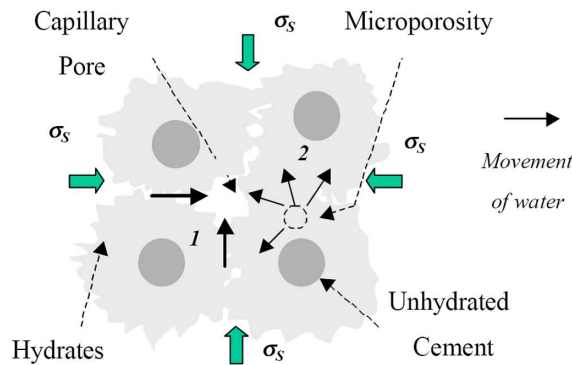


Figure 1.3.6: Volumetric reversible and irreversible mechanism for basic creep used by Benboudjema (after [14])

The use of the water mass conservation law for a representative volume leads to:

$$\dot{\varepsilon}_{rev}^v = \frac{1}{\eta_{rev}^v} [h \sigma^v - k_{rev}^v \varepsilon_{rev}^v] - 2 \dot{\varepsilon}_{ir}^v \quad (1.3.24)$$

$$\dot{\varepsilon}_{ir}^v = \frac{1}{\eta_{ir}^v} \langle [2 k_{rev}^v \varepsilon_{rev}^v - k_{ir}^v \varepsilon_{ir}^v] - [h \sigma^v] \rangle \quad (1.3.25)$$

$$\varepsilon^v = \varepsilon_{rev}^v + \varepsilon_{ir}^v \quad (1.3.26)$$

$$\langle x \rangle = (x + |x|)/2 \quad (1.3.27)$$

where ε_{rev}^v and ε_{ir}^v are reversible and the irreversible spherical creep strain respectively; η_{rev}^v and η_{ir}^v are the apparent viscosities of the water at two different scales of the material (macroscopic and microscopic). These apparent quantities depend upon the water viscosity and the connected porosity geometry. Further, k_{rev}^v and k_{ir}^v are the apparent stiffness associated to the precedent viscosities and related to the stiffness of the porous material and the skeleton. σ^v - volumetric stress.

$$\eta_{rev}^{dev} \dot{\varepsilon}_{rev}^{dev} + k_{rev}^{dev} \varepsilon_{rev}^{dev} = h \sigma^{dev} \quad (1.3.28)$$

$$\eta_{ir}^{dev} \dot{\varepsilon}_{ir}^{dev} = h \sigma^{dev} \quad (1.3.29)$$

$$\varepsilon^{dev} = \varepsilon_{rev}^{dev} + \varepsilon_{ir}^{dev} \quad (1.3.30)$$

where ε_{rev}^{dev} and ε_{ir}^{dev} are the reversible and the irreversible deviatoric creep strain respectively; η_{rev}^{dev} and η_{ir}^{dev} are the apparent viscosities related to strongly absorbed and unabsorbed water in the C-S-H porosity and k_{rev}^{dev} is the stiffness of the strongly absorbed water, associated to its bearing capacity. σ^{dev} is the deviatoric stress.

The extension of this model for early-age is presented in [15]. The hydration and temperature fields are considered the same way as in [104] by Ulm. The effect of age on basic creep of concrete is taken into account by relating the material parameters to the degree of hydration.

Three-dimensional viscoelastic model for creep developed within the framework of the thermodynamics is presented in [19] by Boudjelal. Instead of scalar compliance, a tensorial compliance is introduced, but it depends on evolution parameter of internal variables (temperature and humidity) in the integral form.

There are approaches which allows to obtain failure curve during creep using some simple probabilistic models [78].

In [45] Granger presented the approach to homogenize the creep properties in series-parallel model, at which part of the cement paste in parallel is considered to fill the voids when the aggregate is at the maximum compactness and the remaining portion of the paste corresponds to the series coupling. This model also uses the compliance function.

There is a model [37], which tries to combine the solidification and deterioration theory in description of visco-elastic properties with the compliance function.

In [50] Bolander investigated effects of inclusion type, volume fraction and arrangement on concrete basic creep using rigid-body-spring networks (RBSN, can be considered as lattice model) with conventional rate-type creep laws. Hardening of the cement paste is considered. Non-drying and constant temperature environment is considered.

RBSN approach requires a Voronoi discretization of the material. Each contiguous pair of Voronoi nodes is connected via rigid arms and a zero-size spring set located at the midpoint of the common boundary segment. This element of the random lattice has three degrees of freedom at each node. Spring stiffnesses are scaled according to the geometry of the Voronoi diagram, so that the elastic modulus of the material is realized.

Time-dependent deformations and aging of concrete are modeled using the Maxwell chain representation of the relaxation function in place of the linear springs at the midpoint of the boundary segment. Result of this study indicates that spatial arrangement of the inclusion within RVE can have a significant effect. This effect was checked on two configurations: one inclusion in the center of RVE with/without additional parts of inclusions at the corners.

The paper [107] of Breugel is based on the explicit modeling of the microstructure evolution of the hydrating cement paste provided by hydration model HYMOSTRUC. But the output of hydration model (evolution of microstructure) is used implicitly - it is used only for parallel-series coupling description of an anhydrous cement, cement gel and air/water.

The combination of solidification theory for early-age creep description and thermodynamics formulation (as in [104] with chemical affinity) is presented in [88]. Effective stress concept is used. Shrinkage is modeled with the Biot's theory. Numerical agreement for shrinkage, basic creep and drying creep is achieved.

Compliance function could also be introduced as a piece-wise linear curves in logarithm of time [58], it is aimed to describe the creep behavior at very early loading ages (before 2 days).

Interesting creep formulation for early-age concrete was used in [95] for thermo-chemo-mechanical modeling of the foundation slab. The short-term creep (associated to the micro-diffusion movement of water in the capillary pores; reversible) has the form [94]:

$$\tau_v(\xi) \dot{\boldsymbol{\varepsilon}}^v = J_\infty^v \mathbb{G} : \boldsymbol{\sigma} - \boldsymbol{\varepsilon}^v \quad (1.3.31)$$

$$\mathbb{G} = E \mathbb{C}^{-1} \quad (1.3.32)$$

where J_∞^v represents the asymptotic value of the creep function in compression and $\tau_v(\xi) =$

$\tau_{v,\infty}$ ξ is the characteristic time of micro diffusion process of water.

The long-term creep is considered as irrecoverable and thermo-activated. It is related to a dislocation mechanism between the interfoliar layers of C-S-H. The following equations describe the evolution of the long-term creep [94]:

$$\boldsymbol{\varepsilon}^f = 1/\eta_f \mathbb{G} : \boldsymbol{\sigma} \quad (1.3.33)$$

$$1/\eta_f = k^0 \Gamma(t) e^{\left[-\frac{2U}{R}\left(\frac{1}{T}-\frac{1}{T_0}\right)\right]} \quad (1.3.34)$$

$$\dot{\Gamma} = -H\dot{\gamma} \quad (1.3.35)$$

$$\dot{\gamma} = k \Gamma^p e^{\left[-\frac{U}{R}\left(\frac{1}{T}-\frac{1}{T_0}\right)\right]} \quad (1.3.36)$$

where η_f is a viscosity term that depends on the temperature reflecting the thermoactivation of long-term creep. U is the long-term creep activation energy, such that $U/R = 2700 \text{ K}$; Γ represents the thermodynamic force responsible for long-term creep; γ is an internal variable that models the dislocation between the nano layers of C-S-H; H (MPa) is a material characteristic parameter that may be determined by means of a compressive creep test performed at a reference temperature T_0 ; the terms p , k ($\text{MPa}^p \text{s}^{-1}$) and k^0 ($\text{MPa}^{-1} \text{s}^{-1}$) are material constants.

1.4 Modelling of Microstructure of Cement

In order to predict mechanical properties detailed information on microstructure is needed. Simplified approaches which deals with volume fraction of each hydration product will never yield different properties for same amount of porosity but different arrangements. This is just one of many examples.

That microstructure can be obtained by 3d Tomography or 2D Back Scattered Electron (*BSE*) images. Disadvantage is that currently maximum four (generally three) phases can be distinguished: porosity, Portlandite, other hydration products (mainly C-S-H), unhydrated clinker. Still this microstructure is of grate help for modeling as a verification tool.

Microstructure hydration can be divided by into vector models (MIC[18]) and voxel-based models (Hymostruct[106], CemHyd3D[16]). Le us give some details on latter since it will be used in current studies.

CemHyd3D was developed in *NIST* based on *BSE* images observed under an electron microscope. The physics behind is modelling of reaction and diffusion by cellular automata with probability functions. Each voxel represent one phase, initially there are unhydrated clinkers and water only. Edge of such voxel is $1\mu m$. This size should be as small as possible to capture all important processes (dissolution, transport and diffusion) but is limited from validation point of view due to resolution limit of experimental techniques. Hydration products are, with certain probabilities, formed on the grains exposed to water contact and they nucleate in the available pore space. This dissolution probabilities reflect dependence of hydration kinetics on temperature, alkalis (alkalinity of the water-filled porosity) and saturation. Initial random 3D microstructure, which should reflect clinker Particle size distribution (*PSD*) is obtained with the help of autocorrelation functions. Clinkers are considered to be spherical initially. *RVE* remains periodic during modeling which is beneficial for application of homogenization procedures. It is well known that cellular automata do not have intrinsic time, but rather cycles of different “rules” which reflect diffusion. Mapping of such cycles to time introduces additional fitting, therefore verification is done based on degree of hydration but not time. Example of such microstructure is presented in Fig. 1.4.1. Recommended *RVE* for cement paste is not less than $100\mu m$.

It should be noted, that resolution of *CemHyd3D* model equal to $1\mu m$ means that all the detailed information below is lost. Therefore even though micromechanical consideration and state of the art knowledge of different phases in cement paste may lead to details below that level, mechanical representation of such models have to be brought to $1\mu m$ scale. This difficulties can be overcome by vector models such as MIC[18] which

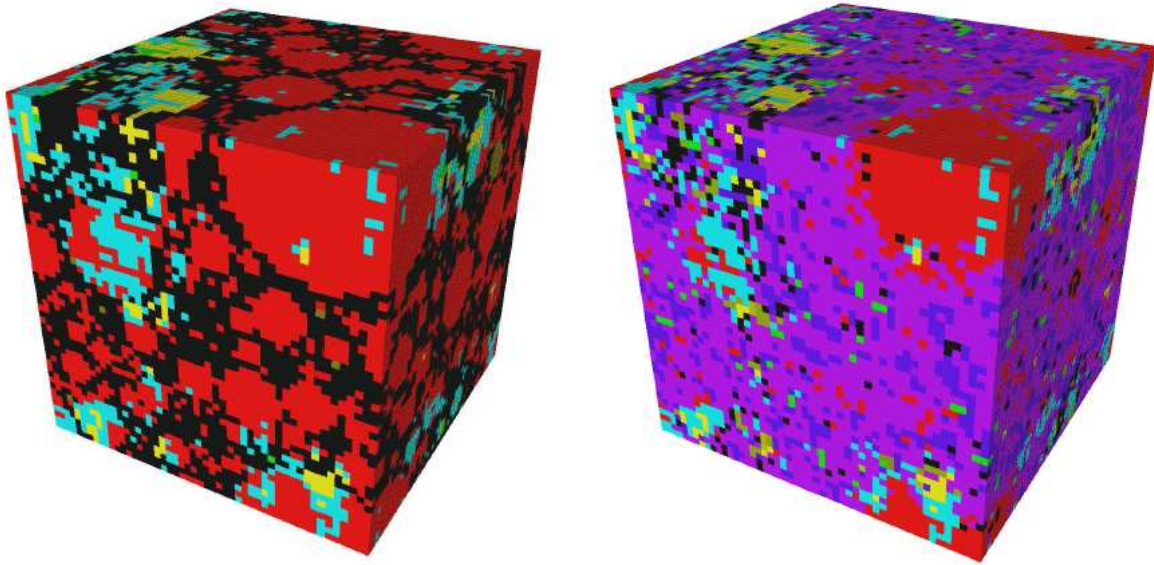


Figure 1.4.1: Microstructure $50 \times 50 \times 50 \mu m$, $w/c = 0.24$, initial (left) and at the degree of hydration of 0.63 (right). Red = C_3S , cyan = C_2S , green = $CCCA$, yellow = $CCCCAF$, black = porosity, violet = C-S-H, blue = CH(after [111])

do not have intrinsic resolution (radius of spheres in such model can be arbitrary small number). However difficulties in meshing and application of homogenization procedures arise immediately. Current studies of such models are limited to pure elastic behavior and percolation threshold.

Another problem which arises in all microstructure models is state before percolation. Commonly, clinkers are placed in water and reaction starts. But before percolation threshold, cement is not solid but liquid. Therefore description of model is not realistic from that point of view. It could also be noted that interparticle forces can lead to some agglomeration which can not be described just by diffusion and dissolution. Yet, current developments of such models do not consider this issues.

More detailed review of *CemHyd3D* can be found in [111].

1.5 State of the Art: Models of the C-S-H Structure and Creep Theories

1.5.1 C-S-H Microstructure

There is no unified microstructure model of the C-S-H. Two main approaches compete: one considers a globular structure of the C-S-H, whereas the other considers a layered structure.

Tab. 1.5.1 presents a summary of the nano-models for the C-S-H (after [51]).

Authors	Primary Experimental Basis	Type	Selected Characteristics
Powers (1958)	Water sorption, Volume of pores	Colloid	All products of gel particles, Gel pore volume 28 %
Kantro, Brunauer, Weiss (1970)	Hysteresis of water sorption	Layer, Tobermorite	High surface area gel
Feldman, Sereda (1970)	Nitrogen sorption, Length vs. RH, Modulus vs RH, Weight vs RH	Layers	Clay like structure with important role of inter-layer water
Wittmann (1979)	Modulus vs RH	Colloid	Important role of water in spaces between particles
Jennings (2000)	Density, Composition, Surface area, Fractal	Colloid	Reconcile as many different physical characteristics as possible

Table 1.5.1: Summary of the nano-models of the C-S-H (after [51]).

First of all let us review the colloidal approach. Jennings and Thomas [102] propose a globular model of the structure at the nanometer scale. The visco-elastic deformation is the result of globules movement under the stresses or drying. These globules can form two different structures: C-S-H_{HD}-1.670 kg/m³, C-S-H_{LD}-1.400 kg/m³. This model also takes into account the fractal nature of the C-S-H structure. In other words the “main” particles do not have a unique size (such as radius) but rather “spread” over different nano-scales. According to this approach [53]: “The low-density C-S-H first forms as an open fractal structure consisting of a random agglomeration of 5 nm C-S-H globules with a relatively low packing density. This structure is easily deformed to produce the irreversible changes associated with drying and creep. With the passage of time, or following the application of elevated temperature, drying, or load, the low-density C-S-H

densifies to approach a random jam-packed structure and becomes increasingly resistant to irreversible deformation.” However there is a discussion on this work [76].

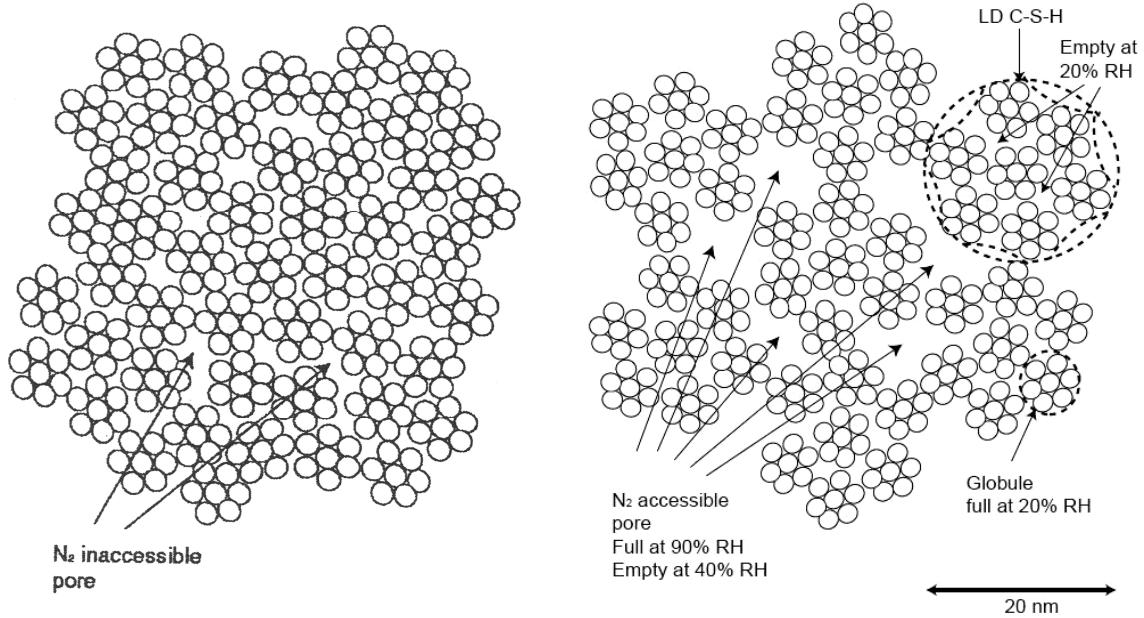


Figure 1.5.1: 2-D scheme of C-S-H_{HD} (left) and C-S-H_{LD} (right) at water/cement ratio = 0.4 (after [51])

The average packing density of the C-S-H_{HD} structure is 74%, which is just that of close-packed spheres, i.e. the face centered cubic structure or one of its hexagonal variants, in which each sphere is in contact with 12 nearest neighbors. The C-S-H_{LD} structure is more complex, with a packing density that varies with scale such that the structure is fractal over length scales up to a maximum of about 60 nm. In addition, the C-S-H_{LD} structure varies with the curing conditions and environment. As a result of the different packing densities and nearest neighbors, the C-S-H_{HD} and C-S-H_{LD} structures have different mechanical properties which have been measured directly by nanoindentation [28].

This approach is based on the results of measurements using three techniques [53]: small-angle neutron scattering (SANS), nanoindentation, and equilibrium drying. When interpreted together, they give a more complete and detailed picture of the nanostructure of the C-S-H gel phase as a function of aging, drying, and heating.

One of the postulates of this model is that C-S-H continues to densify (increase in the specific surface area measured by gas sorption) even after the end of the hydration, also the pore distribution is not constant.

Direct experimental measurement of the nanomechanical properties of the solid C-S-H phase is currently still out of reach. However, using this approach, the value of the solid

C-S-H indentation modulus (m_s) can be obtained from the inverse application of a micromechanical model to the homogenized data [53]. The information that is available for the two types of C-S-H are the porosities (φ^{LD} , φ^{HD}) determined by mass density measurements from SANS, and composite stiffness values (M_{LD} , M_{HD}) determined independently by nanoindentation. Using this data, an inverse application of the self-consistent model, commonly employed for polycrystalline materials, yields separate estimates of the solid C-S-H indentation stiffness for the C-S-H_{LD} ($m_s=65.9$ GPa) and C-S-H_{HD} ($m_s=62.9$ GPa). The two values are very close, suggesting that the two types of C-S-H are comprised of the same solid phase and thus that their different mechanical performance is related to differences in their nanometer-scale porosity, in agreement with the colloid model.

One can predict the indentation modulus of an aggregated system of particles by the self-consistent scheme with an intrinsic solid stiffness of $m_s=65$ GPa (average value of the two estimates). Figure 25 shows the predicted indentation modulus of such a system as a function of the packing density.

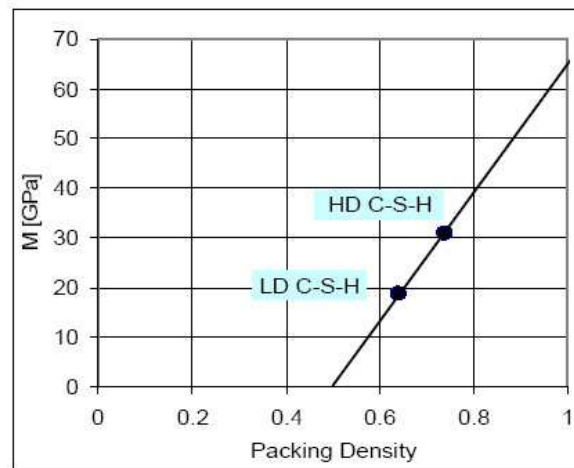


Figure 1.5.2: Micromechanical prediction (solid line) of the indentation modulus of an aggregation of spherical particles (with $m_s=65$ GPa) versus the packing density (1-porosity). The experimental modulus values of C-S-H_{LD} and C-S-H_{HD} are also plotted, using the packing densities of C-S-H globules specified by the colloid model (after [53])

Jennings [53] also presented data of measurements heat curing effect on the microstructure:

It can be readily observed that the mean values of the indentation modules of the two types of C-S-H are essentially constant, indicating that the heat curing process does not change the intrinsic packing density of C-S-H, but mainly affects the volume fraction.

The 28 days heat cured specimen has a significantly lower volume fraction of C-S-H_{LD}. This is in agreement with the fact that elevated temperature curing is known to result in

	28 d @ 20°C	1 d @ 60°C 27 d @ 20°C	28 d @ 60°C	27 d @ 20°C 1 d @ 60°C
	LD / HD	LD / HD	LD / HD	LD / HD
M (GPa)	18.8 / 31.0	17.8 / 29.8	18.0 / 28.5	18.3 / 29.1
f (%)	51 / 25	50 / 29	28 / 31	48 / 30

Table 1.5.2: Indentation modulus, M , and volume fraction, f , for the $C-S-H_{LD}$ and $C-S-H_{HD}$ phases as determined from indentation measurements of white Portland cement paste specimens mixed at a water/cement ratio of 0.5 and given the curing time and temperature indicated (after [53])

a coarser macroporosity and a consequent reduction in macroscopic strength.

It is also possible to extract some visco-elastic properties from the nanoindentation [109]. A first-order estimate of the creeping process of the material can be obtained by fitting the time-dependent deformation during the holding period to a logarithmic function of the form:

$$h = A \ln \left(\frac{t}{B} + 1 \right) \quad (1.5.1)$$

where A and B are empirical constants representing a length scale and time scale of the creeping process, h - penetration depth in nanoindentation experiment. Fig. 1.5.3 displays the frequency plots of A and $1/B$ for the control and the heat cured specimens.

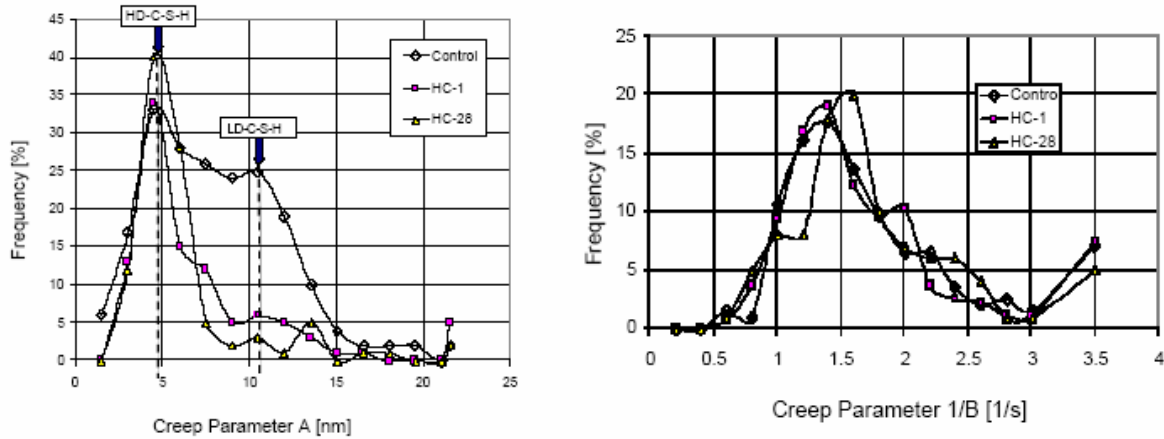


Figure 1.5.3: Distribution of the creep parameters A and $1/B$ determined from multiple indents across a grid on each paste. Assignment of the peaks to $C-S-H_{LD}$ and $C-S-H_{HD}$ at left for parameter A is based on the indentation module (after [53])

As expected, the only creeping phase in cement paste is the $C-S-H$; other phases (Port-

landite, clinker) act as a restraint to the system. Of particular interest is the observation that the fitted creep magnitude A has a similar bi-modal frequency distribution as the stiffness (Fig. 1.5.3, left). This indicates that the C-S- H_{LD} creeps more than C-S- H_{HD} . The fitted time constant B for the three samples is on the average the same (Fig. 1.5.3, right), which is an indication that the same rate-determining process relating to creep is at work in both C-S- H_{LD} and C-S- H_{HD} . Overall, these results suggest that the origin of creep is situated within the globule, and the propensity to creep is scaled with the internal porosity of the structure, i.e. the packing density.

Because the C-S- H_{HD} structure is tightly packed, its basic configuration is very stable and is unaffected by heating, drying, or aging. On drying, water can be lost only at humidity levels below about 50% RH, and this water can reversibly re-enter the structure on rewetting.

One of the key features of the modeled C-S- H_{LD} structure shown in Fig. 1.5.4 is that it has a volume fractal structure, as is observed directly by SANS. The two circles shown in Fig. 1.5.4 are centered on a region of highest packing density. The smaller circle represents the scale of the more densely packed C-S- H_{LD} units proposed in the colloid model, and the larger circle shows the smallest volume that contains the average packing density of the structure. The fractal exponent and correlation length of the structure of Fig. 1.5.4, estimated from the change in packing density with distance away from the densest regions, are in reasonable agreement with the values measured directly by SANS.

As it appears now, the origin of creep is situated within the globule, most probably a sliding of C-S-H sheets. But this sliding is affected at the scale of the C-S-H packing around the two characteristic limit modes by the packing density. It is suggested, that the individual creep sliding in one single globule is blocked by an adjacent globule. Hence, as the packing density increases, the degree of restraint of the sliding increases as well. This is why the lower packed C-S- H_{LD} creeps more than the higher packed C-S- H_{HD} . Since it has been shown here that age, heating, and drying all increase the C-S- H_{LD} density, an explanation for the decrease in creep rate resulting from these processes is obtained.

Proposed structure of the C-S-H can explain drying cycles effect and non-reversible deformation. During first cycle of drying capillary forces lead to the collapse of the C-S- H_{LD} . This deformation, of course, is not reversible on re-wetting. For C-S- H_{HD} water can be lost at humidity levels below 50% and this water can reversibly re-enter the structure on rewetting.

Concluding the review of this model, Jennings [54] proposed the relationship between RH and pores to dry (Tab. 1.5.3).

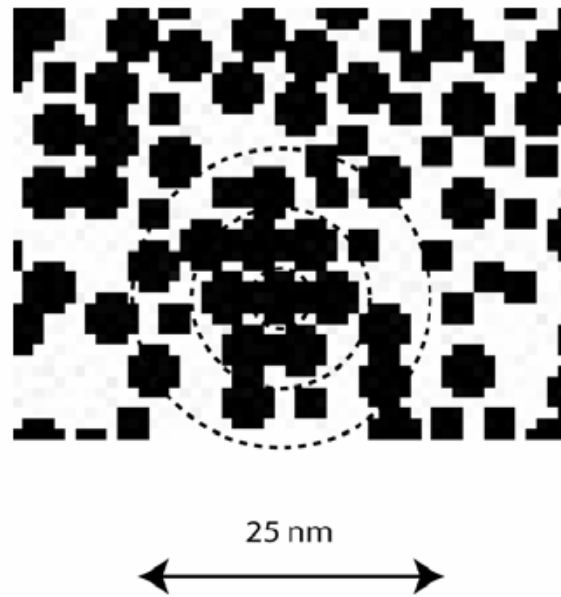


Figure 1.5.4: The intermediate $C-S-H_{LD}$ structure, consisting of a relatively loose packing of 5 nm globules. Shown is a 2D slice from a 3D nanostructure generated by a computer simulation based on autocatalytic growth of spheres. The smaller squares are spheres (globules) lying just above or below the plane. The overall packing density is 52% and each globule on average contacts 6.3 nearest neighbors (after [53])

Relative Humidity (RH)	85%	76%	54%	33%	<33%
Pore diameter (nm)	13	7.8	3.4	1	<1
Origin of pores	Capillary pores	$C-S-H_{LD}$ (gel pores)	$C-S-H_{LD}$ (gel pores)	$C-S-H_{HD}$	$C-S-H$ "building blocks"

Table 1.5.3: Theoretical relationship between relative humidity and pore size. Larger pores will empty (dry) and smaller pores will remain saturated (after [54])

1.5.2 Microstructural Creep Theories

Tamtsia et al. [101] proposed the following classification of creep theories:

Viscous shear theory

A mechanism proposed by Ruetz and called the adsorption theory suggests that creep occurs through slip between $C-S-H$ particles in a shear process in which water acts as

a lubricant. The sliding process takes place in the very thin, multi-molecular layers of adsorbed water.

Interlayer theory

The ‘interlayer’ hypothesis proposed by Feldman and Sereda is that creep of cement paste is a manifestation of the gradual crystallization or aging of a poorly crystallized layered silicate material, accelerated by drying or stress; the adsorbed water does not play a significant role in the mechanism. According to this theory the basic unit of C-S-H gel is a layer, they do not form particles and are distributed randomly so that occasional “interlayer spacings” form throughout the C-S-H gel. Water vapor can move reversibly in and out of these interlayer spacings.

Seepage theory

The seepage theory ascribes the volume changes due to the application of an external load to the change in the internal vapor pressure and hence, in the gel water content. It predicts water loss from the specimen during basic creep. Powers describes a process where the disjoining pressure following the variations in moisture content of cement paste is exerted by the load-bearing water in areas of hindered adsorption. The external load squeezes some of this water out into areas of unhindered adsorption by a time-dependent diffusion process. Powers states that C-S-H gel consists of randomly-arranged colloidal particles, each containing a few closely-bonded structural layers. On drying, these layers collapse and do not permit reentry of water.

Energy theory

Ishai suggests that, whereas the diffusion of inter- and intracrystalline adsorbed water is the principal creep mechanism even in immersed bodies, this moisture movement is not connected with the drying shrinkage that occurs in the normal range of relative humidity. The creep process, which takes place in the inter- and intracrystalline spaces and the respective adsorbed water, is different both in type and origin. The applied load causes a decrease in those interparticle spaces within the range of the physical forces reducing the energy level of the system. The process is therefore irreversible.

Thermal activation theory

According to Wittmann, diffusion of water does not play a major role in the creep mechanism. He does consider, however, that water plays an indirect role through its effect on disjoining pressure which, in turn, weakens interparticle bonds. After the strength of these

forces is reduced, the particles slide apart with respect to each other and creep is therefore increased. The hypothesis is that time-dependent strains are the results of thermally activated processes that can be described by the rate process theory. Creep strains will originate through deformation of a microvolume of paste, designated as a ‘creep center’. This area will undergo deformation to a lower energy state if external energy is applied to the material by means of either load or temperature.

C-S-H gel made up of discrete particles bonded together by Van-der Waals forces, with a bonding strength strongly affected by moisture content.

Various other mechanisms have been invoked to account for creep phenomena in cement paste. These include microcracking, which may even occur at high relative humidity as a result of shrinkage stress developed near non-shrinking CH crystals. Recrystallisation under load (sometimes referred to as aging) reflected by the changes in surface area measurement at different degrees of reaction and different loading and drying conditions and slip between paste and aggregate are other possible considerations.

Polymerization and irreversible creep

Bentur et al. suggested that irreversible creep might be related to aging due to silicate polymerization of the C-S-H, induced by loading or drying.

Let us illustrate the shear theory. The creep taking place in hardened cement paste is believed to be mainly due to microsliding between adjacent sheets of C-S-H.

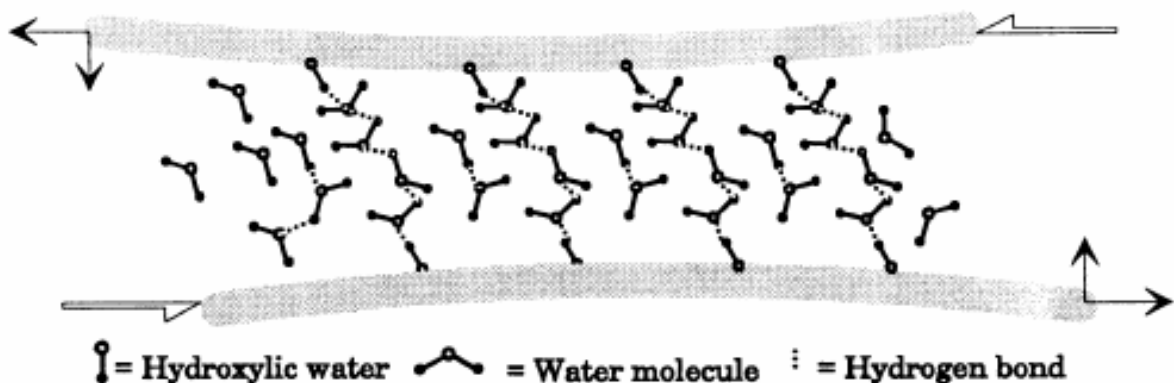


Figure 1.5.5: Sliding between C-S-H sheets resulting in breaking and reconstitution of hydrogen bonds

The chemically bounded water may facilitate sliding of C-S-H sheets one over the other by acting as lubricant. The sliding taking place may be followed by the changing orientation of intra- and intercrystallite water as the surface of the C-S-H sheets approach each other resulting in further layering or aging as suggested by Feldman.

However, Tamtisa et al. [101] have an experimental proof, that cement paste dried to an intermediate humidity equal to 42% RH and re-saturated creeps significantly more than saturated cement paste that has not been dried. This is attributed to the pore coarsening effect due to drying and possible increase in creep sites due to increased layering of C-S-H. And also that hardened cement paste specimens that have been fully dried (if there is no moisture exchange with the surrounding medium) creep as much or more than saturated reference specimens!

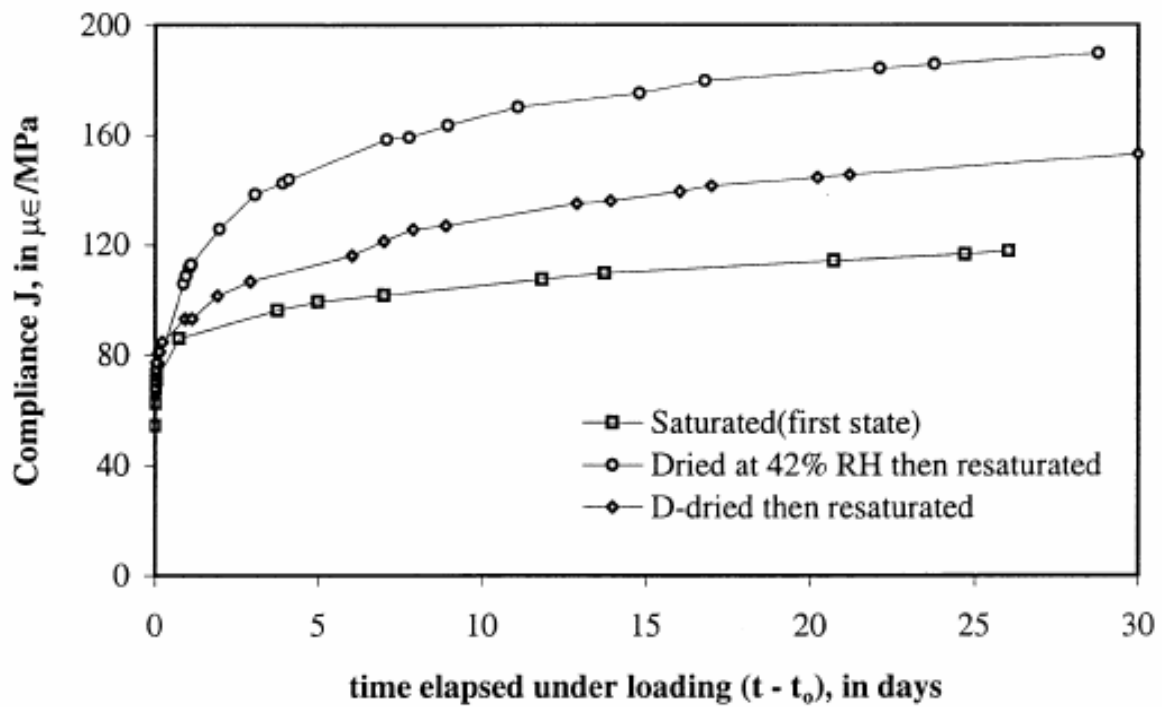


Figure 1.5.6: Compliance of hydrated cement paste ($w/c = 0.5$) after re-saturation from different drying pre-treatments (after [101])

Microprestress theory

The most sophisticated mathematical theory of creep relies on the concept of microprestresses [12, 11], which are attributed to volume changes as the hydration product forms, as well as to changes in disjoining pressure. Increased stress at these "creep sites" increases the ease of bond breakage, thereby increasing the creep rate.

First Bazant [9, 10] proposed the solidification theory for concrete creep. Creep is caused by slips due to bond ruptures (with restorations at adjacent sites) in the hardened Portland cement paste. The paste is strongly hydrophylic, having a disordered colloidal microstructure, porosity about 0.4 to 0.55 and an enormous internal surface area - about $500 \text{ m}^2/\text{cm}^3$; its main component is the tri-calcium silicate hydrate gel

($3CaO \cdot 2SiO_3 \cdot 3H_2O$, in short $C_3S_2H_3$ or C-S-H); it forms crystalline sheets and needles of colloidal dimensions, weakly bound by Van-der Waals forces. It is based on the following structural model (Fig. 1.5.7):

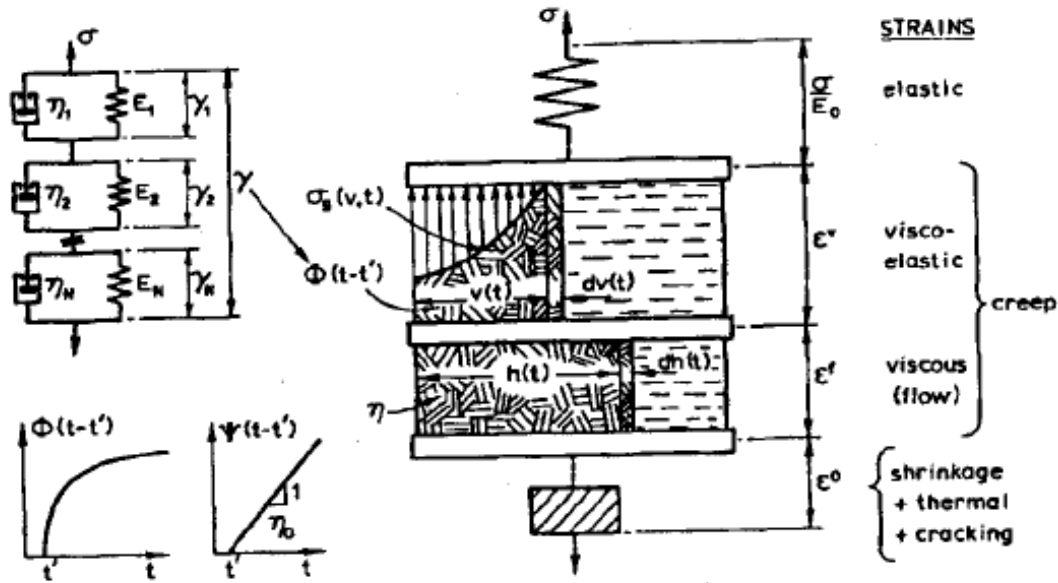


Figure 1.5.7: Structural model in solidification theory (after [9])

The total strain is the sum of elastic strain, visco-elastic strain, viscous strain and strain due to shrinkage. Elastic strain results from the deformation of the mineral aggregate pieces (anhydrous cement grains, calcium hydroxide crystals, crystalline particles: sheets and needles). Due to their physico-chemical nature the elastic properties of all these microscopic components are constant (nonaging). Growth of the volume fractions v of the solidified matter (hydrated cement) is associated with the viscoelastic and viscous strains. The elementary volume $dv(t)$ which solidifies at time t is represented by a layer deposited on the surface of the material that previously solidified from a solution. The main hypothesis is that **volume elements $dv(t)$ solidified at various times are all subjected to the same strain**, which is equal to the overall (macroscopic) creep strain $\varepsilon^v(t)$, this implies a parallel coupling of all these volume elements.

Then the microprestress $\sigma_g(v, t)$ in the solidified matter is introduced. $\sigma_g(v, t)$ at time t is defined as the stress at the location where the solidification occurred when the volume of all the solidified matter was v . In other words v can be considered as a “coordinate” of the solidified material. A layer of thickness $dv(t)$ is assumed to solidify and bind with the previously solidified matter at time t , at which the volume of all the solidified matter

is $v(t)$. Due to parallel coupling of the solidifying layers equilibrium requires:

$$\int_{\tau=0}^t \sigma_g[v(\tau), t] dv(\tau) = \sigma(t) \quad (1.5.2)$$

The solidifying material on the microscale is considered to be nonaging and linearly viscoelastic. The stress-strain relation has the form

$$\varepsilon^v(t) - \varepsilon^v(\tau) = \int_0^t \Phi(t - t') \sigma_g[v(\tau), dt'] \quad (1.5.3)$$

$\varepsilon^v(t) - \varepsilon^v(\tau)$ - viscoelastic strain suffered by the element $v(\tau)$ $\sigma_g[v(\tau), dt'] = 0$, $t' < \tau$ - stress in the element $v(\tau)$ $\Phi(t - t')$ - microscopic creep compliance function of the solidified matter, representing the creep strain at time t , caused by a unit microstress $\sigma_g = 1$ applied at time t' .

At the time at which layer $dv(\tau)$ solidifies it must be free of stress

$$\sigma_g[v(\tau), \tau] = 0 \quad (1.5.4)$$

In Fig. 1.5.7 it corresponds to the absence of the stresses at the $dv(t)$.

One should be careful with the volume fraction $v(t)$. It cannot be interpreted as the volume fraction of hydrated cement v_k , since creep also occurs at the high ages of concrete at which there is no growth of the v_k .

The $v(t)$ is interpreted as the effective load-bearing volume fraction of hydrated cement. This fraction can continue to grow significantly up to high ages as a result of progressive formation of bonds. So solidified volume that is not yet densely bonded cannot be counted as a part of $v(t)$.

Microprestress σ_g can be eliminated from the system (1.5.2,1.5.3,1.5.4):

$$\dot{\varepsilon}^v(t) = \frac{1}{v(t)} \int_0^t \dot{\Phi}(t - t') d\sigma(t') \quad (1.5.5)$$

Then the creep rate is accelerated (nonlinearity is added)

$$\dot{\varepsilon}^v(t) = \frac{F[\sigma(t)]}{v(t)} \int_0^t \dot{\Phi}(t - t') d\sigma(t') \quad (1.5.6)$$

Viscous strain $\varepsilon^f(t)$ is described in the same manner

$$\dot{\varepsilon}^f(t) = \frac{F[\sigma(t)]}{h(t)} \int_0^t \dot{\Psi}(t - t') d\sigma(t') \quad (1.5.7)$$

$\Psi(t - t')$ - microscopic viscous compliance function, representing the strain at time t , caused by a unit microstress $\sigma_g = 1$ applied at time t' . The $h(t)$ is also kind of an effective volume fraction of hydrated cement connected with viscous strain. $\Psi(t - t') = (t - t')/\eta_0$ leads to

$$\dot{\varepsilon}^f(t) = \frac{F[\sigma(t)]}{\eta(t)} \sigma(t) \quad (1.5.8)$$

where $\eta(t) \equiv h(t)\eta_0$.

Choosing appropriate material functions and parameters one can obtain a more precise form of the compliance function. Usually $\Phi(t - t')$ is expressed as Dirichlet series, this approach leads to a Kelvin-chain model with a finite number of units and thus a finite retardation spectrum. The formulation of the solidification theory with a continuous retardation spectrum can be found in [4].

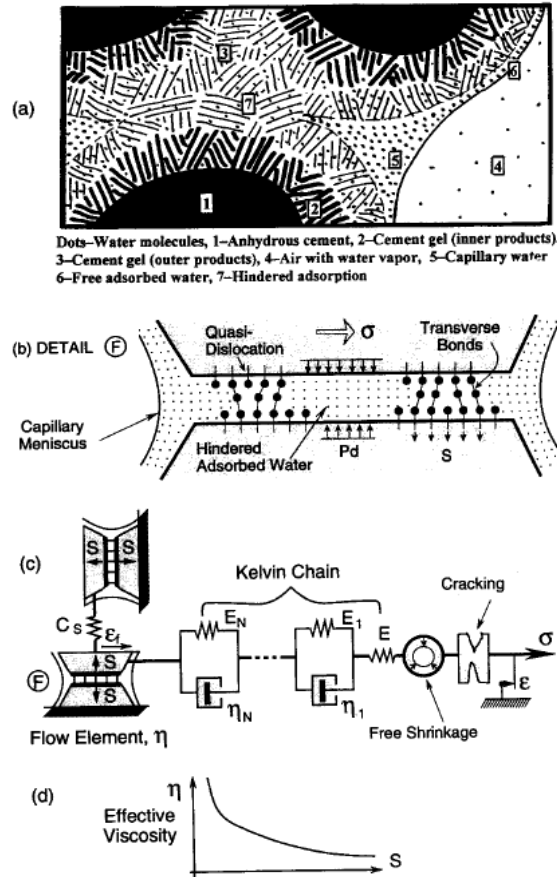


Figure 1.5.8: (a) Idealized microstructure of hardened cement paste; (b) micropore in the cement gel, disjoining pressure P_d and microprestress S ; (c) Kelvin chain structural model with flow element and microprestress relaxation mechanism; (d) dependence of flow viscosity on microprestress (after [12])

Later [12, 11] solidification theory was improved by introducing the microprestress.

Microprestress is a dimensionless measure of the stress peaks whose locations determine the creep sites in the microstructure. The microprestress is considered to be unaffected by the applied load and to be produced solely by chemical volume changes and by changes in the disjoining pressure in the hindered adsorbed water layers (up to ten water molecules or 2.7 nm in thickness) confined between sheets of calcium silicate hydrates. Since a local thermodynamic equilibrium, i.e., the equality of the chemical potentials of the hindered adsorbed water and the water vapor in the nearest capillary pores gets established very rapidly (within a fraction of a second), the disjoining pressure, in turn, is a function of temperature T as well as the relative humidity h of the water vapor in the capillary pores. The rate of bond breakages is logically a power function, and particularly a quadratic function of the level of microprestress.

The main idea is that the local microdiffusion flux J_m of water molecules between the hindered adsorbed layers and the capillary pores in the hardened cement paste somehow accelerate the process of breakage of atomic bonds in the solidified calcium silicate hydrate, which is the cause of creep. Because the microdiffusion must be almost infinitely faster than the long-term creep, J_m must be essentially proportional to the rate \dot{h} of relative humidity h in the capillary pore, which leads to the conclusion that the creep viscosity should change proportionally to \dot{h} .

Due to presence of capillary forces, in small pores (less than ten water molecules in width) there is a very high transverse compressive stress, called the disjoining pressure P_d . In such pores the full thickness of the adsorption layers cannot develop. These forces are carried partly by the solid framework around the micropore and partly by bridges or bonds between the opposite walls of the same micropore. Due to large pressure the solid part of microstructure of the hardened cement gel is permanently in a pretensioned state. This stress is called microprestress.

Because the distances of water diffusion between the micropores and the adjacent capillary pore are very short, the hindered adsorbed water establishes thermodynamic equilibrium with the capillary water very fast. Therefore, the disjoining pressure responds to changes of capillary tension and surface tension almost instantly. This means that surface tension γ has the form

$$\gamma = -C_1 RT \ln(h)/M + \gamma_1 \quad (1.5.9)$$

where R - universal gas constant; M - molecular weight of water; T - absolute temperature; C_1, γ_1 - constants. Thus

$$\dot{\gamma} = -c_1 \frac{\dot{h}}{h} \quad (1.5.10)$$

It is proposed that the variation of viscosity of slip is caused by relaxation of a transverse normal stress (called microprestress). So the creep of hardened cement gel originates in

the gel microstructure from the shear slips, which are driven by the shear stress and also influenced by normal stresses (microprestresses) across the slip planes. These microprestresses are locally self-equilibrated and independent of the applied macroscopic stress. The microprestress is generated as a reaction to the disjoining pressure in the micropore. The last is the function of the relative vapor pressure in the capillary pores, which is independent of the applied macroscopic stress.

The microstructure of hardened cement gel contains disperse, highly localized sites at which the atomic bonds are under a very high tensile stress. It is proposed that many of such highly stressed bonds are the bridges across the micropores containing the hindered adsorbed water and that the layers of hindered adsorbed water are the slip planes giving rise to the creep. The creep is the macroscopic result of numerous interatomic bond breaks happening at different times at different overstressed sites in the hindered adsorbed layers. Because the tensile stress reduces the activation energy barrier for bond rupture, frequency of bond breakage increases as the tensile stress across the slip plane increases. Shear slip is the result of breakage of atomic bonds and restoration of bonds with adjacent atoms, which may be called quasidislocation. Each bond breakage relaxes the shear stress at particular site. This relaxation causes the creep rate under a constant applied macrostress to decline. This aging is not associated with the volume growth of the hydration products.

The macroscopic creep due to shear slip at the creep sites is modeled by a viscous flow element:

$$\varepsilon_f = \frac{\sigma}{\eta(S)} \quad (1.5.11)$$

The relaxation of the microprestress S is modeled as another similar flow element and a spring of stiffness C_s coupled in series. Because of isotropy of the material and because the phenomena that generate the microprestress have no preferred orientation, the value of S (macroscopic characteristic of the average microprestress at all creep sites) must be the same for all directions. Therefore the slip plane of the latter flow element is also subjected to normal stress S . Hence, the equation for the relaxation of the microprestress reads:

$$\frac{\dot{S}}{C_s} + \frac{S}{\eta(S)} = \frac{\dot{\gamma}}{C_s} \quad (1.5.12)$$

$\dot{\gamma}$ - rate of the instantaneous microprestress during the initial rapid hydration induced by crystal growth pressure and large localized shrinkage at locations close to the micropore, later by capillary tension and surface tension which affect disjoining pressure.

Assuming $1/\eta(S) = c_p S^{p-1}$ one can obtain from (1.5.12) and (1.5.10)

$$\dot{S} + c_0 S^p = -c_1 \frac{\dot{h}}{h} \quad (1.5.13)$$

where $c_0 = C_s c_p$.

Such improvement of the model can be considered as a replacement of the simple flow element with the more complex but with more precise physical interpretation and mechanisms.

Later Bazant [6] has incorporated the temperature in (1.5.13):

$$\dot{S} + c_0 S^p = c_1 \left| \dot{T} \ln h + T \frac{\dot{h}}{h} \right| \quad (1.5.14)$$

Considering variable environment also endochronous hydration time can be introduced [6], capturing the effect of h and T on hydration. The absolute value is introduced to ensure that S could never be negative and to reflect the experimental observation that not only drying and cooling but also wetting and heating accelerate creep. A switch from heating to cooling, or drying to wetting, or vice versa, would of course deactivate the current creep sites but it is reasonable to expect that it would activate other creep sites at different locations. The fact that changes of water content w or humidity h produce new microprestress peaks and thus activate new creep sites explains the drying creep effect (called also the Pickett effect). A part of this effect, however, is caused by the fact that microcracking in a companion load-free specimen makes its overall shrinkage less than the shrinkage in an uncracked (compressed) specimen, thus increasing the difference between the two (which defines creep).

The concept of microprestress is also needed to explain the stiffening due to aging. One physical cause of aging is that the hydration products gradually fill the pores of hardened cement paste. But hydration ceases after about one year, yet the effect of age at loading t' is strong even after many years (experiments show a very large creep difference between specimens loaded at 1 year and 7 years of age). The explanation is that the peak microstress gradually relaxes with time, which reduces the number of creep sites and also the rate of bond breakages at these sites.

The fact that the relaxation rate of microprestress S must depend on S is obvious. But why should it be proportional to a power function of S , and particularly a quadratic function? The explanation is provided by asymptotic scaling considerations. A power function is logical because the long-term aging shows no distinct characteristic time, and because it affects similarly the creep curves at different applied stress levels. To get a clue about the exponent of the power function, consider the asymptotic case of constant hygro-thermal state ($\dot{h} = \dot{T} = 0$, sealed specimens, basic creep). In that case

$$\dot{S} = -c_0 S^2 \quad (1.5.15)$$

This represents microprestress relaxation that causes the strain in the flow element to grow exactly as a logarithmic function of time, which is necessary for matching long-term creep tests.

In the opposite asymptotic case of $\dot{h} \rightarrow \infty$ (1.5.15) reduces to

$$\dot{S} = -c_1 \dot{h}/h \quad (1.5.16)$$

which implies $S = -c_1 \ln(h) + \text{const.}$ This property means that, if the change of pore humidity h is very fast, the microprestress varies solely as a function of h . The same holds true for a very fast change of temperature.

In (1.5.14) there is a microprestress relaxation law, which replaces the age-dependence of viscosity. The long-term aging of flow viscosity is simply a consequence of relaxation of the microprestress.

The evolution of distributions $h(x, t)$ may be considered uncoupled from the stress and deformation problem (except when large cracks, wider than about 0.5 mm develop). This evolution may be solved numerically from the diffusion equation whose simplified form is

$$\dot{h} = \nabla \cdot (C(h) \nabla h) + \dot{h}_s(t_e) \quad (1.5.17)$$

where $\dot{h}_s(t_e)$ - function defining the selfdesiccation caused by hydration (which is mild in normal concretes but strong in high strength concretes), $C(h)$ - diffusivity, which decreases about 20 times as h drops from 100% to 60%.

As data fitting with finite element programs confirms, the free (unrestrained) shrinkage strain rates may be very simply expresses as

$$\dot{\epsilon}_{sh} = k_{sh} \dot{h} \quad (1.5.18)$$

where k_{sh} - shrinkage coefficient. Since the values of $\dot{\epsilon}_{sh}$ at various points of the structure are in general incompatible, the calculation of the overall shrinkage of test specimens as well as structures is a stress analysis problem, in which creep and cracking must be taken into account.

The temperature effect on creep rate may be captured by an Arrhenius-type dependence of the viscosities of the units of the Kelvin (or Maxwell) chain. This is, however, only one effect of temperature, an effect in which a temperature rise increases the creep rate. There is another, opposite, effect of temperature on creep, arising from the temperature dependence of the rate of hydration, as captured by t_e . This dependence causes that a temperature rise accelerates the aging process due to hydration, which in turn reduces the creep rate. The former effect usually prevails but in very young concrete not always.

Application of micro-prestress solidification theory to study the temperature effect is presented in [7]. Both compliance and heating effect can be satisfactory model and are in agreement with the experiment data.

A kind of application of solidification theory to the microplane M4 model is presented in [116]. In that case the Maxwell chain is more effective than Kelvin chain, because of the kinematic constraint of the microplanes used in M4. So the continuous relaxation spectrum for Maxwell chain was formulated based on the solidification theory. Continuous retardation spectrum is obtained by inverse Laplace transform. The Maxwell approximation depends on n parameter in power-log law and satisfactory for low n , which is the case for concrete.

Comparison of this model with the other (GZ - Gardner and Zhao 1993 and CEB-FIP - Thomas Telford 1990) which propose different compliance functions can be found in [5] with the following criteria: statistical comparison to data bank, fitting of individual test curves, physically based theory, extrapolation of short range data. Also there is a notion of thermodynamically inadmissible behavior of the GZ and CEB-FIP models.

An application of Bazant's B3 model to the shotcrete is presented in [64] for the analysis of tunnels with application of thermo-chemo plasticity. The formulation with fracture and crack band approach with high temperature for the micro-prestress theory is presented in [8]. The high-temperature ranges impose certain differences compared with the room-temperature:

- Upon surpassing 100 °C, the sorption-desorption isotherms of free pore water (capillary water and adsorbed water) develop a discontinuity at the saturation point
- The water permeability and diffusivity of concrete increases by almost two orders of magnitude as 100°C is surpassed
- While below 100°C the diffusion equation for water transport has a negative sink term describing the rate of conversion of free pore water into water chemically combined in the calcium silicate hydrates, above 300 °C there is a significant positive sink term describing the release of hydrate water as free water in the nanopores and capillary pores of concrete. This goes along with the fact that chemical reactions of hydration of cement, responsible for the aging property of creep and the gain of strength with time, progress only below 100°C (and slightly more if water is pressurized), while above 300°C these reactions get reversed and cause dehydration, accompanied by negative aging in the creep law and a significant loss of strength.

1.6 Conclusions

As we see from this literature review, cement and concrete are very complex materials. Their complexity arise from:

- chemical system with many reactions going simultaneously
- apparent chemical shrinkage (volume of products is less than volume of reactants)
- presence of water and its possible movement if loaded, capillary forces
- complex 3D microstructure of cement paste which highly depends on w/c , initial system, hydration conditions, temperature and others
- aging phenomena, even after complete stop of hydration. It is probably the result of increase of polymerization length of C-S-H.
- unknown microstructure of main component - C-S-H. Presence of number of different theories which try to reasonably guess it at the scale of tens of nm.
- unavailability to test different phases separately since hydration products are hard to form in as a bulk phase. One of the few ways to measure is nanoindentation technique.

However, engineers still need to deal with this material, therefore exist many of simplified, mostly unphysical (except for B3) codes, which are easy to use and are fitted to experimental database. However, as it was shown in [75], they produce very different results for the same problem.

A possible way to overcome this simplified engineering approach is to use complicated models, which are usually based on certain assumptions of origin of the phenomena. Yet, parameters in such models have to be fitted based on experimental data before being used and therefore these models can not help to design concrete.

It is obvious that in order to be able to design concrete, microstructure have to be considered explicitly. This can be achieved by either using chemical hydration models such as CemHyd3d or MIC or by experimental techniques, such as Tomography, which can provide resolutions up to hundreds of nm per voxel.

Natural question of mechanical description of phases in such microstructure arises. In present study we will use nanoindentation technique to “load” phases, present in RVE. Inverse analysis of indentation experiment still needs hypothesis regarding mechanical model to be done.

And even once we have trustful microstructure and mechanical description of each phase, we still have number of methods to calculate properties of considered RVE.

Therefore, current study is focused on nanoindentation experiment and its inverse analysis, as well as different homogenization techniques at the level of cement paste, as a most complicated level of concrete.

2 Homogenization Techniques

2.1 Mean Field Elastic Homogenization

In this chapter we briefly describe the mean field elastic homogenization approach.

Let us consider RVE of elastic heterogeneous material composed of n phases with the volume fractions f_r , such that $\sum_r f_r = 1$. The RVE is subjected on its boundary, denoted ∂V , to a displacement condition of the Hashin-type:

$$\partial V : \mathbf{u}(\mathbf{x}) = \mathbf{E} \cdot \mathbf{x} \quad (2.1.1)$$

where $\mathbf{u}(\mathbf{x})$ is a microscopic displacement field, \mathbf{x} denotes a position vector at the microscopic scale and \mathbf{E} is a macroscopic strain, related to the microscopic strain $\boldsymbol{\varepsilon}(\mathbf{x})$ by the volume averaging relation:

$$\mathbf{E} = \langle \boldsymbol{\varepsilon}(\mathbf{x}) \rangle_V = \frac{1}{V} \int_V \boldsymbol{\varepsilon}(\mathbf{x}) dV = \sum_r f_r \boldsymbol{\varepsilon}_r \quad (2.1.2)$$

where $\boldsymbol{\varepsilon}_r$ is strain averaged over the phase. Analogously, the microscopic stress and the macroscopic stress are related by the volume averaging relation:

$$\boldsymbol{\Sigma} = \langle \boldsymbol{\sigma}(\mathbf{x}) \rangle_V \quad (2.1.3)$$

To connect the macroscopic strain \mathbf{E} with the microscopic strain $\boldsymbol{\varepsilon}$ the linear strain localization condition is postulated for each phase r :

$$\boldsymbol{\varepsilon}_r = \mathbb{A}_r : \mathbf{E} \quad (2.1.4a)$$

$$\langle \mathbb{A} \rangle_V = \sum_r f_r \mathbb{A}_r = \mathbb{I} \quad (2.1.4b)$$

where \mathbb{A} is a fourth-order localization or concentration tensor. It depends on the morphology, elastic properties and fractions of the phases. Considering linear elastic constitutive law for each microscopic phase $\boldsymbol{\sigma} = \mathbb{C} : \boldsymbol{\varepsilon}$ together with strain localization condition (2.1.4a) stress volume averaging relation (2.1.3) delivers the linear homogenization formula for the macroscopic elasticity:

$$\boldsymbol{\Sigma} = \langle \boldsymbol{\sigma} \rangle_V = \langle \mathbb{C} : \boldsymbol{\varepsilon} \rangle_V = \langle \mathbb{C} : \mathbb{A} \rangle_V : \mathbf{E} = \left(\sum_r f_r \mathbb{C}_r : \mathbb{A}_r \right) : \mathbf{E} = \mathbb{C}_{\text{hom}} : \mathbf{E} \quad (2.1.5)$$

f_r -volume fraction of phase, \mathbb{C}_r - stiffness tensor of the phases, \mathbb{C}_{hom} - homogenized stiffness:

$$\mathbb{C}_{\text{hom}} = \sum_r f_r \mathbb{C}_r : \mathbb{A}_r \quad (2.1.6)$$

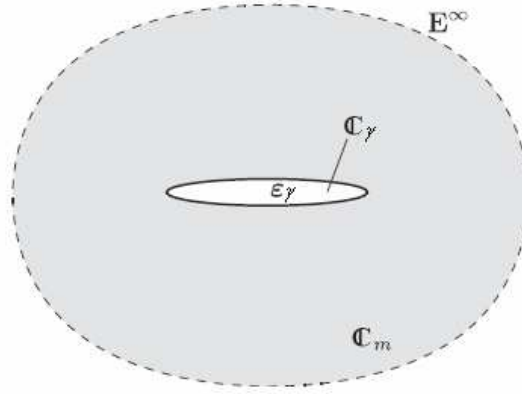


Figure 2.1.1: Eshelby's problem: single inclusion in an infinite matrix subjected to remote uniform strains

The average strains of each phase are set equal to the strains in a single ellipsoidal inclusion with stiffness \mathbb{C}_r embedded in an infinite matrix of stiffness \mathbb{C}_m , subjected to the fictitious (uniform) strains \mathbf{E}^∞ at infinity (Fig. 2.1.1). This problem was analytically solved by Eshelby [39] [40]. The average strains of the inclusion is given by the formula

$$\epsilon_r = [\mathbb{I} + \mathbb{P}_r^m : (\mathbb{C}_r - \mathbb{C}_m)]^{-1} : \mathbf{E}^\infty \quad (2.1.7)$$

where \mathbb{P}_r^m is the fourth-order Hill tensor characterizing the interaction between the inclusion and the infinite matrix. Integral and closed-form solutions for \mathbb{P}_r^m are available for a number of inclusion shapes and symmetries of the elasticity tensor. \mathbb{P}_r^m can be written in the following form

$$\mathbb{P}_r^m = \mathbb{S}_r^m : \mathbb{C}_m^{-1} \quad (2.1.8)$$

where \mathbb{S}_r^m - is the Eshelby tensor of phase r , which depends on \mathbb{C}_m , the geometry and the orientation of phase r . For the phase, chosen to be matrix with respect to the others phases $\mathbb{C}_r = \mathbb{C}_m$ and (2.1.7) reads

$$\epsilon_m = \mathbf{E}^\infty \quad (2.1.9)$$

The strains \mathbf{E}^∞ , prescribed at infinity of the matrix surrounding a single phase, must be related appropriately to the macroscopic strains \mathbf{E} , imposed as uniform boundary condition onto the RVE.

If the phases are sufficiently far apart from each other (dilute concentration) \mathbf{E}^∞ can be approximated as

$$\mathbf{E}^\infty = \mathbf{E} \quad (2.1.10)$$

Using (2.1.10) in (2.1.7) and comparing with (2.1.4a) leads to the dilute formulation of

the localization tensor:

$$\mathbb{A}_r^{(D)} = [\mathbb{I} + \mathbb{P}_r^m : (\mathbb{C}_r - \mathbb{C}_m)]^{-1} \quad (2.1.11)$$

Inserting (2.1.11) to (2.1.6) lead to the well-known dilute estimate of \mathbb{C}_{hom} .

In the case of the nondilute concentration of the phases the interactions have to be considered. The simplest consideration of the phases interactions is to define the fictitious remote strain \mathbf{E}^∞ such that the strain average rule (2.1.2) is satisfied, i.e. insertion of (2.1.7) into (2.1.2) reads

$$\mathbf{E} = \langle [\mathbb{I} + \mathbb{P}_r^m : (\mathbb{C}_r - \mathbb{C}_m)]^{-1} \rangle_V : \mathbf{E}^\infty \quad (2.1.12)$$

Back-substitution of (2.1.12) into (2.1.7) yields the well-known Mori-Tanaka localization tensor estimate

$$\mathbb{A}_r^{(MT)} = [\mathbb{I} + \mathbb{P}_r^m : (\mathbb{C}_r - \mathbb{C}_m)]^{-1} : \langle [\mathbb{I} + \mathbb{P}_\alpha^m : (\mathbb{C}_\alpha - \mathbb{C}_m)]^{-1} \rangle_V^{-1} \quad (2.1.13)$$

Insertion of (2.1.13) into the (2.1.6) gives the Mori-Tanaka stiffness estimate \mathbb{C}_{hom} . At this case \mathbb{C}_m represents one of the phases which is chosen to be matrix for all other inclusions.

For the self-consistent scheme, the homogenized medium is chosen as a reference, i.e. $\mathbb{C}_m \equiv \mathbb{C}_{\text{hom}}$. This leads to the self-consistent formulation of localization tensor

$$\mathbb{A}_r^{(SC)} = [\mathbb{I} + \mathbb{P}_r^{\text{hom}} : (\mathbb{C}_r - \mathbb{C}_{\text{hom}})]^{-1} : \langle [\mathbb{I} + \mathbb{P}_\alpha^{\text{hom}} : (\mathbb{C}_\alpha - \mathbb{C}_{\text{hom}})]^{-1} \rangle_V^{-1} \quad (2.1.14)$$

Using (2.1.14) in (2.1.6) leads to solution of nonlinear tensorial equation.

The most common case is to consider phases to be isotropic and inclusions to be spherical. The first assumption leads to

$$\mathbb{C}_r = 3K_r\mathbb{J} + 2G_r\mathbb{K} \quad (2.1.15a)$$

$$\mathbb{C}_{\text{hom}} = 3K_{\text{hom}}\mathbb{J} + 2G_{\text{hom}}\mathbb{K} \quad (2.1.15b)$$

where K_r, G_r - bulk and shear modules of the phase r . $J_{ijkl} = \frac{1}{3}\delta_{ij}\delta_{kl}$, $\mathbb{K} = \mathbb{I} - \mathbb{J}$.

The second assumption of spherical inclusion implies the following form of the Eshelby tensor \mathbb{S}_r^m

$$\mathbb{S}_r^m = \alpha_m\mathbb{J} + \beta_m\mathbb{K} \quad (2.1.16)$$

with

$$\alpha_m = \frac{3K_m}{3K_m + 4G_m}, \beta_m = \frac{6(K_m + 2G_m)}{5(3K_m + 4G_m)} \quad (2.1.17)$$

where K_m, G_m - bulk and shear modules of the reference medium.

Substituting (2.1.15) and (2.1.16) to (2.1.13), (2.1.14) and using with (2.1.6) and (2.1.8)

leads to the following system of equations

$$K_{hom} = \sum_r f_r K_r \left[1 + \frac{\alpha_m}{K_m} (K_r - K_m) \right]^{-1} < \left[1 + \frac{\alpha_m}{K_m} (K_\alpha - K_m) \right]^{-1} >_V^{-1} \quad (2.1.18a)$$

$$G_{hom} = \sum_r f_r G_r \left[1 + \frac{\beta_m}{G_m} (G_r - G_m) \right]^{-1} < \left[1 + \frac{\beta_m}{G_m} (G_\alpha - G_m) \right]^{-1} >_V^{-1} \quad (2.1.18b)$$

In case of Mori-Tanaka homogenization, K_m and G_m are known in advance and chosen to be the properties of one of the phases. Whereas for the Self-Consistent scheme, $K_m \equiv K_{hom}$ and $G_m \equiv G_{hom}$, this lead to the solution of system of two nonlinear equations

$$K_{hom} = \sum_r f_r K_r \left[1 + \frac{\alpha_{hom}}{K_{hom}} (K_r - K_{hom}) \right]^{-1} < \left[1 + \frac{\alpha_{hom}}{K_{hom}} (K_\alpha - K_{hom}) \right]^{-1} >_V^{-1} \quad (2.1.19a)$$

$$G_{hom} = \sum_r f_r G_r \left[1 + \frac{\beta_{hom}}{G_{hom}} (G_r - G_{hom}) \right]^{-1} < \left[1 + \frac{\beta_{hom}}{G_{hom}} (G_\alpha - G_{hom}) \right]^{-1} >_V^{-1} \quad (2.1.19b)$$

In general homogenized constitutive equation depends on the choice of morphology (e.g. isotropic spherical Eshelbian-type inclusions) and reference medium in which inclusions are embedded (matrix for Mori-Tanaka scheme and homogenized medium for self-consistent scheme).

The link between the homogenized strain \mathbf{E} of the RVE with numerous penny-shaped microcracks and the structure mechanics stress used to model single crack initiation and propagation Σ_∞ is presented at [80]. The key to this link is that both scientific fields rely on matrix-inclusion problems dealing with a single crack embedded in an infinite matrix subjected to the remote uniform loading. They suggest setting the fictitious strains \mathbf{E}^∞ equal to the ones caused by Σ^∞ in the fracture mechanics problem, i.e.

$$\mathbf{E}^\infty = \mathbb{C}_m^{-1} : \Sigma^\infty \quad (2.1.20)$$

Using (2.1.20) in (2.1.5) yields

$$\Sigma^\infty = \mathbb{C}_m : \mathbb{C}_{hom}^{-1} : \Sigma \quad (2.1.21)$$

which can be specified for the penny-shaped cracks and different homogenization schemes [80]. The numerous quasistatic crack propagation mode I in the case of constant crack density using this approach was described.

Classical example for application of described above homogenization technique to cement paste is [81] in which concrete was considered as a multiscale material. Only C-S-H phase has a creep properties. Applying MT/SC homogenization schemes the goal-oriented optimization of the early-age creep properties of concrete becomes possible.

There are other matrix-inclusion approaches in literature, for example - two scale model[45]. At the macro scale composite action is described by a parallel-series model in which part of the cement paste accommodates elastic deformation of the grains and is in parallel with the inclusions while the other is in series. At the micro scale the aging is considered as the extension of the previous proposed solidification theory.

As an alternative to mean field approaches, detailed description of microstructure using *FEM* can be done. Neubauer [74] presented the three-phase (aggregate, bulk cement paste, ITZ) model for the elastic shrinkage of the mortar. Homogenization is done numerically for 2D case using FEM. ITZ is considered as a homogeneous shell around the aggregate with the width of $20\mu m$. Generation of the aggregate distribution was done according to the statistical law. They found that Young modules of the ITZ should be $1/3$ of the bulk paste. At this approach the intrinsic shrinkage strain is considered – strain of the phase without any restriction (e.g. neighborhood phases CH, unhydrated grains, etc). The results show a minimum in shrinkage as a function of ITZ/paste Young's modulus ratio, for a given unrestrained shrinkage in the ITZ relative to the bulk cement paste.

As an alternative approach to the homogenization we can mention multi-resolution wavelet analysis to the concrete materials [61]. Successive Haar transformations lead to a recursive separation of the response into coarse- and fine-scale features. In the limit, this recursive process results in a homogenization parameter which is an effective measure of stiffness and strain energy capacity of the coarse scale features.

Another example of homogenization is [62]. Le has used the MT scheme at the level of cement paste. Volumetric and deviatoric compliances of C-S-H are considered.

2.2 Mean Field Strength Homogenization

2.2.1 Introduction

Our goal is to obtain a macroscopic strength domain of a heterogeneous material knowing microscopic strength domains of each phase in the material and certain information on the microstructure. The presented description follows [35].

Limit analysis aims to find the maximum load Σ , which corresponds to the plastic collapse of the heterogeneous material, that is a state at which an ability to dissipate applied load is exhausted. The behavior of each phase at plastic collapse is assumed to follow the principle of maximum dissipation

$$\sigma = \frac{\partial \pi_r(\mathbf{d})}{\partial \mathbf{d}} \quad (2.2.1)$$

where \mathbf{d} is strain rate and π_r is the maximum dissipation capacity (support function) of phase r

$$\pi_r(\mathbf{d}) = \sup_{\sigma^* \in G_r} \sigma^* : \mathbf{d} \quad (2.2.2)$$

The strength domain of each phase G_r is considered to be convex.

The RVE of the considered microstructure is then loaded by a homogeneous strain rate, which is described by the following system of equations

$$\nabla \cdot \sigma = 0 \quad \text{in } V \quad (2.2.3a)$$

$$\sigma = \frac{\partial \pi_r(\mathbf{d})}{\partial \mathbf{d}} \quad \text{in } V_r \quad (2.2.3b)$$

$$\mathbf{d} = \frac{1}{2}(\nabla \mathbf{v} + \mathbf{v} \nabla) \quad \text{in } V \quad (2.2.3c)$$

$$\mathbf{v} = \mathbf{D} \cdot \mathbf{x} \quad \text{on } \partial V \quad (2.2.3d)$$

From the convexity of strength domains G_r , the maximum dissipation capacity of the system reads

$$\Pi^{hom}(\mathbf{D}) \equiv \sup_{\Sigma \in G^{hom}} \Sigma : \mathbf{D} = \inf_{\mathbf{d} \in K(\mathbf{D})} \pi(\mathbf{d}(\mathbf{v}), \mathbf{x}) \quad (2.2.4)$$

where

$$K(\mathbf{D}) = \{\mathbf{v}(\mathbf{x}) \mid \mathbf{v}(\mathbf{x}) = \mathbf{D} \cdot \mathbf{x} \quad \text{on } \partial V\} \quad (2.2.5)$$

is the set of kinematically admissible strain rate.

The relationship between macroscopic stress at plastic collapse Σ and the macroscopic strain rate \mathbf{D} is

$$\Sigma = \frac{\partial \Pi^{hom}}{\partial \mathbf{D}} \quad (2.2.6)$$

2.2.2 Effective Strain Rate Approach

The aim is to estimate the solution of the system (2.2.3). Mean field elastic linear homogenization theories cannot be applied straight away due to nonlinearity of the (2.2.3b). There are different ways of approaching this problem. One of them is to introduce the Effective Strain Rate into (2.2.3b) [35, 21]. Assuming that the maximum dissipation capacity of a phase depends only on the first and second invariants of strain

$$\pi_r(\mathbf{d}) = \pi_r(I'_1, J'_2) \quad (2.2.7)$$

with

$$\mathbf{d} = \frac{1}{3}I'_1\mathbf{I} + \boldsymbol{\delta} \quad (2.2.8a)$$

$$I'_1 = \text{tr}(\mathbf{d}) \quad (2.2.8b)$$

$$J'_2 = \frac{1}{2}\boldsymbol{\delta} : \boldsymbol{\delta} \quad (2.2.8c)$$

Eq. (2.2.3b) leads to

$$\boldsymbol{\sigma} = \frac{\partial \pi_r}{\partial I'_1}\mathbf{I} + \frac{\partial \pi_r}{\partial J'_2}\boldsymbol{\delta} \equiv \mathbb{C}^r : \mathbf{d} \quad (2.2.9)$$

with

$$k^r = \frac{1}{I'_1} \frac{\partial \pi_r}{\partial I'_1} \quad (2.2.10a)$$

$$2\mu^r = \frac{\partial \pi_r}{\partial J'_2} \quad (2.2.10b)$$

The last equation clearly shows the nonlinearity in 'secant' stiffness tensor, which is overcome by the introduction of an effective strain rate:

$$\boldsymbol{\sigma} = \mathbb{C}^r(\mathbf{x}) : \mathbf{d} \approx \mathbb{C}_{appr}^r(\mathbf{d}^r) : \mathbf{d} \quad (2.2.11)$$

where \mathbf{d}^r is a suitably chosen strain rate measure for phase r . The simplest choice is an average (first moment) of the strain rate over phase r :

$$\mathbf{d}^r = \overline{\mathbf{d}(\mathbf{x})}^r \quad (2.2.12)$$

Second-order moments proved to be a much better choice for strength homogenization:

$$\sqrt{J_2^r} = \sqrt{\frac{1}{2}\boldsymbol{\delta} : \boldsymbol{\delta}^r} \quad (2.2.13)$$

Thus, these are the steps of the Effective Strain Rate secant homogenization technique:

1. Eq. (2.2.11) reduces the nonlinear problem to a standard problem of heterogeneous elasticity, thus all the machinery of Eshelby homogenization is applicable.
2. It is necessary to choose a reference strain rate \mathbf{d}^r to be used in the linearization and then develop it as a function of the macroscopic strain rate $\mathbf{d}^r = \mathbf{d}^r(\mathbf{D})$. This is done in the linear elasticity framework.
3. The final step is solving the nonlinear problem $\Sigma = \mathbb{C}^{hom}(\mathbf{D}) : \mathbf{D}$.

Second-Order Moment for a Reference Strain Rate

As it was mentioned before, the second-order moment is a better choice as a reference strain rate. Let us now develop this estimate for phase r , present in the microstructure. By definition

$$d_d^r = \sqrt{\boldsymbol{\delta} : \boldsymbol{\delta}^r} \quad (2.2.14)$$

$$d_v^r = \sqrt{\overline{d_v^2}^r} \quad (2.2.15)$$

where $d_v = \text{tr}(\mathbf{d})$. The macroscopic strain rate energy density is

$$W = \frac{1}{2} \mathbf{D} : \mathbb{C}^{hom} : \mathbf{D} \quad (2.2.16)$$

Assuming isotropic elastic material, it is expressed as

$$W = \frac{1}{2} K^{hom} D_v^2 + G^{hom} \boldsymbol{\Delta} : \boldsymbol{\Delta} \quad (2.2.17)$$

Similarly, the strain rate energy density of phase α reads

$$w_\alpha = f_\alpha \left(\frac{1}{2} k^\alpha d_v^2 + g^\alpha \boldsymbol{\delta} : \boldsymbol{\delta} \right) \quad (2.2.18)$$

where f_α is a volume fraction of the phase α . It is obvious that

$$W = \sum_{\alpha} w_\alpha \quad (2.2.19)$$

Now, let us develop the derivatives of (2.2.19) with respect to k^r and g^r considering that the local strain rate field of phase α is a function of k^α and g^α :

$$\frac{1}{2} \frac{\partial K^{hom}}{\partial g^r} D_v^2 + \frac{\partial G^{hom}}{\partial g^r} \Delta : \Delta = f_r \left(\overline{\delta} : \overline{\delta}^r + \overline{\sigma} : \frac{\partial \overline{\mathbf{d}}}{\partial g^r}^r \right) \quad (2.2.20a)$$

$$\frac{1}{2} \frac{\partial K^{hom}}{\partial k^r} D_v^2 + \frac{\partial G^{hom}}{\partial k^r} \Delta : \Delta = f_r \left(\overline{d_v^2}^r + \overline{\sigma} : \frac{\partial \overline{\mathbf{d}}}{\partial k^r}^r \right) \quad (2.2.20b)$$

The first terms after the equality signs are exactly squares of second-order moments ((2.2.14), (2.2.15)), and the last terms equal zero. So, these equations can be rewritten as

$$\frac{1}{2} \frac{\partial K^{hom}}{\partial g^r} (D_v)^2 + \frac{\partial G^{hom}}{\partial g^r} \Delta : \Delta = f_r (d_d^r)^2 \quad (2.2.21a)$$

$$\frac{1}{2} \frac{\partial K^{hom}}{\partial k^r} (D_v)^2 + \frac{\partial G^{hom}}{\partial k^r} \Delta : \Delta = f_r (d_v^r)^2 \quad (2.2.21b)$$

Perfectly Brittle Behavior

Considering each phase to be perfectly brittle, previously obtained results can be used to approximate the yield limit of the composite by the stress level, at which at least one phase reaches its yield surface.

Eq. (2.2.21) are (second-order) estimates of the strain rate in each phase and therefore can be directly used in the yield functions of each phase to find when the end of elastic stage. Let us show it considering J_2 plasticity.

The quadratic deviatoric stress average σ_d^r is defined by analogy to (2.2.14) and is related to d_d^r by $\sigma_d^r = 2g^r d_d^r$. Using (2.2.21a) this leads to

$$\sigma_d^r = \frac{2g_r}{\sqrt{f_r}} \left[\frac{1}{2} \frac{\partial K^{hom}}{\partial g^r} (D_v)^2 + \frac{\partial G^{hom}}{\partial g^r} (D_d)^2 \right]^{\frac{1}{2}} \quad (2.2.22)$$

Now, let us consider that RVE is subjected to uniaxial tension $\Sigma = -\Sigma_{11} e_1 e_1$ where e_i are the base vectors. $\Sigma_v = -\Sigma_{11}$ and $\Sigma_d = \sqrt{2/3} \Sigma_{11}$. The macroscopic stress and strain rate are related by

$$D_v = \Sigma_v / 3K^{hom} \quad (2.2.23a)$$

$$D_d = \Sigma_d / 2G^{hom} \quad (2.2.23b)$$

Thus, (2.2.22) reads

$$\sigma_d^r = \frac{2 g_r}{\sqrt{f_r}} \left[\frac{1}{2} \frac{\partial K^{hom}}{\partial g^r} \left(\frac{1}{3K^{hom}} \right)^2 \Sigma_{11}^2 + \frac{2}{3} \frac{\partial G^{hom}}{\partial g^r} \left(\frac{1}{2G^{hom}} \right)^2 \Sigma_{11}^2 \right]^{\frac{1}{2}} \quad (2.2.24)$$

which can be rewritten as

$$\sigma_d^r = \Sigma_{11} \frac{2 g_r}{\sqrt{f_r}} \left(-\frac{1}{18} \frac{\partial}{\partial g^r} \left(\frac{1}{K^{hom}} \right) - \frac{\partial}{\partial g^r} \left(\frac{1}{G^{hom}} \right) \frac{1}{6} \right)^{\frac{1}{2}} \quad (2.2.25)$$

The obtained equation can be directly used in J_2 yield limit function for each phase r in order to calculate the critical load Σ_{11}^r at which yield limit is reached. Thus, using perfect brittle assumption, the strength at the level of RVE is

$$\Sigma = \min(\Sigma_{11}^r) \quad (2.2.26)$$

This approach was used in [79] for prediction of cement paste strength from volume fractions of its constituents.

2.2.3 LCC Homogenization Method

The limitation of the Effective Strain Rate approach is the necessity of choosing the particular averaging measure. In order to overcome it, the concept of Linear Comparison Composite (LCC) was introduced [22, 23]. The principle is similar: approximation of a non-linear behavior by a linear one, but the main difference is that parameters of the linear behavior are fictitious and are variables of the problem. These parameters are then suitably chosen in order to find the lowest upper bound of the dissipation energy of a homogeneous material. In our description of this method, we will follow [110]. Let us consider a fictitious comparison composite in which the behavior of each phase is given by

$$\boldsymbol{\sigma} = \mathbb{C}_\alpha : \mathbf{d} + \boldsymbol{\tau}_\alpha \quad (2.2.27)$$

The strain rate energy of such composite material is

$$w_0(\mathbf{x}, \mathbf{d}) = \sum_{\alpha} \chi_{\alpha}(\mathbf{x}) w_{\alpha}(\mathbf{d}) \quad (2.2.28a)$$

$$w_{\alpha}(\mathbf{d}) = \frac{1}{2} \mathbf{d} : \mathbb{C}_{\alpha} : \mathbf{d} + \boldsymbol{\tau}_{\alpha} : \mathbf{d} \quad (2.2.28b)$$

where $\chi_\alpha(\mathbf{x})$ are indicator functions, such that $\chi_\alpha(\mathbf{x}) = 1$ if \mathbf{x} is in phase α , and 0 otherwise. Considering $w_0 = \pi + w_0 - \pi$, the following estimate can be obtained:

$$\inf_{\mathbf{v} \in K(\mathbf{D})} \overline{w_0(\mathbf{x}, \mathbf{d}(\mathbf{v}))} \geq \inf_{\mathbf{v} \in K(\mathbf{D})} \overline{\pi(\mathbf{x}, \mathbf{d}(\mathbf{v}))} + \inf_{\mathbf{v} \in K(\mathbf{D})} \overline{w_0(\mathbf{x}, \mathbf{d}(\mathbf{v})) - \pi(\mathbf{x}, \mathbf{d}(\mathbf{v}))} \quad (2.2.29)$$

The first term is the macroscopic strain rate energy $W_0(\mathbf{D})$ of the LCC:

$$W_0(\mathbf{D}) = \inf_{\mathbf{v} \in K(\mathbf{D})} \overline{w_0(\mathbf{x}, \mathbf{d}(\mathbf{v}))} \quad (2.2.30)$$

The second is $\Pi^{hom}(\mathbf{D})$ and the last one, multiplied by -1 , can be overestimated by:

$$\begin{aligned} & - \inf_{\mathbf{v} \in K(\mathbf{D})} \overline{w_0(\mathbf{x}, \mathbf{d}(\mathbf{v})) - \pi(\mathbf{x}, \mathbf{d}(\mathbf{v}))} = \\ & \sup_{\mathbf{v} \in K(\mathbf{D})} \overline{\pi(\mathbf{x}, \mathbf{d}(\mathbf{v})) - w_0(\mathbf{x}, \mathbf{d}(\mathbf{v}))} \leq \sum_{\alpha} f_{\alpha} \nu_{\alpha} \end{aligned} \quad (2.2.31)$$

where

$$\nu_{\alpha} = - \sup_{\mathbf{d}} \overline{\pi(\mathbf{d}) - w_{\alpha}(\mathbf{d})} \quad (2.2.32)$$

is a constant in each phase of the volume fraction f_{α} . As a result, the following upper bound for Π^{hom} is obtained:

$$\Pi^{hom}(\mathbf{D}) \leq W_0(\mathbf{D}) + \sum_{\alpha} f_{\alpha} \nu_{\alpha} \quad (2.2.33)$$

Our aim is to find the elastic parameters of a fictitious LCC that will lead to the lowest possible estimate of Π^{hom} , that is infimum of the right hand side of (2.2.33). Since infimum and supremum can be replaced by stationary points, this new estimate is

$$\widetilde{\Pi^{hom}}(\mathbf{D}) = \text{stat}_{\mathbb{C}_{\alpha}, \tau_{\alpha}} \left(W_0(\mathbf{D}) + \sum_{\alpha} f_{\alpha} \nu_{\alpha} \right) \quad (2.2.34)$$

$$\nu_{\alpha} = \text{stat}_{\mathbf{d}} (\pi(\mathbf{d}) - w_{\alpha}(\mathbf{d})) \quad (2.2.35)$$

Thus, the main steps in the LCC homogenization method are:

1. From linear micromechanics, compute the macroscopic strain rate energy $W_0(\mathbf{D})$.
2. For each phase, compute ν_{α} .
3. Find stationary points of (2.2.34) and (2.2.35) (solve for \mathbb{C}_{α} and τ_{α}). As a result, obtain the estimate of Π^{hom} .

Application of LCC to Matrix-Pore Composite

Let us present constitutive equations for C-S-H, originally developed in [110]. Having in mind that the porous C-S-H phase is the main phase of interest in cement paste, let us consider a composite consisting of solid phase (volume fraction η) and porosity ($\varphi = 1 - \eta$). The solid strength properties are described by a Drucker-Prager model with cohesion c_s and friction coefficient α_s . In order to have smooth yield surface, the Drucker-Prager yield criterion is regularized in the following way:

$$f(\boldsymbol{\sigma}) = 1 - \left(\frac{\sigma_m - S_0}{A} \right)^2 + \left(\frac{\sigma_d}{\sqrt{2}B} \right)^2 \leq 0 \quad (2.2.36)$$

where $\sigma_m = \frac{1}{3} \mathbf{I} : \boldsymbol{\sigma}$ and $\sigma_d = \sqrt{2J_2} = \sqrt{\mathbf{S} : \mathbf{S}}$ with $\mathbf{S} = \boldsymbol{\sigma} - \sigma_m \mathbf{I}$.

The Drucker-Prager model can be obtained by letting

$$B = \alpha_s A \quad (2.2.37a)$$

$$S_0 = \frac{c_s}{\alpha_s} \quad (2.2.37b)$$

$$A \rightarrow 0 \quad (2.2.37c)$$

In order to obtain a dual definition of the strength domain, the following system of equations must be solved:

$$\mathbf{d} = \dot{\lambda} \frac{\partial f}{\partial \boldsymbol{\sigma}} \quad (2.2.38a)$$

$$f(\boldsymbol{\sigma}) = 0 \quad (2.2.38b)$$

$$\boldsymbol{\sigma} : \mathbf{d} = \pi(\mathbf{d}) \quad (2.2.38c)$$

Using $\frac{\partial f}{\partial \boldsymbol{\sigma}} = \frac{1}{3} \frac{\partial f}{\partial \sigma_m} \mathbf{I} + \frac{\partial f}{\partial \sigma_d} \frac{\mathbf{S}}{\sigma_d}$ in (2.2.38a) and dividing it into volumetric and deviatoric parts leads to

$$\sigma_m - S_0 = -\frac{A^2}{2\dot{\lambda}} d_v \quad (2.2.39a)$$

$$\sigma_d = \frac{B^2}{\dot{\lambda}} d_d \quad (2.2.39b)$$

Substituting this into (2.2.38b) and solving for $\dot{\lambda}$ reveals

$$(\dot{\lambda})^2 = \left(\frac{A d_v}{2} \right)^2 - \left(\frac{B d_d}{\sqrt{2}} \right)^2 \quad (2.2.40)$$

Using (2.2.40) and (2.2.39) in (2.2.38c) leads to the following form of the maximum

dissipation energy:

$$\pi = d_v S_0 - \sqrt{(A d_v)^2 - 2(B d_d)^2} \quad (2.2.41)$$

It is convenient to choose the following form of the microscopic stiffness $\mathbb{C}(\mathbf{x})$ and prestress $\boldsymbol{\tau}(\mathbf{x})$:

$$\mathbb{C}(\mathbf{x}) = \begin{cases} \mathbb{C}_s = 3k_s \mathbb{J} + 2g_s \mathbb{K} & \text{in } V_s \\ 0 & \text{in } V_p \end{cases} \quad \boldsymbol{\tau}(\mathbf{x}) = \begin{cases} \tau \mathbf{I} & \text{in } V_s \\ 0 & \text{in } V_p \end{cases} \quad (2.2.42)$$

where V_s and V_p are domains occupied by solid and porosity, respectively. From Levin's theory [35], the macroscopic stress equation of state reads[43]:

$$\boldsymbol{\Sigma} = \mathbb{C}^{hom} : \mathbf{D} + \mathbf{T} \quad (2.2.43)$$

where

$$\mathbb{C}^{hom} = \overline{\mathbb{C}(\mathbf{x}) : \mathbb{A}(\mathbf{x})} = \mathbb{C}_s : \eta \overline{\mathbb{A}^s} = 3K^{hom} \mathbb{J} + 2G^{hom} \mathbb{K} \quad (2.2.44a)$$

$$\mathbf{T} = \overline{\boldsymbol{\tau}(\mathbf{x}) : \mathbb{A}(\mathbf{x})} = \tau \mathbf{I} : \eta \overline{\mathbb{A}^s} = \tau \mathbf{I} : \mathbb{C}_s^{-1} : \mathbb{C}^{hom} = \tau \frac{K^{hom}}{k_s} \mathbf{I} \quad (2.2.44b)$$

are the macroscopic stiffness tensor and the macroscopic prestress, and

$$K^{hom} = g_s \mathcal{K} \left(\frac{k_s}{g_s}, \eta \right) \quad (2.2.45a)$$

$$G^{hom} = g_s \mathcal{M} \left(\frac{k_s}{g_s}, \eta \right) \quad (2.2.45b)$$

where $\mathbb{A}(\mathbf{x})$ is a strain localization tensor. (2.2.45) are solution of the Self-Consistent or Mori-Tanaka homogenization method in the case of solid-pore morphology, for which a closed-form solution exists. From the dimensional analysis, this solution can be written with the help of dimensionless functions \mathcal{K} and \mathcal{M} . The strain rate energy function is obtained by application of the linear homogenization theory [43]:

$$\begin{aligned} W_0(D_v, D_d) &= \frac{1}{2} K^{hom} D_v^2 + G^{hom} D_d^2 + \frac{K^{hom}}{k_s} \tau D_v + \frac{1}{2k_s} \left(\frac{K^{hom}}{k_s} - \eta \right) \tau^2 \\ &= \frac{1}{2} g_s \mathcal{K} D_v^2 + g_s \mathcal{M} D_d^2 + \frac{g_s}{k_s} \mathcal{K} \tau D_v + \frac{1}{2k_s} \left(\frac{g_s}{k_s} \mathcal{K} - \eta \right) \tau^2 \end{aligned} \quad (2.2.46)$$

where $D_v = \mathbf{I} : \mathbf{D}$ and $D_d = \sqrt{\boldsymbol{\Delta} : \boldsymbol{\Delta}}$ with $\boldsymbol{\Delta} = \mathbf{D} - \frac{1}{3} D_v \mathbf{I}$.

Now, we can move on to developing of function ν from (2.2.35) for solid phase (for porosity, ν is zero). The strain rate energy of the solid reads

$$w_s(\mathbf{d}) = \frac{1}{2} k_s d_v^2 + g_s d_d^2 + \tau d_v \quad (2.2.47)$$

Developing the stationarity conditions (vanishing derivatives) of (2.2.35) using expressions of the strain rate energy of the solid (2.2.47) and the maximum dissipation capacity of the regularized Drucker-Prager model (2.2.41) leads to

$$k_s d_v + \tau = S_0 - \frac{A^2 d_v}{\sqrt{(A d_v)^2 + 2(B d_d)^2}} \quad (2.2.48a)$$

$$2g_s d_d = \frac{2B^2 d_d}{\sqrt{(A d_v)^2 + 2(B d_d)^2}} \quad (2.2.48b)$$

The microscopic stiffness components k_s and g_s of the LCC must be positive. This can be achieved by requiring that

$$\tau = S_0 - \frac{2A^2 d_v}{\sqrt{(A d_v)^2 + 2(B d_d)^2}} \quad (2.2.49a)$$

$$k_s = \frac{A^2}{\sqrt{(A d_v)^2 + 2(B d_d)^2}} \quad (2.2.49b)$$

$$g_s = \frac{B^2}{\sqrt{(A d_v)^2 + 2(B d_d)^2}} \quad (2.2.49c)$$

Dividing (2.2.49b) by (2.2.49c) we obtain

$$\frac{k_s}{g_s} = \frac{A^2}{B^2} = \text{const} \quad (2.2.50)$$

Therefore only two independent parameters are left: τ and g_s . For the Drucker-Prager case ((2.2.37)):

$$\frac{k_s}{g_s} = \frac{1}{\alpha^2} \quad (2.2.51)$$

The first and third expressions in (2.2.49) can be rewritten in the following way:

$$S_0 - \tau = \frac{2A^2 d_v}{\sqrt{(A d_v)^2 + 2(B d_d)^2}} \quad (2.2.52a)$$

$$g_s = \frac{B^2}{\sqrt{(A d_v)^2 + 2(B d_d)^2}} \quad (2.2.52b)$$

Dividing one by the other we obtain

$$d_v = \frac{B^2}{2A^2} \frac{S_0 - \tau}{g_s} \quad (2.2.53)$$

Raising (2.2.52b) to the second power and using the obtained result for d_v in (2.2.53)

allows to obtain

$$2d_d^2 = \frac{B^2}{A^2 g_s^2} \left(\left(\frac{S_0 - \tau}{2} \right)^2 - A^2 \right) \quad (2.2.54)$$

Having in hand the solution for the stationarity condition of ν (that is d_v and d_d) we can determine the value of the function itself. Introducing (2.2.54) and (2.2.53) into $\nu = \pi - w_s$ using (2.2.47) and (2.2.41) gives

$$\nu_s = \left(\frac{B(S_0 - \tau)}{2A} \right)^2 \frac{1}{g_s} - \frac{1}{2} \frac{B^2}{g_s} \quad (2.2.55)$$

For the Drucker-Prager case ((2.2.37))

$$\nu_s = (c_s - \alpha\tau)^2 \frac{1}{4g_s} \quad (2.2.56)$$

The final step is finding the stationary value of $\widetilde{\Pi^{hom}}$ ((2.2.34)) for which all the necessary ingredients (ν_s and W_0) are developed. Since there are only two independent variables (τ and g_s), there are two equations coming from (2.2.34):

$$\frac{\partial W_0}{\partial g_s} + \eta \frac{\partial \nu_s}{\partial g_s} = 0 \quad (2.2.57a)$$

$$\frac{\partial W_0}{\partial \tau} + \eta \frac{\partial \nu_s}{\partial \tau} = 0 \quad (2.2.57b)$$

The constant ratio between k_s and g_s ((2.2.50)) simplifies our derivation since we are able to consider dimensionless functions \mathcal{K} and \mathcal{M} in (2.2.45) to be constant. Substituting (2.2.45) and (2.2.55) into (2.2.57b) and using (2.2.50) yields

$$\tau = \frac{A^2 (2\mathcal{K}g_s D_v - \eta S_0)}{\eta A^2 - 2\mathcal{K}B^2} \quad (2.2.58)$$

Using (2.2.56) in (2.2.57a) gives

$$g_s^2 = \frac{B^2 \eta}{A^2} \frac{\eta A^2 (S_0^2 - A^2) + \mathcal{K}B^2 (2A^2 - S_0^2)}{\eta \mathcal{K}A^2 D_v^2 + (2\eta \mathcal{M}A^2 - 4\mathcal{K}\mathcal{M}B^2) D_d^2} \quad (2.2.59)$$

Now, we can use the obtained values of g_s and τ in (2.2.34) in order to have an estimate of the maximum plastic energy capacity $\widetilde{\Pi^{hom}}$. Straightforward substitution of (2.2.59) and (2.2.58) will lead to a cumbersome expression, therefore we first substitute (2.2.58)

into (2.2.34) and group all variables about g_s , which leads to

$$\begin{aligned} \widetilde{\Pi^{hom}} = \frac{g_s}{2} & \frac{\eta \mathcal{K} A^2 D_v^2 + (2\eta \mathcal{M} A^2 - 4\mathcal{K} \mathcal{M} B^2) D_d^2}{A^2 \eta - 2B^2 \mathcal{K}} - \frac{B^2 \mathcal{K} \eta D_v S_0}{A^2 \eta - 2B^2 \mathcal{K}} \\ & + \frac{B^2 \eta}{2A^2 g_s} \frac{\eta A^2 (S_0^2 - A^2) + \mathcal{K} B^2 (2A^2 - S_0^2)}{A^2 \eta - 2B^2 \mathcal{K}} \end{aligned} \quad (2.2.60)$$

We then discover that the numerators in the first and third term are similar to the denominator and numerator in the expression for g_s ((2.2.59)) and substitution of the latter will lead to similar first and third terms. The result can be written as

$$\widetilde{\Pi^{hom}} = \Sigma_0^{hom} D_v + \text{sign}(\eta A^2 - 2\mathcal{K} B^2) \sqrt{(A^{hom})^2 D_v^2 + (\sqrt{2} B^{hom})^2 D_d^2} \quad (2.2.61)$$

with

$$(A^{hom})^2 = \frac{\eta^2 B^2 \mathcal{K} (\eta A^2 (S_0^2 - A^2) + \mathcal{K} B^2 (2A^2 - S_0^2))}{(\eta A^2 - 2\mathcal{K} B^2)^2} \quad (2.2.62a)$$

$$(B^{hom})^2 = \frac{\eta B^2 \mathcal{M} (\eta A^2 (S_0^2 - A^2) + \mathcal{K} B^2 (2A^2 - S_0^2))}{A^2 (\eta A^2 - 2\mathcal{K} B^2)} \quad (2.2.62b)$$

$$\Sigma_0^{hom} = -\frac{\eta B^2 \mathcal{K} S_0}{\eta A^2 - 2\mathcal{K} B^2} \quad (2.2.62c)$$

Comparing (2.2.61) with (2.2.41) we clearly see that (2.2.61) is a Π function of the regularized Drucker-Prager yield criterion. If $\eta A^2 - 2\mathcal{K} B^2 < 0$, the criterion has a hyperbolic form, in return for $\eta A^2 - 2\mathcal{K} B^2 > 0$ it has an elliptical form

$$\left(\frac{\sigma_m - \Sigma_0^{hom}}{A^{hom}} \right)^2 + \left(\frac{\sigma_d}{\sqrt{2} B^{hom}} \right)^2 = 1 \quad (2.2.63)$$

This formula also includes the hyperbolic case, for which $(B^{hom})^2 < 0$. For the case of Drucker-Prager yield function ((2.2.37)), expressions (2.2.62) simplify to

$$\left(\frac{A^{hom}}{c_s} \right)^2 = \frac{\eta^2 \mathcal{K} (\eta - \alpha_s^2 \mathcal{K})}{(\eta - 2\alpha_s^2 \mathcal{K})^2} \quad (2.2.64a)$$

$$\left(\frac{B^{hom}}{c_s} \right)^2 = \frac{\eta \mathcal{M} (\eta - \alpha_s^2 \mathcal{K})}{\eta - 2\alpha_s^2 \mathcal{K}} \quad (2.2.64b)$$

$$\frac{\Sigma_0^{hom}}{c_s} = -\frac{\eta \alpha_s \mathcal{K}}{\eta - 2\alpha_s^2 \mathcal{K}} \quad (2.2.64c)$$

Depending on the sign of $\eta - 2\alpha_s^2 \mathcal{K}$, the yield surface will be hyperbolic, parabolic or

ellipsoidal:

$$\eta - 2\alpha_s^2 \mathcal{K} \left(\frac{k_s}{g_s} = \frac{1}{\alpha_s^2} \right) \begin{cases} < 0 & \text{Elliptic Criterion} \\ 0 & \text{Limit Parabola} \\ > 0 & \text{Hyperbolic Criterion} \end{cases} \quad (2.2.65)$$

2.3 Fast Fourier Transform Homogenization Method

2.3.1 Formulation

In this section we will briefly summarize the Fast Fourier Transform (FFT) algorithm for homogenization proposed in [71]. This method is proposed in order to obtain local and overall responses of nonlinear composites. It is generally directly applied to 2D or 3D microstructures obtained from experimental techniques such as SEM/BSE images, 3D tomography, TEM and others. A general approach to incorporate detailed information on the microstructure (not just volume fractions) is to mesh it and calculate its response to particular loading using FEM. However, serious difficulties arise from meshing. The FFT method avoids difficulties due to meshing and can be used even in the case of nonlinear phase behavior. As an input it requires data sampled in a grid of regular spacing, which is the usual output of all digital image methods. FFT also does not require the formation of the tangent stiffness matrix and therefore consumes less memory and can be used for finer discretization.

Let us consider a RVE of an arbitrary complex heterogeneous medium composed of linear elastic phases. Extension to nonlinear behavior will be discussed later. We then consider periodic boundary conditions. The local strain field $\epsilon(\mathbf{u}(\mathbf{x}))$ is split into its average \mathbf{E} and fluctuation term $\epsilon(\mathbf{u}^*(\mathbf{x}))$:

$$\epsilon(\mathbf{u}(\mathbf{x})) = \epsilon(\mathbf{u}^*(\mathbf{x})) + \mathbf{E} \quad (2.3.1)$$

or equivalently

$$\mathbf{u}(\mathbf{x}) = \mathbf{u}^*(\mathbf{x}) + \mathbf{E} \cdot \mathbf{x} \quad (2.3.2)$$

Periodic boundary conditions require the fluctuation term \mathbf{u}^* to be periodic ($\mathbf{u}^*_{\#}$) and traction $\boldsymbol{\sigma} \cdot \mathbf{x}$ to be anti-periodic ($\boldsymbol{\sigma} \cdot \mathbf{x} - \#$).

Before solving the heterogeneous problem, let us consider a homogeneous linear elastic medium with stiffness \mathbb{C} subjected to a polarization field $\boldsymbol{\tau}(\mathbf{x})$:

$$\begin{cases} \boldsymbol{\sigma}(\mathbf{x}) = \mathbb{C}^0 : \epsilon(\mathbf{u}^*(\mathbf{x})) + \boldsymbol{\tau} & \forall \mathbf{x} \in V \\ \nabla \cdot \boldsymbol{\sigma}(\mathbf{x}) = 0 & \forall \mathbf{x} \in V \end{cases} \quad (2.3.3)$$

The solution of (2.3.3) can be expressed in real and Fourier spaces, respectively, by means of the periodic Green operator $\mathbb{G}^0(\mathbb{C}^0)$:

$$\epsilon(\mathbf{u}^*) = -\mathbb{G}^0 * \boldsymbol{\tau} \quad \forall \mathbf{x} \in V \quad (2.3.4)$$

where $(f * g)(\mathbf{x}) \equiv \int_{R^3} f(\mathbf{y})g(\mathbf{x} - \mathbf{y})d\mathbf{y}$, or, in Fourier space,

$$\hat{\epsilon}^*(\boldsymbol{\xi}) = -\hat{\mathbb{G}}^0 : \hat{\boldsymbol{\tau}}(\boldsymbol{\xi}) \quad \forall \boldsymbol{\xi} \neq 0, \quad \hat{\epsilon}^*(0) = 0 \quad (2.3.5)$$

Operator \mathbb{G}^0 is explicitly known in Fourier space, and when the reference material is isotropic (with Lamé coefficients λ^0 and μ^0), it takes the form

$$\mathbb{G}_{ijkh}^0(\boldsymbol{\xi}) = \frac{1}{4\mu^0 \|\boldsymbol{\xi}\|^2} (\delta_{ki}\xi_h\xi_j + \delta_{hi}\xi_k\xi_j + \delta_{kj}\xi_h\xi_i + \delta_{hj}\xi_k\xi_i) - \frac{\lambda^0 + \mu^0}{\mu^0(\lambda^0 + 2\mu^0)} \frac{\xi_i\xi_j\xi_k\xi_h}{\|\boldsymbol{\xi}\|^4} \quad (2.3.6)$$

Now, let us consider a heterogeneous elastic composite medium with the stiffness $\mathbb{C}(\mathbf{x})$ and macroscopic strain \mathbf{E} :

$$\begin{cases} \boldsymbol{\sigma}(\mathbf{x}) = \mathbb{C}(\mathbf{x}) : (\boldsymbol{\epsilon}(\mathbf{u}^*(\mathbf{x})) + \mathbf{E}) & \forall \mathbf{x} \in V \\ \boldsymbol{\nabla} \cdot \boldsymbol{\sigma}(\mathbf{x}) = 0 & \forall \mathbf{x} \in V \end{cases} \quad (2.3.7)$$

For now, we will consider \mathbf{E} to be prescribed, however boundary conditions with prescribed stress can be considered as well. Let us introduce a reference homogeneous elastic material with \mathbb{C}^0 and polarization stress $\boldsymbol{\tau}(\mathbf{x})$, defined as

$$\boldsymbol{\tau}(\mathbf{x}) = (\mathbb{C}(\mathbf{x}) - \mathbb{C}^0) : \boldsymbol{\epsilon}(\mathbf{u}(\mathbf{x})) \quad (2.3.8)$$

Using this definition, (2.3.7) can be rewritten as

$$\begin{cases} \boldsymbol{\sigma}(\mathbf{x}) = \mathbb{C}^0 : \boldsymbol{\epsilon}(\mathbf{u}^*(\mathbf{x})) + \boldsymbol{\tau}(\mathbf{x}) + \mathbb{C}^0 : \mathbf{E} & \forall \mathbf{x} \in V \\ \boldsymbol{\nabla} \cdot \boldsymbol{\sigma}(\mathbf{x}) = 0 & \forall \mathbf{x} \in V \end{cases} \quad (2.3.9)$$

Comparing the obtained formulation with the auxiliary problem (2.3.5), we notice that the definition of the stress differs in a constant term, yet this term obviously will not affect the solution of the equilibrium equation $\boldsymbol{\nabla} \cdot \boldsymbol{\sigma} = 0$ and so both problems have the same solution. Therefore, the solution of (2.3.9) reads

$$\boldsymbol{\epsilon} = -\mathbb{G}^0 * \boldsymbol{\tau} + \boldsymbol{\Sigma} \quad (2.3.10)$$

or, in Fourier space,

$$\hat{\epsilon}(\boldsymbol{\xi}) = -\hat{\mathbb{G}}^0(\boldsymbol{\xi}) : \hat{\boldsymbol{\tau}}(\boldsymbol{\xi}) \quad \forall \boldsymbol{\xi} \neq 0, \quad \hat{\epsilon}(0) = \mathbf{E} \quad (2.3.11)$$

2.3.2 Algorithm

Before developing (2.3.11) into an algorithm, let us note that $\mathbb{G}^0 * (\mathbb{C}^0 : \epsilon) = \epsilon$. Thus, the algorithm reads:

1. Initialize: $\epsilon^0(x) = \mathbf{E}$, $\sigma^0(x) = \mathbb{C} : \epsilon^0(x)$.
2. Compute (discrete) Fourier transform of stresses $\hat{\sigma}$.
3. Check equilibrium conditions in Fourier space.
4. Update strain in Fourier space: $\hat{\epsilon}(\xi) = \hat{\mathbb{G}}^0(\xi) : \hat{\sigma}(\xi)$ and $\hat{\epsilon}(0) = \mathbf{E}$ (follows from (2.3.11) and (2.3.8)).
5. Compute Inverse (discrete) Fourier transform of total strains ϵ .
6. Update stresses from strains: $\sigma(x) = \mathbb{C}(x) : \epsilon(x)$.

Equilibrium conditions can be easily rewritten in Fourier space and therefore the error serving to check convergence is

$$e = \frac{\left(\overline{\|\xi \cdot \hat{\sigma}\|^2} \right)^{1/2}}{\|\hat{\sigma}(0)\|} \quad (2.3.12)$$

Discrete representation of the problem naturally arises from the regular voxel input from tomography, *BSE* or cement hydration models. Therefore, all unknowns are sampled on that grid ($N_1 \times N_2 \times N_3$). This discretization can be used in discrete Fast Fourier Transform (DFFT) packages ([41]). Corresponding frequencies in Fourier space read for even and odd cases of N_j , respectively:

$$\xi_j = \left(-\frac{N_j}{2} + 1\right) \frac{1}{T_j}, \left(-\frac{N_j}{2} + 2\right) \frac{1}{T_j}, \dots, -\frac{1}{T_j}, 0, \frac{1}{T_j}, \dots, \left(\frac{N_j}{2} - 1\right) \frac{1}{T_j}, \frac{N_j}{2} \frac{1}{T_j} \quad (2.3.13)$$

$$\xi_j = -\frac{N_j - 1}{2} \frac{1}{T_j}, \dots, -\frac{1}{T_j}, 0, \frac{1}{T_j}, \dots, \frac{N_j - 1}{2} \frac{1}{T_j} \quad (2.3.14)$$

where T_j is a period of the unit cell in j -th direction.

Any plastic or visco-plastic behavior can be considered as well. The main difference will be only in the last step of the algorithm: calculation of total stresses from total strain at the current iteration. Of course, one should keep track of all internal variables and update them after equilibrium is reached.

Applying DFFT, the following should be noted. The discrete Fourier transform is exact when the image cut-off frequency f^c (i.e. the frequency above which the Fourier transform

2.3.2 Algorithm

Before developing (2.3.11) into an algorithm, let us note that $\mathbb{G}^0 * (\mathbb{C}^0 : \epsilon) = \epsilon$. Thus, the algorithm reads:

1. Initialize: $\epsilon^0(x) = \mathbf{E}$, $\sigma^0(x) = \mathbb{C} : \epsilon^0(x)$.
2. Compute (discrete) Fourier transform of stresses $\hat{\sigma}$.
3. Check equilibrium conditions in Fourier space.
4. Update strain in Fourier space: $\hat{\epsilon}(\xi) = \hat{\mathbb{G}}^0(\xi) : \hat{\sigma}(\xi)$ and $\hat{\epsilon}(\mathbf{0}) = \mathbf{E}$ (follows from (2.3.11) and (2.3.8)).
5. Compute Inverse (discrete) Fourier transform of total strains ϵ .
6. Update stresses from strains: $\sigma(x) = \mathbb{C}(x) : \epsilon(x)$.

Equilibrium conditions can be easily rewritten in Fourier space and therefore the error serving to check convergence is

$$e = \frac{\left(\overline{\|\xi \cdot \hat{\sigma}\|^2} \right)^{1/2}}{\|\hat{\sigma}(\mathbf{0})\|} \quad (2.3.12)$$

Discrete representation of the problem naturally arises from the regular voxel input from tomography, *BSE* or cement hydration models. Therefore, all unknowns are sampled on that grid ($N_1 \times N_2 \times N_3$). This discretization can be used in discrete Fast Fourier Transform (DFFT) packages ([41]). Corresponding frequencies in Fourier space read for even and odd cases of N_j , respectively:

$$\xi_j = \left(-\frac{N_j}{2} + 1\right) \frac{1}{T_j}, \left(-\frac{N_j}{2} + 2\right) \frac{1}{T_j}, \dots, -\frac{1}{T_j}, 0, \frac{1}{T_j}, \dots, \left(\frac{N_j}{2} - 1\right) \frac{1}{T_j}, \frac{N_j}{2} \frac{1}{T_j} \quad (2.3.13)$$

$$\xi_j = -\frac{N_j - 1}{2} \frac{1}{T_j}, \dots, -\frac{1}{T_j}, 0, \frac{1}{T_j}, \dots, \frac{N_j - 1}{2} \frac{1}{T_j} \quad (2.3.14)$$

where T_j is a period of the unit cell in j -th direction.

Any plastic or visco-plastic behavior can be considered as well. The main difference will be only in the last step of the algorithm: calculation of total stresses from total strain at the current iteration. Of course, one should keep track of all internal variables and update them after equilibrium is reached.

Applying DFFT, the following should be noted. The discrete Fourier transform is exact when the image cut-off frequency f^c (i.e. the frequency above which the Fourier transform

of the image vanishes identically) is less than half of the sampling frequency (Shannon's theorem):

$$f_j^c < \frac{1}{2} \frac{N_j}{T_j} \quad (2.3.15)$$

This condition is not met in general (e.g. a discontinuous field does not have a cut-off frequency). However, an increase of image sampling leads to an increase of cut-off frequency, as expected, and therefore the solution of the discrete problem approaches the solution of the continuous one.

FFT homogenization method was proven to give remarkably good results [66]. Prescribing stress boundary conditions may lead to big displacements in one step, therefore the direction is usually prescribed and the amplitude is considered to be unknown [66]:

$$\Sigma(t) = k(t)\Sigma^0 \quad (2.3.16)$$

requiring that

$$\Sigma^0 : \mathbf{E}(t) = t \quad (2.3.17)$$

The choice of a reference medium (Lame constants for \mathbb{G}) is of great importance. A common approach is to use the mean value among all phases.

It is well known that *FFT* homogenization method does not converge when the contrast between the phases is infinite (void or rigid inclusions) or when the nonlinear behavior of phases results in very different stiffness matrices [66]. In order to overcome this, several modified schemes were introduced [67]: The first one is an accelerated scheme for composites with high contrasts (the rate of convergence is proportional to the square root of the contrast). The second scheme, adequate for composites with infinite contrast, is based on an augmented Lagrangian method. The resulting saddle-point problem involves three steps: 1) solving a linear elastic problem with *FFT*; 2) solving non-linear problem at each individual voxel; 3) updating Lagrange multipliers. Comparison of all schemes can be found in [72].

3 Nanoindentation

3.1 Analytical Solutions for Indentation Problem

3.1.1 Elastic Material

Nanoindentation is a widely used technique for measuring properties of materials at the micron and submicron levels. It consists of establishing contact between a substrate (sample) and an indenter with known properties and geometry. The force P acting on the indenter is applied as the control variable and the corresponding penetration depth h is recorded. Commonly, a trapezoidal loading program with loading, holding and unloading periods is used (Fig. 3.1.1). Elastic properties of the substrate can be evaluated from

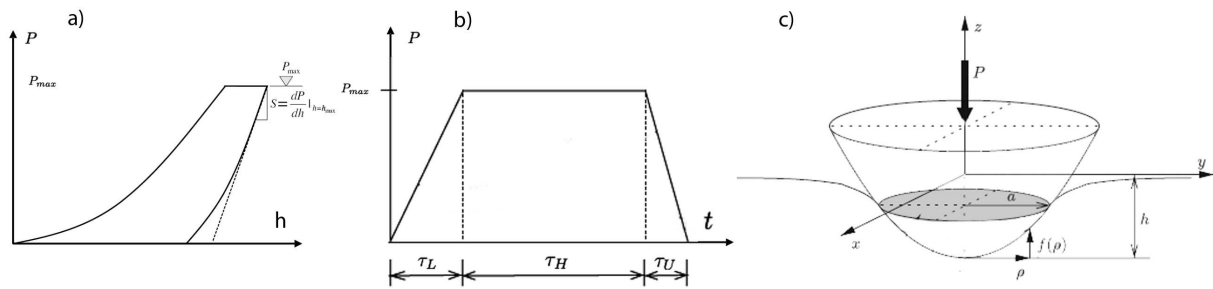


Figure 3.1.1: a) Illustration of the load-penetration P - h curve; b) Trapezoidal loading program used in a nanoindentation experiment; c) Indentation of material by a rigid axisymmetric indenter

the unloading part of the load-penetration curve by the standard Oliver-Pharr procedure [77], which is based on the analytical solution of the contact problem for an axisymmetric indenter and a linear elastic isotropic homogeneous infinite half-space [97]. Although this procedure is based on the assumption of material homogeneity, it has been applied to heterogeneous materials as well [55]. Another problem with the interpretation of indentation results is caused by deviations from an ideal shape of the indenter. The geometry of the actual indentation tip varies due to the production process and wear out during experiments. The associated error can be reduced by calibration based on series of indentations into a reference material with known properties [77]. The results can be used to determine an approximation of the tip shape for which the Oliver-Pharr procedure gives the correct elastic modulus. Usually, the cross-sectional area $A_c = \rho^2\pi$ is approximated by several terms of the series

$$A_c = C_0 f^2 + C_1 f + C_2 f^{1/2} + C_3 f^{1/4} + \dots \quad (3.1.1)$$

where ρ and f are respectively the radius of the section and its distance from the apex of the axisymmetric tip (Fig. 3.1.1), and C_i are constants describing the tip shape.

Vandamme [109] has developed a viscoelastic solution of the contact problem for a

conical indenter using several simple creep models. In view of the current understanding of the structure of C-S-H - the main creeping phase in the cement paste - as a porous medium [29, 55], it is necessary to extend this procedure to visco-elastic two-phased porous materials.

Analysis of the indentation problem with a rigid indenter of an arbitrary axisymmetric shape can be based on the so-called Galin-Sneddon solution [97]. The relation between the penetration depth h and the corresponding load P is parametrically described by

$$h = a \int_0^a \frac{f'(\rho) d\rho}{\sqrt{a^2 - \rho^2}} \quad (3.1.2a)$$

$$P = 2 \frac{E}{1 - \nu^2} \int_0^a \frac{\rho^2 f'(\rho) d\rho}{\sqrt{a^2 - \rho^2}} \quad (3.1.2b)$$

where a is the radius of the projected contact area A_c (Fig. 3.1.1), ρ is the tip radius, and $f(\rho)$ is a smooth function describing the tip shape and implicitly defined by (3.1.1). An ideal conical indenter is described by

$$f(\rho) = \frac{\rho}{\tan(\alpha)} \quad (3.1.3)$$

where α is the semi-apex angle. In (3.1.1), this case would correspond to $C_0 = \pi \tan^2(\alpha)$ and $C_i = 0$, $i > 0$. For $f(\rho)$ given by (3.1.3), the improper integrals in (3.1.2) can be calculated analytically, and the following formula can be derived for evaluation of the indentation modulus from the initial slope of the unloading part of the indentation curve:

$$\frac{E}{1 - \nu^2} = \frac{1}{2} \frac{dP}{dh} \frac{\sqrt{\pi}}{A_c} \quad (3.1.4)$$

3.1.2 Viscoelastic Material

The foregoing elastic solution can be extended to the viscoelastic case by the method of functional equations [63]. It consists of replacing elastic constants in the contact problem solution by Laplace-Carson transform (LCT) of bulk and shear relaxation functions. The second part of (3.1.2) can be rewritten in the form:

$$P(t) = M F(a(t)) \quad (3.1.5a)$$

$$F(a(t)) = 2 \int_0^a \frac{\rho^2 f'(\rho) d\rho}{\sqrt{a^2 - \rho^2}} \quad (3.1.5b)$$

Here, function $F(a(t))$ depends only on the tip geometry, whereas the material proper-

ties are reflected by the indentation modulus $M \equiv E/(1 - \nu^2)$. The viscoelastic solution of the contact problem can then be written as:

$$\hat{P}(s) = \hat{M}(s) \hat{F}(a(s)) \quad (3.1.6)$$

where $\hat{\bullet}(s)$ denotes the LCT of $\bullet(t)$. The LCT of the indentation modulus can be expressed in terms of the LCT $\hat{K}(s)$ and $\hat{G}(s)$ of the bulk and shear relaxation functions as

$$\hat{M}(s) = \frac{4\hat{G}(s) \left(3\hat{K}(s) + \hat{G}(s) \right)}{3\hat{K}(s) + 4\hat{G}(s)} \quad (3.1.7)$$

Using homogenization procedures in the Laplace-Carson domain, it is possible to up-scale the visco-elastic properties from the microstructure level to the level of the indentation experiment. For the self-consistent homogenization scheme, the effective moduli K_{hom} and G_{hom} are obtained by solving the system of two nonlinear equations (2.2.3).

A rearrangement of (3.1.6) yields an expression for the LCT of $F(a(t))$,

$$\hat{F}(a(s)) = \frac{\hat{P}(s)}{\hat{M}(s)} \equiv \hat{P}(s) \hat{Y}(s) \quad (3.1.8)$$

where we have denoted $\hat{Y}(s) \equiv 1/\hat{M}(s)$ - the LCT of the indentation compliance.

Exploiting the properties of the LCT, (3.1.8) can be written in the time domain as

$$F(a(t)) = \int_0^t Y(t - \tau) \dot{P}(\tau) d\tau \quad (3.1.9)$$

where the dot over P denotes the time derivative. To calculate the improper integrals in (3.1.2), $f'(\rho)$ is needed. Thus, (3.1.1) has to be solved for $f(\rho)$. For a simple shape of the indenter (two constants) these integrals can be calculated analytically [48], but for the case when the contact area of the tip is approximated using three or more terms, a closed-form solution is complicated or even not available. Numerical integration can then be used. (3.1.1) is solved for $f(\rho)$ at $\rho_i \in [0, \rho_{max}]$, $i = 1 : N$. Afterwards, $f(\rho_i)$ is interpolated by piecewise cubic Hermite polynomials. The Monte-Carlo integration method is used to compute the integrals. The obtained values $h_i = h(a_i)$ and $F_i = F(a_i)$ are then interpolated for later usage.

For very simple visco-elastic models, such as the Kelvin-Maxwell-Voight model, the exact form of $Y(t)$ can be derived analytically [109]. However, for a logarithmic creep model, even in its simplest form, numerical inversion has to be done. Since the basic creeping phase CSH is believed to be porous, we consider a two-phase polycrystal composite with one phase being viscoelastic and another corresponding to the pores. From

given viscoelastic model parameters and volume fraction of pores, $\hat{K}_{hom}(s)$ and $\hat{G}_{hom}(s)$ for the homogenized medium can be calculated by solving (2.2.3) in the Laplace-Carson domain. Substituting the result into (3.1.7), the indentation modulus $\hat{M}(s)$ and thus $\hat{Y}(s)$ can be calculated. The Stehfest algorithm [100] is used for the inverse transform and calculation of $Y(t)$.

Indentation experiments are usually conducted under trapezoidal load control (Fig. 3.1.1), described by

$$P(t) = \begin{cases} P_L(t) = t/\tau_L P_{max} & 0 \leq t \leq \tau_L \\ P_H(t) = P_{max} & \tau_L \leq t \leq \tau_L + \tau_H \\ P_U(t) = (\tau_L + \tau_H + \tau_U - t)P_{max}/\tau_U & \tau_L + \tau_H \leq t \leq \tau_L + \tau_H + \tau_U \end{cases} \quad (3.1.10)$$

where τ_L, τ_H and τ_U are the loading, holding and unloading durations, respectively. Considering this load history in (3.1.9) leads to

$$F(a(t)) = \frac{P_{max}}{\tau_L} \int_0^t Y(t - \tau) d\tau \quad 0 \leq t \leq \tau_L \quad (3.1.11a)$$

$$F(a(t)) = \frac{P_{max}}{\tau_L} \int_0^{\tau} Y(t - \tau) d\tau \quad \tau_L \leq t \leq \tau_L + \tau_H \quad (3.1.11b)$$

Knowing $Y(t)$, the integrals in (3.1.11) are numerically calculated using an adaptive Simpson quadrature. With $F(t)$ at hand, the previously found interpolation of the values $F(a_i)$ and $h(a_i)$ allows obtaining $h(t)$. Thus, an optimization procedure to fit the experimentally observed penetration depth history can be invoked.

Example of Application and Conclusions

In order to check the proposed method, one and a half year old cement paste CEM I 42.5 prepared at $w/c = 0.4$ has been tested. Indentation has been performed by a Hysitron nanoindenter using a trapezoidal loading program with $\tau_L = 10s$, $\tau_H = 100s$, $\tau_U = 10s$ and the maximum applied force $P_{max} = 1000\mu N$. One of the obtained indentation curves has been considered. The indenter geometry parameters have been determined as $C_0 = 24.5$, $C_1 = 4793$, $C_2 = -82009$, $C_3 = 30934$, $C_4 = -216130$. The Poisson ratio has been set to 0.24. From the Oliver-Pharr procedure, elastic modulus of 31.64 GPa has been obtained. The porosity of CSH has been taken as 0.26 [29, 55]. The deviatoric creep has been described by the logarithmic compliance function

$$J(t - t_0) = 1/G_0 + J \log \left(1 + \frac{t - t_0}{\tau} \right) \quad (3.1.12)$$

with $J = 0.0082 \text{ GPa}^{-1}$ and $\tau = 0.0287 \text{ s}$.

Fig. 3.1.2 shows the best fit of function $F(t)$ and the corresponding fit of the experimental penetration depth curve.

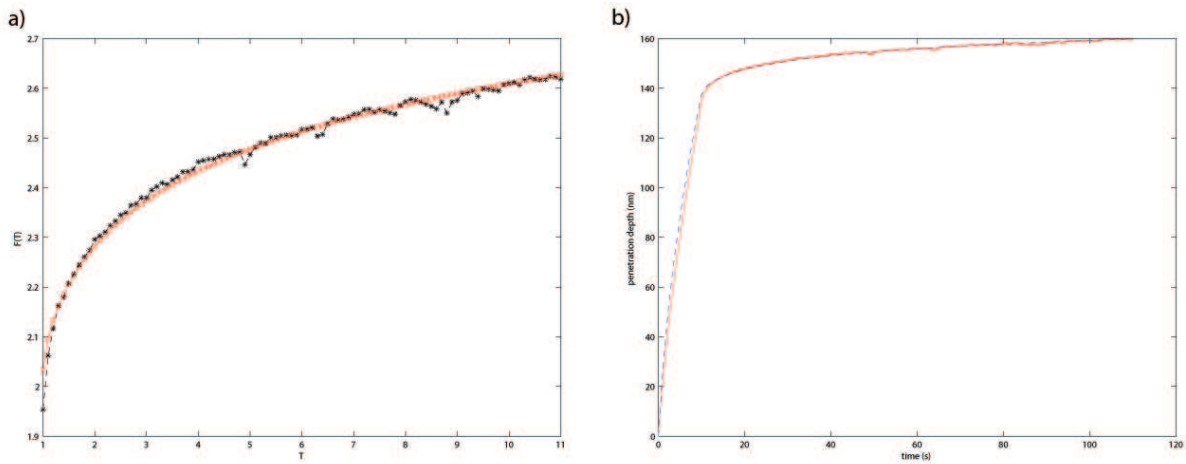


Figure 3.1.2: a) Experimental $F(t)$ curve and its fit in dimensionless form; b) Experimental penetration depth $h(t)$ and the corresponding fit by a porous logarithmic creep model

The considered example shows the applicability of the proposed method to extraction of viscoelastic properties of porous media from the nanoindentation experiment. This method could be useful in further studies of the C-S-H gel in cement paste as well as of other porous media.

3.2 Matrix-inclusion Heterogeneity

When a sharp tetrahedric needle-edged indenter is pressed onto a polished surface, only a small volume around the footprint is affected, typically a spheric volume with a radius of 3 to 4 times the size (the maximal dimension) of the indented prick. Size of the indented phase should be at least one order bigger than the indented prick.

Cement paste is extremely heterogeneous porous substrate. Then a sensible question to be asked is whether it is appropriate to use the method based on the assumption of a homogeneous elastic half-space ([77]) to evaluate Young's modulus. To clarify this point, a series of numerical analyses was carried out. The linear elastic material model was used; however the indent was performed into a hemispherical inclusion with Young's modulus different from that of the surrounding matrix (Fig. 3.2.1). The value of Poisson's ratio was assumed to be the same in the inclusion and the matrix.

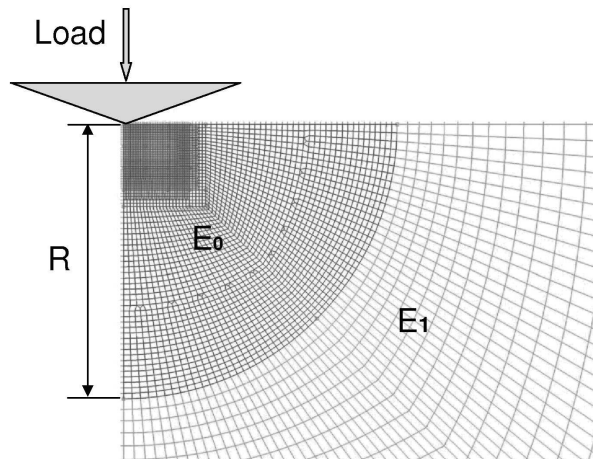


Figure 3.2.1: Axially symmetric FE model for the study of the effect of inhomogeneity on Oliver-Pharr procedure

The simulation involved a single loading cycle. Different ratios between the elastic moduli of inclusion and matrix were studied. Young's modulus was calculated by the Oliver and Pharr (Fig. 3.2.1) method at different penetration depths. Fig. 3.2.2 shows the dependence of the error in the resulting modulus on the penetration depth for different ratios of matrix and inclusion elastic moduli.

As seen in Fig. 3.2.2, when $E_0 = E_1$, the elastic modulus evaluated by the Oliver-Pharr procedure from the FE analysis result was almost equal to the elastic modulus of inclusion regardless of the penetration depth, as expected. Note that the small deviation resulted from a numerical error of the FE calculation. However, the presence of matrix with a different elastic modulus distorts the results of the Oliver-Pharr procedure. The error increases with increasing penetration depth and increasing difference between elastic

moduli of matrix and inclusion (Fig. 3.2.2).

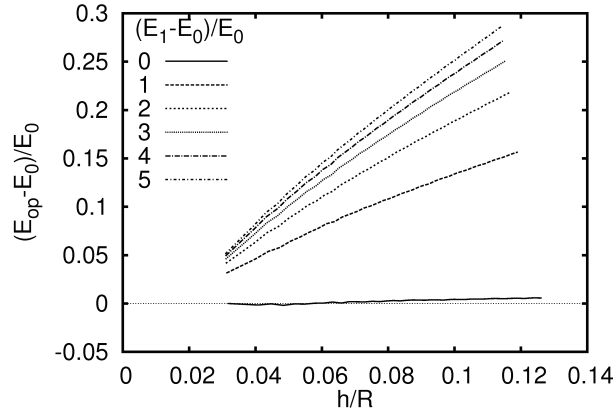


Figure 3.2.2: Normalized difference between the elastic modulus evaluated by Oliver-Pharr procedure (E_{op}) and the actual modulus of inclusion (E_0) for different normalized indentation depths (h/R) and different ratios between matrix and inclusion moduli $(E_1 - E_0)/E_0$

As found by Constantinides and Ulm ([29]) and Miller et al. ([68]), the elastic moduli of C-S-H and the surrounding unhydrated grains in cement paste are in the ranges of 20-40 GPa and 110-120 GPa, respectively. Then the ratio $(E_1 - E_0)/E_0$ falls in the range of 1.75 – 5. Considering that the typical size of the hydrated phase inclusions is several μm , it follows from Fig. 3.2.2 that reasonable values of Young's modulus (and perhaps other properties) are obtained by indents with h in the order of a few hundred nm.

3.3 Conclusions

Visco elastic semi-analytical solution of porous media for arbitrary indenter shape was developed. This method could be useful in further studies of the C-S-H gel in cement paste as well as of other porous media.

By analyzing the sensitivity of the evaluation of microscale Young's modulus to the size of the indented inclusion we were able to estimate the appropriate indentation depth.

4 Finite Element Method

4.1 Mathematical Formulation of Plastic Model

4.1.1 Return Mapping Algorithm

In order to use the results of nonlinear homogenization in *FEM* software, the tangent consistent matrix as well as return mapping algorithm should be implemented. Our aim in this chapter is to develop all the necessary algorithms for elliptic yield surfaces ((2.2.63)). All the derivation will be done in general form so that the results can be applied either to the small displacement case ($\boldsymbol{\sigma}$ - Cauchy stress), or to the Updated Lagrangian Hencky formulation ($\boldsymbol{\sigma}$ - Kirchoff stress).

Let us start from the return mapping algorithm. The basic constitutive equation can be written in the tensorial form as

$$\boldsymbol{\sigma} = \mathbb{C}^{el} : (\boldsymbol{\epsilon} - \boldsymbol{\epsilon}^{pl}) \quad (4.1.1)$$

where $\boldsymbol{\epsilon}^{pl}$ is the plastic strain and $\boldsymbol{\epsilon}$ is the total strain at the end of the current time step. The associative flow rule is considered (J - Jacobian of deformation gradient, \mathbf{F}):

$$\Delta \boldsymbol{\epsilon}^{pl} = \frac{\Delta \lambda}{J} \frac{\partial f(\boldsymbol{\sigma})}{\partial \boldsymbol{\sigma}} \quad (4.1.2)$$

where $f(\boldsymbol{\sigma})$ is the yield surface and $\Delta \lambda$ is unknown scalar. The definition of trial stresses at current time step t is

$$\boldsymbol{\sigma}^T = {}^{t-1}\boldsymbol{\sigma} + \mathbb{C}^{el} : \Delta \boldsymbol{\epsilon} \quad (4.1.3)$$

where ${}^{t-1}\boldsymbol{\sigma}$ is the stress at the previous end of the time step $t - 1$ and $\Delta \boldsymbol{\epsilon}$ is the strain increment. Using (4.1.3), (4.1.1) can be rewritten as

$$\boldsymbol{\sigma} = \boldsymbol{\sigma}^T - \mathbb{C}^{el} : \Delta \boldsymbol{\epsilon}^{pl} \quad (4.1.4)$$

Let us now introduce stress measures

$$p = -\frac{1}{3} \boldsymbol{\sigma} : \mathbf{I} \quad (4.1.5a)$$

$$q = \sqrt{\frac{3}{2} \mathbf{S} : \mathbf{S}} \quad (4.1.5b)$$

where $\mathbf{S} = \boldsymbol{\sigma} - \frac{1}{3} \boldsymbol{\sigma} : \mathbf{I}$, and therefore

$$\boldsymbol{\sigma} = -p\mathbf{I} + \frac{2}{3}q\mathbf{n} \quad (4.1.6)$$

with

$$\mathbf{n} = \frac{3}{2q} \mathbf{S} = \frac{3}{2q^T} \mathbf{S}^T \quad (4.1.7)$$

From isotropy of elastic constitutive equations follows:

$$\frac{\mathbf{S}}{2G} = \boldsymbol{\epsilon}_d^{el} = \boldsymbol{\epsilon}_d^T - \Delta\lambda \frac{\partial f}{\partial \mathbf{S}} = \boldsymbol{\epsilon}_d^T - \Delta\lambda \frac{\partial f}{\partial q} \frac{3}{2q} \mathbf{S} \quad (4.1.8)$$

where $\boldsymbol{\epsilon}_d$ - deviatoric strain. This equation guaranties that $\boldsymbol{\epsilon}_d^T \propto \mathbf{S}^T \propto \mathbf{S}$. The isotropy also guaranties that the deviatoric part of plastic strain is proportional to \mathbf{n} :

$$\Delta\boldsymbol{\epsilon}^{pl} = \frac{1}{3} \Delta\epsilon_p \mathbf{I} + \Delta\epsilon_q \mathbf{n} \quad (4.1.9)$$

where $\Delta\epsilon_p = \text{tr}(\Delta\boldsymbol{\epsilon}^{pl})$ and $\Delta\epsilon_q$ is a proportionality coefficient. Using (4.1.9) in (4.1.4) and rewriting in p and q space leads to

$$p = p^T + K \Delta\epsilon_p \quad (4.1.10a)$$

$$q = q^T - 3G \Delta\epsilon_q \quad (4.1.10b)$$

The associative flow rule (4.1.2) can be rewritten in p/q space as

$$\Delta\epsilon_p = - \frac{\Delta\lambda}{J} \frac{\partial f(p, q)}{\partial p} \quad (4.1.11a)$$

$$\Delta\epsilon_q = \frac{\Delta\lambda}{J} \frac{\partial f(p, q)}{\partial q} \quad (4.1.11b)$$

$\Delta\lambda$ can be eliminated from these two equations, leading to

$$\Delta\epsilon_p \frac{\partial f}{\partial q} + \Delta\epsilon_q \frac{\partial f}{\partial p} = 0 \quad (4.1.12)$$

The second nonlinear equation is a condition of the stress being on the yield surface

$$f(p/J, q/J) = 0 \quad (4.1.13)$$

The yield surface is considered in the following general form:

$$f(p/J, q/J) = A(p/J)^2 + B(p/J) + C(q/J)^2 - D \quad (4.1.14)$$

As a result, (4.1.12) and (4.1.13) are solved in terms of $\Delta\epsilon_p$ and $\Delta\epsilon_q$ using 4.1.10a and

4.1.10a:

$$p = p^T + K \Delta\epsilon_p \quad (4.1.15a)$$

$$q = q^T - 3G \Delta\epsilon_q \quad (4.1.15b)$$

$$\Delta\epsilon_p \frac{\partial f}{\partial q} + \Delta\epsilon_q \frac{\partial f}{\partial p} = 0 \quad (4.1.15c)$$

$$f(p/J, q/J) = 0 \quad (4.1.15d)$$

4.1.2 Algorithmic Tangent Stiffness Matrix

By definition, an algorithmic tangent stiffness tensor is

$$\mathbb{C}^{alg} = \frac{\partial \Delta\sigma}{\partial \Delta\epsilon} \quad (4.1.16)$$

The deviatoric part of the constitutive equation (4.1.1) reads

$$\mathbf{S} = 2G (\epsilon_d^T - \epsilon_d^{pl}) \quad (4.1.17)$$

where

$$\epsilon_d^{pl} = \Delta\epsilon_q \mathbf{n} = \Delta\epsilon_q \frac{3}{2q} \mathbf{S} \quad (4.1.18)$$

Considering (4.1.18), (4.1.17) can be rewritten as

$$\left(1 + \frac{3G}{q} \Delta\epsilon_q\right) \mathbf{S} = 2G \epsilon_d^T = \mathbf{S}^T \quad (4.1.19)$$

Taking double product of it with itself, one obtains

$$q + 3G \Delta\epsilon_q = 2G \overline{\epsilon_d}^T = q^T \quad (4.1.20)$$

where $\overline{\epsilon_d}^T = \sqrt{\frac{3}{2} \epsilon_d^T : \epsilon_d^T}$ is the effective deviatoric trial strain. Differentiation of (4.1.19) and (4.1.20) leads to

$$\partial q = \partial q^T - 3G \partial \Delta\epsilon_q \quad (4.1.21)$$

$$\left(1 + \frac{3G}{q} \Delta\epsilon_q\right) \partial \mathbf{S} + \mathbf{S} \frac{3G}{q} \left(\partial \Delta\epsilon_q - \frac{\Delta\epsilon_q}{q} \partial q\right) = 2G \partial \epsilon_d^T \quad (4.1.22)$$

Differential of q^T can be calculated in the following way:

$$\partial q^T = 2G \partial \epsilon_d^T = \frac{1}{2} \frac{2G}{\bar{\epsilon}_d^T} \frac{3}{2} 2\epsilon_d^T : \partial \epsilon_d^T = \frac{6G^2}{q^T} \epsilon_d^T : \partial \epsilon_d^T = \frac{3G}{q^T} \mathbf{S}^T : \partial \epsilon_d^T \quad (4.1.23)$$

and therefore

$$\partial q = 3G \left(\frac{\mathbf{S}^T}{q^T} : \partial \epsilon_d^T - \partial \Delta \epsilon_q \right) \quad (4.1.24)$$

Substituting (4.1.24) into (4.1.22) leads to

$$\left(1 + \frac{3G}{q} \Delta \epsilon_q \right) \partial \mathbf{S} + \mathbf{S} \frac{3G}{q} \left(\partial \Delta \epsilon_q - \frac{\Delta \epsilon_q}{q} 3G \left(\frac{\mathbf{S}^T}{q^T} : \partial \epsilon_d^T - \partial \Delta \epsilon_q \right) \right) = 2G \partial \epsilon_d^T \quad (4.1.25)$$

$$\left(1 + \frac{3G}{q} \Delta \epsilon_q \right) \partial \mathbf{S} + \frac{3G}{q} \mathbf{S} \partial \Delta \epsilon_q \left(1 + \frac{3G}{q} \Delta \epsilon_q \right) - \frac{9G^2}{q^2 q^T} \Delta \epsilon_q \mathbf{S} \mathbf{S}^T : \partial \epsilon_d^T = 2G \partial \epsilon_d^T \quad (4.1.26)$$

Noticing that $(1 + \frac{3G}{q} \Delta \epsilon_q) = \frac{q^T}{q}$ from (4.1.15b), last equation is rewritten as

$$\partial \mathbf{S} = -\frac{3G}{q} \mathbf{S} \partial \Delta \epsilon_q + \frac{9G^2}{q(q^T)^2} \Delta \epsilon_q \mathbf{S} \mathbf{S}^T : \partial \epsilon_d^T + 2G \partial \epsilon_d^T \frac{q}{q^T} \quad (4.1.27)$$

From (4.1.7) it follows

$$\mathbf{S} \mathbf{S}^T = \frac{4q q^T}{9} \mathbf{nn} \quad (4.1.28)$$

Using (4.1.28) in (4.1.27) leads to the final expression

$$\partial \mathbf{S} = \left(2G \frac{q}{q^T} \mathbb{J} + \frac{4G^2}{q^T} \Delta \epsilon_q \mathbf{nn} \right) : \partial \epsilon_d^T - 2G \partial \Delta \epsilon_q \mathbf{n} \quad (4.1.29)$$

where \mathbb{J} is the fourth-order unit tensor with components $J_{ijkl} = \frac{1}{2}(\delta_{ik}\delta_{jl} + \delta_{jk}\delta_{il})$. For all cases in which three direct strains are defined by the kinematic solution the following holds:

$$\partial \epsilon_d^T = \left(\mathbb{J} - \frac{1}{3} \mathbf{II} \right) : \partial \epsilon = \partial \epsilon_d \quad (4.1.30)$$

From the volumetric part of the elastic constitutive equations follows

$$\partial p = -K \mathbf{I} : \partial \epsilon + K \partial \Delta \epsilon_p \quad (4.1.31)$$

And so the differential of the σ is

$$\partial \sigma = K \mathbf{II} : \partial \epsilon - K \mathbf{I} \partial \Delta \epsilon_p + \left(2G \frac{q}{q^T} \mathbb{J} + \frac{4G^2}{q^T} \Delta \epsilon_q \mathbf{nn} \right) : \partial \epsilon_d^T - 2G \partial \Delta \epsilon_q \mathbf{n} \quad (4.1.32)$$

Introducing tensor \mathbb{Z}

$$\mathbb{Z} = 2G \frac{q}{q^T} \mathbb{J} + \left(K - \frac{2G}{3} \frac{q}{q^T} \right) \mathbf{II} + \frac{4G^2}{q^T} \Delta \epsilon_q \mathbf{nn} \quad (4.1.33)$$

and using (4.1.30) in (4.1.32) leads to

$$\partial \boldsymbol{\sigma} = \mathbb{Z} : \partial \boldsymbol{\epsilon} - K \mathbf{I} \partial \Delta \epsilon_p - 2G \partial \Delta \epsilon_q \mathbf{n} \quad (4.1.34)$$

Unknown variables $\partial \Delta \epsilon_p$ and $\partial \Delta \epsilon_q$ can be found from the linearization of the initial system of nonlinear equations:

$$\Delta \epsilon_p \frac{\partial f}{\partial q} + \Delta \epsilon_q \frac{\partial f}{\partial p} = 0 \equiv \Gamma_1 \quad (4.1.35a)$$

$$f(p/J, q/J) = 0 \equiv \Gamma_2 \quad (4.1.35b)$$

$$d\Gamma_1 = f_q d\Delta \epsilon_p + f_p d\Delta \epsilon_q + \Delta \epsilon_p (f_{qp} dp + f_{qq} dq) + \Delta \epsilon_q (f_{pp} dp + f_{pq} dq) = 0 \quad (4.1.36a)$$

$$d\Gamma_2 = f_p d\left(\frac{p}{J}\right) + f_q d\left(\frac{q}{J}\right) = \frac{1}{J} \left(f_p dp + f_q dq - (f_p p + f_q q) \frac{dJ}{J} \right) = 0 \quad (4.1.36b)$$

We notice that

$$dp = -\frac{1}{3} d\boldsymbol{\sigma} : \mathbf{I} \quad (4.1.37a)$$

$$\mathbf{n} : d\boldsymbol{\sigma} = \mathbf{n} : \frac{2}{3} (dq \mathbf{n} + q d\mathbf{n}) = \frac{2}{3} \mathbf{n} : \mathbf{n} dq = dq \quad (4.1.37b)$$

Therefore (4.1.36) can be rewritten in the following form:

$$f_q d\Delta \epsilon_p + f_p d\Delta \epsilon_q = \left[\frac{1}{3} (\Delta \epsilon_p f_{qp} + \Delta \epsilon_q f_{pp}) \mathbf{I} - (\Delta \epsilon_p f_{qq} + \Delta \epsilon_q f_{pq}) \mathbf{n} \right] : d\boldsymbol{\sigma} \quad (4.1.38a)$$

$$0 d\Delta \epsilon_p + 0 d\Delta \epsilon_q = \left[\frac{f_p}{3J} \mathbf{I} - \frac{f_q}{J} \mathbf{n} \right] : d\boldsymbol{\sigma} + \frac{1}{J} (f_p p + f_q q) I : d\boldsymbol{\epsilon}^T \quad (4.1.38b)$$

Let us rewrite (4.1.38) introducing the following constants:

$$\Lambda_{11} d\Delta \epsilon_p + \Lambda_{12} d\Delta \epsilon_q = (B_{11} \mathbf{I} + B_{12} \mathbf{n}) : d\boldsymbol{\sigma} \quad (4.1.39a)$$

$$\Lambda_{21} d\Delta \epsilon_p + \Lambda_{22} d\Delta \epsilon_q = (B_{21} \mathbf{I} + B_{22} \mathbf{n}) : d\boldsymbol{\sigma} + B_3 \mathbf{I} : d\boldsymbol{\epsilon}^T \quad (4.1.39b)$$

Substituting (4.1.34) into (4.1.39) leads to

$$(\Lambda_{11} + 3B_{11}K) d\Delta\epsilon_p + (\Lambda_{12} + 3GB_{12}) d\Delta\epsilon_q = (B_{11}\mathbf{I} + B_{12}\mathbf{n}) : \mathbb{Z} : d\epsilon \quad (4.1.40a)$$

$$(\Lambda_{21} + 3B_{21}K) d\Delta\epsilon_p + (\Lambda_{22} + 3GB_{22}) d\Delta\epsilon_q = ((B_{21}\mathbf{I} + B_{22}\mathbf{n}) : \mathbb{Z} + B_3\mathbf{I}) : d\epsilon \quad (4.1.40b)$$

or

$$A \cdot (d\Delta\epsilon_p \ d\Delta\epsilon_q) \equiv B \quad (4.1.41)$$

Determinant of A is $\Delta = (\Lambda_{11} + 3B_{11}K)(\Lambda_{22} + 3GB_{22}) - (\Lambda_{12} + 3GB_{12})(\Lambda_{21} + 3B_{21}K)$, its inverse is

$$A^{-1} = \frac{1}{\Delta} \begin{pmatrix} (\Lambda_{22} + 3GB_{22}) & -(\Lambda_{12} + 3GB_{12}) \\ -(\Lambda_{21} + 3B_{21}K) & (\Lambda_{11} + 3B_{11}K) \end{pmatrix} \quad (4.1.42)$$

Thus the solution of (4.1.40) reads

$$\begin{aligned} d\Delta\epsilon_p = & \left(\left\{ \frac{1}{\Delta} (\Lambda_{22} + 3GB_{22}) B_{11} - \frac{1}{\Delta} (\Lambda_{12} + 3GB_{12}) B_{21} \right\} \mathbf{I} + \right. \\ & \left. + \left\{ \frac{1}{\Delta} (\Lambda_{22} + 3GB_{22}) B_{12} - \frac{1}{\Delta} (\Lambda_{12} + 3GB_{12}) B_{22} \right\} \mathbf{n} \right. \\ & \left. \right\} : \mathbb{Z} - \frac{1}{\Delta} (\Lambda_{12} + 3GB_{12}) B_3 \mathbf{I} : d\epsilon \end{aligned} \quad (4.1.43a)$$

$$\begin{aligned} d\Delta\epsilon_q = & \left(\left\{ -\frac{1}{\Delta} (\Lambda_{21} + 3B_{21}K) B_{11} + \frac{1}{\Delta} (\Lambda_{11} + 3B_{11}K) B_{21} \right\} \mathbf{I} + \right. \\ & \left. \left\{ -\frac{1}{\Delta} (\Lambda_{21} + 3B_{21}K) B_{12} + \frac{1}{\Delta} (\Lambda_{11} + 3B_{11}K) B_{22} \right\} \mathbf{n} \right. \\ & \left. \right\} : \mathbb{Z} + \frac{1}{\Delta} (\Lambda_{11} + 3KB_{11}) B_3 \mathbf{I} : d\epsilon \end{aligned} \quad (4.1.43b)$$

or introducing parameters C_{ij}

$$d\Delta\epsilon_p = (\{C_{11}\mathbf{I} + C_{12}\mathbf{n}\} : \mathbb{Z} + C_{13}\mathbf{I}) : d\epsilon \quad (4.1.44a)$$

$$d\Delta\epsilon_q = (\{C_{21}\mathbf{I} + C_{22}\mathbf{n}\} : \mathbb{Z} + C_{23}\mathbf{I}) : d\epsilon \quad (4.1.44b)$$

Substitution (4.1.44) to (4.1.34) leads to

$$\begin{aligned} d\sigma = & \mathbb{Z} : d\epsilon - K\mathbf{I}\{(C_{11}\mathbf{I} + C_{12}\mathbf{n}) : \mathbb{Z} + C_{13}\mathbf{I}\} : d\epsilon - \\ & 2G\mathbf{n}\{(C_{21}\mathbf{I} + C_{22}\mathbf{n}) : \mathbb{Z} + C_{23}\mathbf{I}\} : d\epsilon \end{aligned} \quad (4.1.45a)$$

Definition of the algorithmic tangent stiffness can be written in the following way:

$$d\sigma = \mathbb{C}^{alg} : d\epsilon \quad (4.1.46)$$

Therefore from (4.1.45) it follows

$$\mathbb{C}^{alg} = d_0 \mathbb{J} + d_1 \mathbf{II} + d_2 \mathbf{nn} + d_3 \mathbf{In} + d_4 \mathbf{nI} \quad (4.1.47)$$

with

$$d_0 = 2G \frac{q}{q^T} \quad (4.1.48a)$$

$$\begin{aligned} d_1 &= K - \frac{2G}{3} \frac{q}{q^T} - K(3KC_{11} + C_{13}) = \\ &= K - \frac{2G}{3} \frac{q}{q^T} - 3K^2C_{11} - C_{13}K \end{aligned} \quad (4.1.48b)$$

$$d_2 = \frac{4G^2}{q^T} \Delta \epsilon_q - 4G^2 C_{22} \quad (4.1.48c)$$

$$d_3 = -2KC_{12}G \quad (4.1.48d)$$

$$d_4 = -6GC_{21}K - 2GC_{23} \quad (4.1.48e)$$

For the small strain case, C_{13} and C_{23} are zero. If Updated Lagrangian Hencky formulation is considered, obtained tangent matrix relates Kirchoff stress with logarithmic strains (Hencky):

$$\mathbb{C}^{alg} : d\epsilon = d\tau = Jd\sigma + dJ\sigma = J(d\sigma + \sigma \mathbf{I} : d\epsilon) \quad (4.1.49)$$

and therefore

$$d\sigma = \left(\frac{1}{J} \mathbb{C}^{alg} - \sigma \mathbf{I} \right) : d\epsilon = \frac{1}{J} \left(\mathbb{C}^{alg} + p\mathbf{II} - \frac{2}{3}q\mathbf{nI} \right) : d\epsilon \quad (4.1.50)$$

In other words, $d_0 - d_4$ constants read

$$d_0 = 2 \frac{G}{J} \frac{q}{q^T} \quad (4.1.51a)$$

$$\begin{aligned} d_1 &= \frac{1}{J} \left\{ K - \frac{2G}{3} \frac{q}{q^T} - K(3KC_{11} + C_{13}) + p \right\} = \\ &= \frac{1}{J} \left\{ K - \frac{2G}{3} \frac{q}{q^T} - 3K^2C_{11} - C_{13}K + p \right\} \end{aligned} \quad (4.1.51b)$$

$$d_2 = \frac{1}{J} \left\{ \frac{4G^2}{q^T} \Delta \epsilon_q - 4G^2 C_{22} \right\} \quad (4.1.51c)$$

$$d_3 = \frac{1}{J} \{-2KC_{12}G\} \quad (4.1.51d)$$

$$d_4 = \frac{1}{J} \left\{ -6GC_{21}K - 2GC_{23} - \frac{2}{3}q \right\} \quad (4.1.51e)$$

4.2 Large-strain Formulation

4.2.1 Multiplicative Decomposition

In the small strain case considered model represents coupled in series elastic element, viscous and plastic. Evaluation of visco-elastic and plastic strains are not dependent on each other.

Multiplicative decomposition of deformation gradient into visco-elastic and plastic parts reads

$${}^t_0\mathbf{F} = {}^t_\tau\mathbf{F}^{ve} \cdot {}^\tau_0\mathbf{F}^p \quad (4.2.1)$$

From now on, the left-side indexes will be omitted.

$$\det(\mathbf{F}) = \det(\mathbf{F}^{ve}) \det(\mathbf{F}^p) = J^{ve} J^p \quad (4.2.2)$$

Jacobians of visco-elastic and plastic deformations are assumed to be nonnegative and so polar decomposition is possible:

$$\mathbf{F} = \mathbf{R} \cdot \mathbf{U} \quad (4.2.3a)$$

$$\mathbf{F}^{ve} = \mathbf{R}^{ve} \cdot \mathbf{U}^{ve} \quad (4.2.3b)$$

$$\mathbf{F}^p = \mathbf{R}^p \cdot \mathbf{U}^p \quad (4.2.3c)$$

The elastic Hencky right logarithmic measure is

$$\mathbf{H}^{ve} = \ln(\mathbf{U}^{ve}) \quad (4.2.4)$$

$$\mathbf{L} = \dot{\mathbf{F}} \cdot (\mathbf{F}^p)^{-1} = \dot{\mathbf{F}}^{ve} \cdot (\mathbf{F}^{ve})^{-1} + \mathbf{F}^{ve} \cdot \dot{\mathbf{F}}^p \cdot (\mathbf{F}^p)^{-1} \cdot (\mathbf{F}^{ve})^{-1} \equiv \mathbf{L}^{ve} + \mathbf{L}^p \quad (4.2.5)$$

All variables are considered in visco-elastically relaxed intermediate configuration τ . $\boldsymbol{\sigma}$ - Cauchy stress; $\bar{\boldsymbol{\sigma}} = (R^{ve})^T \cdot \boldsymbol{\sigma} \cdot R^{ve}$ - rotated Cauchy stress; $\boldsymbol{\tau} = J \boldsymbol{\sigma}$ - Kirchhoff stress; $\bar{\boldsymbol{\tau}} = J (R^{ve})^T \cdot \boldsymbol{\sigma} \cdot R^{ve}$ - rotated Kirchhoff stress; Rotated Kirchhoff stress and right Hencky strain commute:

$$J^e \boldsymbol{\sigma} : \mathbf{D}^e = \bar{\boldsymbol{\tau}} : \dot{\mathbf{H}} \quad (4.2.6)$$

where $\mathbf{D}^e \equiv \text{sym}(\mathbf{L}^e)$. For visco-elasto-plastic case the following work-conjugate can be proven:

$$J \boldsymbol{\sigma} : \mathbf{D} = \bar{\boldsymbol{\tau}} : \dot{\mathbf{H}}^{ve} + \bar{\boldsymbol{\tau}} : \bar{\mathbf{D}}^p = J \bar{\boldsymbol{\sigma}} : \dot{\mathbf{H}}^{ve} + J \bar{\boldsymbol{\sigma}} : \bar{\mathbf{D}}^p \quad (4.2.7)$$

where $\bar{\mathbf{D}}^p = \text{sym}(\bar{\mathbf{L}}^p)$ with

$$\bar{\mathbf{L}}^p = (\mathbf{F}^{ve})^{-1} \cdot \bar{\mathbf{L}} \cdot \mathbf{F}^{ve} = \dot{\mathbf{F}}^p \cdot (\mathbf{F}^p)^{-1} \quad (4.2.8)$$

The yield condition is written in terms of Cauchy stress

$$f(I_1(\boldsymbol{\sigma}), J_2(\boldsymbol{\sigma})) = 0 \quad (4.2.9)$$

with the associated flow rule

$$\overline{\mathbf{D}}^p = \dot{\lambda} \frac{\partial f(I_1(\overline{\boldsymbol{\tau}}), J_2(\overline{\boldsymbol{\tau}}))}{\partial \overline{\boldsymbol{\tau}}} \quad (4.2.10)$$

The skewsymmetric part of $\overline{\mathbf{L}}^p$ is assumed to be zero:

$$\overline{W}^p = \text{skw}(\overline{\mathbf{L}}^p) = 0 \quad (4.2.11)$$

We notice that

$$I_1(\boldsymbol{\sigma}) = \frac{1}{J} I_1(\overline{\boldsymbol{\tau}}) \quad (4.2.12a)$$

$$J_2(\boldsymbol{\sigma}) = \frac{1}{J^2} J_2(\overline{\boldsymbol{\tau}}) \quad (4.2.12b)$$

Volumetric and deviatoric creep are considered to be expressed in exponential series, which corresponds to Kelvin chain:

$$J^D(t - t_0) = \frac{1}{\mu_0} + \sum_i \frac{1}{D_i^D} \left[1 - \exp\left(-\frac{t - t_0}{\tau_i^D}\right) \right] \quad (4.2.13a)$$

$$J^V(t - t_0) = \frac{1}{k_0} + \sum_i \frac{1}{D_i^V} \left[1 - \exp\left(-\frac{t - t_0}{\tau_i^V}\right) \right] \quad (4.2.13b)$$

Using exponential algorithm, visco-elastic constitutive equations can be written as

$$\Delta \overline{S} = 2\mu^{eff} (\Delta \mathbf{H}' - \Delta \mathbf{H}^{cr'}) \quad (4.2.14a)$$

$$\text{tr}(\Delta \overline{\boldsymbol{\tau}}) = 3 k^{eff} \text{tr}(\Delta \mathbf{H} - \Delta \mathbf{H}^{cr}) \quad (4.2.14b)$$

where \mathbf{H}^{cr} is the accumulated visco-elastic strain due to creep at constant stress, μ^{eff} and k^{eff} are the effective bulk and shear modulus.

4.2.2 Numerical Implementation Details in FEM Software Adina

The trial elastic gradient of place is considered, followed with polar decomposition and calculation of Hencky strain:

$$\mathbf{F}_*^{ve} = {}^{t+\Delta t}\mathbf{F} \cdot ({}^t\mathbf{F}^p)^{-1} \quad (4.2.15a)$$

$$\mathbf{F}_*^{ve} = \mathbf{R}^{ve} \cdot \mathbf{U}_*^{ve} \quad (4.2.15b)$$

$$\mathbf{H}_*^{ve} = \ln(\mathbf{U}_*^{ve}) \quad (4.2.15c)$$

The trial stress is calculated from (4.2.14). If the yield condition (4.2.9) is not satisfied ($f < 0$), then the stress and strains at the end of the current time step equal to trial. Otherwise ($f > 0$), the following system of equation is solved:

$$f\left(\frac{I_1(\bar{\boldsymbol{\tau}})}{J}, \frac{J_2(\bar{\boldsymbol{\tau}})}{J^2}\right) = 0 \quad (4.2.16a)$$

$$\Delta \mathbf{H}^p = \Delta \lambda \frac{\partial f(I_1(\bar{\boldsymbol{\tau}}), J_2(\bar{\boldsymbol{\tau}}))}{\partial \bar{\boldsymbol{\tau}}} \quad (4.2.16b)$$

$$\bar{S}_* - \bar{S} = 2\mu^{eff} \Delta \mathbf{H}^{p'} \quad (4.2.16c)$$

$$tr(\bar{\boldsymbol{\tau}}_* - \bar{\boldsymbol{\tau}}) = 3 k^{eff} tr(\Delta \mathbf{H}^p) \quad (4.2.16d)$$

Once the final stress and strains are obtained, the Cauchy stress is calculated as

$${}^{t+\Delta t}\boldsymbol{\sigma} = ({}^{t+\Delta t}J)^{-1} \mathbf{R}^{ve} \cdot \bar{\boldsymbol{\tau}} \cdot (\mathbf{R}^{ve})^T \quad (4.2.17)$$

Using the condition (4.2.11), the plastic deformation gradient can be integrated from (4.2.8) as

$${}^{t+\Delta t}\mathbf{F}^p = \exp(\Delta \mathbf{H}^p) \cdot {}^t\mathbf{F}^p \quad (4.2.18)$$

All aforementioned holds for an isotropic constitutive equations, in such a case the principal directions of the Cauchy stress coincides with the right principal directions. Another main hypothesis is $skw(\bar{\mathbf{L}}^p) = 0$ from which follows $\dot{\mathbf{H}}^p = \bar{\mathbf{D}}^p$.

This is a general numerical algorithm, which has certain implementation issues in the FEM software Adina. Parts of the algorithm which deal with polar decomposition and calculation of Hencky trial strain and rotation of Kirchoff stress to Cauchy and plastic gradient of place are done outside of the user subroutine and therefore are not available for implementation of the constitutive equations. Only the calculation of trial and final stresses, increments of the inelastic deformation and the tangent matrix are to be programmed in FORTRAN in the user sub-routine. Everything inside the user subroutine is considered to be in the right basis.

Calculation of the plastic deformation gradient is done in the following way:
The user subroutine returns

$$\Delta \mathbf{H}^p = {}^{t+\Delta t} \mathbf{H}^p - {}^t \mathbf{H}^p = \mathbf{H}_*^{ve} - {}^{t+\Delta t} \mathbf{H}^{ve} \quad (4.2.19)$$

Then, outside of the user subroutine ADINA does:

$${}^{t+\Delta t} \mathbf{H}^{ve} = \mathbf{H}_*^{ve} - \Delta \mathbf{H}^p \quad (4.2.20)$$

$${}^{t+\Delta t} \mathbf{U}^{ve} = \exp({}^{t+\Delta t} \mathbf{H}^{ve}) \quad (4.2.21)$$

$${}^{t+\Delta t} \mathbf{F}^{ve} = \mathbf{R}^{ve} \cdot {}^{t+\Delta t} \mathbf{U}^{ve} \quad (4.2.22)$$

$${}^{t+\Delta t} \mathbf{F}^p = {}^{t+\Delta t} \mathbf{F}^{ve-1} \cdot {}^{t+\Delta t} \mathbf{F} \quad (4.2.23)$$

This procedure guarantees

$${}^{t+\Delta t} \mathbf{F} = \mathbf{F}_*^{ve} \cdot {}^t \mathbf{F}^p = {}^{t+\Delta t} \mathbf{F}^{ve} \cdot {}^{t+\Delta t} \mathbf{F}^p \quad (4.2.24)$$

And so the Jacobians are

$$J = J_*^{ve} {}^t J^p = {}^{t+\Delta t} J^{ve} {}^{t+\Delta t} J^p \quad (4.2.25a)$$

$$J_*^{ve} = \prod_i \lambda_i^* = \exp \left(\sum_i \ln(\lambda_i^*) \right) \quad (4.2.25b)$$

$${}^{t+\Delta t} J^{ve} = \prod_i \lambda_i^{ve} = \exp \left(\sum_i \ln(\lambda_i^{ve}) \right) \quad (4.2.25c)$$

where $\ln(\lambda_i^*)$ are the principal values of \mathbf{H}_*^{ve} and $\ln(\lambda_i^{ve})$ are the principal values of ${}^{t+\Delta t} \mathbf{H}^{ve} = \mathbf{H}_*^{ve} - \Delta \mathbf{H}^p$. After the calculation of stresses and plastic deformation, the plastic Jacobian is updated according to

$${}^{t+\Delta t} J^p = \frac{J_*^{ve} {}^t J^p}{{}^{t+\Delta t} J^{ve}} \quad (4.2.26)$$

Since during transformation from Kirchoff stress to Cauchy stress Adina assumes that $J \approx 1$ and so does not divide by Jacobian, obtained Kirchoff stresses should be divided by J at the end of the subroutine in order to obtain the correct Cauchy stress.

Unfortunately ADINA has a bug in (4.2.21) of this algorithm: ADINA assumes that the principal directions of ${}^{t+\Delta t} \mathbf{H}^{ve}$ are the same as the principal directions of \mathbf{H}_*^{ve} , which is not always true.

4.3 Dimensionless Form of Constitutive Equations

From the numerical point of view, it is always preferable to formulate and solve the problem in the dimensionless form, that is the form, where all the constitutes are dimensionless. In that section we will discuss a dimensionless form of (4.1.15) for elliptic yield criteria (2.2.63) resulting from the homogenization of the Drucker-Prager material.

First of all, (2.2.63) can be rewritten in the following form:

$$\frac{A}{c_s^2}p^2 + \frac{B}{c_s}p + \frac{C}{c_s^2}q^2 - 1 = 0 \quad (4.3.1)$$

with

$$A = \frac{\eta - 2\alpha_s^2\mathcal{K}}{\eta^2\mathcal{K}} \quad (4.3.2a)$$

$$B = -\frac{2\alpha_s}{\eta} \quad (4.3.2b)$$

$$C = \frac{1}{3\eta\mathcal{M}} \quad (4.3.2c)$$

Constants A, B, C are dimensionless. The natural choice of the stress dimension in such a case is c_s :

$$\tilde{p} = \frac{p}{c_s} \quad (4.3.3a)$$

$$\tilde{q} = \frac{q}{c_s} \quad (4.3.3b)$$

$$\tilde{p}^T = \frac{p^T}{c_s} \quad (4.3.3c)$$

$$\tilde{q}^T = \frac{q^T}{c_s} \quad (4.3.3d)$$

$$\tilde{K} = \frac{K}{c_s} \quad (4.3.3e)$$

$$\tilde{G} = \frac{G}{c_s} \quad (4.3.3f)$$

Eq. (4.3.1) and (4.1.15) can be rewritten as

$$\tilde{f} = A\tilde{p}^2 + B\tilde{p} + C\tilde{q}^2 - 1 \quad (4.3.4)$$

$$\tilde{p} = \tilde{p}^T + \tilde{K} \Delta\epsilon_p \quad (4.3.5a)$$

$$\tilde{q} = \tilde{q}^T - 3\tilde{G} \Delta\epsilon_q \quad (4.3.5b)$$

$$\Delta\epsilon_p \frac{\partial \tilde{f}}{\partial \tilde{q}} + \Delta\epsilon_q \frac{\partial \tilde{f}}{\partial \tilde{p}} = 0 \quad (4.3.5c)$$

$$\tilde{f}(\tilde{p}/J, \tilde{q}/J) = 0 \quad (4.3.5d)$$

At last, let us note the limit case of (4.3.2) with $\eta \rightarrow 1$:

$$A = -\alpha_s^2 \quad (4.3.6a)$$

$$B = -2\alpha_s \quad (4.3.6b)$$

$$C = \frac{1}{3} \quad (4.3.6c)$$

4.4 Numerical Aspects of the Considered System of Nonlinear Equations

In this section we would like to study in detail system of equation (4.1.15) and its solutions. Homogenization of Drucker-Prager yield surface leads to elliptic, hyperbolic or parabolic cases (2.2.65). We would consider only small deformation, case that is $J \equiv 1$. Writing homogenized parameters in dimensionless form (4.3.2) leads to

$$\begin{aligned} A > 0 & \quad \text{Elliptic Criterion} \\ A = 0 & \quad \text{Limit Parabola} \\ A < 0 & \quad \text{Hyperbolic Criterion} \end{aligned} \tag{4.4.1}$$

whereas other parameters have constant sign: $B < 0$, $C > 0$, $D > 0$.

Derivations of the yield condition (4.1.14) are

$$\frac{\partial f}{\partial p} = 2Ap + B \tag{4.4.2a}$$

$$\frac{\partial f}{\partial q} = 2Cq \tag{4.4.2b}$$

As it will be shown, system of equations (4.1.15) has several solutions, although there is always only one, which is physically correct. Let us start by considering an elliptic case.

4.4.1 Elliptic Case

System of two nonlinear equations (4.3.5) has two unknowns: $\Delta\epsilon_p$ and $\Delta\epsilon_q$. The rationale behind formulation in 2D instead of 1D case with λ as a single unknown parameter is an ability to easily incorporate trapezoidal integration rule [114] and hardening [113] in pressure dependent material models. Yet, in such formulation no constraints are usually considered and thus not physical solution are possible (for example with $q < 0$). Usually, Newton-Raphson method is considered, however we will use more robust “Double Dogleg” method implemented in Minpack Fortran and C++ library[70].

Figure 4.4.1 represents an example, where solution procedure converged to a wrong root, which corresponds to a negative q .

In order to force the solution procedure to converge only to meaningful roots, we propose to incorporate constraints as additional nonlinear equations and solve a nonlinear least-

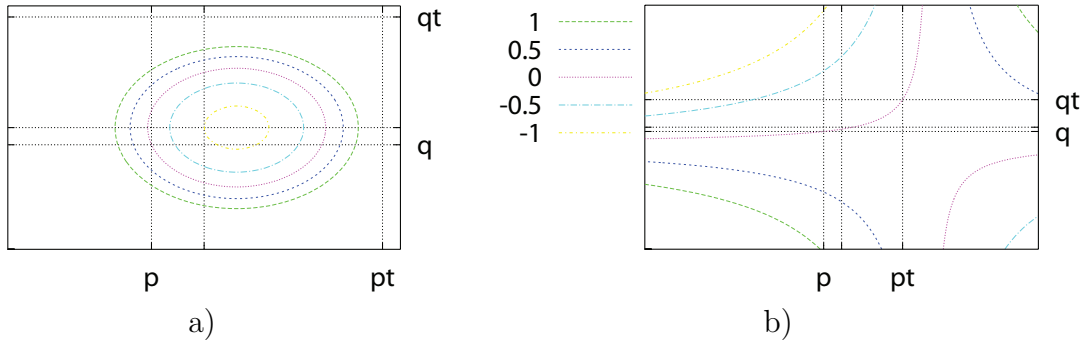


Figure 4.4.1: Isolines of yield equation (4.1.14) (a) and flow equation (4.1.12) (b) with trial and final stress states. Unmarked grid corresponds to zero.

square problem instead. Adding constraint $q > 0$ can be done in the following way:

$$p = p^T + K \Delta\epsilon_p \quad (4.4.3a)$$

$$q = q^T - 3G \Delta\epsilon_q \quad (4.4.3b)$$

$$\Delta\epsilon_p \frac{\partial f}{\partial q} + \Delta\epsilon_q \frac{\partial f}{\partial p} = 0 \quad (4.4.3c)$$

$$f(p, q) = 0 \quad (4.4.3d)$$

$$q - \sqrt{q^2} = 0 \quad (4.4.3e)$$

The least-square problem corresponding to this system of equation can be solved, for example, by a modification of the Levenberg-Marquardt algorithm [70]. The disadvantage is that the derivative of the added equation is not continuous. Yet, in our studies we were able to exclude unphysical roots coming from lack of constraints.

Unfortunately, this is not the only problem arising when solving an elliptic system of equations. Considering perfectly plastic case for elliptic yield surface, where the region of allowed stress states is finite, could lead to $p^T \gg p$ and $q^T \gg q$ and thus $\lambda \gg 1$, $\Delta\epsilon_p \gg 1$, $\Delta\epsilon_q \gg 1$. This has an impact on the solution of the considered system of equation. The system becomes ill-conditioned and flow equation (4.4.3c) cannot be solved with required accuracy (Fig. 4.4.2). The difference between final and trial states easily reaches several orders of magnitude in case of solving a punch indentation problem!

This can be overcome only by formulation in one dimension with λ as a main unknown parameter.

$$p = \frac{p^T - \lambda K B}{1 + \lambda 2 K A} \quad (4.4.4a)$$

$$q = -\frac{q^T}{1 + \lambda 6 G C} \quad (4.4.4b)$$

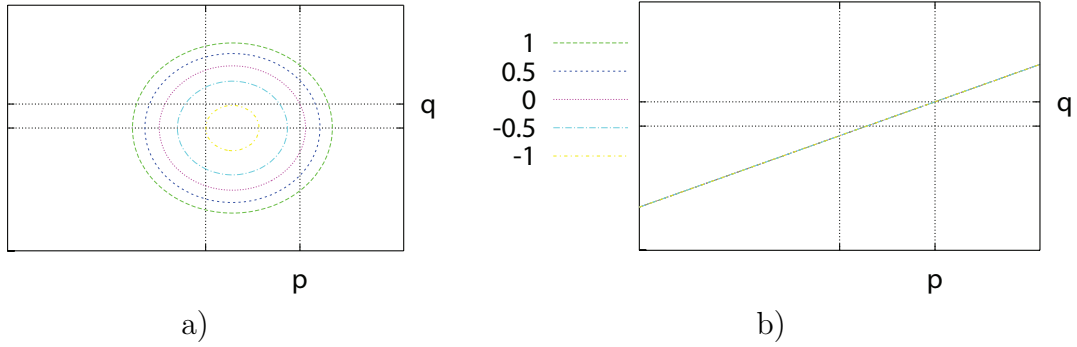


Figure 4.4.2: Isolines of yield equation (4.1.14) (a) and flow equation (4.1.12) (b) with relatively big trial and final stress states. Unmarked grid corresponds to zero.

It is obvious that

$$p(0) = p^T \quad (4.4.5a)$$

$$p(\infty) = -\frac{B}{2A} \quad (4.4.5b)$$

$$q(0) = q^T \quad (4.4.5c)$$

$$q(\infty) = 0 \quad (4.4.5d)$$

The derivatives of both functions have a constant sign:

$$p = -\frac{K(B + p^T 2A)}{(1 + \lambda 2KA)^2} \quad (4.4.6a)$$

$$q = -\frac{6GCq^T}{(1 + \lambda 6GC)^2} \quad (4.4.6b)$$

For the elliptic case ($A > 0$) both $p(\lambda)$ and $q(\lambda)$ are monotonous continuous functions. Intersection of the yield surface with p -axis ($q = 0$) is $q = \frac{-B \pm \sqrt{B^2 + 4AD}}{2A}$ and thus the point $(p, q) = (-\frac{B}{2A}, 0)$ is always inside the yield surface. Therefore, it follows that in the range $\lambda \geq 0$ there is one and only one solution of the considered nonlinear equation. It is worth to note that in the case of infinite trial stress the derivative of the considered function rapidly decreases and is close to zero, thus the bisection method is preferable to Newton-Raphson.

4.4.2 Hyperbolic Case

Now, let us consider the hyperbolic case $A < 0$. One important difference from elliptic case is that $p(\lambda)$ (4.4.4b) is not anymore continuous function in $\lambda \geq 0$ and has a discontinuous

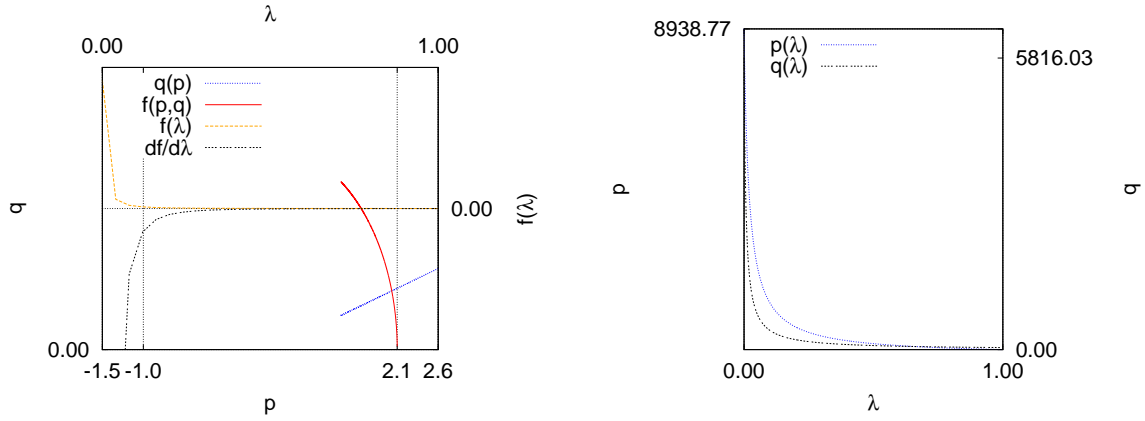


Figure 4.4.3: Case $A > 0$. Left: yield surface $f(p, q)$, parametric line $(p(\lambda), q(\lambda))$, yield surface $f(\lambda)$ and its derivative $df/d\lambda$; Right: Dependence of final stress p, q on λ . Solution corresponds to $\lambda \approx 100$

point

$$\lambda_{inf} \equiv -\frac{1}{2KA} \quad (4.4.7)$$

For $p^T < -\frac{B}{2A}$

$$p \xrightarrow{\lambda - \lambda_{inf} \rightarrow (+0)} \infty \quad (4.4.8)$$

whereas for $p^T > -\frac{B}{2A}$

$$p \xrightarrow{\lambda - \lambda_{inf} \rightarrow (+0)} -\infty \quad (4.4.9)$$

The first case is presented in Fig. 4.4.4. The physically meaningful solution $\lambda_{sol} > \lambda_{inf}$. Yet, the Newton-Raphson method cannot be applied straight away since the derivative of the function changes its sign. In order to overcome this, the solution of $f'(\lambda) = 0$ was obtained as an algebraic approximation using Mathematica software and is provided as a right border of the region, which contains a root. Having at hand the finite region with the monotonous continuous function, both the Newton-Raphson and the bisection methods can be used in order to obtain the solution numerically.

For the second case ($p^T > -\frac{B}{2A}$), $\lambda_{sol} \in [0, \lambda_{inf}]$. The considered nonlinear function is monotonous and continuous and thus the Newton-Raphson or the bisection methods can be applied straight away. Fig. 4.4.5 represents this case.

4.4.3 Consistent Tangent Matrix

Considering the perfectly plastic case for the elliptic yield surface, where the region of allowed stress state is finite, could lead to $p^T \gg p$ and $q^T \gg q$ and thus $\lambda \gg 1$, $\Delta\epsilon_p \gg 1$, $\Delta\epsilon_q \gg 1$. This, in turn, leads to ill conditioned tangent matrix ((4.1.48)) which becomes infinite. Therefore, we will use elastic stiffness matrix only.

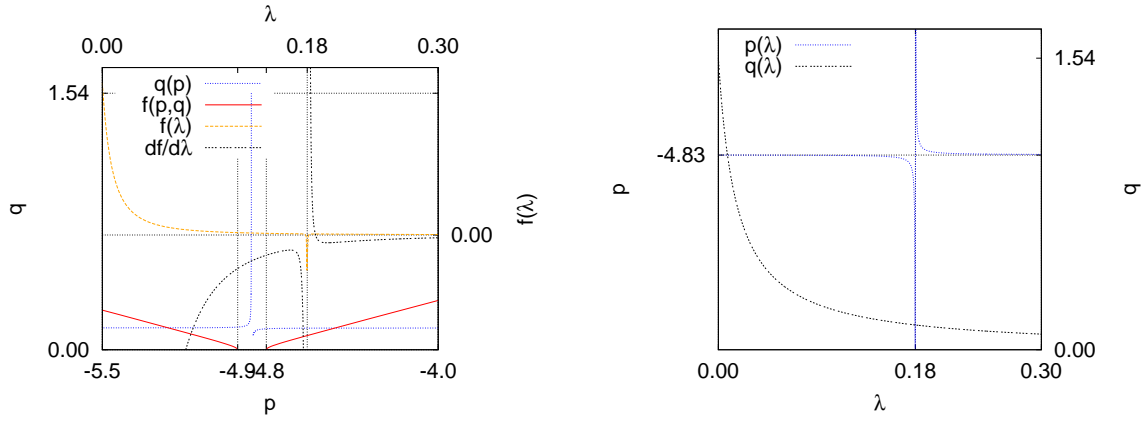


Figure 4.4.4: Case $p^T < -B/2A$. Left: yield surface $f(p, q)$, parametric line $(p(\lambda), q(\lambda))$, yield surface $f(\lambda)$ and its derivative $df/d\lambda$; Right: Dependence of final stress p, q on λ .

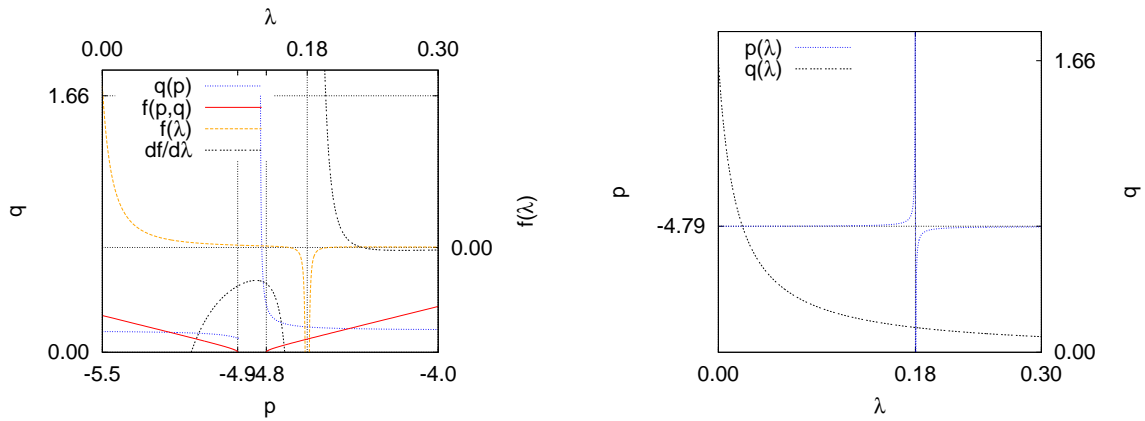


Figure 4.4.5: Case $p^T > -B/2A$. Left: yield surface $f(p, q)$, parametric line $(p(\lambda), q(\lambda))$, yield surface $f(\lambda)$ and its derivation $df/d\lambda$; Right: Dependence of final stress p, q on λ .

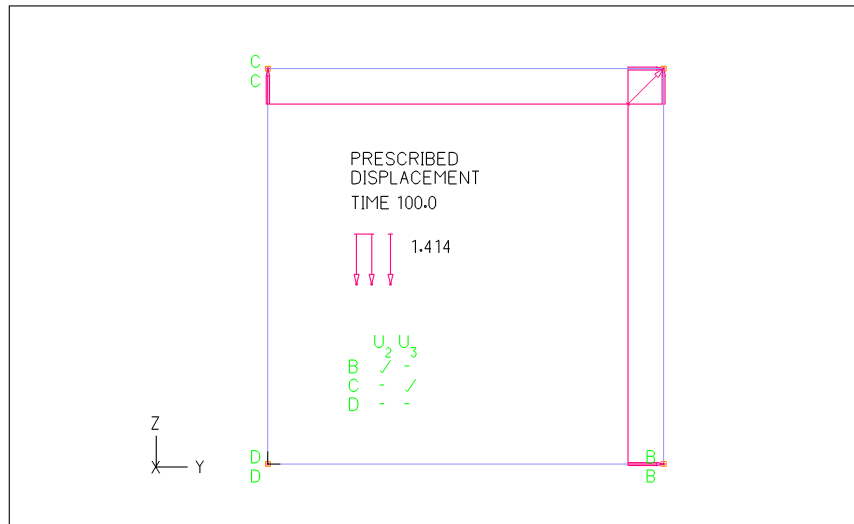


Figure 4.5.3: Plane-strain formulation of the volumetric load in Adina

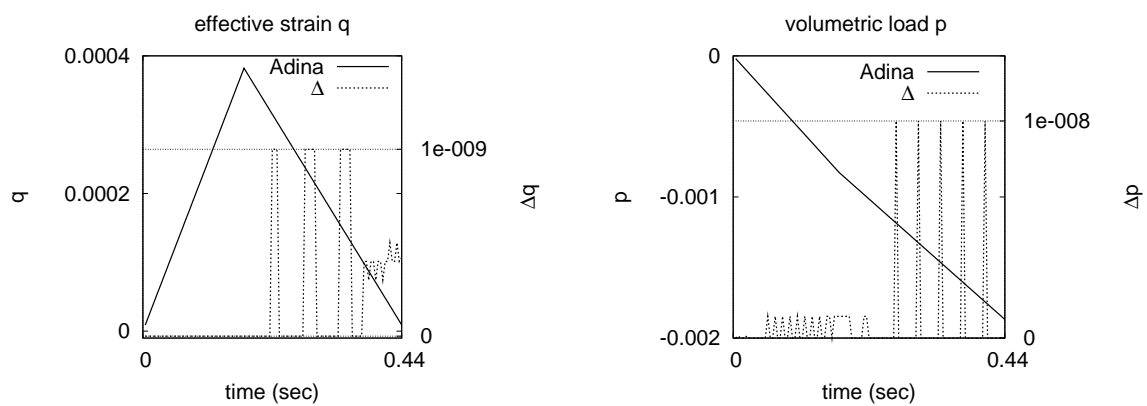


Figure 4.5.4: Comparison of the results in the case of the volumetric load

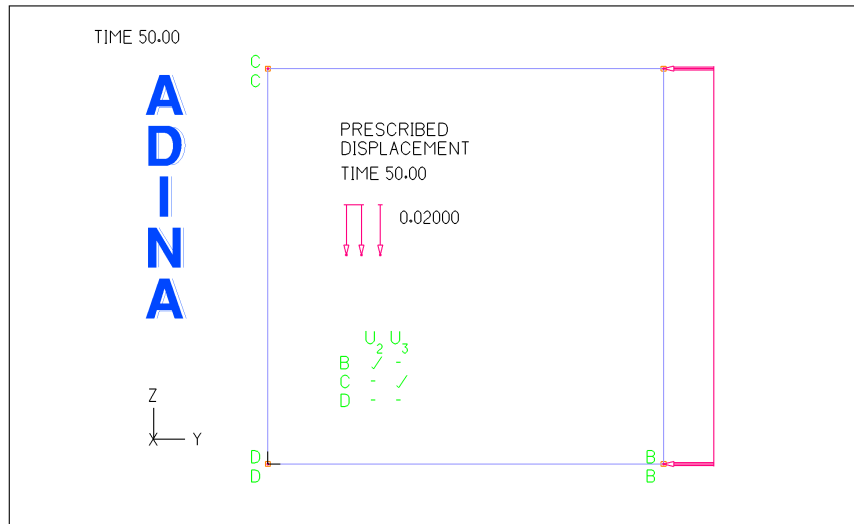


Figure 4.5.5: Plane-strain formulation of the uniaxial load in Adina

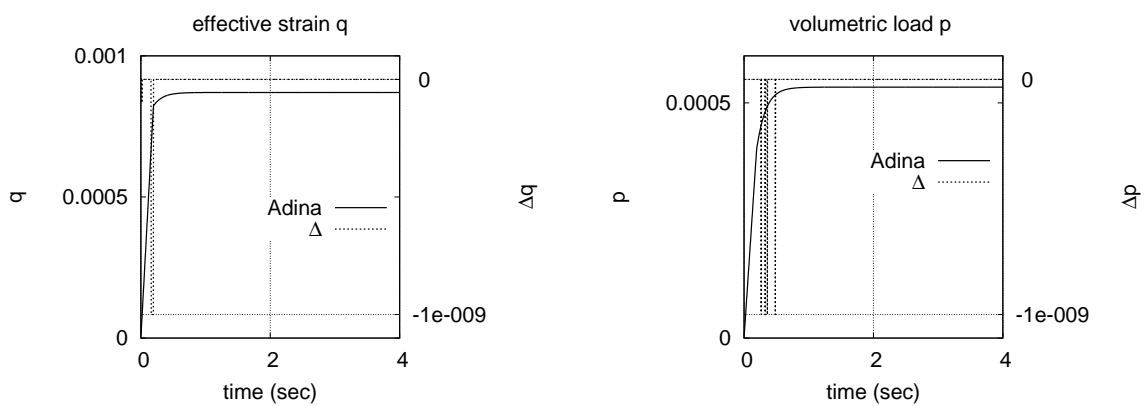


Figure 4.5.6: Comparison of the results in the case of the uniaxial load

4.6 Analysis of NI with Matrix-pore Model

For NI experiment, $50 \times 50 \mu\text{m}$ region meshed with 4 node linear elements was considered. The smallest mesh element size was $50 \times 50 \text{ nm}$ and the coarsest is $1 \times 1 \mu\text{m}$. Mesh refinement was done as shown in Fig. 4.6.1. Small-strain case was considered.

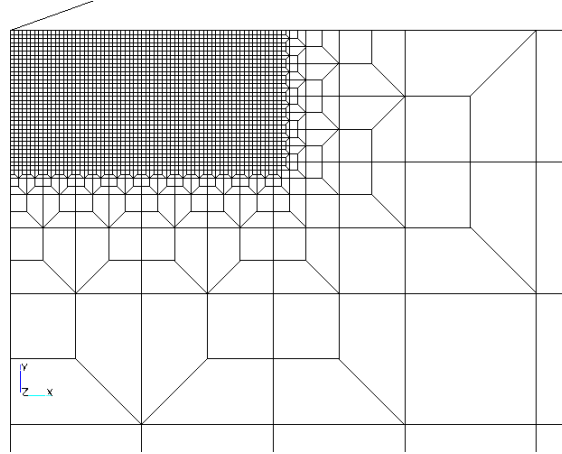


Figure 4.6.1: Part of the mesh, used in FEM study of NI experiment

FEM study of nanoindentation experiment using the proposed [110] matrix-pore elasto-plastic constitutive equations with plastic parameters $c_s = 0.39$, $\alpha_s = 0.207$ and porosity $\varphi = 0.24$ clearly reveals the following effect. During the first few iterations, the elements that are in contact with the tip become perfectly plastic (Fig. 4.6.2), thus the zone with which the tip is in contact allows any (infinite) displacements without transfer of forces to adjacent elements. As a result, it leads to absolute compaction of these elements and negative volume.

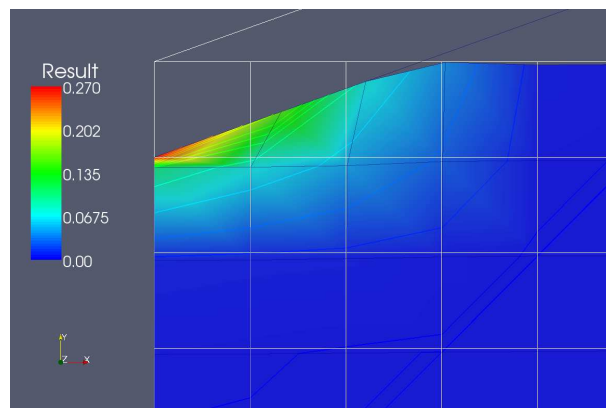


Figure 4.6.2: Maximum principal plastic strain

In order to illustrate this, let us consider one of the simplest elasto-plastic models - $J2$ a.k.a. Von Mises. Elastic properties are chosen as follows: $E = 30 \text{ GPa}$, $\nu =$

0.24. In order to make models equivalent, we will use indentation hardness H - one of the parameters which is available from NI experiments and which mostly reflects plastic properties. Building block intrinsic properties for matrix-pore model were obtained in [110] for values of H about 1 GPa. Assuming $J2$ material, this value can be recalculated dividing by 2.8 [26], thus we end up with the yield limit value of the same range as considered before cohesion c_s . The latter will be used as the yield limit for this illustration purposes. Isotropic hardening with hardening parameter of 10 GPa is considered. All FEM calculations are done in displacement control with 0.5 nm step.

Figure 4.6.3 shows results of indentation of von Mises media with and without hardening. Plotted mesh corresponds to 50 nm penetration depth, whereas typical values of penetration depths in NI of cement paste are hundreds of nm!

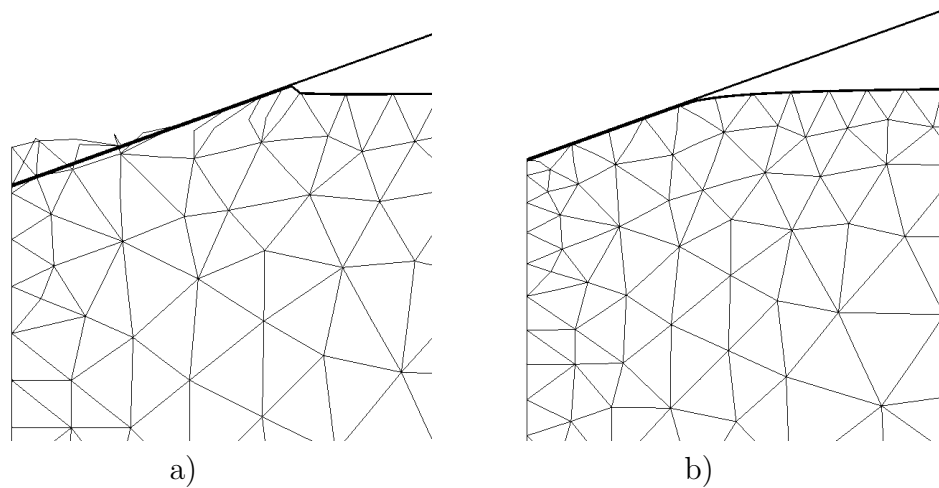


Figure 4.6.3: Mesh after indentation about 50 nm for von Mises model with (b) and without (a) hardening.

4.7 Multicycle Loading and Norton Visco-plastic Model

Up to now we were considering just one loading-holding-unloading cycle. In order to study the behavior of cement paste phases under multiple loading cycles the following experimental and numerical investigation has been done.

Samples of white cement paste (CEM-I 52,5 White, Holcim, SK) with water/cement ratio of 0.5 were prepared and stored in water for 28 days. Before testing, a 4 mm thick slice from the bulk material was cut and polished on coarse to very fine emery papers to achieve a smooth and flat surface. The specimens were washed in an ultrasonic bath to remove dust. The resulting surface roughness, which was verified by atomic force microscopy (AFM), was in the range of several tens of nm.

Indentation was performed with Nanotest (Micro Materials, UK) nanoindenter equipped with Berkowich type indenter. Each indent was performed under force control, with the loading history shown in Fig. 4.7.1. After identifying by ESEM those indents that hit exclusively the hydrated phase, a cluster of P-h curves was obtained. From these curves a typical one was selected for the forthcoming numerical reproduction.

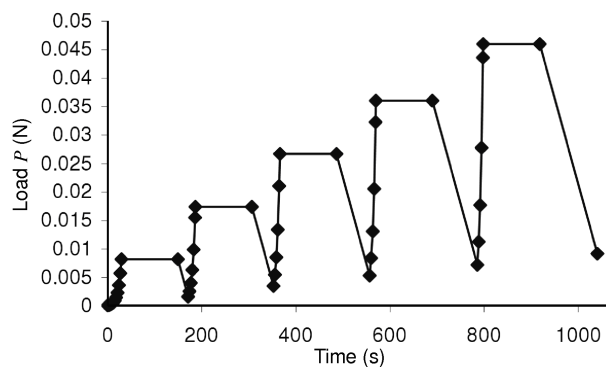


Figure 4.7.1: Nanoindentation loading program

Nanoindentation was modeled as a contact problem of a deformable body (specimen), which was pushed against a rigid conical indenter. Large deformations and large displacements were taken into account. Note that the constitutive relations discussed hereafter were applied to the Cauchy stress and logarithmic strain. The problem was reduced to two dimensions by assuming axial symmetry. Fig. 4.7.2 shows the FE mesh and boundary conditions used. The analyses were carried out with the general-purpose FE program ADINA.

Among other models (see [59] for details), Norton's visco-plastic constitutive law was implemented in Adina, inspired by its usage for description of superplasticity of metals.

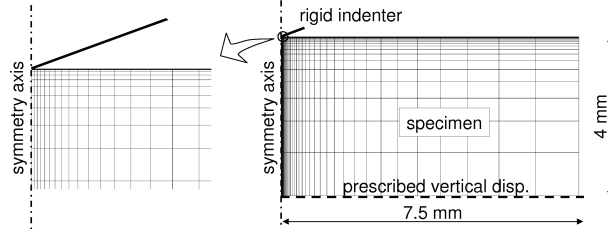


Figure 4.7.2: Axially symmetric FE model of nanoindentation experiment

The stress-strain law is written as:

$$\boldsymbol{\sigma} = D : (\boldsymbol{\epsilon} - \boldsymbol{\epsilon}^{VP}) \quad (4.7.1)$$

where $\boldsymbol{\epsilon}^{VP}$ = viscoplastic strain tensor. The evolution of viscoplastic strain was described by the associated flow rule:

$$\dot{\boldsymbol{\epsilon}}^{VP} = \dot{\lambda} \frac{\partial f}{\partial \boldsymbol{\sigma}} \quad (4.7.2)$$

with the Mises yield function.

For the viscoplastic model, the stress is allowed to be outside the yield surface. The power relation-ship between the norms of the overstress $\boldsymbol{\sigma}^{VP} = \boldsymbol{\sigma} - \bar{\boldsymbol{\sigma}}$ and of the viscoplastic strain rate $\dot{\boldsymbol{\epsilon}}^{VP}$ was prescribed as:

$$\|\boldsymbol{\sigma} - \bar{\boldsymbol{\sigma}}\| = \sigma_Y (t_{ch} \|\dot{\boldsymbol{\epsilon}}^{VP}\|)^m \quad (4.7.3)$$

where $\bar{\boldsymbol{\sigma}}$ = projection of the stress on the yield surface; t_{ch} = characteristic time; m = rate sensitivity parameter. Equation 4.7.3 is known as Norton's power law.

The viscoplastic model differs from the viscoelastic ones by the existence of an elastic domain in which the behavior is elastic and thus time-independent. Creep or relaxation can occur only if the stress level exceeds the yield limit. For simplicity, no plastic hardening was considered; otherwise the number of material parameters to be identified would be too high.

To find the best fit with the current model, a trial and error procedure was utilized. As seen in Fig. 4.7.3, this model could capture the first loading-dwell-unloading cycle. However for the second cycle there was a significant mismatch.

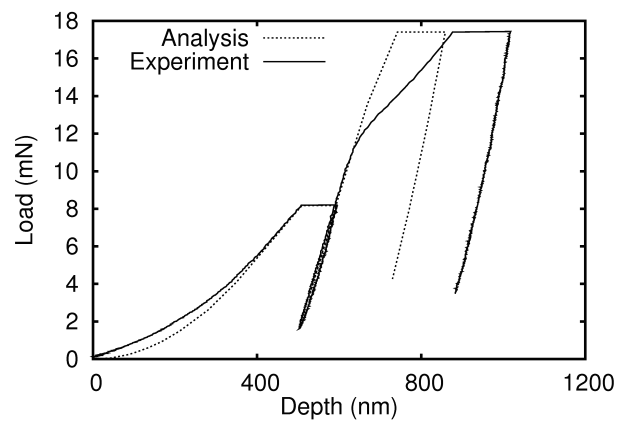


Figure 4.7.3: Response calculated with Norton's viscoplastic model.

4.8 Conclusions

In this chapter we have presented a detailed implementation of the proposed matrix-pore visco-plastic model for small and large strains along with the consistent tangent matrix.

The study of an elliptic-hyperbolic perfectly plastic constitutive equation reveals certain numerical problems while solving the resulting system of nonlinear equations. These problems lead to a false and physically meaningless solution or low accuracy of the solution. Detailed numerical procedure formulated in 1D is proposed for both elliptic and hyperbolic cases, which allows to overcome the problems mentioned above.

FEM study of nanoindentation experiment using proposed [110] matrix-pore elasto-plastic constitutive equations with parameters $c_s = 0.39$, $\alpha_s = 0.207$ and porosity $\varphi=0.24$ clearly reveals the following effect. During the first few iterations, the elements that are in contact with the tip become perfectly plastic, thus the zone with which the tip is in contact allows any (infinite) displacements without transfer of forces to adjacent elements. As a result, it leads to absolute compaction of these elements and negative volume. A similar effect was demonstrated for von Mises elasto-plastic model. Isotropic hardening was shown to help to overcome this issue.

Therefore, it seems that scaling relationships for NI experiments for any model should be obtained using FEM with appropriate loading range, which would correspond to experimentally observed penetration depths. As for parameters of matrix-pore model proposed in [110], it was shown that they do not allow sufficient penetration depths in FE calculations and thus either higher cohesion or hardening should be used.

Study of cement phases behavior under multicycle NI loading poses additional difficulties even in qualitative description of the second loading cycle.

5 Analysis of Nanoindentation Results

5.1 Introduction

In this chapter we will apply nanoindentation technique to studied cement paste materials. The force acting on the indenter is applied as the control variable and the corresponding penetration depth is recorded. Commonly, a trapezoidal loading program with loading, holding and unloading periods is used (Fig. 5.1.1b).

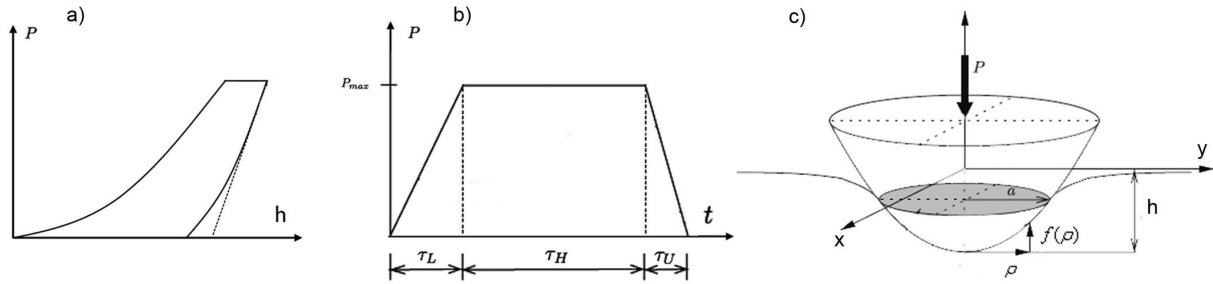


Figure 5.1.1: a) Illustration of the load-penetration curve; b) trapezoidal loading program used in a NI experiment; c) indentation of a substrate by a rigid axisymmetric indenter.

Elastic properties of the substrate can be evaluated from the unloading part of the load-penetration curve (Fig. 5.1.1a) by the standard Oliver-Pharr procedure [77], which is based on the analytical solution of the contact problem for an axisymmetric indenter and a linear elastic isotropic homogeneous infinite half-space [97]. Since the assumption of an infinite half-space is used in the solution, the surface roughness of the sample should be small compared to the penetration depth [60, 68].

The Oliver-Pharr procedure determines the so-called indentation modulus $M = E/(1 - \nu^2)$, related to Young's modulus E and Poisson's ratio ν of the substrate, provided that the indenter is much stiffer than the substrate. It is assumed that the unloading part of the experimental load-penetration curve corresponds to purely elastic response, and the indentation modulus is evaluated as

$$M = \frac{1}{2} \frac{dP}{dh} \frac{\sqrt{\pi}}{\sqrt{A_c}} \quad (5.1.1)$$

where dP/dh is the initial slope of the unloading curve and A_c is the contact area just before unloading. The contact depth can also be obtained as

$$h_c = h_{max} - \epsilon \frac{P_{max}}{dP/dh} \quad (5.1.2)$$

where h_{max} is the maximum penetration depth (at the onset of unloading), P_{max} is the maximum applied load, and $\epsilon \approx 0.75$.

Equations (5.1.1) and (5.1.2) are exact for a conical indenter, but the Berkovich indenter is pyramidal and its real shape slightly deviates from the theoretical perfect geometry. Still, the equations can be used, provided that the dependence of the projected contact area A_c on the indentation depth h is calibrated by indentation of reference samples with known properties, instead of being derived from an assumed perfectly conical shape.

Another parameter, which is commonly calculation from indentation curve is hardness

$$H = \frac{P_{max}}{A_c} \quad (5.1.3)$$

Although the described procedure is based on the assumption of material homogeneity, it has been applied to heterogeneous materials as well, using the so-called “grid” indentation method [28], also called the statistical indentation method (SNI). The idea is to make a large enough number of “random” indents (usually arranged in a regular grid) covering a certain representative area of the sample and then process the results statistically.

A more rigorous approach would be to select the indentation points such that they correspond to a certain phase. This will be called the “manual” indentation technique, because the exact position of the indentation points is to be set “manually” by the operator, and not automatically by the machine. The “manual” indentation technique will be applied here to the calcium-silicate-hydrate gel (C-S-H), and the results will be compared to the statistically processed results of the grid indentation method.

C-S-H, the main phase in the hardened cement paste, is a porous medium [55, 2, 28, 29]. When applying the NI technique, it is important to choose the indentation depths correctly, so that the result is representative of the porous material behavior. If the indents are too small, the response will be affected by surface roughness and will not be representative of the particular phase. If the indents are too big, the results are affected by heterogeneities such as big capillary pores, unhydrated clinkers or other hydration products, and for very large indents will actually yield the average properties of cement paste. The size of a representative volume element (RVE) of C-S-H can be estimated from transmission electron microscope (*TEM*) images (Fig. 5.1.2). The characteristic size of high-density C-S-H (C-S-H_{HD}) building blocks (globules) varies between 3-6 nm, while the diameter of low-density C-S-H (C-S-H_{LD}) fibers reaches 100 nm (Fig. 5.1.2c)! Moreover, the C-S-H_{LD} exhibits high porosity on the sub-micron level. Therefore, indents in the range of 100 – 200 nm are deep enough to capture mechanical behavior of C-S-H_{HD} phase only, whereas C-S-H_{LD} requires much deeper indents (probably around 500 nm). Indentation depths ranging between 100 – 200 nm are usually considered to be representative of both phases [28, 82, 115, 98, 34, 29, 55, 68, 48]. One of the aims of the current

study is to investigate the size effect in NI.

During the SNI analysis, the obtained results are described by a combination of Gaussian distributions with weight factors that are usually considered to be equal to the volume fractions of mechanically different phases. These results can be compared with volume fractions obtained by back-scattered electron (BSE) image analysis and X-ray diffraction (XRD). To the best of the authors' knowledge, such a comparison has never been done for cement paste.

Considering the matrix-pore morphology of C-S-H, scaling relationships were developed in order to link the NI parameters (M, H) with the intrinsic properties of C-S-H building blocks and porosity [110, 21]. This implies the choice of a certain plasticity model for the building blocks. At the end, the least-square fit of experimentally obtained parameters can be constructed. In that formulation, porosity is the only parameter allowed to change for each indent, whereas other properties are constant and attributed to the building blocks. However, the repeatability of such fitting and the influence of the penetration depth have not been studied yet.

In this chapter, the following aspects are covered:

1. The effect of the penetration depth on NI results (RVE for C-S-H phase).
2. The comparison of the well established “grid” indentation technique with the proposed “manual” approach, which allows to access the real properties of a single phase with the minimum possible bias due to the heterogeneous nature of the sample.
3. The comparison of volume fractions obtained from SNI method to BSE and XRD. Given a reliable volume fraction, the estimate of C-S-H elastic properties is studied using the self-consistent (SC) homogenization scheme and results from deep ($\approx 3 \mu\text{m}$) indents.
4. The application of scaling relationships to NI results from different penetration depths and its repeatability.

5.2 Materials and Preparation

For the present study, AALBORG white cement (C_3S 67.3, C_2S 23.3, C_4AF 0.4, C_3A 3.6, C 0.6, gypsum, hemihydrate, anhydrite 4.3, Fe_2O_3 0.3, Na_2O equivalent 0.19) and pure alite cement, both mixed at water-cement ratio $w/c = 0.4$, were used.

All samples were cured for 1 day in room conditions, then demolded and stored in saturated conditions. Before NI, a small, coin-size sample was cut using a diamond saw. After that it was left for about one hour in room conditions and then manually polished

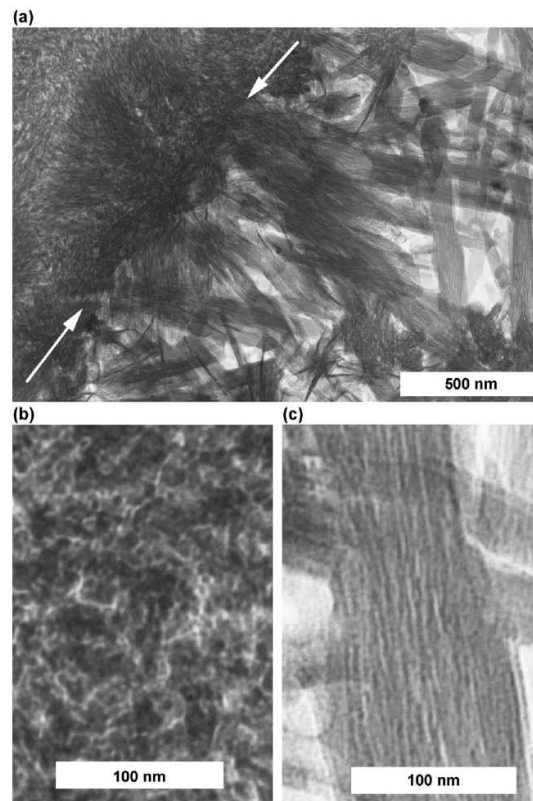


Figure 5.1.2: (a) A transmission electron microscope (TEM) micrograph showing outer C-S-H and inner C-S-H present in a hardened C_3S paste with $w/c = 0.4$ hydrated at 20°C for 8 years. White arrows indicate the boundary between inner C-S-H and outer C-S-H; the inner C-S-H is in the upper left part of the micrograph. (b) An enlargement of a region of inner C-S-H. (c) An enlargement of a fibril of outer C-S-H. (Reprinted with permission from [85]).

using Struers silicon-carbide papers of 100, 2000 and 4000 finesses. Before indentation, the sample was cleaned for 2 minutes in ultrasonic bath. The resulting root-mean-square roughness, measured by Hysitron Nanoindenter on the $60 \mu\text{m}$ area with 1 Hz scanning rate after average plane subtraction, was $30 - 40 \text{ nm}$ for all samples, which is sufficient for 150 nm and deeper indentation [68].

A Berkovich tip was used in all NI experiments reported here. The tip area function was calibrated on a silica sample using the standard procedure [47]. Four grids, each with 10×10 indents (400 indents in total) with $30 \mu\text{m}$ step, were used for each study. The indentation of each grid took about 8 hours. After the processing of each grid, the Hysitron Nanoindenter was recalibrated by “air indents” [47] and the samples were repolished in order to decrease the effect of carbonation. Other important Hysitron NI settings were as follows: Z Piezo analog feedback settle time = 60 s, Z Piezo digital feedback settle time = 45 s, Approach Z piezo attenuation = 90%, Approach integral gain = 240, DriftMonitorTime = 40 s, DriftAnalysisTime = 20 s.

Four loading programs, which all had the same loading/unloading rate and dwelling period but differed by the maximum load, were applied:

1. 1 – 30 – 1 – 1: 1 second of loading up to 1 mN, 30 s of holding constant force, 1 s of unloading;
2. 2 – 30 – 2 – 2: 2 s of loading up to 2 mN, 30 s of holding constant force, 2 s of unloading;
3. 4 – 30 – 4 – 4: 4 s of loading up to 4 mN, 30 s of holding constant force, 4 s of unloading;
4. 5 – 30 – 5 – 5: 5 s of loading up to 5 mN, 30 s of holding constant force, 5 s of unloading.

5.3 Methods

According to the conventional Oliver-Pharr procedure [77], the indentation modulus $M = E/(1 - \nu^2)$ and the hardness $H = P_{max}/A_c$ can be evaluated from the NI curve. Following Vandamme [28], an additional parameter

$$C = \frac{P_{max}}{2a_u x_1} \quad (5.3.1)$$

which characterizes long-term creep, was calculated from the data recorded during the holding period. In (5.3.1), a_u is the radius of contact before unloading and x_1 is a parameter obtained by fitting the evolution of penetration depth during the holding period by

the function $h(t_L + t) - h(t_L) = x_1 \ln(x_2 t + 1) + x_3 t + x_4$. In [28], the purpose of parameter x_3 was to capture the thermal drift of the *CSM* nanoindenter used in that study. The present results have been obtained on the Hysitron machine, which measures the thermal drift before each NI and subtracts its influence from the measured results. Therefore, x_3 can be set to zero.

In total, three parameters (M , H and C) are evaluated from one indent. A statistically representative set of indents can be analyzed assuming that the distribution of each parameter is a combination of several Gaussian distributions, each corresponding to a different phase. The probability density function of several parameters collected in a column matrix \mathbf{x} is thus written as

$$f(\mathbf{x}) = \sum_{j=1}^P \frac{f_j}{(2\pi)^{3/2} |\mathbf{S}_j|^{1/2}} \exp \left(-\frac{1}{2} (\mathbf{x} - \boldsymbol{\mu}_j)^T \cdot \mathbf{S}_j^{-1} \cdot (\mathbf{x} - \boldsymbol{\mu}_j) \right); \quad (5.3.2)$$

where f_j is the volume fraction of phase j , $\boldsymbol{\mu}_j$ are the mean values of the parameters in phase j , and \mathbf{S} is the 3×3 covariance matrix, which was previously considered as diagonal [28]. Inspired by the idea privately communicated by F.-J. Ulm [103], we deal with a general non-diagonal matrix, which means that the variables M , H and C are not considered as statistically independent. This is more realistic, since some correlation among the mechanical properties can certainly be expected.

The Expectation Maximization (EM) algorithm was used to obtain the maximum likelihood estimates of the parameters in a Gaussian mixture model using Matlab. The number of phases (i.e., of Gaussian distributions combined in the mixture) was set to $P = 4$ and kept constant during all estimates for the ease of comparison. The first two phases (with the lowest mean values of indentation modulus and hardness) are assumed to be low- and high-density C-S-H. The third phase corresponds to portlandite (calcium hydroxide, CH), and the fourth phase does not seem to have a direct physical meaning, as will be explained later. After estimation of the parameters, clustering can be performed, and each indent is attributed to one of the phases. An example of Gaussian mixture deconvolution in 3D is presented in Fig. 5.3.1.

In order to obtain more information from the analysis, a matrix-pore morphology of C-S-H is assumed. Recently, several authors have used the matrix-pore morphology of C-S-H either during modeling of NI experiment or for homogenization of elastic properties of cement paste [110, 33, 87, 21]. This is in line with the recent understanding of C-S-H as a porous material [2, 52]. Mathematical output from such studies for the case of plasticity is a hardness scaling relationship, based on a certain hypothesis of C-S-H building block plasticity and morphology and using the Mori-Tanaka or self-consistent methods. For the present study we consider the Drucker-Prager yield condition at the level of C-S-H, with

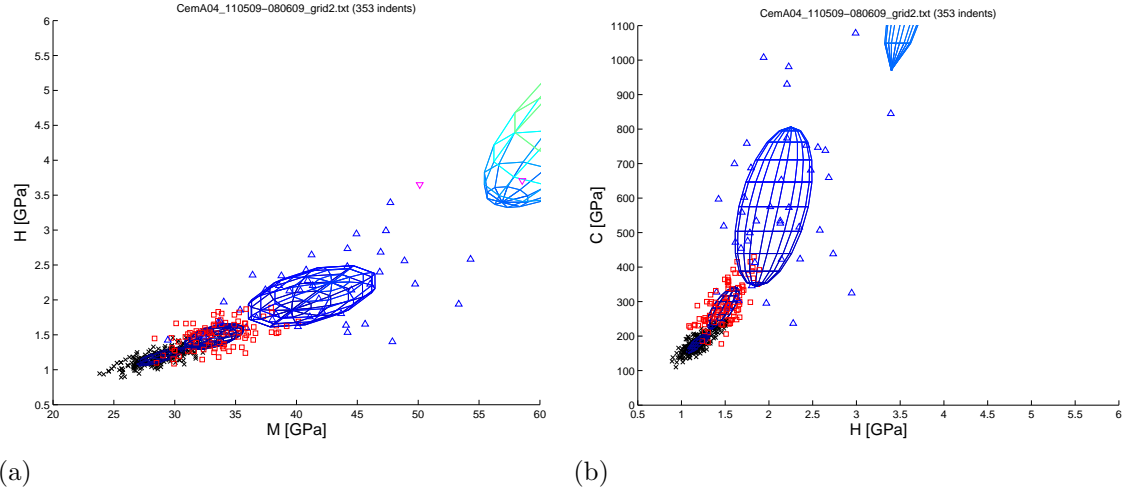


Figure 5.3.1: Example of Gaussian mixture deconvolution of NI data with clustering: a) plane of parameters M and H , b) plane of parameters H and C .

the yield function given by $f^s(\sigma) = \sqrt{J_2} + \alpha_s \sigma_m - c_s$, where σ is the stress tensor, J_2 is its second deviatoric invariant, σ_m is the mean stress (one third of the first stress invariant), and α_s and c_s are material parameters (internal friction coefficient and cohesion). The scaling relationship is based on the self-consistent method, as reported for example in [110] for the indenter tip half-angle 70.3, and is described by the relation

$$\frac{H}{c_s} = \Pi_1(\alpha_s, \phi) + \alpha_s \phi \Pi_2(\alpha_s, \phi); \quad (5.3.3)$$

where ϕ is porosity and Π_i are known functions.

As for elasticity, the conventional self-consistent homogenization of a two-phase material can be applied in order to obtain the homogenized elastic moduli, which can then be transformed into indentation moduli M . In the current study we do not consider any creep scaling relationships. Our final goal in investigating the plasticity scaling relationships is to “fit” the experimentally obtained parameters H and M of C-S-H with the fixed building block elastic (E , ν) and plastic (c_s , α_s) parameters, with porosity as the only parameter having different values for different indents. Low- and high-density C-S-H is assumed to be the first and second phase (with the lowest moduli) in the Gaussian mixture. The elastic properties of C-S-H building blocks are set to $E = 65$ GPa and $\nu = 0.3$, which are the results from atomistic modeling [105]. Therefore, least-square fit of the experimentally obtained indentation moduli M and hardness parameters H can be done using $N + 2$ parameters, namely c_s , α_s , and ϕ_i , $i = 1, \dots, N$, where N is the total number of indents.

5.4 Results and Discussion

5.4.1 Repeatability of SNI and Packing-Density Fit

Before starting the analysis of experimental results, we have to check the repeatability of the considered experimental procedure and evaluation technique. For this purpose, 400 indents in a 20×20 grid with $20 \mu\text{m}$ spacing were performed twice on the same white cement sample at age 28 days under loading program 2-30-2-2. The results are presented in Tab. 5.4.1. The resulting differences between the mean values obtained from the two grids are below 10%.

grid1					grid2				
	M	H	C	f		M	H	C	f
μ_1	30.06	1.25	185.49	0.54	μ_1	28.88	1.19	180.81	0.53
	4.97	0.26	58.94			4.69	0.24	51.12	
S_1	0.26	0.02	3.74		S_1	0.24	0.02	3.29	
	58.94	3.74	1039.11			51.12	3.29	871.51	
μ_2	36.04	1.54	299.09	0.31	μ_2	33.23	1.47	281.48	0.31
	21.66	0.77	231.79			6.28	0.26	84.31	
S_2	0.77	0.05	12.04		S_2	0.26	0.04	8.19	
	231.79	12.04	4996.99			84.31	8.19	3688.76	
μ_3	39.41	2.03	524.89	0.10	μ_3	41.26	2.05	575.33	0.13
	34.78	1.72	744.99			29.64	1.22	382.72	
S_3	1.72	0.20	24.69		S_3	1.22	0.20	45.60	
	744.99	24.69	26938.83			382.72	45.60	53464.55	
μ_4	62.59	4.51	2343.87	0.05	μ_4	65.88	4.94	2571.66	0.04
	245.26	21.81	27590.06			112.03	13.26	14273.20	
S_4	21.81	2.65	3310.56		S_4	13.26	2.61	2458.32	
	27590.06	3310.56	4755069.09			14273.20	2458.32	2551119.05	

Table 5.4.1: Results of SNI analysis of 20×20 indents at $20 \mu\text{m}$ spacing under 2-30-2-2 mN loading performed on white cement at age 28 days.

Assuming that the first two phases should represent C-S-H_{LD} and C-S-H_{HD}, we can determine the porosity ϕ_i for each indent and the plastic parameters c_s and α_s of the building blocks. The resulting plastic parameters are shown in the first two rows of Tab. 5.4.3. There is a large difference between the parameter values obtained on two grids (but the same material), which could be due to the least-square simultaneous fitting.

In [110], the following ranges were reported for different pastes and water/cement ratios: $c_s = 0.39 \pm 27.5\%$, $\alpha_s = 0.207 \pm 68.1\%$. Most of the values found here are outside of this range, and so the determination of the plastic parameters cannot be considered as reliable and repeatable.

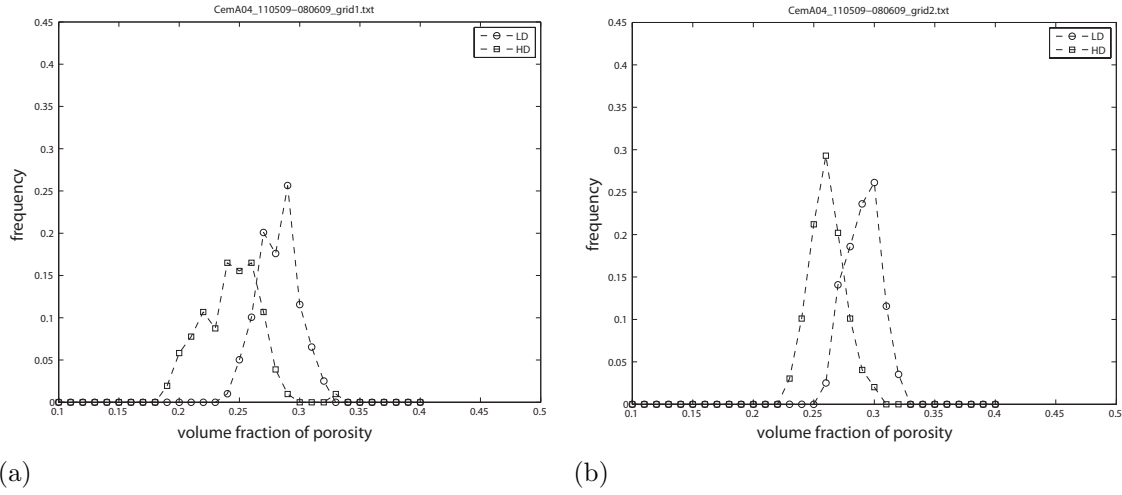


Figure 5.4.1: Porosity obtained from scaling relationship fit for C-S-H_{HD} and C-S-H_{LD} from 400 indents with 2-30-2-2 mN loading.

5.4.2 Comparison of SNI Volume Fractions with Data from BSE and XRD

From the results in Tab. 5.4.1 it is clear that SNI does not capture the properties of unhydrated clinkers, which are known to have elastic moduli around 120 GPa. The fourth phase in our analysis (with mean value of indentation modulus near 64 GPa) corresponds to artifacts of the method and represents indents located either in the vicinity of a grain or probably on its boarder and therefore affected by the soft matrix, which leads to indentation moduli between 50 and 80 GPa. It is also clear that we do not capture any phase corresponding to porosity.

In order to extend this investigation, further comparison can be done with the analysis of Back-Scattered Electron (BSE) images and results of X-Ray diffraction (XRD). XRD results were provided by Vanessa Kocaba (EPFL, Switzerland) in terms of mass fractions and were recalculated into volume fractions based on known densities of individual phases. Since pores cannot be detected by this technique, the volume fractions are considered as the volume of each phase divided by the total volume of the solid material (excluding pores). A BSE image of white cement of size 1250×850 μm with resolution 0.57 pix/ μm was used. The image was segmented into 4 regions according to the gray level: 0-45, 46-95, 96-170 and 170-255, where 0 means black and 255 means white. The regions correspond to porosity, C-S-H, portlandite and unhydrated clinker. The threshold of the last region (clinker) was chosen according to the local minimum in the histogram, whereas the first two were estimated by visual inspection of the image. The results of segmentation and the image histogram are presented in Fig. 5.4.2.

It is clearly seen that the volume fractions obtained by SNI do not agree with those

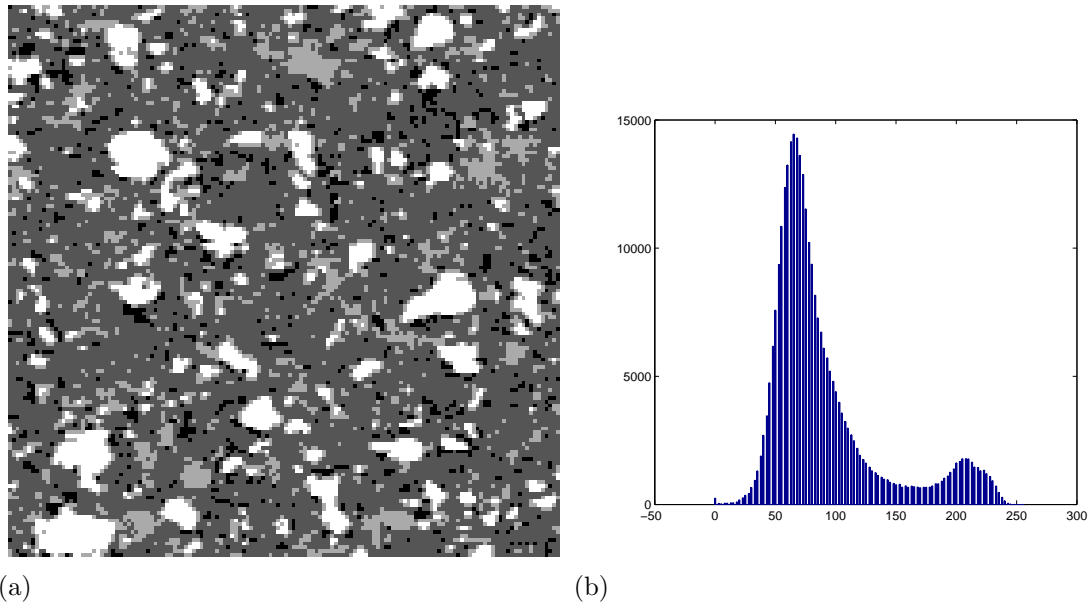


Figure 5.4.2: BSE image analysis: a) $200 \times 200 \mu\text{m}^2$ ($144 \times 144\text{px}$) crop of the $1250 \times 850 \mu\text{m}^2$ image; b) image histogram.

vol %	porosity	C-S-H	CH	clinker
SNI grid1	n.a.	85	10	n.a.
SNI grid2	n.a.	84	13	n.a.
BSE	4	66	18	10
XRD	n.a.	53	21	15

Table 5.4.2: Volume fraction of phases determined by SNI, BSE and XRD on white cement at age 28 days.

obtained by XRD and BSE. We consider XRD results to be the closest to reality. The difference in volume fraction of C-S-H from XRD and BSE is most likely due to the low resolution of the BSE image used. By covering the same area with several pictures, more porosity could be distinguished and therefore less area would be attributed to C-S-H.

Based on this comparison we can conclude that the volume fractions obtained by SNI are not representative of separate phases in cement paste, even though they are repeatable. What is mechanically tested by indentation is most probably an intermixture of hydration product phases, which leads to mechanically different media. Since the modulus of CH is known to be around 40 GPa [99], we can conclude that the third peak indeed represents CH but only partly. The rest is intermixed with C-S-H. This hypothesis is also confirmed by a recent XRD study of nanoindentation points [25].

5.4.3 Choice of Penetration Depth

The mechanical properties obtained from NI experiments might be affected by the penetration depth reached in the tests. Usually, the maximum force is prescribed as a control variable, and the depth depends on the selected load level. Several loading programs with maximum force ranging from 1 to 5 mN were used to study this effect. The resulting penetration depths range from 150 nm to 600 nm. The matrix-pore scaling relationships were applied in all cases to the first two phases, which are supposed to correspond to C-S-H_{LD} and C-S-H_{HD}.

In order to assess the quality of the fit, R-squared correlation is calculated as

$$R^2 = 1 - \frac{\sum_i (y_i - f_i)^2}{\sum_i (y_i - \bar{y})^2}; \quad (5.4.1)$$

where y_i are experimentally obtained values, \bar{y} is their mean value and f_i are associated modeled values. A comparison of the obtained plastic properties of C-S-H building blocks is presented in Tab. 5.4.3.

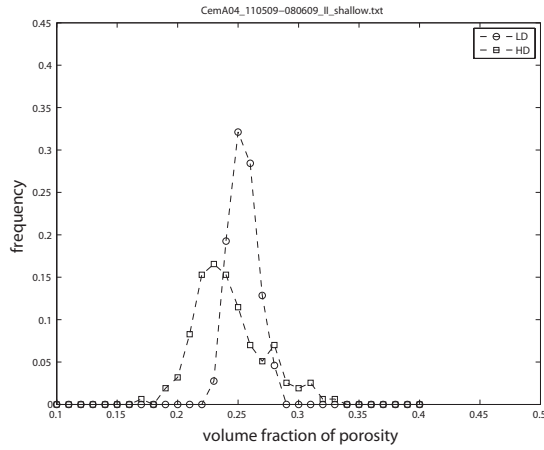
	α_s	c_s	$R^2 (M)$	$R^2 (H)$
2 mN, 20x20 (1)	0.12	0.79	0.88	0.96
2 mN, 20x20 (2)	0.38	0.46	0.82	0.97
1 mN, 4 grids 10x10	0.05	0.90	0.79	0.90
2 mN, 4 grids 10x10	0.09	0.82	0.89	0.95
4 mN, 4 grids 10x10	0.06	0.81	0.89	0.91
5 mN, 4 grids 10x10	0.00	1.07	0.91	0.75

Table 5.4.3: Application of scaling relationships to results of SNI on white cement at age 28 days with different loading programs. $R^2 (M)$ and $R^2 (H)$ are R-squared correlation for indentation moduli and hardness respectively.

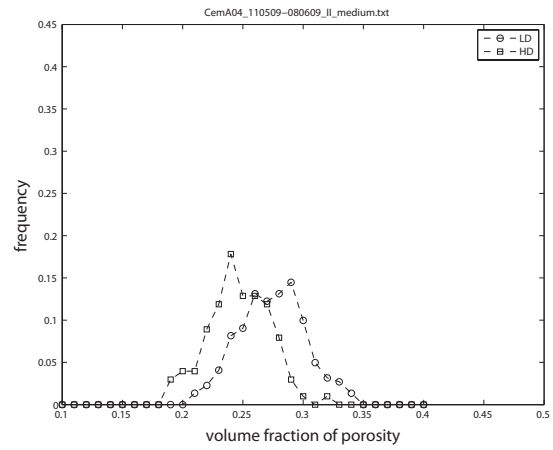
From Fig. 5.4.4 we can see that different penetration depths lead to very different results. This cannot be explained by the surface roughness effect only, since the deviation from an ideal plane (in the root-mean-square sense) is 30 nm in all samples, i.e., small enough to provide unbiased results even at low load levels.

The discrepancies can probably be explained as follows: For deeper indents, the effect of nearby porosity is stronger, which leads to a shift of elastic moduli towards smaller values. The question is, how deep should one indent be, in order to obtain representative properties of C-S-H_{LD}? Loading up to 5 mN is definitely too high since it even shifts the third peak from 40 GPa to 30 GPa and the first two are too close (22 and 24 GPa) to have a distinct physical meaning (Fig. 5.4.4).

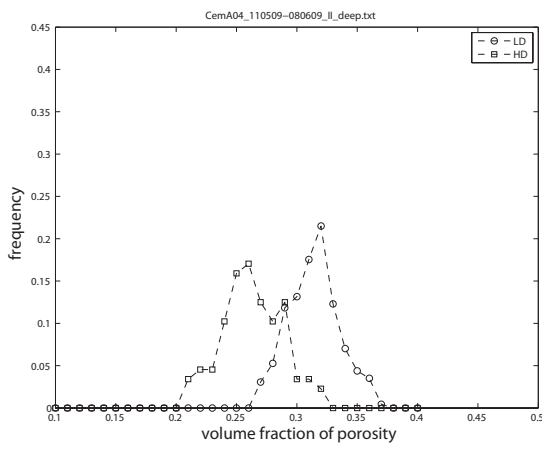
Another possible explanation is the influence of damage. The deeper we indent, the more damage is induced, and therefore the decrease of elastic properties is more pro-



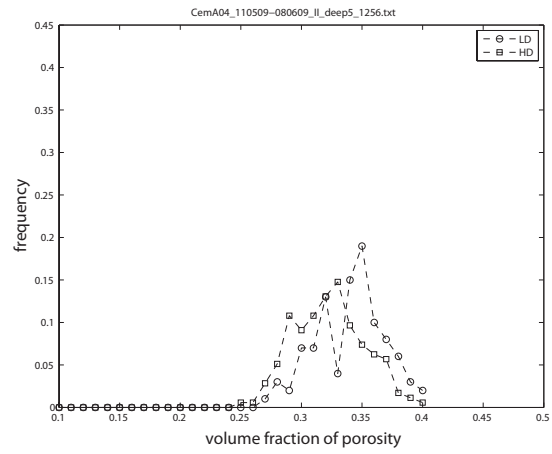
(a)



(b)



(c)



(d)

Figure 5.4.3: Porosity of C-S- H_{HD} and C-S- H_{LD} , obtained with scaling relationships applied to 4 grids, each with 100 indents, at different loading levels: a) 1-30-1-1 mN, b) 2-30-2-2 mN, c) 4-30-4-4 mN, d) 5-30-5-5 mN.

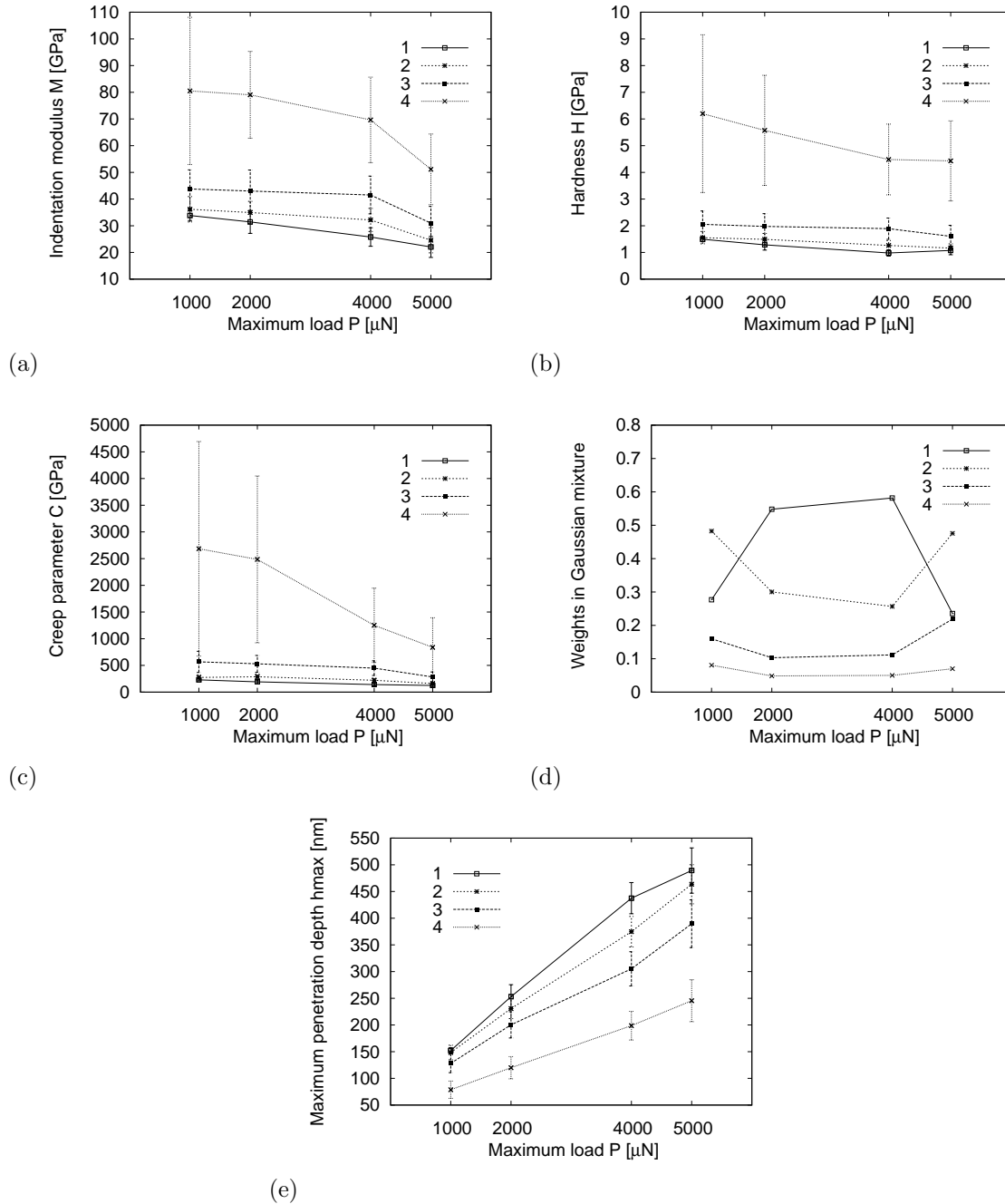


Figure 5.4.4: Results of SNI with four phases depending on maximum load: a) Indentation modulus, b) hardness, c) creep parameter, d) weights in Gaussian mixture model, e) maximum penetration depth.

nounced; see Fig. 5.4.4, 2 and 4 mN loading.

In order to shed some light on this matter, we produced 100 indents into the same paste using the 60-30-60-90 mN loading program, which results in penetration depths about 3 μm and thus represents the homogenized properties of cement paste. We can take three volume fractions from XRD analysis (Tab. 5.4.2) and assume that the rest is attributed to porosity. Then, using typical elastic properties of CH ($E = 38$ GPa and $\nu = 0.305$), clinker ($E = 130$ GPa, $\nu = 0.3$) and porosity ($E = 0$ GPa, $\nu = 0$), we can check the effect of different elastic moduli of C-S-H (keeping its $\nu = 0.24$) on the elastic properties of cement paste using the self-consistent homogenization scheme. This can be compared to the indentation moduli extracted from deep indents (Tab. 5.4.4).

	M	E	ν
SC: 20 GPa	22.37	23.75	0.24
SC: 25 GPa	25.84	27.46	0.24
SC: 30 GPa	29.04	30.88	0.24
NI: P=90 mN, $h \approx 3 \mu\text{m}$	25 ± 5	n.a.	n.a.

Table 5.4.4: Self-consistent homogenization of cement paste elastic properties based on XRD volume fractions compared with results from NI at the level of cement paste.

We can conclude that the mean properties of C-S-H (C-S-H_{LD} and C-S-H_{HD}) should be around 25 GPa. This proves indirectly that the results obtained from the 4-30-4-4 mN loading are the most realistic ones for both C-S-H phases. Yet it has to be stressed that the volume fractions obtained from this loading are different from those obtained from XRD analysis.

5.4.4 “Manual” and “Grid” Indentation Methods

In order to increase the accuracy of the “grid” indentation method, a new “manual” method is proposed. The main idea is to choose preferred indentation points in advance such that NI would “hit” a particular phase and thus increase the accuracy of the obtained results. This approach will be illustrated on the C-S-H_{HD} phase.

Using BSE images, C-S-H_{HD} can be identified as a rim around the unhydrated clinker. Based on a BSE image, several preferable regions were chosen for NI (Fig. 5.4.5). Then these regions were detected in the optics of the Hysitron NI machine. A precise navigation and choice of NI points was done in an atomic force microscope (AFM), which is coupled with NI. Since the output from AFM is a height profile, it is impossible to distinguish between different phases. However, clinkers, which have a much higher elastic modulus, are represented by “elevations” in AFM, and also certain scratches could

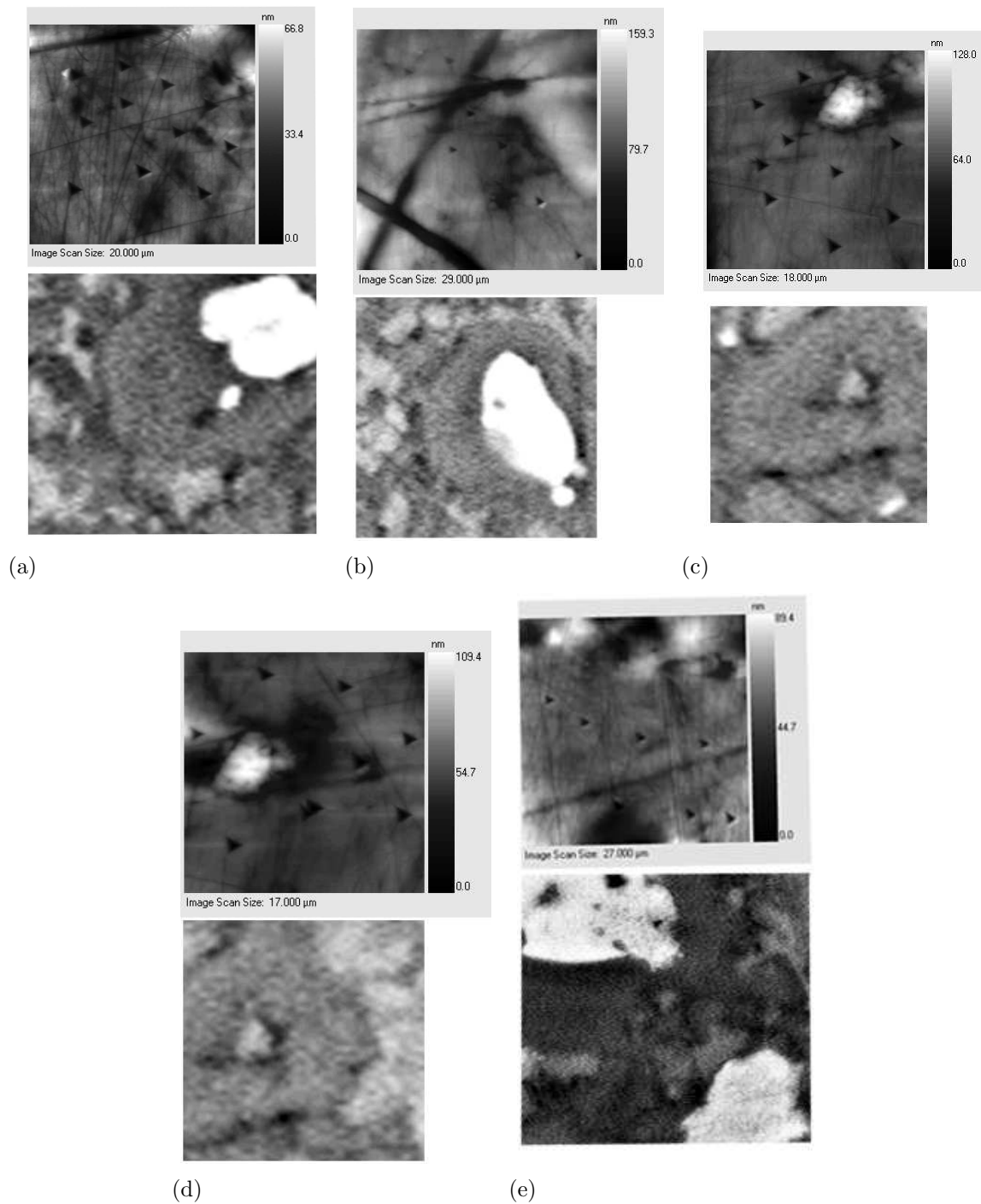


Figure 5.4.5: BSE (bottom) and AFM (top; after indentation; average plane is subtracted) images illustrating the proposed “manual” indentation technique and the choice of NI points for white AALBORG cement paste with $w/c = 0.4$.

be identified. Comparing this information to the BSE image, 5 – 9 points for NI were reasonably prescribed on the area of about $20 - 30 \text{ nm}^2$ (Fig. 5.4.5). Unfortunately, the accuracy of the Hysitron Tribo Indenter on such areas is not sufficient to “hit” exactly the prescribed points (Fig. 5.4.6). Therefore, the area was scanned again after each series and only indents which really went into C-S-H_{HD} were used in the analysis.

The described method was applied to the white *AALBORG* cement paste mixed at $w/c = 0.4$. The total number of indents made by the “manual” method was 63. A filtering procedure reduced the total number of indents to 22. The loading program 10-60-5-1 mN was used, and the resulting penetration depths were $126 \pm 16 \text{ nm}$. Histograms of the indentation modulus M obtained from the “grid” indentation technique and “manual” indentation technique performed on C-S-H_{HD} are compared in Fig. 5.4.7.

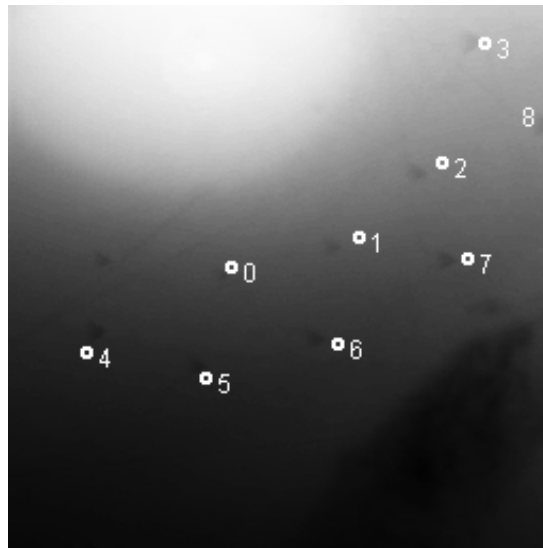


Figure 5.4.6: AFM image with prescribed points for NI in Hysitron software. The scan size is 34 nm.

We can see that even when the indents are precisely pointed into the C-S-H_{HD} phase, the results show a big scatter. A part of the histogram with indentation moduli higher than 60 GPa could be explained by the proximity of the grain, which could happen to be under the indentation point in some cases. In order to account for those indents, it is proposed to apply a second loading cycle and compare the indentation moduli obtained from two unloading curves. The increase of M with the penetration depth can be considered as an indication of a clinker in the vicinity of the indentation point. A considerable decrease can be attributed to big capillary pores nearby.

Using the proposed approach, a sample of alite paste mixed at $w/c = 0.4$ was studied as well. The loading program was 10-100-5-1 mN, the resulting penetration depths were $230 \pm 49 \text{ nm}$. After a filtering procedure, 72 indents into C-S-H_{HD} were used (Fig. 5.4.8).

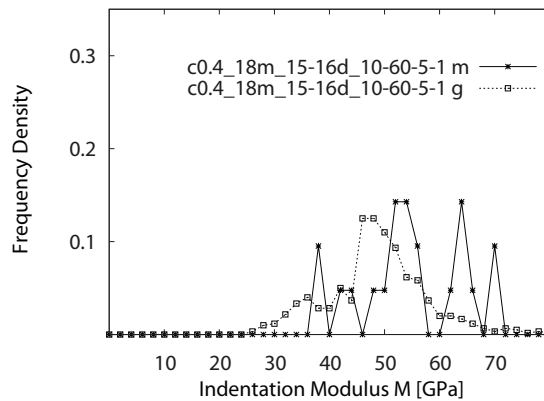


Figure 5.4.7: Comparison of the “grid” (g , 600 random indents) and “manual” (m , 21 indents into C-S-H_{HD}) indentation techniques on a white cement paste sample $w/c = 0.4$, hydrated for 18 months in saturated conditions; the time of exposure to room conditions is around 14 days.

The obtained histogram of indentation modulus is presented in Fig. 5.4.9.

The indentation moduli obtained on alite paste are considerably different from the properties of C-S-H_{HD} obtained on white *AALBORG* cement paste with $w/c = 0.4$ (Fig. 5.4.7). An effect of intermixture of CH and C-S-H manifests itself by a peak in the indentation moduli around 40 GPa (Fig. 5.4.9).

5.4.5 Comparison of the Results Between Prague and Vienna NI Groups

In order to check that experiments have been done properly, with no error in calibration, colleagues at the Technical University of Vienna have been asked to test one of the samples studied here – white cement paste $w/c = 0.4$. After cutting at the age of 2 months, the sample was polished using the procedure described above. Then it was split into two parts, one of which was indented in Prague (5-6 days after cutting) and the other in Vienna (14-15 days after cutting) using practically the same loading programs and number of indents for “grid” NI. Comparing the histogram of indentation moduli (Fig. 5.4.10) we can conclude that both laboratories produce almost the same results, which increases the confidence in the results reported here.

5.5 Conclusion

The following conclusions can be drawn:

1. The agreement between volume fractions obtained by SNI method, BSE image analysis and XRD is poor. Therefore, what is tested by SNI is not only pure phases

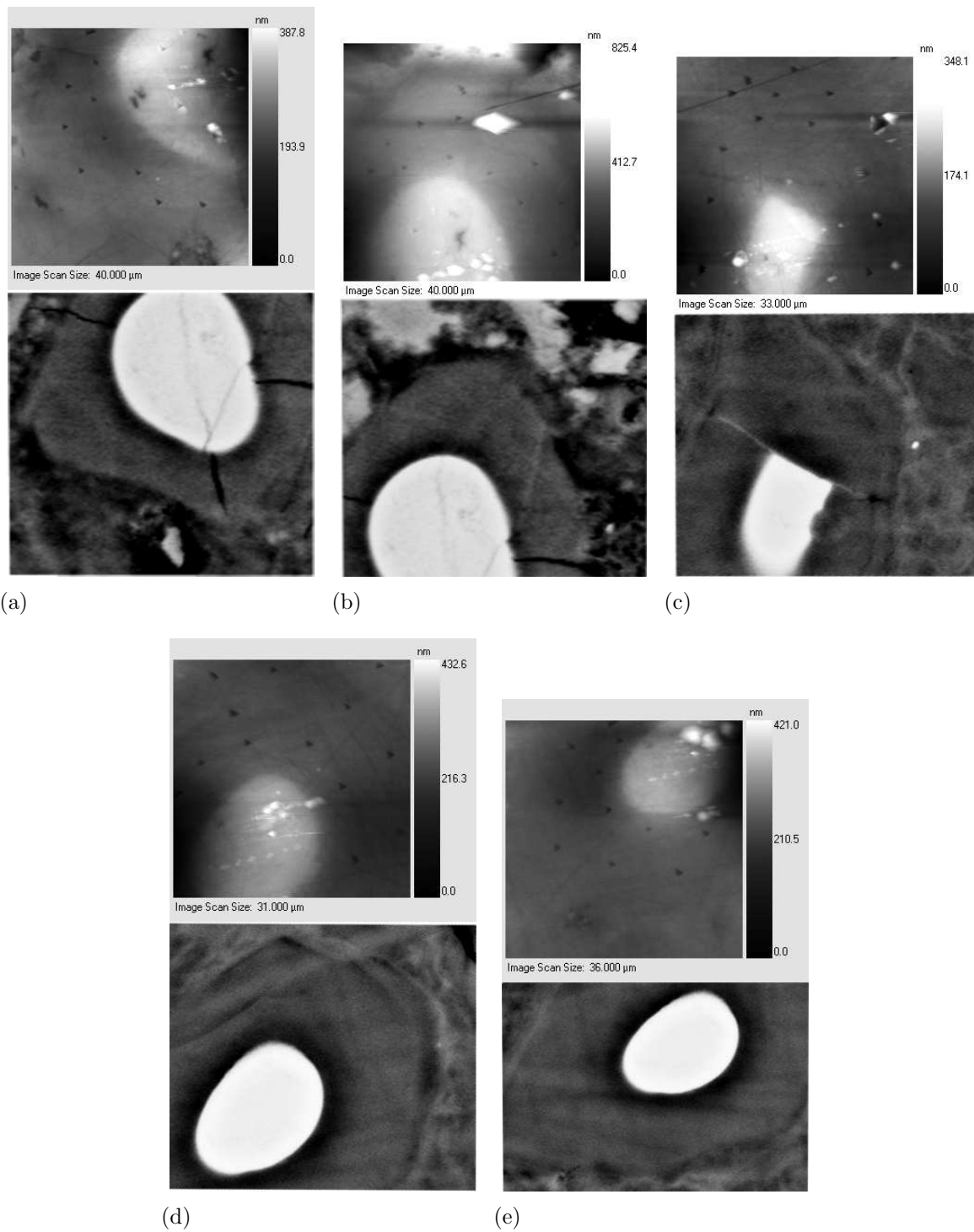


Figure 5.4.8: BSE (bottom) and AFM (top; after indentation; average plane subtracted) images showing the regions selected for C-S-H_{HD} indentation of alite paste.

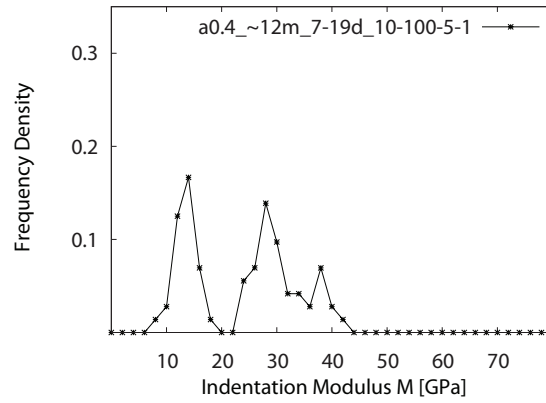


Figure 5.4.9: Indentation moduli histogram for alite sample with $w/c = 0.4$, $h_{max} = 230 \pm 49$ nm (72 indents).

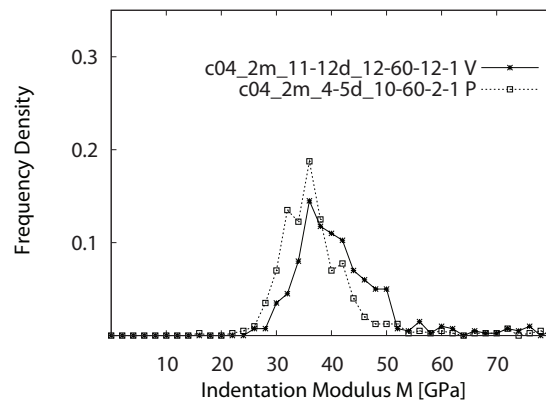


Figure 5.4.10: Comparison of NI results obtained from 400 indents using the “grid” indentation done by the Prague (P) and Vienna (V) groups on the same white cement paste sample, $w/c = 0.4$, age = 2 months.

(like CH with known elastic properties around 40 GPa), but their intermixture, particularly C-S-H and CH. That is why the volume fraction of CH from SNI is less than that obtained from XRD and BSE.

2. The least-square fit of NI results by scaling relationships can have several minima and therefore can result in different C-S-H building block properties even when applied to similar experimental data sets.
3. The manual indentation method clearly shows the complexity of the properties of the C-S-H rim around an unhydrated grain, confirming again the hypothesis of intermixture of C-S-H and CH. In the case of Alite paste, two distinct peaks in the histogram can be attributed to C-S-H_{HD} (around 30 GPa) and a mixture of C-S-H_{HD} and CH (around 40 GPa). Application to cement paste shows a much bigger scatter.
4. An increase of penetration depths leads to a general shift in NI results toward lower elastic moduli. Possible explanations are:
 - The surface roughness is too high for 1 mN indents.
 - There is an effect of damage (2 mN and 4 mN loading).
 - The change of effective media with the increase of indentation depth by increasing the effect of large capillary pores in the vicinity of the indentation point. 500 nm deep indents are shown to lead to a noticeable artificial decrease of the obtained elastic properties, thus indentation results cannot be trusted.
 - Assuming the RVE size of C-S-H_{LD} to be 500 nm, based on a TEM image (Fig. 5.1.2), leads to the necessity of penetration depths bigger than usually used ≈ 200 nm in order to capture the representative properties of C-S-H_{LD}.
5. C-S-H properties obtained by the 4-30-4-4 mN loading are in the best agreement with the estimated mean elastic properties of the C-S-H phase. This estimate is based on the comparison of results from very deep (about 3 μm) indents and the results of SC homogenization of cement paste elastic properties based on XRD volume fractions.

6 Homogenization of Cement Paste Properties

6.1 Introduction

In this chapter we will present results on homogenization of strength properties of cement paste. These results have been obtained in collaboration with Jan Skoček, PhD student at the Danish Technical University, who has been developing particle modeling for cement paste [96], which is compared here with homogenization methods, described in Chapter 2.

In the case of the Ordinary Portland Cement (OPC) paste, a simple relationship linking the strength of the cement paste with its porosity was proposed and widely used [84] for a long time. However, in today's blended cements, systems with higher porosity and at the same time higher strength are often found. Thus, the arrangement of the phases in the RVE plays an important role and the simple relationship cannot be used anymore. It is well understood that the modeling of microstructures of such systems and models linking microstructures with mechanical properties are necessary for the strength prediction.

Several approaches for estimation of the strength of multiphase materials can be found and were discussed in Chapter 2. When the microstructure is relatively simple (such as matrix-pore inclusions in case of, for example, reinforced concrete or poly-crystals in metals), a homogenization based on the definition of Linear Comparison Composite (LCC) [22, 23] or methods based on the second-order moment estimate of stresses and strains in each phase of the heterogeneous material [35, 36] can be used. In both cases, the non-linear constitutive laws of various phases are linearized in such a way that the traditional elastic homogenization schemes can be applied. These approaches are formulated as variational problems which are aimed at finding the dissipation capacity of the heterogeneous material. In other words, the collapse occurs when the limit of the maximum plastic dissipation is reached. The main problem in analytical homogenization methods is that the secant stiffness tensor is not uniform in each phase. It can be approached either by defining a reference state for each phase based on the first- or second-order moment or by introducing the LCC with a-priori unknown properties. The correct capturing of the average strain and stress field per phase is the main problem in mean-field homogenization schemes. The problem becomes even more pronounced for complex microstructures such as the cement paste where stress localization is hard to capture. Still, the formulation with quadratic stress average for von Mises yield condition was successfully applied to cement paste assuming acircular (needle-type) geometry of hydration products [79]. It should be noted that the authors of [79] were not looking for the solution of a variational problem. Based on second-order estimates, the load level at which the yield condition is satisfied at least in one phase was considered as a composite strength estimate. The same results can be achieved by solving the linear elastic problem with *FEM* or *FFT* [71] (Chapter 2)

methods, thus giving physically similar but more precise estimates thanks to considering explicitly the actual microstructure. Nevertheless, Pichler et al. [79] obtained satisfactory agreement between the analytical model prediction and experimental results for the early-age strength evolution of cement pastes mixed at different w/c . However, the deviatoric yield limit of C-S-H was not obtained experimentally (e.g. from nanoindentation) but was fitted, resulting in a value about 20 MPa [79]. Yet, results of nanoindentation clearly show a hardness value of C-S-H in the range 0.5-1.5 GPa [98, 29] which can be recalculated into the yield limit assuming von Mises (J_2) plasticity dividing by 2.8 [26, 110]. This estimate leads to one order of magnitude higher value of J_2 strength than the strength used in [79].

In order to incorporate the information about the real microstructure of cement paste, a discretization of digital images with the variational formulation of the lower bound (statically admissible stress fields) with Drucker-Prager yield criterion was done in [42]. This formulation is similar to the one mentioned above with the difference that an estimation of stress and strain in each phase is not needed thanks to the discretization of the microstructure in a way similar to *FEM* leading, as a result, to a nonlinear programming problem. It is interesting to note, that the cohesion of C-S-H equal to 120 MPa was used [42], which led to a meaningful homogenized strength of about 10-20 MPa and on the other hand agrees with nanoindentation experiments. Therefore, the question of possibility of application of the mean field strength homogenization schemes to the cement paste complex microstructure naturally arises. The answer to this question is one of the aims of this chapter. Let us note that none of the above mentioned method considers interface strength criteria.

All aforementioned methods are based on the yield limit theory and perfect plasticity, approaching the problem from different sides. However, in-situ observations of the crack propagation in the cement paste loaded in compression [69] showed that cracks parallel to the loading direction are formed in the specimen prior the peak load is reached. Therefore, it can be expected that the localized tensile failure of the C-S-H and other phases in the microstructure will be as important as the yielding of the C-S-H. The importance of the localized failure will be even more pronounced in the cement paste subjected to tension. Therefore a particle model similar to the model used for simulations of the fracture process in concrete [30] was modified for the cement paste [96]. Such an approximative model is suitable for handling complex heterogeneous materials and can combine the yielding with the localized failure of the C-S-H with reasonable computational costs.

In this Chapter, the mean-field strength homogenization approach used in [79], approaches based on the solution of linear-elastic problems with *FEM* and *FFT* and a modified particle model [96] based on [30] are utilized to predict the tensile and compres-

sive strength of three cement pastes. Seven different microstructures were considered: the first one was measured [17], and the others are simulated using CemHyd3D [16] hydration model for two different types of cements. Critical aspects of every method are identified, discussed and compared with other methods.

The authors are aware of the existence of more advanced numerical models for strength predictions of heterogeneous materials, see e.g. [42, 79, 83], and of very simplified approaches and strong assumptions used in certain places of this study. However, the main goal was to critically review available approaches considering the same hypothesis, discuss their robustness and efficiency and identify the missing gaps in knowledge necessary for practical application of the approaches. The more advanced models not considered in the comparison share the most important assumptions with approaches studied in this chapter, and the main findings are therefore valid for them as well, as discussed in Conclusions.

6.2 Investigated Materials and Microstructures

Seven different cement microstructures were studied. The first one was an X-ray microtomography image, see [17] for details, of cement paste with W/C of 0.3 made from cement 133 hydrating for 7 days (see [17] for all the details). The cement is labeled as NIST Cem in the sequel. This particular microstructure was chosen due to its longest hydration time which is comparable with other microstructures. Focusing initially on performance at later ages allows us to use simpler models since the effects of the artificial connectivity in the model and related problems with the resolution of the input play significantly smaller role compared to the early-age performance, see [24].

The others microstructures were generated using CemHyd3D [16]. The first generated cement was Aalborg White cement, labeled as Cem A in the sequel, and the second one an OPC labeled as Cem C. Microstructures corresponding to 1, 7 and 28 days of hydration were considered. Composition of the cements can be found in Table 6.2.1. Particle size distribution curves for Cem A and Cem C are plotted in Figure 6.2.1 and the evolution of the heat of hydration for W/C= 0.4 is plotted in Figure 6.2.2.

6.2.1 Material Properties of Cement Phases

In order to avoid any fitting of phase properties, nanoindentation was considered to provide mechanical properties of the main hydration product - C-S-H - in cement paste [29] from which C-S-H_{LD} and C-S-H_{HD} properties can be obtained among others. For the sake of comparison of results obtained from modeled microstructures (Cem A and C mod-

Content [%]	Cem A	Cem C
C ₃ S	67.1	62.3
C ₂ S	23.6	18.4
C ₄ AF	0.00	7.1
C ₃ A	3.5	6.0
C	0.8	0
MgO	0.2	0.7
Sulfate	4.2	5.1
CaCO ₃	0.6	0.5

Table 6.2.1: Chemical composition of the investigated cements measured by Rietveld analysis.

eled in CemHyd3D) with the measured one (NIST Cem), where only three phases were distinguished - porosity, hydrates and unhydrated clinker (separation thresholds were set according to recommendations from [17]), the elastic properties of C-S-H were set to 25.55 GPa in all calculations (average values from [111, 29]) and Poisson's ratio was set to 0.24. In addition, in the case of the modeled microstructures (Cem A and Cem C), the elastic properties of the other phases were used from [111]. The C-S-H was considered to be the only phase allowed to yield/crack. Regarding the strength/yield properties of C-S-H, the only experimentally available strength parameter is hardness $H = P_{max}/A_c$, where P_{max} is the maximum load during the indentation and A_c is the contact area. Using different hypotheses regarding the yield surface of C-S-H, different scaling relationships relating H to the yield surface properties can be obtained. For $J2$ plasticity with $f_{y,J2} \ll E$ (which is the case of cementitious materials) this scaling relationship reads $f_{y,J2} = H/2.8$ [26].

Phase	E [GPa]	ν [-]	$f_{y,J2}$ [GPa]	H [GPa]
Porosity	0.001	0.4999	Inf	Inf
Clinker	135.0	0.3	Inf	Inf
Hydrates	25.5	0.24	0.214	0.6

Table 6.2.2: Assumed material properties of the cement paste phases.

Along with $J2$ plasticity, we use the matrix-pore constitutive equations for C-S-H (2.2.63) presented in Section 2.2.3 and originally developed in [110], which assume Drucker-Prager plasticity at the level of C-S-H building blocks. Such a description was used for both types of C-S-H and also for all hydrates in the case of experimentally obtained microstructure. This choice corresponds to the weakest link and therefore is a safe estimate.

The material properties of the phases are summarized in Table 6.2.2. But since our goal is not the modelling of experimentally observed values, but rather comparison of different approaches, the mechanical properties used here serve as estimates only and their precise values are not important.

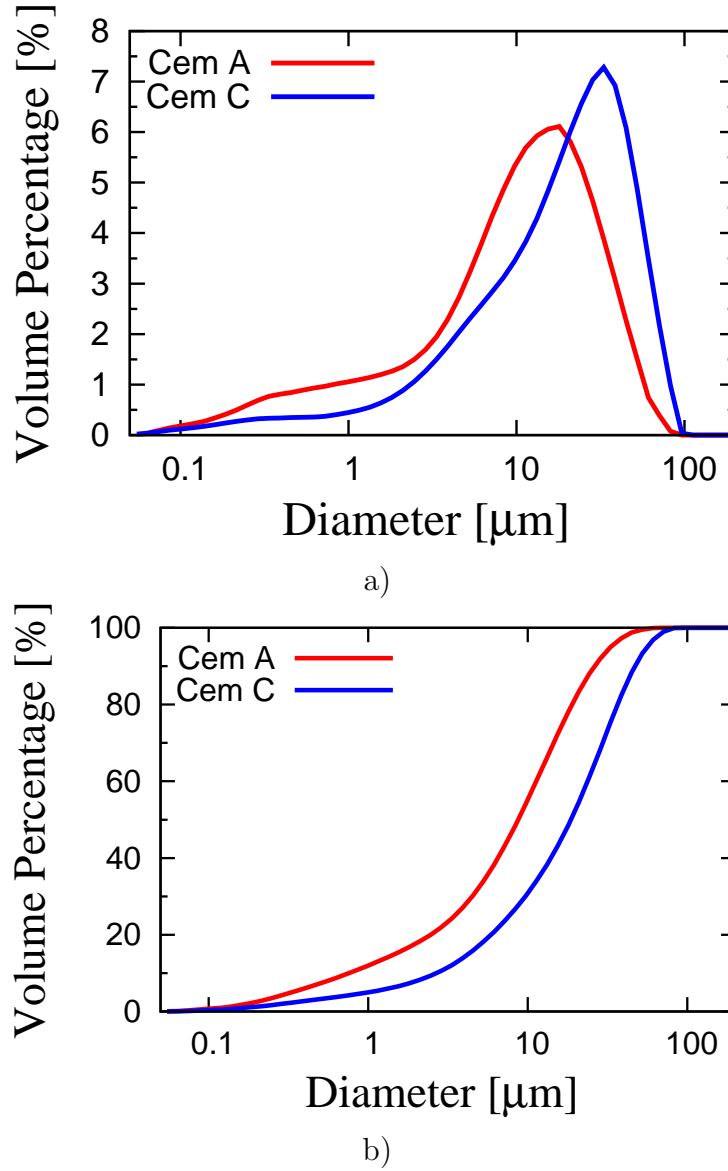


Figure 6.2.1: Particle size distribution curves, a), and cumulative particle size distribution curves, b), for Cem A and Cem C.

6.3 Utilized Methods

Mean field elastic homogenization (Section 2.1) and strength homogenization with the perfectly brittle assumption based on second-order estimates (Section 2.2.2) were used. $J2$ plasticity and constitutive equations based on LCC homogenization method (2.2.63) are considered for C-S-H. Fast Fourier Transform (Section 2.3) along with FEM for solution of linear elastic boundary value problem were used.

The following properties of the C-S-H building block were considered [110]: $\alpha_s = 0.207$, $c_s = 0.392$. The porosity of C-S-H_{LD} was set to 0.31, which together with used values of α_s and c_s yields [110] indentation hardness $H = 0.5945$ GPa, slightly different from $H = 0.60$

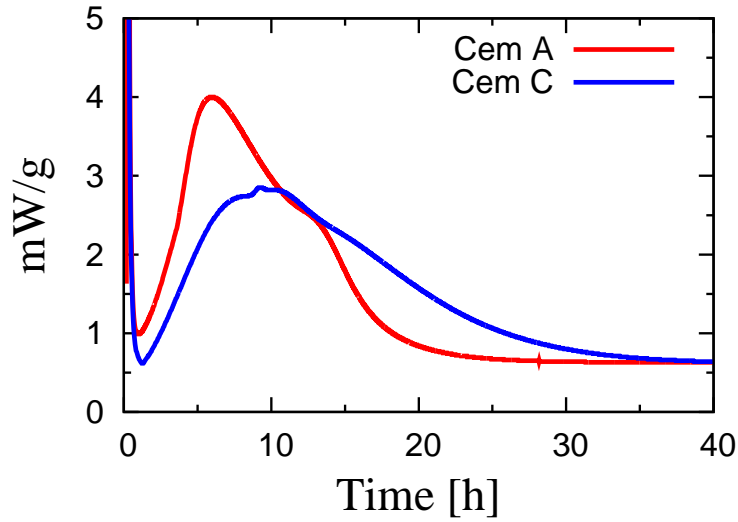


Figure 6.2.2: Calorimetric record of heat of hydration of Cem A and Cem C cement pastes.

GPa considered before for $J2$ plasticity and thus the models are comparable. In [55], C-S-H_{LD} porosity was reported to be 0.36, therefore our choice of this parameter is also meaningful. Homogenized plastic parameters are: $(A^{hom}/c_s)^2 = 1.0113$, $(B^{hom}/c_s)^2 = 0.3144$, $(\Sigma_0^{hom}/c_s) = -0.2799$. A comparison of $J2$ and elliptical yield surfaces is presented in Fig. 6.3.1.

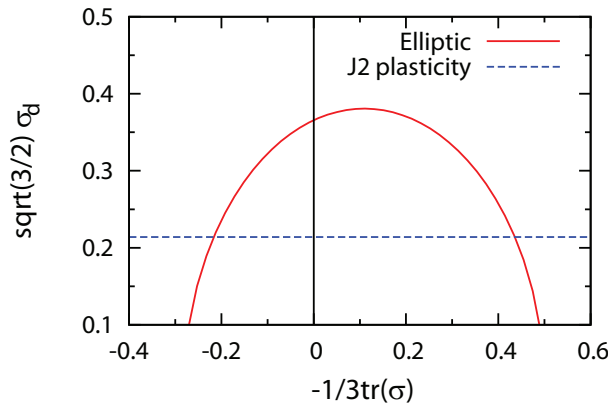


Figure 6.3.1: Comparison of the considered yield surfaces for C-S-H.

6.3.1 Finite Elements Method

The *FEM* was applied in a very straightforward and simple way. The voxel representation of the microstructure obtained from the hydration model or the X-ray photomicrography was directly discretized using 8-node linear brick elements. The model was then loaded with mixed boundary conditions - DOFs in the loaded direction were prescribed on the

two opposite faces (0 at one side and a nonzero displacement on the other size). At one of the corner nodes at the first face, all DOFs were set to zero to avoid a rigid body motion. The remaining DOFs of the model were kept unconstrained.

Three types of analyses were performed: 1) Full nonlinear plastic analysis of the measured microstructure (NIST Cem) with a reduced size computed in Abaqus and used as a benchmark solution for the comparison with the particle model, see Section 6.3.2. 2) Simple linear analysis to find the strength based on the perfectly brittle assumption and second-order estimates (Section 2.2.2) and effective elastic properties of the microstructures with reduced sizes loaded in tension and compression, respectively, used for comparison with *FFT* and with *J2* homogenized yield criterion (2.2.26). 3) Linear computations on the level of individual struts of the particle model, see Section 6.3.2, used to access the elastic and non-elastic properties of the struts.

In all the analyses, material properties from Table 6.2.2 and elastic properties of other phases than C-S-H from [111] were assumed.

6.3.2 Particle Model for Cement Paste

Particle models (PM) for simulation of the fracture propagation in concrete are based on the assumption that all the cracking and possibly other non-linear phenomena take place in the matrix phase, i.e. mortar in the case of concrete, between the particles, i.e. aggregates. This assumption allows significantly simplified formulations of kinematics compared to the classical FEM and volumes with a large number of particles can be modeled with a reasonable computational time and memory requirements. The assumptions made for concrete can be extended to the case of the cement paste since most of the plastic yielding and cracking takes place in hydrates and the unhydrated clinkers can be viewed as aggregates.

Let us summarize the main steps of the particle model used here, which has been developed in [96]. The model of Cusatis [30] was chosen as the base. The unhydrated clinkers were approximated by spherical particles conserving the volumes of clinkers and the positions of centers of gravity. Then the volume was tessellated according to the procedure described in [30, 31, 32].

In contrast to the case of mortar or concrete where the matrix phase can be considered as a homogeneous material, the properties of the matrix phase, or rather of the interparticle volume, differ significantly for individual contacts in the cement paste microstructure. The increased heterogeneity of the material is the result of the hydration which is, in terms of positioning of some hydration products, essentially a random process. Therefore, the simple averaging of the elastic stiffnesses along the struts as well as the concept of one set of material properties used in the case of concrete have to be abandoned and every strut

has to be treated separately.

After the discretization of the microstructure by the struts, the diameters of the particles were set to zero. The entire volume between two nodes was homogenized using the *FFT* and *FEM* for every strut (perfectly brittle behavior was considered in all cases). The SC was not used for the homogenization of the microstructure on the struts level since it assumes the RVE. However, the investigated internodal volumes were too small and heterogeneous to be considered as RVEs. The internodal volume was discretized by voxels aligned with the orientation of the strut. Then the obtained volume was homogenized using the *FFT* or *FEM* and effective Young's modulus, Poisson's ratio, tensile (f_t), shear (f_s) and compressive (f_c) strengths of the internodal volumes were obtained and assigned to the strut discretizing the connection. Since the internodal volume was small (typically ≈ 100 voxels), it was assumed that the perfectly brittle assumption should lead to a reasonable approximation of the yield limit of the strut. In cases where there were not any C-S-H voxels in the internodal volume, struts were assumed to be elastic without any strength limits. The comparison of the homogenization based on the *FEM* and *FFT* is shown in the following Section.

Comparison of *FFT* and *FEM* on the Level of Struts

Figures 6.3.2 and 6.3.4 compare Young's moduli of the struts obtained by the *FFT* and *FEM* for Cem A and Cem C, respectively. Figures 6.3.3 and 6.3.5 present the comparison of the tensile strength of the struts for the same materials. Figure a) corresponds to 1 day of hydration, b) and c) to 7 and 28 days, respectively.

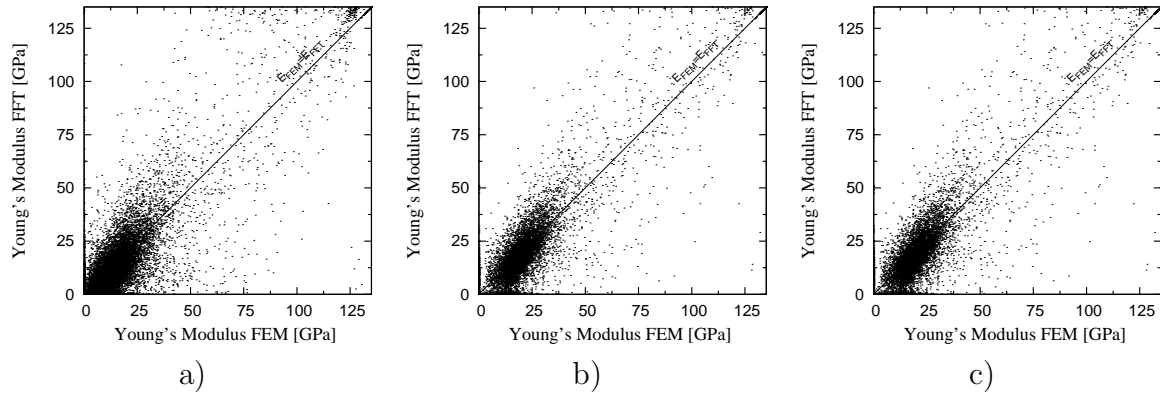


Figure 6.3.2: Comparison of Young's moduli of the struts predicted by the *FFT* and *FEM*, respectively, for Cem A after 1, 7 and 28 days of hydration, respectively.

Figure 6.3.6 compares tensile and compressive strengths of the struts using the yield condition (2.2.63).

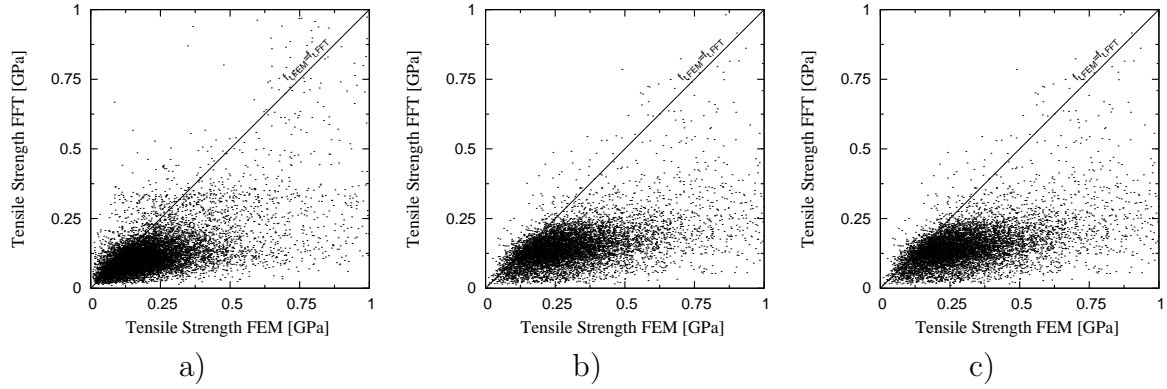


Figure 6.3.3: Comparison of the tensile strengths of the struts predicted by the *FFT* and *FEM*, respectively, for Cem A after 1, 7 and 28 days of hydration, respectively.

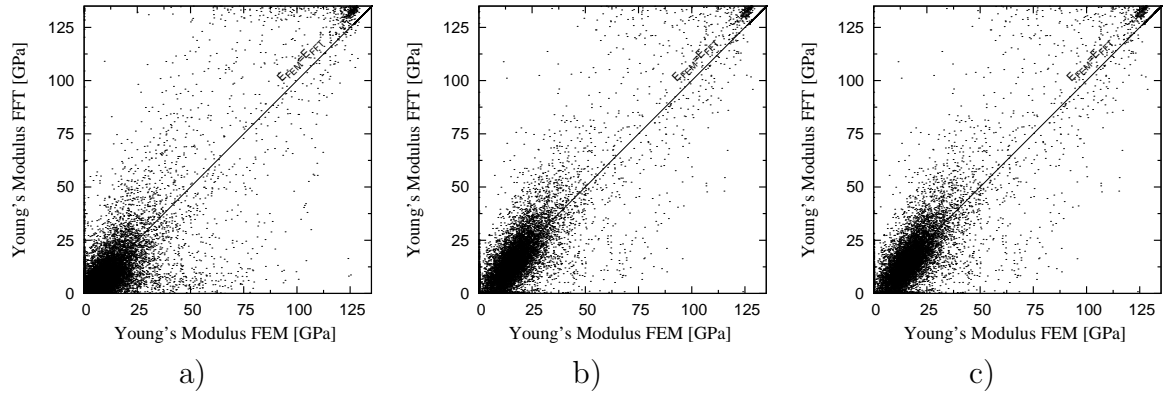


Figure 6.3.4: Comparison of Young's moduli of the struts predicted by the *FFT* and *FEM*, respectively, for Cem C after 1, 7 and 28 days of hydration, respectively.

The elastic properties predicted by *FFT* and *FEM* homogenizations are consistent. However, the strength predicted by the *FFT* homogenization is systematically lower compared to the strength predicted by the *FEM* homogenization. Probably, this is induced by the fact that each strut is an arbitrary microstructure, which is not periodic. Therefore, computed Discrete *FFT* is not equal to *FFT* and thus the whole *FFT* homogenization algorithm converges to slightly biased stress fields. The latter leads to the bias in strength calculation.

The effect of hydration is visible especially comparing plots for 1 day with plots for 28 days. For both cements as well as for both methods, Young's moduli show a shift to larger values and the scatter is smaller due to decreasing volumes of stiff clinker and weak porosity and increasing volume of hydrates. The strength experiences a similar trend that is more pronounced for the *FEM* homogenization because of the aforementioned reasons.

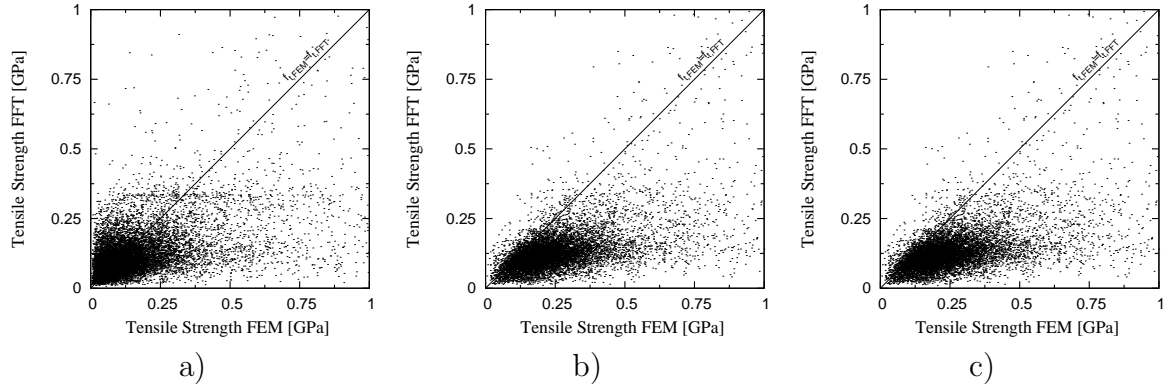


Figure 6.3.5: Comparison of the tensile strengths of the struts predicted by the *FFT* and *FEM*, respectively, for Cem C after 1, 7 and 28 days of hydration, respectively.

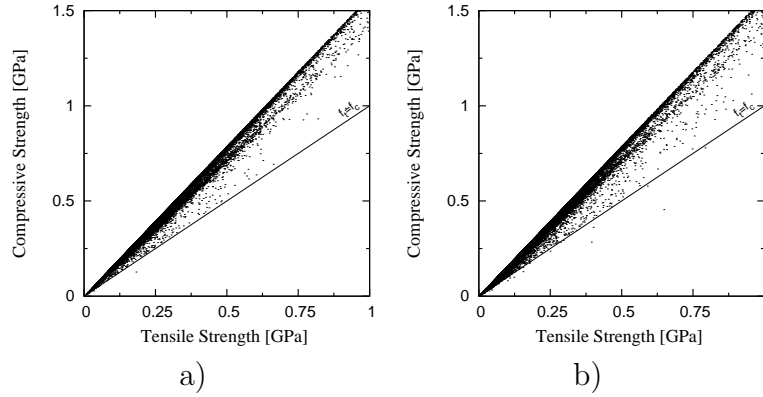


Figure 6.3.6: Comparison of tensile and compressive strengths of the struts for Cem A, a), and Cem C, b), considering the (2.2.63) yield criterion. $f_t = f_c$ for the *J2* plasticity yield criterion.

Figure 6.3.7 demonstrates the differences between the *FEM* and *FFT* on microstructures of NIST Cem with edges of $60 \mu\text{m}$ (red dots) and $150 \mu\text{m}$ (black dots).

Simulation of Global Response

The original particle model proposed in [30] was utilized and modified [96]. The material behaves elastically until the elastic boundary depending on the tensile, shear and compressive strength is reached. Then a nonlinear behavior occurs. In the presented implementation, the response was considered elasto-brittle for $\omega > \omega_0$, see [30] for explanations and Figure 6.3.8 for an illustration, and perfectly plastic otherwise. It means that when the contact was loaded in tension or in mixed-mode with shear and tension, it ruptured in a brittle manner when the elastic boundary was reached. In the case of

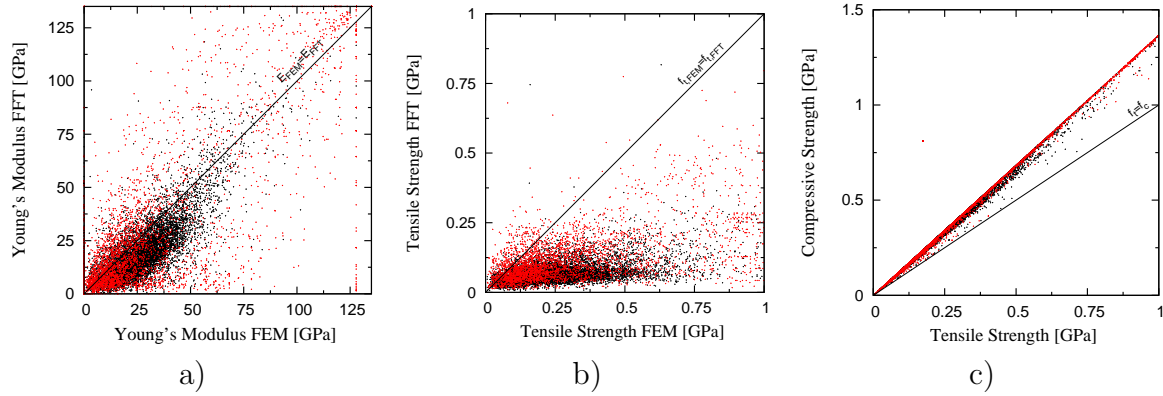


Figure 6.3.7: Comparison of Young's modulus, a), tensile strengths, b), of the struts predicted by the *FFT* and *FEM*, respectively, and comparison of tensile and compressive strengths, c), on microstructures of NIST Cem with edges of $60\ \mu\text{m}$ (red dots) and $150\ \mu\text{m}$ (black dots).

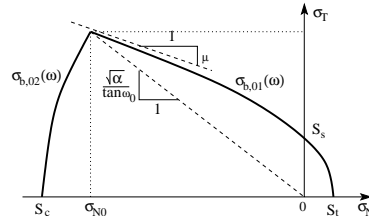


Figure 6.3.8: Material models of the struts: elastic domain. Brittle cracking occur when the domain is reached for $\omega > \omega_0$ and plastic yielding for $\omega < \omega_0$.

mixed-mode compression, the contact yielded.

The particle model with the *FEM*-based homogenization of the internodal volume and yield condition (2.2.63) was used to simulate a uniaxial compression test on cubical microstructures cut from the NIST tomography data with size of edges equal to $60\ \mu\text{m}$ (RVE_{60}). The microstructure was chosen such that it did not contain any large unhydrated grains that would bridge the entire microstructure, see Figure 6.3.9. Two simulations - one considering plastic yielding even for the mixed mode with tension, red line in Figure 6.3.11, and one with the brittle cracking, blue line in Figure 6.3.11 - were done. The microstructure was also modeled using the full non-linear analysis in Abaqus. Material properties from Table 6.2.2 and *J2* plasticity (for C-S-H) were assumed. Figure 6.3.10 shows the distribution of elastic and plastic strains at the last step of the analysis. Simulated stress-strain curves are plotted in Figure 6.3.11. It can be seen that the particle model simulation assuming the yielding of contacts even under tension is, despite its simplicity, roughly comparable to the full non-linear *FEM* analysis in Abaqus. In the later stages, the particle model simulation shows a plastic plateau while the simulation in Abaqus shows a hardening. In the case of the particle model, basically every

strut has a yield limit while in the *FEM* discretization, interconnected blocks of clinker exist due to the coarse discretization assumed. Comparing the responses simulated by the particle model with and without brittle cracking of the contact shows the importance of the tensile cracking even in the compressive test. It is interesting to compare computational times needed: the overall computational time of the particle model was about 10×shorter compared to the full *FEM* analysis. The *FEM*-based homogenization of the internodal volumes was the most time-demanding procedure and was coded without any optimization with respect to the performance. Therefore, it can be expected that the difference could be even bigger.

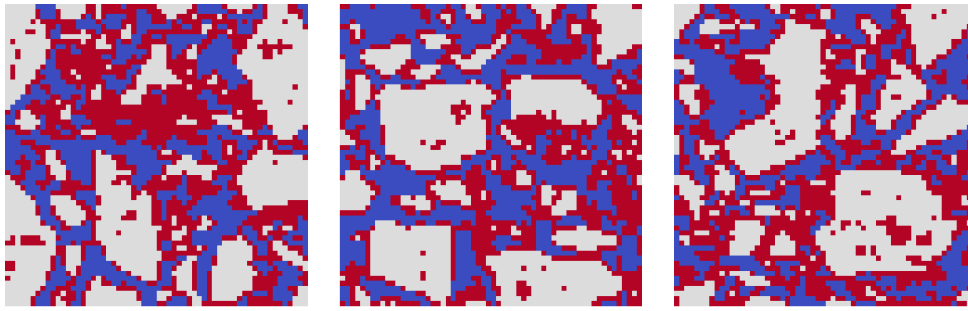


Figure 6.3.9: Microstructure of $60 \times 60 \times 60 \mu\text{m}$ used for initial comparison of the methods - three mutually orthogonal cut planes going through the center of the microstructure.

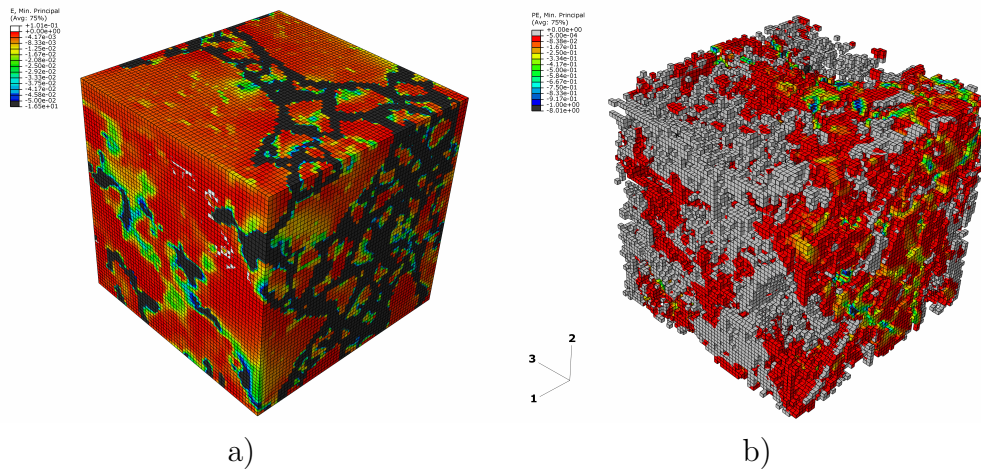


Figure 6.3.10: Elastic strain in all phases, a), and plastic strain in C-S-H after the last step of the full non-linear *FEM* analysis in Abaqus for RVE_{60} . The microstructure was loaded in direction 1.

Further, the particle model with the *FEM*-based homogenization of the internodal volume and the (2.2.63) and J_2 yield conditions was used to study an effect of the size

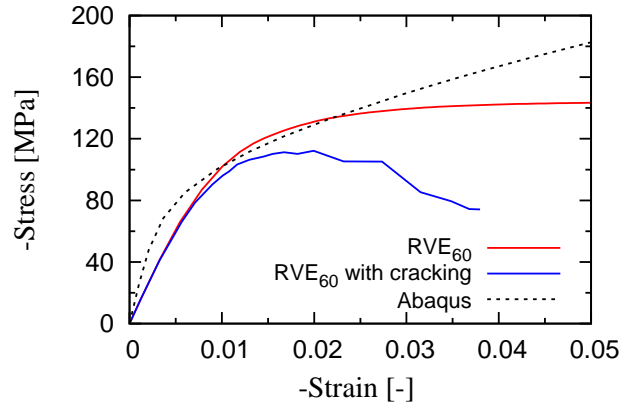


Figure 6.3.11: Comparison of stress-strain curves predicted by the particle model with and without cracking and the stress-strain curve from the full nonlinear *FEM* analysis in Abaqus.

of the microstructure on the stress-strain response in uniaxial compression and tension, respectively. The brittle cracking of contact was considered. Two sizes of the microstructure were considered: the already introduced RVE_{60} and $150 \mu\text{m}$ microstructure, RVE_{150} . Comparison of the stress-strain curves for the two sizes is plotted in Figure 6.3.12a) for uniaxial tension and in Figure 6.3.12b) for uniaxial compression. As expected, the choice of the smaller microstructure such that it did not contain any cement grains larger than $60 \mu\text{m}$ is reflected in the responses by both lower elastic modulus and lower strength compared to the large microstructure where the plastic zone as well as the fracture process zone are larger due to the presence of larger cement grains. The difference can be seen already at the level of individual struts in Figure 6.3.7. Comparing the effect of the $J2$ yield condition and yield condition (2.2.63) on the global response, it can be seen that the responses are qualitatively similar.

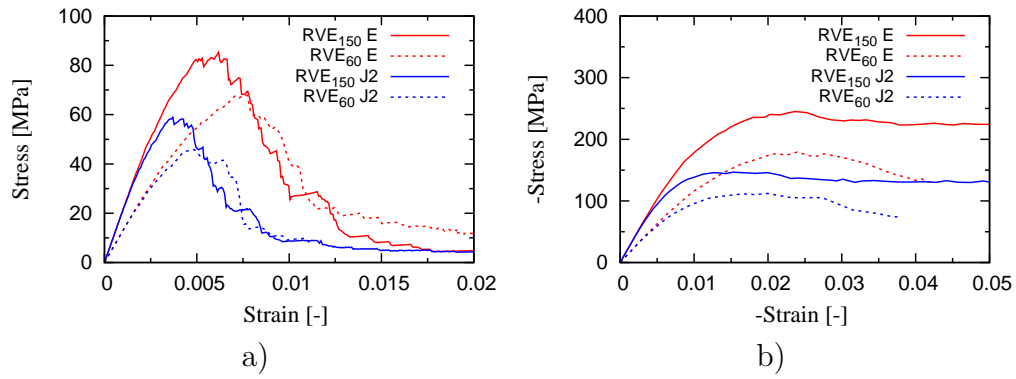


Figure 6.3.12: Simulations of the uniaxial tensile test, a), and the uniaxial compressive test, b), on the NIST cement microstructure of 60 and 150 μm assuming $J2$ and (2.2.63) yield condition, respectively.

6.4 Results and Discussion

6.4.1 Real Microstructure

Initially, all the introduced methods were compared on the example of the small NIST Cem microstructure RVE_{60} . In the case of SC, the $J2$ plasticity was assumed while the other methods also considered yield condition (2.2.63). FEM and FFT were used to find the strength based on the perfectly brittle assumption and second-order estimates. The particle model included the cracking of contact in tension and the strengths correspond to the peak loads in Figure 6.3.12 for RVE_{60} . The results are summarized in Table 6.4.1.

Method	Young's Modulus [GPa]	Compressive Strength [MPa]	Tensile Strength [MPa]
SC_{J2}	23.117	128.721	128.721
FFT_{J2}	17.278	11.591	11.591
FEM_{J2}	19.629	18.244	18.244
$PM - FEM_{J2}$	12.973	112.156	45.828
FFT_E	17.278	28.026	21.818
FEM_E	19.629	31.480	24.003
$PM - FEM_E$	12.973	179.157	67.960
FFT_E^{150}	20.678	54.960	42.571
FFT_{J2}^{150}	20.678	54.736	54.736

Table 6.4.1: Comparison of elastic and inelastic properties of the RVE predicted by the investigated methods.

As can be seen from the Table, the scatter of the predicted elastic and strength properties is large. Young's modulus predicted by the $PM-FEM$ is significantly lower compared to the other methods. This is due to the utilized volume tessellation. The tessellation is based on centers of gravity [30] and cannot simulate the elastic loading exactly, as is the case for models based on Voronoi tessellation [38]. The difference in Young's modulus between FFT and FEM is caused by the different boundary conditions assumed by the methods. The FEM model was loaded by mixed boundary conditions, see Section 6.3.1, while the FFT model was loaded by periodic boundary conditions which should, in general, give the best results [111]. The SC method does not consider the actual arrangement of phases which led to the overestimation of Young's modulus.

Comparison of strength properties is more difficult. FFT and FEM were used to find the strength based on the perfectly brittle assumption. This estimate is far from the maximum capacity of the material (compare values from Table 6.4.1 with full non-linear analysis plotted in Figure 6.3.11). However, the predictions are consistent between FFT and FEM and consistent with Figure 6.3.1. The SC prediction of strength, which is

based on the same brittle assumption, are much higher compared to FFT and FEM calculations with the same $J2$ plasticity. This indeed means that second-order strain rate and stress estimates used in the Effective Strain Rate approach (2.2.21) do not hold for the studied microstructures. Thus, their modification is needed. The Linear Comparison Composite (LCC) method could potentially give better results. See, for example, [65], where comparable results were obtained from FEM and analytical homogenization methods of porous elastomers.

The PM simulation combining the yielding and cracking of C-S-H predicted not only the values of tensile and compressive strength, but provided the entire responses in terms of stress-strain curves, see Figure 6.3.12.

6.4.2 Modeled Microstructure

Discussion at the end of Section 6.3.2 about the influence of the size of the microstructure modeled clearly showed that the $60\ \mu\text{m}$ microstructure is not representative. However, modeling of a larger microstructure with the edge of $150\ \mu\text{m}$ using the FEM would be very time consuming or even impossible due to insufficient memory of the machine used. Therefore only PM and FFT were used for the prediction. The numerically predicted microstructures of Cem A and Cem C at three different times - after 1, 7 and 28 days of hydration - were studied. The goal of this study was to investigate whether the approximate particle model can model the difference between the two cements observed experimentally [] and whether the evolution of the strength properties with the evolving hydration can be captured. PM with yield condition (2.2.63) and brittle cracking in tension was used. For FFT both $J2$ and elliptic yield surfaces were considered.

Figure 6.4.1 shows simulations of uniaxial tension, a), and uniaxial compression, b), for Cem A and different times of hydration. Figure 6.4.2 shows the same for Cem C.

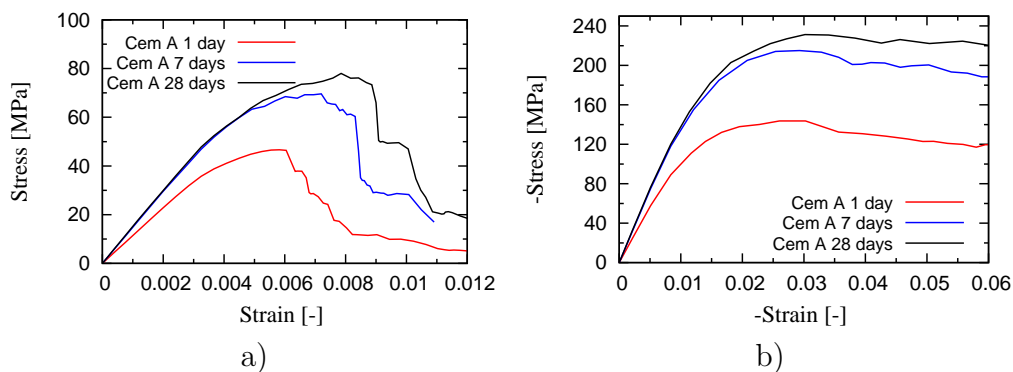


Figure 6.4.1: Simulations of the uniaxial tensile test, a), and the uniaxial compressive test, b), on Cem A microstructures.

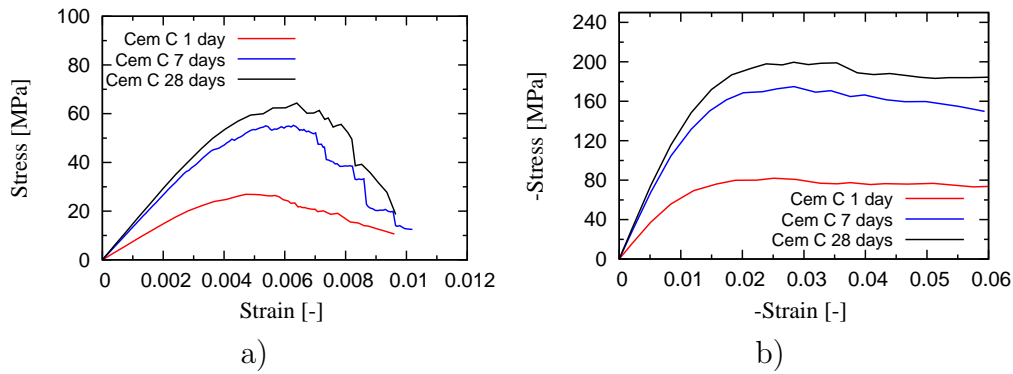


Figure 6.4.2: Simulations of the uniaxial tensile test, a), and the uniaxial compressive test, b), on Cem C microstructures.

Tensile and compressive strength in the case of the particle model were obtained as a maximum load in stress-strain curves (Figures 6.4.2 and 6.4.1). Comparison of these results with those obtained from *FFT* method assuming brittle material are presented in Figures 6.4.3 and 6.4.4.

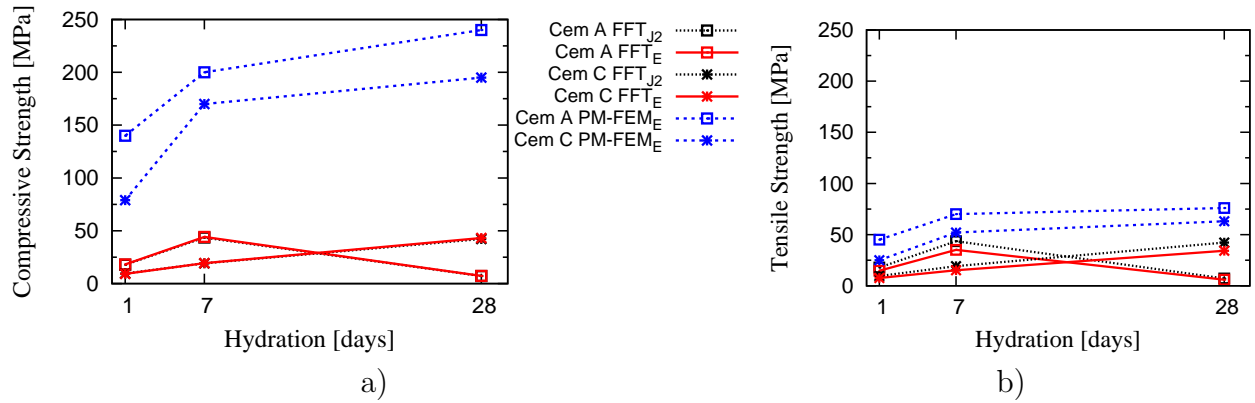


Figure 6.4.3: Compressive and tensile strength, modeled with particle model and elastic limit approximation via *FFT* for CemA and CemC 150 μm RVE microstructures at different age.

As mentioned before for *NIST* microstructure, the particle model gives much higher compressive and tensile strength values. This indeed means that the perfectly brittle assumption is too crude estimate.

It is important to notice that the perfectly brittle assumption could sometimes lead to conceptually wrong results (consider results for CemA at 28 days, Figure 6.4.3). That is obviously due to excessive stress in one of the C-S-H voxels. Further study on that issue is necessary.

Nevertheless, elastic properties obtained from *FFT* method are more accurate com-

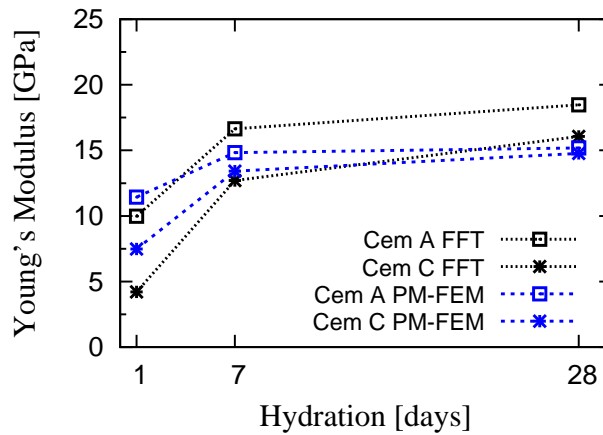


Figure 6.4.4: Elastic moduli calculated with *FFT* and *PM* for CemA and CemC microstructures at different age.

pared to the PM as already discussed.

The effect of hydration on the elastic and strength properties on the level of individual struts was already discussed in Section 6.3.2, showing the improvement of properties with time. The improvement of the properties of struts is reflected by the change of the predicted behavior of microstructures. The longer the hydration, the higher the tensile and compressive strength. Further, it can be seen for both cements that responses in 7 and 28 days are significantly less ductile compared to responses after 1 day.

6.5 Conclusions

In this Chapter, the mean-field strength homogenization approach used in [79], approaches based on the solution of linear-elastic problems with *FEM* and *FFT* and a modified particle model [96] based on [30] were utilized to predict the tensile and compressive strength of three cement pastes. Seven different microstructures were considered: the first one was measured in [17], and the others are simulated using CemHyd3D [16] hydration model for two different types of cements. Two material models of C-S-H were used for every model - *J2* plasticity and the elliptical yield condition resulting from the porous nature of the C-S-H.

The following conclusions can be drawn:

- Methods based on the perfectly brittle assumption applied to heterogeneous stress field resulting from *FEM* and *FFT* calculation or to the second-order stress estimates give inconsistent results for considered microstructures and cannot be used for reliable predictions:

- Second-order stress estimates do not reflect the actual microstructure and significantly overestimate strengths compared to results from *FFT* and *FEM* calculations.
- *FFT* and *FEM* reflect the microstructure, however, the perfectly brittle assumption is significantly dependent on the discretization and should be used very carefully as a strength approximation of cement paste.
- Particle model with *FEM* brittle homogenization of the internodal volume provides simulations of compression without cracking matching favorably the nonlinear *FEM* solution with significantly reduced computational time.
- Cracking of the C-S-H plays an important role in the compressive test and contributes significantly to the difference between the compressive and tensile strengths.
- The size of the microstructure is an important parameter influencing significantly the strength.
- The type of the yield condition (*J2* or elliptic) changes the responses only in the quantitative way while qualitatively the difference is not pronounced.

7 Conclusions

7.1 Conclusions

This thesis deals with three main topics: nanoindentation experiments, their finite element analysis and homogenization of cement paste properties. Let us summarize the main findings for each topic:

7.1.1 Experiments

- The agreement between volume fractions obtained by SNI method, BSE image analysis and XRD is poor. Therefore, what is tested by SNI is not only pure phases (like CH with known elastic properties around 40 GPa), but their intermixture, particularly C-S-H and CH. That is why the volume fraction of CH from SNI is less than that obtained from XRD and BSE.
- The least-square fit of NI results by scaling relationships can have several minima and therefore can result in different C-S-H building block properties even when applied to similar experimental data sets.
- The manual indentation method clearly shows the complexity of the properties of the C-S-H rim around an unhydrated grain, confirming again the hypothesis of intermixture of C-S-H and CH. In the case of alite paste, two distinct peaks in the histogram can be attributed to C-S-H_{HD} (around 30 GPa) and a mixture of C-S-H_{HD} and CH (around 40 GPa). Application to cement paste shows a much bigger scatter.
- An increase of penetration depths leads to a general shift in NI results toward lower elastic moduli. Possible explanations are:
 - The surface roughness is too high for 1 mN indents.
 - There is an effect of damage (2 mN and 4 mN loading).
 - The change of effective media with the increase of indentation depth by increasing the effect of large capillary pores in the vicinity of the indentation point. 500 nm deep indents are shown to lead to a noticeable artificial decrease of the obtained elastic properties, thus the indentation results cannot be trusted.
 - Assuming the RVE size of C-S-H_{LD} to be 500 nm, based on a TEM image, leads to the necessity of penetration depths bigger than usually used (≈ 200 nm) in order to capture the representative properties of C-S-H_{LD}.
- C-S-H properties obtained by the 4-30-4-4 mN loading are in the best agreement with the estimated mean elastic properties of the C-S-H phase. This estimate is based on

the comparison of results from very deep (about $3\ \mu\text{m}$) indents and the results of SC homogenization of cement paste elastic properties based on XRD volume fractions.

7.1.2 Homogenization

- Based on the self-consistent homogenization scheme and Laplace-Carson transform, a semi-analytical procedure for solution of indentation of matrix-pore visco-elastic composite was proposed. Its applicability was demonstrated on a test example. The tip shape can be arbitrary, as long as it is described by constants $C_0 - C_8$.
- Methods based on the perfectly brittle assumption applied to heterogeneous stress field resulting from *FEM* and *FFT* calculation or to the second-order stress estimates give inconsistent results for considered microstructures and cannot be used for reliable predictions:
 - Second-order stress estimates do not reflect the actual microstructure and significantly overestimate strengths compared to results from *FFT* and *FEM* calculations.
 - *FFT* and *FEM* reflect the microstructure, however, the perfectly brittle assumption is significantly dependent on the discretization and should be used very carefully as a strength approximation of cement paste.
- Particle model with *FEM* brittle homogenization of the internodal volume provides simulations of compression without cracking matching favorably the nonlinear *FEM* solution with significantly reduced computational time.
- Cracking of the C-S-H plays an important role in the compressive test and contributes significantly to the difference between the compressive and tensile strengths.
- The size of the microstructure is an important parameter influencing significantly the strength.
- The type of the yield condition (*J2* or elliptic) changes the responses only in a quantitative way while qualitatively the difference is not pronounced.

7.1.3 FE Analysis of NI Experiment

- Study of indentation of elastic matrix-inclusion heterogeneity clearly shows an error induced in the Oliver-Pharr procedure by the presence of the matrix.

- The study of an elliptic-hyperbolic perfectly plastic constitutive equation reveals certain numerical problems while solving the resulting system of nonlinear equations. These problems lead to a false and physically meaningless solutions or low accuracy of the solution. Detailed numerical procedure formulated in 1D is proposed for both elliptic and hyperbolic cases, which allows to overcome the problems above mentioned.
- FEM study of nanoindentation experiment using proposed [110] matrix-pore elasto-plastic constitutive equations with parameters $c_s = 0.39$, $\alpha_s = 0.207$ and porosity $\varphi = 0.24$ clearly reveals the following effect. During the first few iterations, the elements that are in contact with the tip become perfectly plastic, the zone with which the tip is in contact allows any (infinite) displacements without transfer of forces to adjacent elements. As a result, it leads to absolute compaction of these elements and negative volume. A similar effect was demonstrated for von Mises elasto-plastic model. Isotropic hardening was shown to help to overcome this issue. Therefore, it seems that scaling relationships for NI experiments for any model should be obtained using FEM with appropriate loading range, which would correspond to experimentally observed penetration depths.
- Study of cement phases behavior under multicycle NI loading poses additional difficulties even in qualitative description of the second loading cycle.

Bibliography

- [1] P. Acker and F.-J. Ulm. Creep and shrinkage of concrete: physical origins and practical measurements. *Nuclear Engineering and Design*, 203:143–158, 2001.
- [2] A.J. Allen, J.J. Thomas, and H.M. Jennings. Composition and density of nanoscale Calcium-Silicate-Hydrate in cement. *Nature materials*, 6:311–316, 2007.
- [3] D. Atrushi and T. Kanstad. Comparison between tensile and compressive creep of early age high performance concrete (HPC). In G. Pijaudier-Cabot, B. Gerard, and P. Acker, editors, *Creep, shrinkage and durability of concrete and concrete structure. Proceedings of the seventh international conference CONCREEP*, pages 435–440, Nantes, France, 12-14 Septembre 2005.
- [4] Z.P. Bažant. Continuous retardation spectrum for solidification theory of concrete creep. *Journal of engineering mechanics*, 121(2), 1995.
- [5] Z.P. Bažant. Criteria for rational prediction of creep and shrinkage of concrete. *Revue Francaise de Genie Civil* 3, 3-4:61–89, 1999.
- [6] Z.P. Bažant. Creep of concrete. *Encyclopedia of materials: Science and technology*, 2C:1797–1800, 2001.
- [7] Z.P. Bažant, L. Cedolin, and G. Cusatis. Temperature effect on concrete creep modeled by microprestress-solidification theory. In F.-J. Ulm, Z.P. Bažant, and F.H. Wittmann, editors, *Creep, shrinkage and durability mechanics of concrete and other quasi-brittle materials. Proceedings of the syxth international conference CONCREEP-6@MIT*, Cambridge MA, USA, 20-22 August 2001.
- [8] Z.P. Bažant and G. Cusatis. Concrete creep at high temperature and its interaction with fracture: recent progress. In G. Pijaudier-Cabot, B. Gerard, and P. Acker, editors, *Creep, shrinkage and durability of concrete and concrete structure. Proceedings of the seventh international conference CONCREEP*, pages 449–460, Nantes, France, 12-14 Septembre 2005.

- [9] Z.P. Bažant, A.B. Huggard, and S. Baweja. Solidification theory for concrete creep. I: Formulation.
- [10] Z.P. Bažant, A.B. Huggard, and S. Baweja. Solidification theory for concrete creep. II: Verification and application.
- [11] Z.P. Bažant, A.B. Huggard, and S. Baweja. Microprestress-solidification theory for concrete creep. II: Algorithm and verification. 1997.
- [12] Z.P. Bažant, A.B. Huggard, S. Baweja, and F.-J. Ulm. Microprestress-solidification theory for concrete creep. I: Aging and drying effects. 1997.
- [13] F. Beltzung, F.H. Wittmann, and L. Holzer. Influence of composition of pore solution on drying shrinkage. In F.-J. Ulm, Z.P. Bažant, and F.H. Wittmann, editors, *Creep, shrinkage and durability mechanics of concrete and other quasi-brittle materials. Proceedings of the syxth international conference CONCREEP-6@MIT*, Cambridge MA, USA, 20-22 August 2001.
- [14] F. Benboudjema, F. Meftah, A. Sellier, and J.M. Torrenti. A basic creep model for concrete subjected to multiaxial loads. In *In: Proc., 4th int. conf. on fracture mechanics of concrete and concrete structures*, pages 161–168, 2001.
- [15] F. Benboudjema, J.M. Torrenti, and F. Meftah. Effect of basic creep on the early-age behaviour of concrete. In G. Pijaudier-Cabot, B. Gerard, and P. Acker, editors, *Creep, shrinkage and durability of concrete and concreet structure. Proceedings of the seventh international conference CONCREEP*, pages 381–386, Nantes, France, 12-14 Septembre 2005.
- [16] D.P. Bentz. CEMHYD3D: A Three-Dimensional Cement Hydration and Microstructure Developement Modeling Package. version 2.0. Report, Building and Fire Research Laboratory, National Institute of Standards and Technology, Gaithersburg, Mariland 20899, 2000.
- [17] D.P. Bentz, S. Mizell, S. Satterfield, J. Devaney, W. George, P. Ketcham, J. Graham, J. Porterfield, D. Quenard, F. Vallee, H. Sallee, E. Boller, and J. Baruchel. The visible cement data set. *Journal of Research of the National Institute of Standards and Technology*, 107(2):137–148, 2002.
- [18] S. Bishnoi and K.L. Scriviner. mic: A new platform for modelling the hydration of cements. *Cement and Concrete Research*, 39(4):266–274, April 2009.

- [19] M.T. Boudjelal, M. Fafard, B. Bissonnette, and M. Pigeon. Numerical modeling of tensile creep of concrete under variable humidity and relative temperature. In F.-J. Ulm, Z.P. Bažant, and F.H. Wittmann, editors, *Creep, shrinkage and durability mechanics of concrete and other quasi-brittle materials. Proceedings of the syxth international conference CONCREEP-6@MIT*, Cambridge MA, USA, 20-22 August 2001.
- [20] J.J. Brooks. The influence of pore stress on creep of hardened cement paste. In F.-J. Ulm, Z.P. Bažant, and F.H. Wittmann, editors, *Creep, shrinkage and durability mechanics of concrete and other quasi-brittle materials. Proceedings of the syxth international conference CONCREEP-6@MIT*, Cambridge MA, USA, 20-22 August 2001.
- [21] S. Carioua, F.-J. Ulm, and L. Dormieux. Hardness-packing density scaling relations for cohesive-frictional porous materials. *Journal of the Mechanics and Physics of Solids*, 56(3):924–952, 2008.
- [22] P. Ponte Castaneda. Exact second-order estimates for the effective mechanical properties of nonlinear composite materials. *J. Mech. Phys. Solids*, 44(6):827–862, 1996.
- [23] P. Ponte Castaneda. Second-order homogenization estimates for nonlinear composites incorporating field fluctuations: I - theory. *J. Mech. Phys. Solids*, 50:737–757, 2002.
- [24] R. Chamrová. *Modelling elastic properties of the hydrating cement paste from a vector microstructural model*. PhD thesis, EPFL Lausanne, 2010.
- [25] J.J. Chane, L. Sorelli, M. Vandamme, F.-J. Ulm, and G. Chanvillard. A coupled nanoindentation/SEM-EDX study on low water/cement ratio Portland cement paste: Evidence for C-S-H/CH nanocomposites. *to be submitted*, 2010.
- [26] Y-T. Cheng and C-M. Cheng. Scaling, dimensional analysis, and indentation measurements. *Materials Science and Engineering*, R 44:91–149, 2004.
- [27] J.-L. Clement. Is the behaviour of the concrete viscoelastic linear? In G. Pijaudier-Cabot, B. Gerard, and P. Acker, editors, *Creep, shrinkage and durability of concrete and concreet structure. Proceedings of the seventh international conference CON-CREEP*, pages 45–50, Nantes, France, 12-14 Septembre 2005.

- [28] G. Constantinides and F.-J. Ulm. The effect of two types of C-S-H on the elasticity of cement-based materials: Results from nanoindentation and micromechanical modeling. *Cement and Concrete Research*, 34:67–80, 2004.
- [29] G. Constantinides and F.-J. Ulm. The nanogranular nature of C-S-H. *Journal of the Mechanics and Physics of Solids*, 55:64–90, 2007.
- [30] G. Cusatis, Z.P. Bažant, and L. Cedolin. Confinement-Shear Lattice Model for Concrete Damage in Tension and Compression: I. Theory. *Journal of Engineering Mechanics*, 2003.
- [31] G. Cusatis, Z.P. Bažant, and L. Cedolin. Confinement-shear lattice CSL model for fracture propagation in concrete. *Computer Methods in Applied Mechanics and Engineering*, 195(52):7154 – 7171, 2006. Computational Modelling of Concrete.
- [32] G. Cusatis and L. Cedolin. Two-scale study of concrete fracturing behavior. *Engineering Fracture Mechanics*, 74(1-2):3 – 17, 2007. Fracture of Concrete Materials and Structures.
- [33] D. Davydov and M. Jirásek. Modeling of nanoindentation by a visco-elastic porous model with application to cement paste. In Z. Bittnar, V. Šmilauer, P.J.M. Bartos, and J. Zeman, editors, *Nanoindentation in Construction 3*, pages 187–192, Prague, Czech Republic, May 31 - June 2 2009.
- [34] M.J. DeJong and F.-J. Ulm. The nanogranular behavior of C-S-H at elevated temperatures (up to 700 C). *Cement and Concrete Research*, 37:1–12, 2007.
- [35] L. Dormieux, D. Kondo, and F.-J. Ulm. *Microporomechanics*. John Wiley & Sons, Ltd., 2006.
- [36] L. Dormieux, A. Molinari, and D. Kondo. Micromechanical approach to the behavior of poroelastic materials. *J. Mech. Phys. Solids*, 50:2203–2231, 2002.
- [37] B. Eierle and K. Schikora. Computational viscoelasticity of aging materials. In *European conference on computational mechanics*, Munchen, Germany, August 31-September 3 1999.
- [38] J. Eliáš. *Discrete Simulation of Fracture Process in Disordered Materials*. PhD thesis, Brno University of Technology, Faculty of Civil Engineering, 2009.
- [39] J.D. Eshelby. The determination of the elastic field of an ellipsoidal inclusion. *Proceedings of Royal Society*, 241:376–396, 1957.

- [40] J.D. Eshelby. The elastic field outside an ellipsoidal inclusion. *Proceedings of Royal Society*, 252:561–569, 1959.
- [41] M. Frigo and S.G. Johnson. The design and implementation of FFTW3. *Proceedings of the IEEE*, 93(2):216–231, 2005. Special issue on “Program Generation, Optimization, and Platform Adaptation”.
- [42] F.P. Ganneau, F.-J. Ulm, J. Gondzio, and E.J. Garboczi. An algorithm for computing the compressive strength of heterogeneous cohesive-frictional materials - application to cement paste. *Computers and Geotechnics*, (34):254–266, 2007.
- [43] B. Gathier and F.-J. Ulm. Multiscale strength homogenization - application to shale nanoindentation. Master’s thesis, Cambridge, Civil and Environmental Engineering Department, Massachusetts Institute of Technology, 2008.
- [44] E.M. Gatner. A proposed mechanism for the C-S-H during the hydration of tricalcium silicate. *Cement and Concrete Research*, 27(5):665–672, 1997.
- [45] L.P. Granger and Z.P. Bažant. Effects of composition on basic creep of cement paste and concrete. *Journal of engineering mechanics*, 121(11):1261–1270, 1995.
- [46] Z.C. Grasley, J.J. Valenza II, G.W. Scherer, and D.A. Lange. Measuring permeability and bulk modulus of cementitious materials. In G. Pijaudier-Cabot, B. Gerard, and P. Acker, editors, *Creep, shrinkage and durability of concrete and concrete structure. Proceedings of the seventh international conference CONCREEP*, pages 213–218, Nantes, France, 12-14 Septembre 2005.
- [47] Hysitron Inc. User manual, NRL-M-100 v. 8.1.1. *Minneapolis, USA*, <http://www.hysitron.com>, 2007.
- [48] A. Jager, R. Lackner, and J. Eberhardsteiner. Identification of viscoelastic properties by means of nanoindentation taking the real tip geometry into account. *Mechanica*, 42:293–306, 2007.
- [49] J.Bisschop, L. Pel, and J.G.M. van Mier. Effect of aggregate size and paste volume on drying shrinkage microcracking in cement-based composites. In F.-J. Ulm, Z.P. Bažant, and F.H. Wittmann, editors, *Creep, shrinkage and durability mechanics of concrete and other quasi-brittle materials. Proceedings of the syxth international conference CONCREEP-6@MIT*, Cambridge MA, USA, 20-22 August 2001.
- [50] J.Bolander, S.Berton, and E.Emerick. Inclusion interacitno effects on cocrrete creep. In F.-J. Ulm, Z.P. Bažant, and F.H. Wittmann, editors, *Creep, shrinkage and durability mechanics of concrete and other quasi-brittle materials. Proceedings of the*

- syxth international conference CONCREEP-6@MIT*, Cambridge MA, USA, 20-22 August 2001.
- [51] H.M. Jennings. Colloid model of C-S-H and implications to the problem of creep and shrinkage. *Materials and Structures, Concrete Structures and Engineering*, 37:59–70, 2004.
- [52] H.M. Jennings. Refinements to colloid model of C-S-H in cement: CM-II. *Cement and Concrete Research*, 38:275–289, 2008.
- [53] H.M. Jennings, J.J. Thomas, J.S. Gevrenov, G. Constantinides, and F.-J. Ulm. Nanostructure of C-S-H gel in cement paste as a function of curing conditions and relative humidity. In G. Pijaudier-Cabot, B. Gerard, and P. Acker, editors, *Creep, shrinkage and durability of concrete and concreet structure. Proceedings of the seventh international conference CONCREEP*, pages 19–37, Nantes, France, 12-14 Septembre 2005.
- [54] H.M. Jennings, J.J. Thomas, J.S. Gevrenov, G. Constantinides, and F.-J. Ulm. Nanostructure of c-s-h gel in cement paste as a function of curing conditions and relative humidity. In G. Pijaudier-Cabot, B. Gerard, and P. Acker, editors, *Creep, shrinkage and durability of concrete and concreet structure. Proceedings of the seventh international conference CONCREEP*, pages 19–37, Nantes, France, 12-14 Septembre 2005.
- [55] H.M. Jennings, J.J. Thomas, J.S. Gevrenov, G. Constantinides, and F.-J. Ulm. A multi-technique investigation of the nanoporosity of cement paste. *Cement and Concrete Research*, 37:329–336, 2007.
- [56] G. Ji, O. Bjontegaard, D. Atrushi, T. Kanstad, and E.J. Sellevold. Compressive and tensile creep of young concrete with mineral additives. In G. Pijaudier-Cabot, B. Gerard, and P. Acker, editors, *Creep, shrinkage and durability of concrete and concreet structure. Proceedings of the seventh international conference CONCREEP*, pages 369–374, Nantes, France, 12-14 Septembre 2005.
- [57] M. Jirásek and Z.P. Bažant. *Inelastic analysis of structures*. John Wiley & Sons, Ltd., 2002.
- [58] J.-E. Jonasson, M. Larson, and S. Utsi. Linear logarithmic creep model. In G. Pijaudier-Cabot, B. Gerard, and P. Acker, editors, *Creep, shrinkage and durability of concrete and concreet structure. Proceedings of the seventh international conference CONCREEP*, pages 375–380, Nantes, France, 12-14 Septembre 2005.

- [59] P. Kabele, D. Davydov, P. Jun, J. Nemeček, and M. Jirásek. Study of micromechanical behavior of cement paste by integration of experimental nanoindentation and numerical analysis. In *Concreep 08*, Ise-Shima, Japan, 2008.
- [60] J.-Y. Kim, S.-K. Kang, J.-J. Lee, J.-I. Jang, Y.-H. Lee, and D. Kwon. Influence of surface-roughness on indentation size effect. *Acta Materialia*, 55:3555–3562, 2007.
- [61] K. Willam and I. Rhee. Multi-resolution analysis of heterogeneous concrete materials at two-scales of observation. In F.-J. Ulm, Z.P. Bažant, and F.H. Wittmann, editors, *Creep, shrinkage and durability mechanics of concrete and other quasi-brittle materials. Proceedings of the syth international conference CONCREEP-6@MIT*, Cambridge MA, USA, 20-22 August 2001.
- [62] Q.V. Le, Y. Le Pape, F. Meftah, and Q.C. He. Upscaling techniques for modeling the basic creep of cement paste. In G. Pijaudier-Cabot, B. Gerard, and P. Acker, editors, *Creep, shrinkage and durability of concrete and concrete structure. Proceedings of the seventh international conference CONCREEP*, pages 113–118, Nantes, France, 12-14 Septembre 2005.
- [63] E.H. Lee and J.R.M. Radok. The contact problem for viscoelastic bodies. *Journal of Applied Mechanics*, 82:438–444, 1960.
- [64] J. Macht, R. Lackner, C. Hellmich, and H.A. Mang. Numerical modeling of tensile creep of concrete under variable humidity and relative temperature. shotcrete creep properties - review of material test and structural analyses of tunnels. In F.-J. Ulm, Z.P. Bažant, and F.H. Wittmann, editors, *Creep, shrinkage and durability mechanics of concrete and other quasi-brittle materials. Proceedings of the syth international conference CONCREEP-6@MIT*, Cambridge MA, USA, 20-22 August 2001.
- [65] J.C. Michel, O. Lopez-Pamies, P. Ponte Castaneda, and N. Triantafyllidis. Microscopic and macroscopic instabilities in finitely strained porous elastomers. *Journal of the Mechanics and Physics of Solids*, 55:900–938, 2007.
- [66] J.C. Michel, H. Moulinec, and P. Suquet. Effective properties of composite materials with periodic microstructure: a computational approach. *Comput. Methods Appl. Mech. Engrg.*, 172:109–143, 1999.
- [67] J.C. Michel, H. Moulinec, and P. Suquet. A computational scheme for linear and non-linear composites with arbitrary phase contrast. *Int. J. Numer. Meth. Engng.*, 52:139–160, 2001.

-
- [68] M. Miller, C. Bobko, M. Vandamme, and F.-J. Ulm. Surface roughness criteria for cement paste nanoindentation. *Cement and Concrete Research*, 38(4):467–476, April 2008.
- [69] S. Mindess and S. Diamond. A device for direct observation of cracking of cement paste or mortar under compressive loading within a scanning electron microscope. *Cement and Concrete Research*, 12(5):569 – 576, 1982.
- [70] J.J. More, B.S. Garbow, and K.E. Hillstorn. User Guide for MINPACK-1, Argonne National Laboratory Report ANL-80-74. Report, Argonne, III, 1980.
- [71] H. Moulinec and P. Suquet. Numerical method for computing the overall response of nonlinear composites with complex microstructure. *Comput. Methods Appl. Mech. Engrg*, (157):69–94, 1998.
- [72] H. Moulinec and P. Suquet. Comparison of fft-based methods for computing the response of composites with highly contrasted mechanical properties. *Physica B*, 338:58–60, 2003.
- [73] K.M. Nemati. Volume changes and creep of concrete. <http://courses.washington.edu/cm425/SHR&CRE.pdf>, 2007.
- [74] C.M. Neubauer, H.M Jennings, and E.J. Garboczi. A three-phase model of the elastic and shrinkage properties of mortar. *Advanced cement based materials*, (4):6–20, 1996.
- [75] O.R.B. Nogales. *Nonlinear modelling of concrete structures*. Ph.D. thesis, Czech Technical University, 2007.
- [76] I. Odler. Discussion of the paper A model for the microstructure of calcium silicate hydrate in cement pastes by H. M. Jennings. *Cement and Concrete Research*, 30:1337–1338, 2000.
- [77] W.C. Oliver and G.M. Pharr. An improved technique for determining hardness and elastic modulus using load and displacement sensing indentation experiments. *Material Research*, 7:1564–1582, 1992.
- [78] D. Panneerselvam and V.P. Panoskaltsis. A nonlinear viscoelastic model for concrete’s creep and creep failure. In *15th ASCE Engineering Mechanics Conference*, Columbia University, New York, June 2-5 2002.

- [79] B. Pichler, C. Hellmich, and J. Eberhardsteiner. Spherical and acicular representation of hydrates in a micromechanical model for cement paste: prediction of early-age elasticity and strength. *Acta Mech*, 203(3-4):137–162, 2009.
- [80] B. Pichler, C. Hellmich, and H.A. Mang. A combined fracture-micromechanics model for tensile strain-softening in brittle materials, based on propagation of interacting microcracks. *International journal for numerical and analytical methods in geomechanics*, (31):111–132, 2007.
- [81] C. Pichler, R. Lackner, and H.A. Mang. Multiscale model for early-age creep of cementitious materials. In G. Pijaudier-Cabot, B. Gerard, and P. Acker, editors, *Creep, shrinkage and durability of concrete and concrete structure. Proceedings of the seventh international conference CONCREEP*, pages 361–367, Nantes, France, 12-14 Septembre 2005.
- [82] C. Pichler, R. Lackner, and F.-J. Ulm. Identification of logarithmic-type creep of Calcium-Silicate-Hydrates (CSH) by means of nanoindentation. *Strain*, 45(1):17–25, 2008.
- [83] O. Pierard. *Micromechanics of inclusion-reinforced composites in elasto-plasticity and elasto-viscoplasticity: modeling and computation*. Ph.D. thesis, Universite Catholique de Louvain, 2006.
- [84] T. C. Powers and T. L. Brownyards. Studies of the physical properties of hardened cement paste. Bulletin 22, Research Laboratories of the Portland Cement Association, Chicago, 1948.
- [85] I.G. Richardson. Tobermorite/jennite- and tobermorite/calcium hydroxide-based models for the structure of C-S-H: applicability to hardened pastes of tricalcium silicate, β -dicalcium silicate, Portland cement, and blends of Portland cement with blast-furnace slag, metakaolin, or silica fume. *Cement and Concrete Research*, (34):1733–1777, 2004.
- [86] H. Sadouki and F.H. Wittmann. Shrinkage and microcracking in the composite structure of normal and high strength concrete. In F.-J. Ulm, Z.P. Bažant, and F.H. Wittmann, editors, *Creep, shrinkage and durability mechanics of concrete and other quasi-brittle materials. Proceedings of the syxth international conference CONCREEP-6@MIT*, Cambridge MA, USA, 20-22 August 2001.
- [87] J. Sanahuja, L. Dormieux, and G. Chanvillard. Modelling elasticity of a hydrating cement paste. *Cement and Concrete Research*, 37:1427–1439, 2007.

- [88] B.A. Schrefler, D. Gawin, and F. Pesavento. Modelling of concrete as a multiphase viscous porous material. In G. Pijaudier-Cabot, B. Gerard, and P. Acker, editors, *Creep, shrinkage and durability of concrete and concrete structure. Proceedings of the seventh international conference CONCREEP*, pages 77–82, Nantes, France, 12-14 Septembre 2005.
- [89] K.L. Scrivener. The microstructure of concrete. In J.P. Skalny, editor, *Materials Science of Concrete I*, American Ceramic Society, Westerville, OH, 1989.
- [90] K.L. Scrivener. Microscopy methods in cement and concrete science. *World cement research and development*, pages 92–112, 1997.
- [91] K.L. Scrivener. Backscattered electron imaging of cementitious microstructures: understanding and quantification. *Cement and concrete composites*, 26:935–945, 2004.
- [92] K.L. Scrivener. The interfacial transition zone (ITZ) between cement paste and aggregate in concrete. *Interface science*, 12:409–419, 2004.
- [93] K.L. Scrivener. Quantitative study of portland cement hydration by X-ray diffraction. reitveld analysis and independent methods. *Cement and Concrete Research*, 34:1541–1547, 2004.
- [94] J. Sercombe, C. Hellmich, F.J. Ulm, and H. Mang. Modeling of Early-Age Creep of Shotcrete. I: Model and Model Parameters. *Journal of Engineering Mechanics*, 126(3):284–291, 2000.
- [95] M.M. Silvosio, E.M.R. Fairbairn, and R.D. Toledo Filho. Early-age analysis of a foundation slab: sensitivity to creep parameters. In G. Pijaudier-Cabot, B. Gerard, and P. Acker, editors, *Creep, shrinkage and durability of concrete and concrete structure. Proceedings of the seventh international conference CONCREEP*, pages 429–434, Nantes, France, 12-14 Septembre 2005.
- [96] J. Skoček. *Fracture propagation in cementitious materials, Multi-scale approach: measurements and modeling*. PhD thesis, Technical University of Denmark, 2010.
- [97] I.N. Sneddon. The relation between load and penetration in the axisymmetric Boussinesq problem for a punch of arbitrary profile. *International journal of Engineering and Science*, 3:47–57, 1965.
- [98] L. Sorelli, G. Constantinides, F.-J. Ulm, and F. Toutlemonde. The nano-mechanical signature of Ultra High Performance Concrete by statistical nanoindentation techniques. *Cement and Concrete Research*, 38:1447–1456, 2008.

-
- [99] S. Speziale, H.J. Reichmann, F. Schilling, H.R. Wenk, and P.J.M. Monteiro. Determination of the elastic constants of portlandite by Brillouin spectroscopy. *Submitted to CCR*, 2010.
- [100] H. Stehfest. Numerical inversion of laplace transforms. *Communications of the ACM*, 13(1):438–444, 1970.
- [101] B.T. Tamtsia and J.J. Beaudoin. Basic creep of hardened cement paste. a re-examination of the role of water. *Cement and Concrete Research*, 30:1465–1475, 2000.
- [102] J.J. Thomas and H.M. Jennings. A colloidal interpretation of chemical aging of the C-S-H gel and its effects on the properties of cement paste. *Cement and Concrete Research*, 36(1):3038, 2006.
- [103] F.-J. Ulm. Private communication at NICOM3 conference. *Prague*, 2009.
- [104] F.-J. Ulm and O. Coussy. Couplings in early-age concrete: from material modeling to structural design. *International Journal of Solids Structures*, 35(31-32):4295–4311, 1998.
- [105] F.-J. Ulm and M. Vandamme. Probing nano-structure of C-S-H by micro-mechanics based indentation techniques. In Z. Bittnar, V. Šmilauer, P.J.M. Bartos, and J. Zeman, editors, *Nanoindentation in Construction 3*, pages 43–53, Prague, Czech Republic, May 31 - June 2 2009.
- [106] K. van Breugel. Simulation of hydration and formation of structure in hardening cement-based materials. *Cement and Concrete Research*, 25(2):319–331, 1995.
- [107] K. van Breugel and S.J. Lokhorst. Numerical simulation of the effect of microstructural development on creep of hardening concrete. In F.-J. Ulm, Z.P. Bažant, and F.H. Wittmann, editors, *Creep, shrinkage and durability mechanics of concrete and other quasi-brittle materials. Proceedings of the syxth international conference CONCREEP-6@MIT*, Cambridge MA, USA, 20-22 August 2001.
- [108] Jan G.M. van Mier. *Fracture processes of concrete*. 1997.
- [109] M. Vandamme and F.-J. Ulm. Viscoelastic solutions for conical indentation. *International Journal of Solids Structures*, 43:3142–3165, 2006.
- [110] M. Vandamme and F.-J. Ulm. *The nanogranular origin of concrete creep: A nanoindentation investigation of microstructure and fundamental propeties of calcium-silicate-hydrates*. Ph.D. thesis, Massachusetts Institute of Technology, 2008.

- [111] V. Šmilauer. *Elastic properties of hydrating cement paste determined from hydration models*. PhD thesis, Czech Technical University in Prague, Faculty of Civil Engineering, Czech Technical University in Prague, Prague, Czech Republic, 2005.
- [112] X. Xu, L. Lohaus, and M.J. Setzer. Damping behaviour of hardened cement paste in a temperature range between 20c and 80c: Effect of the disjoining pressure. In F.-J. Ulm, Z.P. Bažant, and F.H. Wittmann, editors, *Creep, shrinkage and durability mechanics of concrete and other quasi-brittle materials. Proceedings of the syxth international conference CONCREEP-6@MIT*, Cambridge MA, USA, 20-22 August 2001.
- [113] Z.L. Zhang. Explicit consistent tangent moduli with a return mapping algorithm for presure-dependent elastoplasticity models. *Comput. Methods Appl. Mech. Engrg.*, 121:29–44, 1995.
- [114] Z.L. Zhang. On the accuracies of numerical integration algorithms for Gurson-based pressure-dependent elastoplastic consitutive models. *Comput. Methods Appl. Mech. Engrg.*, 121:15–28, 1995.
- [115] W. Zhu, J.J. Hughes, N. Bicanic, and C.J. Pearce. Nanoindentation mapping of mechanical properties of cement paste and natural rocks. *Materials Characterization*, 58:1189–1198, 2007.
- [116] Goangseup Zi and Z.P. Bažant. Continuous relaxation spectrum of concrete creep and its incorporatoin into microplane model m4. In F.-J. Ulm, Z.P. Bažant, and F.H. Wittmann, editors, *Creep, shrinkage and durability mechanics of concrete and other quasi-brittle materials. Proceedings of the syxth international conference CONCREEP-6@MIT*, Cambridge MA, USA, 20-22 August 2001.